Universiteit Antwerpen

Chemical kinetics modeling of non-equilibrium and thermal effects in vibrationally active CO_2 plasmas

Proefschrift voorgelegd tot het behalen van de graad van doctor in de Wetenschappen aan de Universiteit Antwerpen te verdedigen door

Vincent Vermeiren

Promotor: prof. dr. Annemie Bogaerts

Antwerpen, 2020

Contents

List of Figures

List of Tables

Acknowledgments

Aan het begin van mijn doctoraat was ik er reeds van overtuigd dat een goede promotor een cruciaal element was. Dat ben ik nog steeds. Daarom wil ik eerst en vooral mijn promotor Annemie bedanken. Naast een uitzonderlijke academische carrière, waarvan het bewijs met een simpele Google search te vinden valt, heb ik ook bewondering voor uw uitzonderlijke efficiëntie, en uw warme persoonlijkheid. U bent een promotor waarop je kan rekenen. Bedankt om uw vertrouwen in mij te stellen.

Daarnaast wil ik ook Erik en Kristof bedanken voor de interessante gesprekken in de coffeeroom, en de hulp die ik van jullie altijd kon krijgen. Ik bedank Kristof speciaal op deze plek omdat het gewoon een kwestie van tijd is.

Next I want to specifically thank Antonin for all the insight you have offered me throughout the years, even after you left the group. You helped me get a grip on this complex, and sometimes a bit chaotic, research topic. I am glad I got to continue from your work, and very much enjoyed collaborating with you.

Your colleagues are a big part of what makes you want to come to work in the morning. Throughout the years I had the pleasure of meeting a lot of nice and interesting people from remote places like Bulgaria, France, China, India, Ireland, Italy, Iran, Lebanon, the Netherlands, Russia, Sweden, USA, Uzbekistan and of course Koningshooikt. Thanks to all of you for making PLASMANT a great place to work at!

I want to thank the members of the 'coffeebreak group', that took on many different forms throughout the years, for the laughs we shared, and the important discussions about the status of Stijn's dating life. Even during lockdown, our online coffee breaks could really brighten my day.

Thanks also to Antonin, Georgi, Inne, Jonas, Kristof, Stijn, Yannick E and Yannick U, Fanny, and the children (i.e. Claudia, Eline, Elise, and Senne) for the moments we shared outside the office. For the dinner parties, the pool parties with photoshoots, the Theo managed meat lovers birthday BBQs, the Polish birthday

parties with way too much food, the game nights, and the kubb tournaments. Also thanks to Antonin, Georgi, Inne, Maryam, and Quan-Zhi, for the trip we took to Bordeaux-Poitiers and to Georgi (and his uncle) for the trip to Bansko. I also wish the children the best of luck with the rest of their PhD.

Throughout the years, I shared my office with different people. While there was always a nice atmosphere, I was fortunate to end with the best. Thanks to Charlotte, Fanny, and Joachim for the nice times we shared.

I would also like to thank Karel, Luc, Fabiana, and Ingrid for always giving me the technical and administrative help whenever needed, and also Antonin, Georgi, Kevin, Fatme, and Weizong, for always brainstorming about different issues I was facing.

Next, I would like to thank my former colleagues of the department of physics; Matthias, Jonathan, Wout, Rebeca and Victor, for keeping in touch with a defector like me during the past four years. I also owe you all a lot for helping me get through the first five years of university.

Voorts wil ik ook de GZ en 6WeWiB bedanken. Tien jaar nadat we samen afstudeerden vind ik het nog altijd geweldig om met jullie af te spreken. Bedankt voor de weekendjes, cafébezoeken, feesten, en housewarmings. Ik hoop dat we deze activiteiten nog lang kunnen blijven doen. Bedankt ook aan Lies en Tom voor de gezellige etentjes, en aan Jonathan voor de rondleidingen in Gent, en de jeneverkes in het dreupelkot.

Ook wil ik Annelien en Yves bedanken voor de leuke momenten tijdens de kookles. Na deze jaren kunnen we nu verrassend lekkere dingen op ieders bord toveren, met af en toe een beetje pezomus. Ook bedankt voor de pannenkoekenclub, de etentjes, de trip naar Saint-Amant-de-Montmoreau.

Deze tekst zou niet compleet zijn zonder mijn ouders te bedanken. Liefste mams en paps! Met dit doctoraat sluit ik tien jaar universiteit af. Dit zijn voor mij soms uitdagende jaren geweest, die ik niet zonder jullie steun tot een succesvol einde had kunnen brengen. Bedankt om er zowel op de goede als slechte momenten voor mij te zijn. Ik heb zowel mijn verleden als mijn toekomst aan jullie te danken. Ik zie jullie heel graag!

Daarnaast wil ik ook mijn broer Rik bedanken. Jouw humor en positiviteit zorgen altijd voor geweldige momenten. Bedankt voor alle steun, en om de meest fantastische broer te zijn die ik had kunnen krijgen.

Bedankt ook aan mijn oma's en opa's, nonkels en tantes, neven, nichten, petekind, en schoonfamilie om te vragen hoe het met het doctoraat ging, voor de succeswensen, de gebrande kaarsen, de felicitaties, en de moeite om mijn doctoraatstitel van buiten te leren.

Tenslotte wil ik nog de belangrijkste persoon bedanken. Allerliefste Inne! Met twee doctoraten op twee jaar hebben we onze portie stress hopelijk voor

even gehad! Ik ben ongelooflijk blij dat ik je heb leren kennen tijdens deze reis. Je bedanken met zo een klein stukje tekst is eigenlijk oneerlijk. Je gaf me tijdens de jaren zowel praktische als emotionele steun op de momenten dat het moeilijk ging. Onder elke omstandigheid deed je altijd je best voor mij. Een belangrijk deel van dit doctoraat is dan ook mee jouw verdienste. Bedankt voor al deze moeite, en voor alle mooie momenten die we samen deelden! Ik zie je enorm graag en kijk uit naar onze toekomst samen.

CHAPTER 1

Introduction

1.1 General introduction

Since the industrial revolution of the nineteenth century, the global energy demand has continued to increase. Up till today, the primary source to meet this demand comes from the combustion of fossil fuels. The burning of these fuels results in the emission of greenhouse gases into the atmosphere, leading to an increase in the average global temperature. There is now a broad agreement in the scientific community that this increase in emissions, and average global temperature, is correlated with ocean level rising, and more frequent occurrence of extreme weather phenomena like droughts, floods and hurricanes. In order to prevent a further increase of greenhouse gas concentrations in the atmosphere, a huge effort is being directed into reducing the anthropogenic emissions. This is either done by reducing the source emission by the use of increased energy-efficient or low carbon processes, or by capturing the greenhouse gases before emission and either storing them or using them as feedgas to create value-added products. For CO_2 these processes are known as carbon capture and storage (CCS) and carbon capture and utilization (CCU).

Given that the main contribution to global warming comes from energy production, the sector is preparing for the so-called *energy transition* in which a shift is made to more renewable forms of energy production which include wind, solar, and hydrothermal energy sources. While most of these renewable energy sources are becoming more cost competitive with their fossil fuel counterparts, the biggest problem that is halting further implementation of these techniques is their intermittent nature, resulting in a mismatch of supply and demand. This mismatch can be solved by storing the excess electrical energy.

Plasma-based CO_2 conversion allows us to use the excess electrical energy of the renewable energy sources to convert CO_2 into more value-added products and liquid fuels.

1.1.1 Earth's energy budget

While mankind's primary energy source consists out of the combustion of fossil fuels, most of the energy on earth comes from incoming solar radiation. This solar radiation is composed out of ultraviolet to infrared wavelengths [1;2]. While some energy is absorbed and reflected through passage (see figure 1.1), much of the energy reaches the earth's surface, and is absorbed there [1–4]. As the surface warms, some of the absorbed energy is reradiated as infrared radiation. A part of the emitted energy is returned to the earth's surface as back radiation by gases that are sensitive to infrared radiation. These gases are called greenhouse gases, and they play a vital role in keeping the temperature on earth high enough to

create a habitable environment for all living organisms. Without the influence of these gases on the climate, earth would be 30 °C cooler than it is today[1]. The most important natural greenhouse gases are CO_2, CH_4, N_2O, and water vapour. Molecules with a strong infrared absorption have a larger contribution to the back radiation. The strength of this contribution is characterized by the greenhouse potential, also known as the global warming potential (GWP). All values are calibrated with respect to CO_2, whose value is 1. While CO_2 and water vapour are more abundant in the atmosphere, the GWP of some gases with a lower concentration is much higher. Indeed, CH_4 has a GWP of 28, and for N_2O the GWP reaches 265.[2] In order to have an equilibrium climate, a balance needs to exist between the incoming and outgoing radiation. With an increase in greenhouse gas concentrations, more radiant heat is absorbed, leading to an increase in global temperatures.

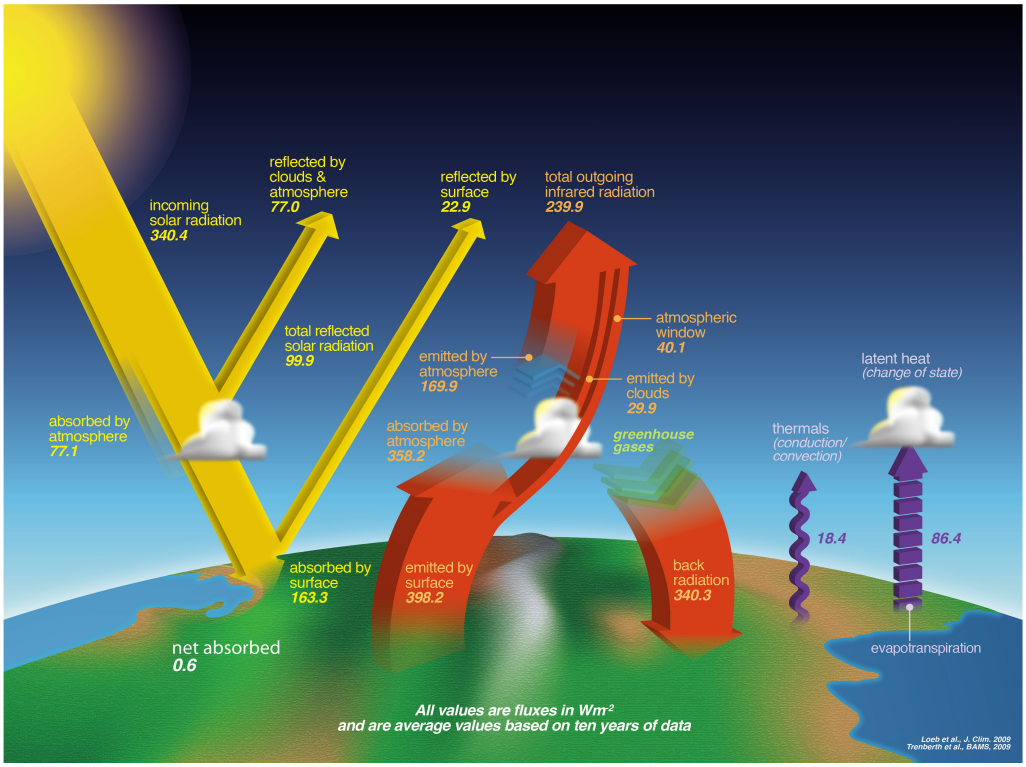

Figure 1.1: Earth's energy budget, showing the incoming and outgoing energy. Figure is taken from ref. 5, based upon data from ref. 3;4

1.1.2 Global warming

The realization that earth's climate might be sensitive to the atmospheric concentrations of gases that create a greenhouse effect is more than a century old.

The first greenhouse experiments in 1760 demonstrated the ability to artificially warm the earth's surface[6]. Through these experiments, it was recognised that air itself could trap thermal radiation. In 1859, John Tyndall identified through laboratory experiments the absorption of thermal radiation of complex molecules (as opposed to the primary atmospheric constituents, N_2 and O_2)[7]. He discovered that changes in the amount of any of the radiatively active constituents of the atmosphere, such as H_2O and CO_2, could explain changes in the climate. G. S. Callendar was the first to theoretically link greenhouse gases with climate change in 1938[8]. He found that a doubling of the atmospheric CO_2 concentration resulted in an increase in the mean global temperature of about 2°C, with considerably more warming at the poles. He already linked the increasing fossil fuel combustion that was supplying the growing energy demand, with a rise in CO_2 concentrations and its greenhouse gas effect.

Since the industrial revolution, antropogenic greenhouse gas emissions are increasing. Of the emitted greenhouse gases, CO_2 is the most important one. In 2015, the contribution from CO_2 to the antropological greenhouse gas potential was 74%. The other emissions came from CH_4 (18.8 %), NO_2 (5.2%), and fluorinated gases (F-gases) (2%)[9]. There is growing evidence[10] and consensus[11] in the scientific community that these emissions are increasing the global temperature. The strong correlation between the increasing CO_2 concentration and rise in global temperatures is illustrated in figure 1.2. The increased awareness led to the Paris climate agreement, which was ratified by 188 countries and the European Union, in which the parties pledged to keep the increase in the average global temperature to 1.5 °C[12] with respect to pre-industrial levels.

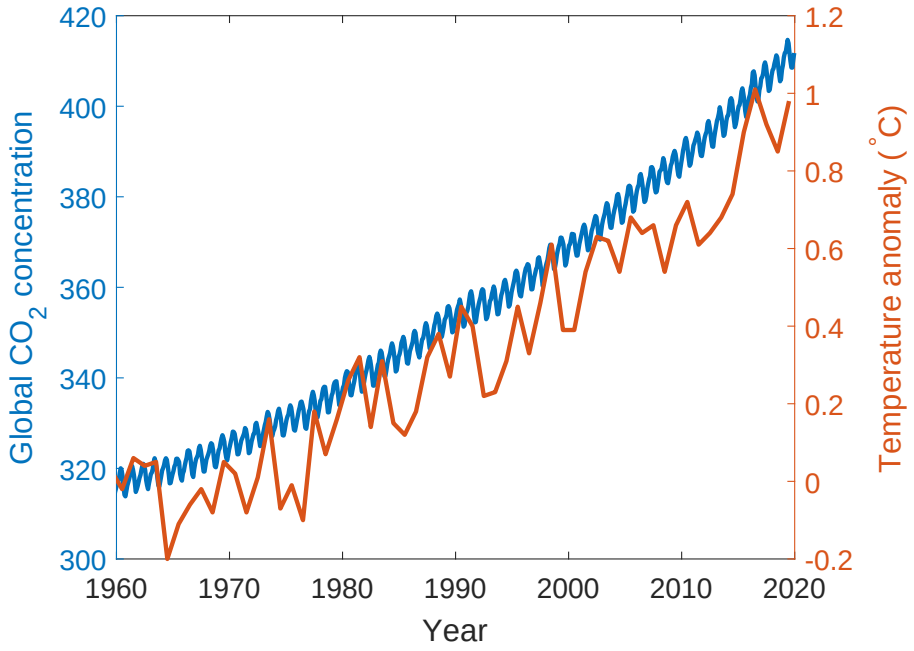

Figure 1.2: Time-evolution of the atmospheric CO_2 concentration (left y-axis) and globally-averaged temperature anomaly since 1960 with respect to the averaged temperature from 1951 to 1980 (right y-axis). Data obtained from NASA/NOAA [13].

1.2 Reshaping the energy landscape

The pledge to keep global warming below 1.5 °C requires a drastic decrease in anthropogenic carbon emissions. With no or limited overshoot, CO_2 emissions should be reduced to net zero by 2050 [14]. This shift towards a carbon-neutral economy requires efforts in multiple different sectors. However, the challenges are different, depending on the sector. Figure 1.3 shows the CO_2 emissions related to different energy services [15], in which the difficult-to-eliminate emissions are highlighted. The latter represent about 27 % of the total emissions. The largest contribution comes from load-following electricity. This phenomenon is a result of the intermittency of renewable energy sources like wind and solar energy, whose production depends on the weather conditions. An energy system in which variable energy sources are major suppliers of electricity will have occasional but substantial and long-term mismatches between supply and demand. Natural gas-fired generators have increasingly been used to provide flexibility because of their relatively low fixed costs [15], their ability to ramp up and down quickly [16], and because of the low cost of natural gas [17]. However, without carbon offset, the

greenhouse gas emissions from those power plants will continue to contribute to global warming.

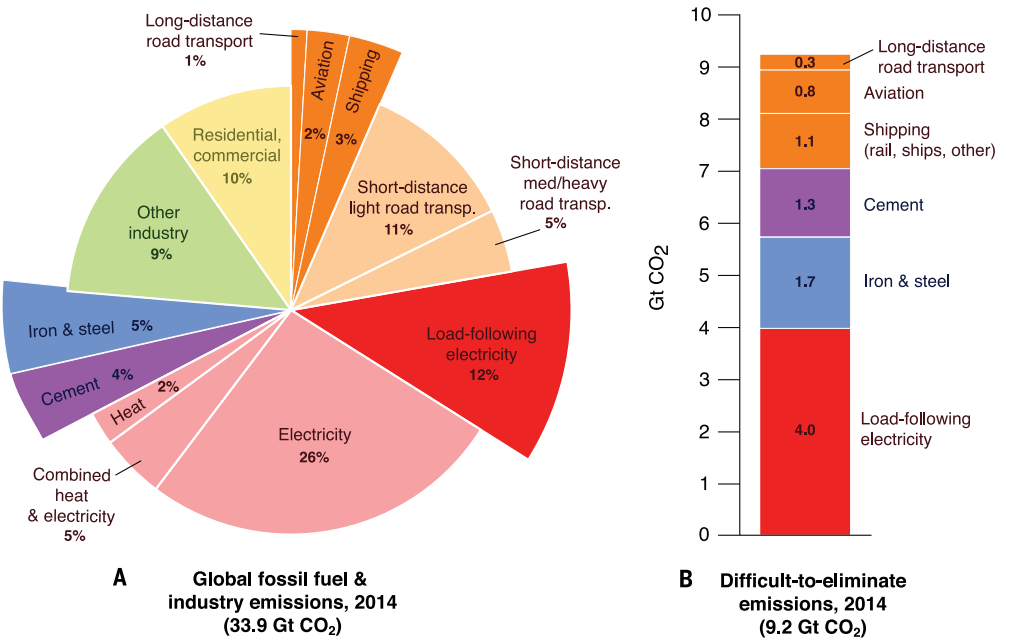

Figure 1.3: A) Estimation of CO_2 emissions related to different energy services, in which the difficult-to-eliminate emissions are highlighted in the extended pie pieces. B) The level of emissions related to difficult-to-decarbonize services. Figure taken from ref. 15.

1.2.1 Energy storage

While the energy productions by these renewables can be smoothed by interconnecting large geographical areas, or by focusing on a mix of different energy sources, additional peak energy storage will be needed to provide the electric grid with the needed flexibility. The existing energy storage techniques can be categorized as

- mechanical: pumped hydrogen storage, compressed air energy storage, and flywheel
- electrochemical: lead-acid, nickle-based, sodium-based, and lithium-ion electrochemical batteries, and redox and hybrid flow batteries
- electrical: supercapacitors and superconducting magnetic energy storage
- thermal: aquiferous and cryogenic low temperature energy storage, and

concrete, phase change materials, and molten salt high temperature energy storage

- chemical: hydrogen and solar fuel

The different technologies that these categories comprise are distinguished by different technical and economical characteristics, such as power density, self-discharge, cycle and discharge efficiency, suitable storage duration, and capital and operation costs[18]. Overviews of these different characteristics and how they positively or negatively affect the implementation of the different techniques can be found in various literature reviews on the matter[18–22].

One of the most attractive aspects of fossil fuels is the fact that they contain high energy density hydrocarbons, making them easily transportable. In figure 1.4 the volumetric and gravimetric energy density of the different storage categories are displayed. From all different techniques, chemical energy storage provides the highest volumetric and gravimetric energy carriers. In chemical energy storage, electric energy is used to enable endothermic reactions to create molecules with a higher formation enthalpy. The exothermic reverse reaction can then be used to release the stored energy.

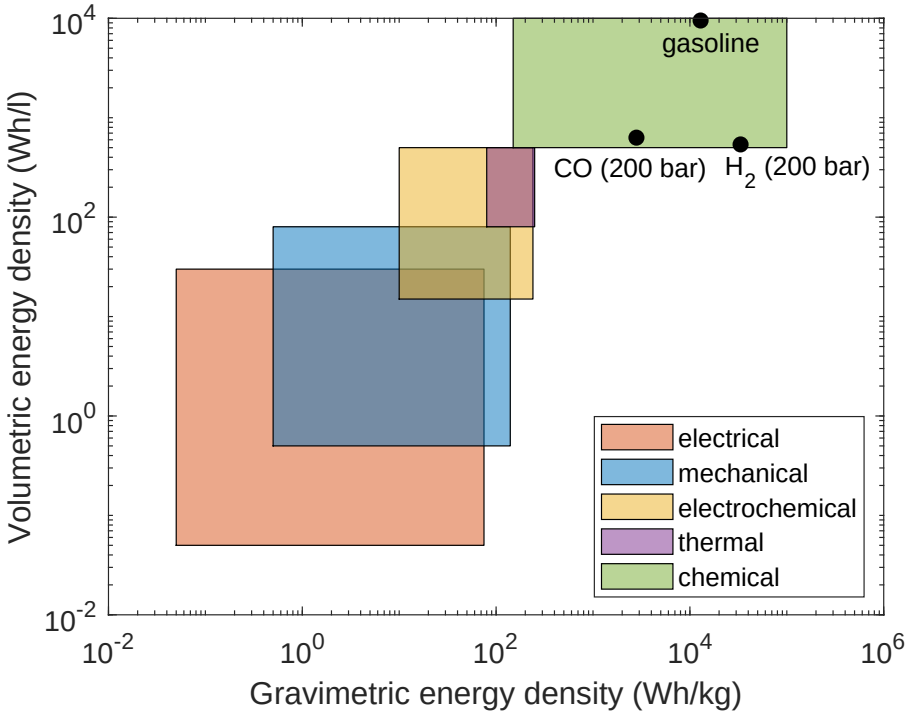

Figure 1.4: Volumetric and gravimetric energy density of the five categories of energy storage, with some specific values for common chemical energy carriers.[15;18]

Two of the main molecules that are used as feedgas for chemical storage are CO_2 and H_2O, creating CO and H_2, respectively. While these gases have a high gravimetric energy density (see figure 1.4) they need to be kept under high pressure in order to reach a higher volumetric energy density. In addition, H_2 is a very small molecule which results in an increased risk of storage leaks[23]. The storage of hydrogen thus requires heavy storage containers[15].

Even in liquid form, these two energy carriers don't posses a high enough volumetric energy density as is the case for liquid hydrocarbons (e.g. gasoline with 9.5 kWh/L, see figure 1.4). These high volumetric energies are however needed in difficult-to-eliminate emission sectors like long-distance transport, aviation and shipping (see figure 1.3).

1.2.2 Synthetic hydrocarbons

Liquid hydrocarbons can also be synthesised through the Fischer-Tropsch process, which uses syngas, a mixture of CO and H_2, as feedgas. The Fischer–Tropsch process involves a series of chemical reactions that produce a variety of hydrocarbons[24]:

$$(2n+1)H_2 + nCO \rightarrow C_nH_{2n+2} + nH_2O \tag{1.1}$$

These reactions occur in the presence of a metal catalyst like Fe, Ni, Co, or Ru[25].

Unfortunately, the Fischer-Tropsch process has a twofold contribution to climate change. Firstly, the combustion of the resulting hydrocarbons produces CO_2, and secondly, fossil fuels are currently used for the production of both H_2 and CO, in processes like coal gasification and methane gas reforming[24;26]. This prohibits a broad implementation of the technology.

There are numerous options for producing low-carbon and renewable hydrogen. The two main options are the fossil fuel-based production processes in which the emitted carbon is captured and stored, or by means of electrolysis using low-carbon power as energy input[26]. In the coming years, renewable electrolytic H_2 production is expected to see a dramatic cost drop, making it cost competitive with so called "grey hydrogen"[26;27].

In order to offset the CO_2 emission from the combustion of the synthetic hydrocarbons, the production of CO should be carbon negative. This can best be achieved by using the CO_2 as feedstock in the production of CO. The scheme that is therefore proposed is shown in figure 1.5.

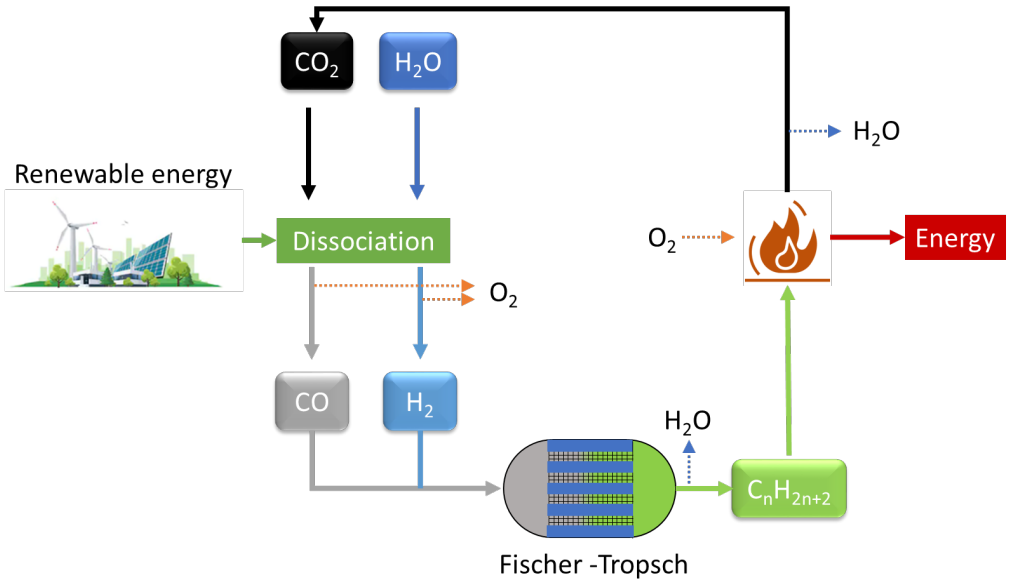

Figure 1.5: The CO_2 neutral solar fuel cycle in which the emitted CO_2 from combustion is captured and converted back into fuels by means of renewable energy.

1.3 CO_2 conversion

The dissociation of CO_2 is an endothermic process that is represented by the following formula

$$CO_2 \rightleftharpoons CO + \frac{1}{2}O_2 \qquad \Delta H^o = 2.93 \frac{\text{eV}}{\text{molec.}} \tag{1.2}$$

In its most efficient form, the process takes place in two steps:

$$CO_2 \rightleftharpoons CO + O \qquad \Delta H^o = 5.51 \frac{\text{eV}}{\text{molec.}} \tag{1.3}$$

$$CO_2 + O \rightleftharpoons CO + O_2 \qquad \Delta H^o = 0.35 \frac{\text{eV}}{\text{molec.}} \tag{1.4}$$

with ΔH^o the standard enthalpy at 300 K. The enthalpy of the first reaction equals the bond breaking energy of the CO_2 molecule. It is very high, since CO_2 is a very stable molecule. The enthalpy of the second reaction is much less, and it is therefore crucial to increase the rate of this reaction in order to reach highly energy-efficient CO_2 conversion[28].

Given the high enthalpy of reaction 1.2, high temperatures are needed to dissociate CO_2. This can be seen in figure 1.6, where the thermodynamic equilibrium

composition of CO_2, CO, O_2 and O is shown as a function of gas temperature, at a pressure of 100 mbar. The mole fractions for the major species under the chemical equilibrium conditions are obtained by minimizing the Gibbs free energy of the mixture at a given pressure and temperature[29]. The maximum achievable energy efficiency lies a little above 50 %.

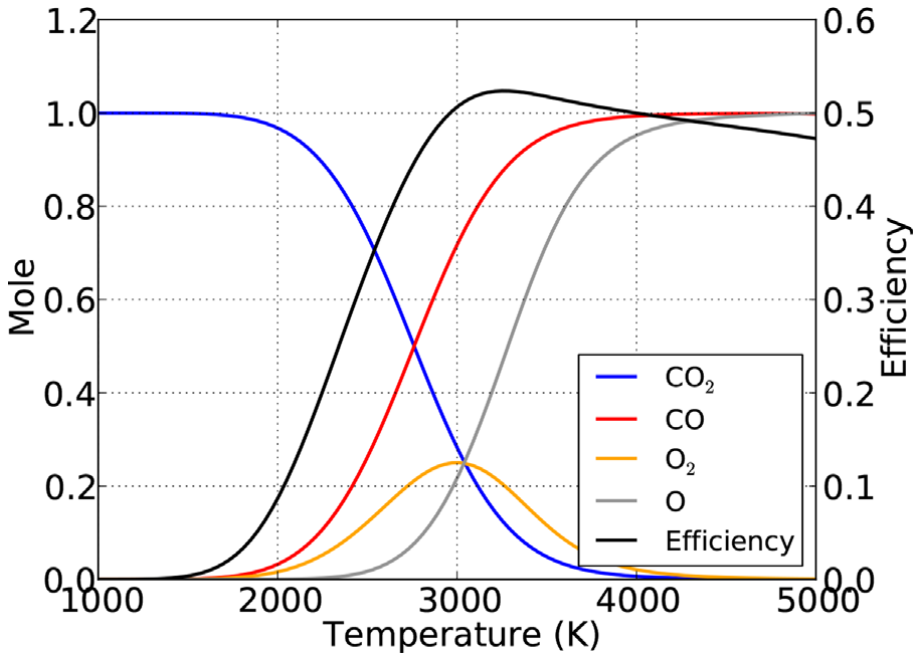

Figure 1.6: The thermodynamic equilibrium composition of CO_2, CO, O_2 and O (left axis), and the corresponding energy efficiency (right axis), as a function of gas temperature, at a pressure of 100 mbar. Figure taken from ref. 29.

The equilibrium compositions of figure 1.6 are for a thermodynamically isolated system. In our work, this is not the case as we include cooling from the reactor walls, when the temperature is calculated self-consistently (i.e. in chapters 5 and 6).

1.4 Plasma-based CO_2 conversion

CO_2 plasmas have gained interest since the invention of CO_2 lasers in 1964[30]. In order to understand the chemical and kinetical processes in the CO_2 lasers, various types of CO_2 plasmas were studied[31–34]. CO_2 plasmas are also of importance in the space community, since CO_2 is an important constituent in many planetary atmospheres. Since CO_2 is the main component of the atmosphere on Mars (> 95 %), non-equilibrium plasmas are discussed as a possible oxygen

supplier in future missions to the planet[35]. Plasma technology gained interest as a possible CO_2 conversion technology when high energy efficiencies of 80-90 % were reported in experiments conducted in the Soviet Union[36;37]. However, these efficiencies have since not been reproduced, and more recent experimental results show maximum efficiencies of around 50 %[29;38;39].

1.4.1 Non-equilibrium plasmas

A plasma is an ionized gas that exists when sufficient energy is added to a gas, liquid or solid to ionize the atoms or molecules. It is therefore sometimes referred to as the "fourth state of matter", although there is no clear transition from the first three states to plasma. A plasma is on average electrically neutral, since the positive and negative charges compensate for each other. The free electric charges -electrons and ions- make the plasma electrically conductive, and strongly responsive to electromagnetic fields.

Next to various types of ions, a plasma also consists of a large number of neutral species, like atoms, molecules, radicals and excited species. The latter can lead to the emission of light by the plasma. Plasmas are estimated to constitute more than 99 % of the visible universe[37]. Next to naturally occurring plasmas, they also serve in man-made applications like electronics, lasers, lamps, and many others[37]. Since the plasma is a multi-component system, it exhibits many different species, each with their own density and temperature. In general, a distinction is made between the electrons and the heavy particles. The plasmas are therefore characterized by their ionization degree (i.e. the density ratio of the charged species to that of the neutral gas), and the temperature of the electrons (T_e) and heavy particles (T_g). The ionzation degree of conventional plasma-chemical systems lies in the range of 10^{-7} - 10^{-4}. The ionization degree is close to unity in thermonuclear plasma systems.

Most plasmas typically have electron temperatures between 1-20 eV[37]. The gas temperature can vary from room temperature in corona and dielectric barrier discharges, to temperatures around 10^8 K in fusion reactors[37]. In electrical discharges, the electrons accumulate most of the energy, since they are much lighter than the heavy particles. A quasi-linear dependence exists between the mean electron energy and the reduced electric field (E/N)[28;37]. The heavy particles subsequently receive their energy through collisions with the high energy electrons. Based upon the temperatures of the electrons and heavy particles, a distinction is made between equilibrium (or thermal) and non-equilibrium (or non-thermal) plasmas. In equilibrium plasmas, the electron and gas temperatures are similar, while in non-equilibrium plasmas, the electron temperature is much higher than the gas temperature. The advantage of thermal plasmas is

that they can reach temperatures of 20000 K or more, whereas the upper limit for burning fossil fuels lies at 2300 K[38]. These types of plasmas are therefore used in metallurgy applications, as well as in the treatment of hazardous waste materials[38;40]. In non-equilibrium plasmas, the electrons acquire enough energy to allow endothermic reactions to take place, either directly or via vibrationally excited states. In this way, the energy can selectively be used to allow these reactions to take place without the necessity to heat the gas. This makes non-equilibrium plasmas particularly interesting for CO_2 conversion.

1.4.2 Dissociation pathways

As mentioned in section 1.4.1, the electrons accumulate most of the electromagnetic energy, since they are much lighter than the heavy particles. The electron energy is subsequently transferred to the heavy particles upon collisions. At low electron temperatures, most of the energy goes into the vibrational levels of CO_2. CO_2 has three vibrational modes (see figure 1.7). These modes are written as (v_1,$v_2^{l_2}$,v_3), where v_1, v_2, and v_3 are the quantum numbers of the symmetric stretch mode, the symmetric bending mode, and the asymmetric stretch mode, respectively. The bending mode of a linear molecule is doubly degenerate. This degeneracy causes an angular momentum around the molecular axis[41]. The quantum number l_2 is associated with the resulting angular momentum, and can take the value of $l_2 = v_2, v_2\text{-}2,\ldots,1$ or 0. Each level (0,$v_2^{l_2}$,0) with $l_2 \neq 0$ is doubly degenerate. Note that additional degeneracies exist between the symmetric stretch and the bending mode levels, since the energy of level $(1, 0, 0)$ is very close to that of level $(0, 2^l, 0)$. The resonance that exists between these levels will be the basis of grouping the symmetric vibrational levels in our model, as will be explained in chapter 3.

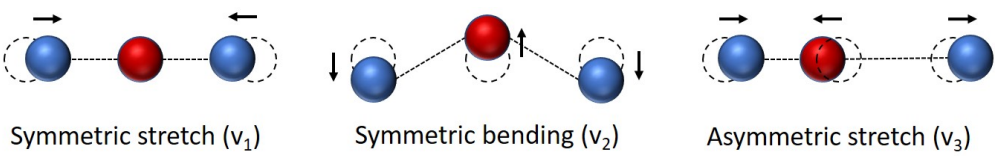

Figure 1.7: Three vibrational modes of CO_2.

In figure 1.8, the electron energy loss fractions are shown as a function of reduced electric field (E/N), and mean electron energy. These loss fractions have been calculated with BOLSIG+[42], a two-term approximation Boltzmann solver, using the cross section set of this work as input. For reduced electric fields lower than 90 Td, over 90 % of the electron energy goes into the vibrational levels of CO_2, and below 60 Td, it is even close to 100 %. At higher E/N, more energy

goes to electronic excitation, direct electron impact dissociation, and ionization.

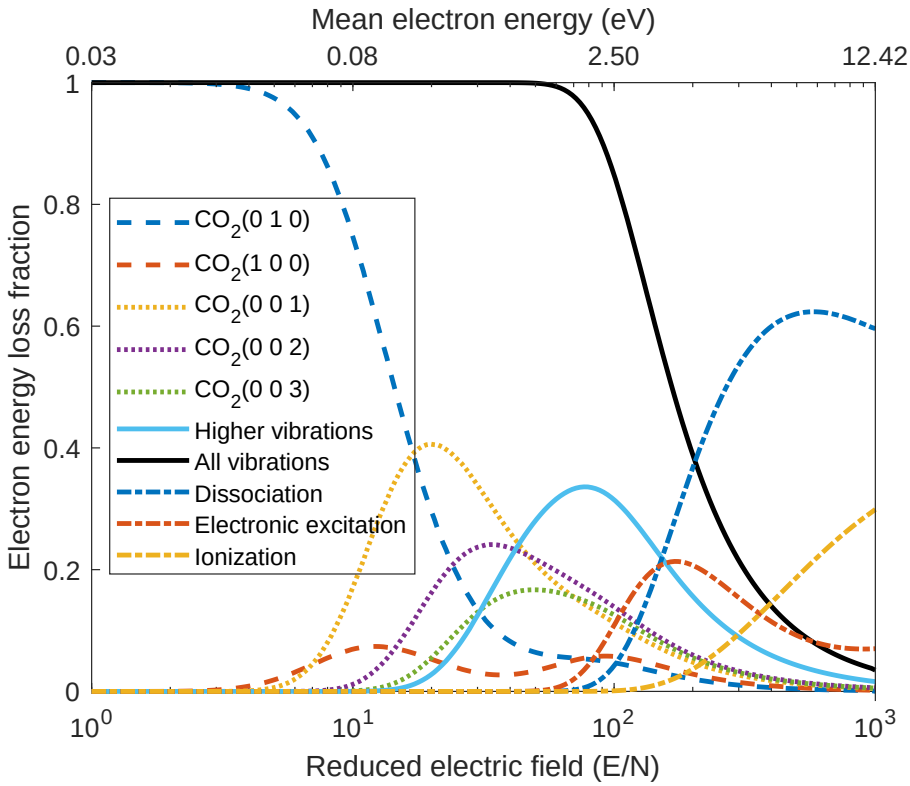

Figure 1.8: Electron energy loss fraction as a function of reduced electric field (bottom x-axis) and mean electron energy (top x-axis).

In low temperature plasmas, two different dissociation pathways arise (see figure 1.9), depending on the electron temperature

- At low electron temperatures, most of the energy goes to the vibrational levels of ground state $CO_2(^1\Sigma^+)$. At reduced electric fields > 20 Td, most of the energy that is put into the vibrational levels goes to the asymmetric mode levels of CO_2. The excitation of these levels is of particular importance, since they experience a very slow vibrational-translational (VT) relaxation, in which vibrational energy is lost to heat, with respect to the two symmetric vibrational modes. This leads to an accumulation of vibrational energy in this mode. Next, they also experience a faster vibrational-vibrational (VV) relaxation in which vibrational energy is transferred from one excited molecule to the other upon collision. VV relaxation thus populates higher vibrational levels, also referred to as "vibrational ladder climbing" (see figure 1.9). This process continues until the vibrational energy

reaches the bond breaking energy of CO_2 at 5.5 eV/molec, and a transfer to the electronically excited $CO_2(^3B_2)$ takes place. The dissociation of this state produces a $CO(^1\Sigma^+)$ molecule and an $O(^3P)$ atom, in their ground state. This process is called vibrational-induced dissociation.

- At high electron temperatures, the electrons can excite the ground state $CO_2(^1\Sigma^+)$ to an electronically excited state $CO_2(^1B_2)$, which dissociates into a ground state $CO(^1\Sigma^+)$ molecule and an electronically excited $O(^1D)$ atom. This process is called direct electron impact dissociation, and has a large energy threshold of 7 eV.

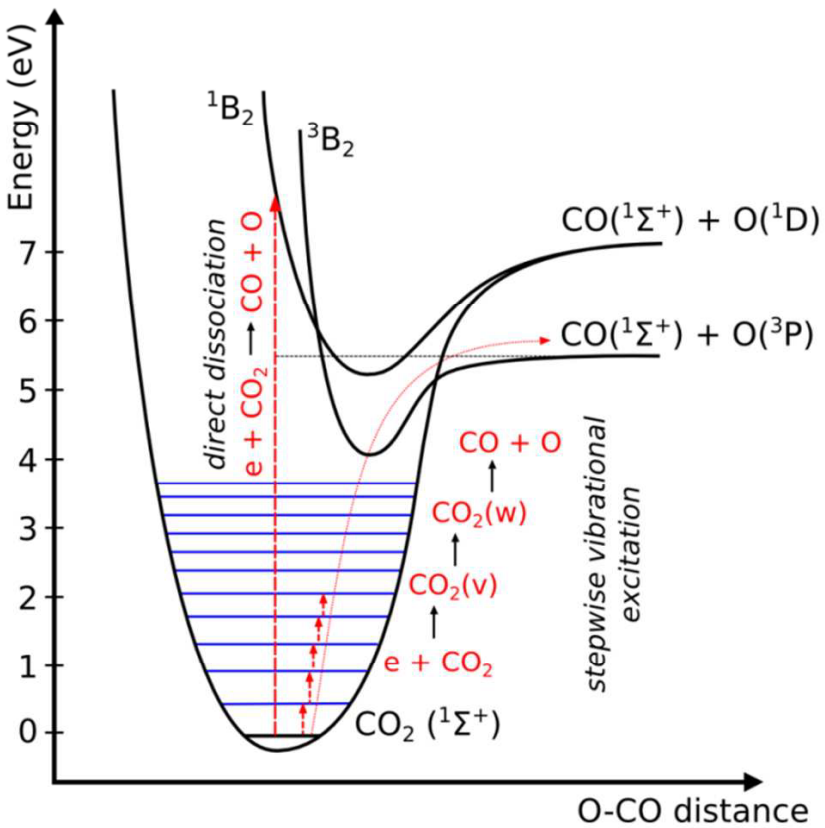

Figure 1.9: Schematic diagram of the first CO_2 electronic and vibrational levels, illustrating the two main CO_2 dissociation pathways in low temperature plasmas, i.e. electron impact dissociation and vibrational-induced dissociation through ladder climbing. Taken from Bogaerts et al.[43].

Due to its low energy requirement, vibrational-induced dissociation provides

an interesting pathway for efficient CO_2 conversion. The efficiency of the process is however limited by VT relaxation, in which the energy is lost to heat. In addition, this VT relaxation becomes more dominant at higher gas temperatures, leading to a fast acceleration in vibrational energy loss. In order to have an efficient vibrational-induced dissociation, it is crucial to have a high vibrational-translational non-equilibrium. A more detailed description of the temperature dependence of the vibrational population and relaxation processes can be found in section 3.5.

When enough vibrational energy is lost to heat, the gas temperature can be high enough (i.e. $\geq$ 2500 K) to allow for thermal dissociation of CO_2. This pathway has the same low energy requirement as vibrational-induced dissociation (i.e. 5.5 eV for $CO_2 \rightarrow CO + O$). While this process can lead to high CO_2 conversions and energy efficiencies (see figure 1.6), it is limited by the energy requirement to heat up the gas.

1.5 Plasmas used for CO_2 conversion

Next to energy-efficient dissociation pathways, plasmas offer many additional advantages for efficient CO_2 conversion. The reactors are characterized by a low investment cost, they do not use rare-earth materials, they are very flexibly turned on and off, and they are very easily scalable since the reactors can be used in parallel[38]. In recent years, CO_2 dissociation experiments have been carried out in many different plasma types. The most common types of plasmas are dielectric barrier discharges (DBDs)[44–51], gliding arc (GA) plasmas[52–54], and microwave (MW) plasmas[29;36;39;55–64]. In the next sections, we will discuss these plasmas in more detail.

1.5.1 Dielectric barrier discharges

A dielectric barrier discharge (DBD) plasma consists of two plane-parallel or concentric metal electrodes, of which at least one is covered with a dielectric barrier. The dielectric material can be glass, quartz, ceramic material, or polymers[38]. The purpose of the dielectric barrier is to restrict the electric current, and thus to prevent the formation of sparks and/or arcs[65]. The DBD configuration consist of planar or cylindrical electrodes with a gap of 0.1 - 1 mm, as is shown in figure 1.10. An AC voltage with amplitude of 1-100 kV and a frequency of a few Hz to MHz is applied between the electrodes[66]. The plasma is ignited when the electric field is high enough to cause breakdown in the gas. The breakdown voltage that is needed is determined through Paschen's Law[38]. Upon breakdown, the plasma usually consists of microdischarge filaments of nanosecond duration[66]. The DBD

is used in many industrial applications, of which the most known is the production of ozone from oxygen[67]. For more detailed information about the physical description of the DBD plasma, and its industrial applications, we refer to various review papers and books[37;66;68].

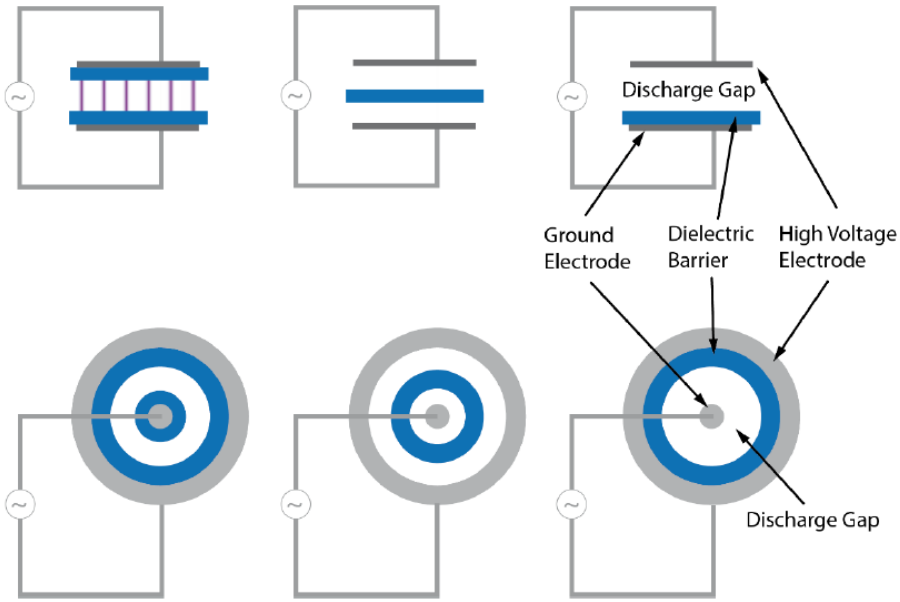

Figure 1.10: Basic planar (top) and cylindrical (bottom) dielectric barrier discharge configurations. Figure taken from ref. 38

A major advantage of the DBD is that it operates at atmospheric pressure, which is beneficial for industrial applications. Furthermore, its simple design makes it one of the more optimal reactors for industrial upscaling. However, the energy efficiencies that are reached in these experiments are typically low. This is generally attributed to the higher reduced electric field, which gives rise to more electronic excitation, ionization, and the inefficient electron impact dissociation process over vibrational-induced dissociation.

An additional advantage of the DBD reactor is that a dielectric material or catalyst can be put directly in the plasma zone[47;48]. This combination of plasma and packing material is also of great interest when a H-source is added to the chemical mixture[69]. Depending on the packing material, different value-added chemicals can selectively be formed. However, more research is needed to demonstrate its potential.

1.5.2 Gliding arc plasmas

A classical gliding arc is an auto-oscillating periodic discharge that is formed using two diverging flat electrodes. A gas flows in between these two electrodes (see figure 1.11 (left)). When a voltage is applied between the two electrodes, a plasma arc is formed at the narrowest gap. The plasma is subsequently dragged by the gas alongside the electrodes towards rising inter-electrode distance. When the arc is too long to be sustained, the plasma extinguishes and is reignited at the shortest inter-electrode distance, repeating the cycle.

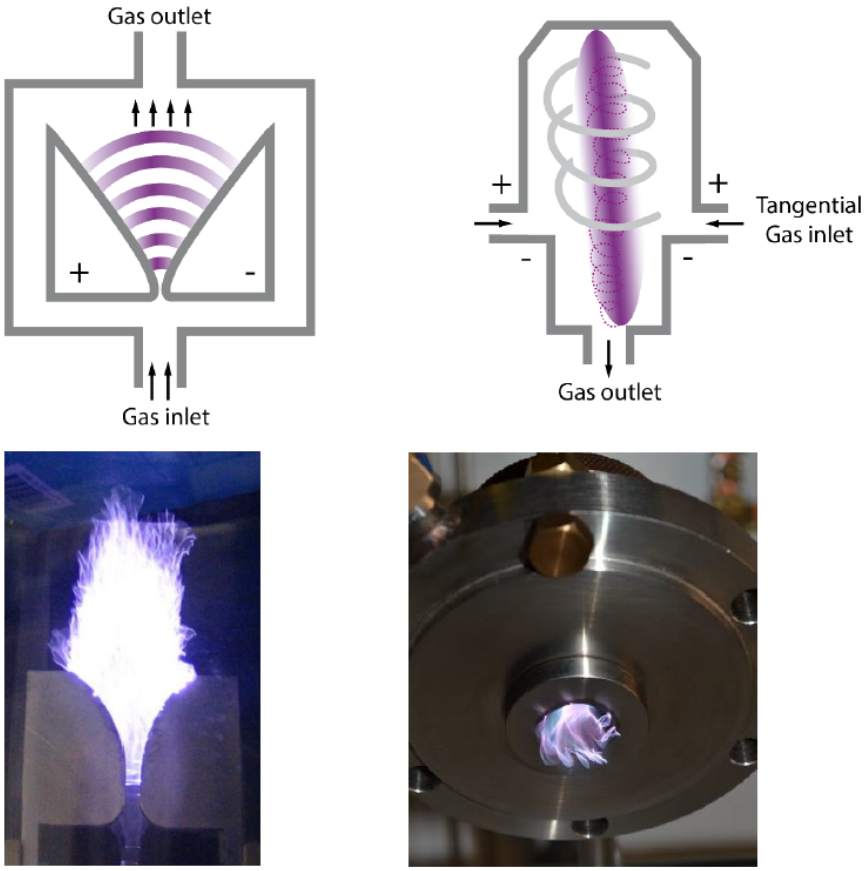

Figure 1.11: Schematic representation of a classical GA (top left) and a GAP (top right) configuration. The corresponding pictures are shown in the bottom. Taken from ref. 38.

The classical gliding arc is characterized by some important disadvantages that make it less interesting[38]. The flat 2D electrode geometry prevents a significant portion (80-90 %) of the gas from passing through the active plasma region[70]. In addition, a high gas flow rate is also needed to drag the arc, which

results in a limited residence time. Therefore, alternative 3D cylindrical GA reactors, such as rotating GA[71] and reverse vortex flow GA (also called GA plasmatron (GAP))[53;54], have been developed. In these reactors, the gas is injected tangentially. In the GAP, the cylindrical reactor body acts as a cathode, while the reactor outlet is the anode (see figure 1.11 right). The reverse vortex flow stabilizes the plasma in the center of the reactor[72;73]. While this design leads to an overall better performance than the classical gliding arc, the fraction of gas passing through the arc is still limited[74].

Similarly to the DBD, a GA plasma generally operates at atmospheric pressure, and has a simple design, making it suitable for industrial implementation. Moreover, higher energy efficiencies are reached with these plasmas, because of a favourably low reduced electric field which gives rise to vibrational population. However, the gas temperature in these plasmas is generally high, which favors thermal dissociation over vibrational-induced dissociation, due to the high VT relaxation[74].

1.5.3 Microwave plasmas

In microwave (MW) plasmas, the applied power does not come from a potential difference between electrodes, but from electromagnetic radiation with typical frequencies between 300 MHz and 300 GHz[75]. There exist many different types of MW plasma sources, such as cavity induced plasmas, free expanding atmospheric plasma torches, electron cyclotron resonance plasmas, and surface wave sustained discharges[66]. Surface wave discharges are the most common for CO_2 conversion. In surface wave sustained discharges, the gas flows through a quartz tube that is transparent to MW radiation. The MW can not fully penetrate the plasma, and instead propagates along the interface between the quartz tube and the plasma column[76;77]. The power flux of the wave decreases when moving away from the MW launcher, as the power is gradually expended in sustaining the plasma. The main surface wave sustained MW discharges, used for CO_2 conversion, is the surfaguide discharge[29;36;39;55–64], where the microwave power is injected via a rectangular waveguide. An example of such setup is shown in figure 1.12. In this setup, the microwave feed line is terminated by a shorting plunger, which is used to maximize the power injected in the discharge tube.

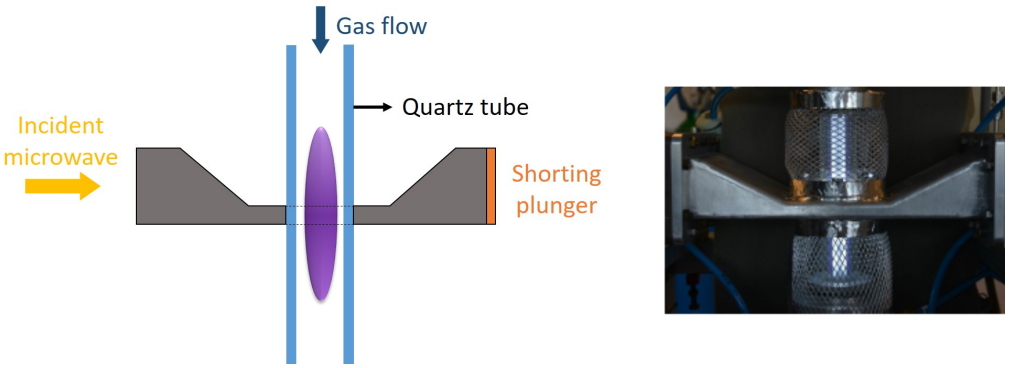

Figure 1.12: Schematic view (left) and picture (right) of a surfaguide microwave plasma. Picture taken from ref. 79.

Similarly as with GA plasmas, the MW plasma is characterized by a low reduced electric field. For diffuse plasmas this can lie between 80-180 Td, while the value is even lower for contracted plasmas (10-60 Td)[78]. These values are optimal for efficient vibrational population. Also in these plasmas, the gas temperature in typical experiments is very high, and the plasma appears to be in (or close to) thermal equilibrium.

1.5.4 Other types of plasmas

Besides the main types of plasmas that are described above, other plasma types are also increasingly being considered for CO_2 conversion, such as nanosecond-pulsed plasmas[80–83], corona discharges[84;85], and atmospheric pressure glow discharges (APGDs)[86;87].

In nanosecond pulsed plasmas, the plasma is excited by repetitive nanosecond power pulses. This leads to a high non-equilibrium with very high plasma densities, for relatively low power consumption because of the short pulse duration. The short pulse duration also offers a good control on the electron energy. Therefore, more energy can be directed towards vibrational-induced dissociation.

Corona discharges are created when sharp points, edges and wires, are used as electrode. When a positive voltage is applied to the electrode, it is considered a positive discharge, and vice versa when a negative voltage is applied. Corona discharges are non-uniform, with a strong electric field, and ionization, close to the electrode, whereas the charged particles are dragged to the other electrode by a weaker electric field.

APGDs stand for a collection of several types of plasmas, which include micro-hollow cathode DC discharges, miniaturised DC glow discharges, and capacitively coupled rf discharges[38;66]. The discharge is strongly related to the DBD, as the plasma is also ignited between two parallel electrodes, and it also operates at

atmospheric pressure. The basic difference is that APGDs are generally homogeneous across the electrodes, whereas the DBD typically consists of microdischarge filaments of nanosecond duration. In essence, an APGD can be considered as a diffuse DBD[66]. An APGD can operate in stable homogeneous glow, or filamentary glow mode.

1.5.5 Energy efficiencies of plasma-based CO_2 conversion

Two important key performance indicators for the industrial application of plasma-based CO_2 dissociation are the achieved energy efficiency and total CO_2 conversion. An overview of the experimental results that were reported in literature, up to 2017, for the various plasmas described above is shown in figure 1.13. For more detailed information, we refer to the review paper of Snoeckx and Bogaerts[38].

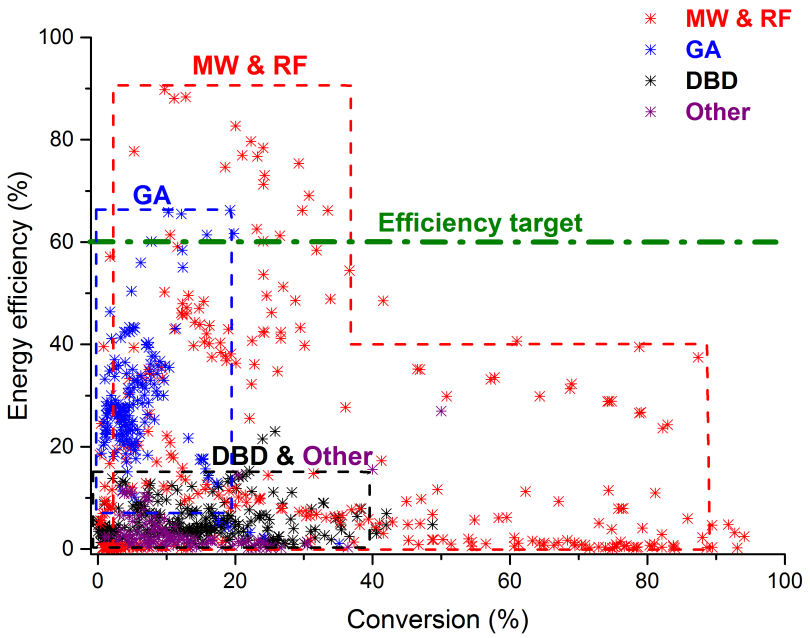

Figure 1.13: Comparison of experimental CO_2 conversion and energy efficiency of different plasma reactors, reported in literature. The 60 % efficiency target is also indicated. Taken from Snoeckx and Bogaerts[38].

It is clear from figure 1.13 that DBD reactors are generally characterized by a low energy efficiency. Most of the results are situated below an energy efficiency of 15 % and a conversion of 40 %, with some exceptions. The highest energy efficiency, reported up to 2017, is 23 % and obtained by Ozkan et al. with a

pulsed power DBD[88].

In GA plasmas, most experiments report maximum efficiencies around 40-50 %[53;54]. These efficiencies are typically found in low current GA plasmas. A maximum effiency of 60 % is found by Kim et al.[89]. The degree of CO_2 conversion typically remains below 15 %, for both the classical GA as well as the GAP, due to the limited fraction of the gas that passes through the arc[70;74]. An exception is found in the work of Indarto et al.[90], where a maximum conversion of 35 % is found.

Figure 1.13 shows that the highest energy efficiencies were reported for MW plasmas. These efficiencies reach 80 % for subsonic flows, and 90 % with a supersonic flow[36]. However, so far, these reported efficiencies have not been reproduced. More recent experiments show maximum energy efficiencies around 50 %[29;39;62;63]. All experiments that were reporting such high energy efficiencies were performed at reduced pressures of 100-600 mbar. These pressures are not optimal for industrial application since there would be an additional energy cost to reducing the pressure. However, for atmospheric pressure, Spencer et al. obtained maximum energy efficiencies of 20 %[91].

The performance of the other types of plasmas that were mentioned in section 1.5.4 are also shown in figure 1.13. In general, the performance of these plasmas is similar to what was observed for a DBD, with maximum conversions of 40 %, and maximum energy efficiencies of 15 %. However, it is important to note that since this figure was published, new experimental values were reported that show maximum values of energy efficiency of about 30 % for ns-pulsed plasmas[82] and APGDs[87].

1.6 State of the art in plasma modeling

In the past years, research on CO_2 plasma-kinetic modeling was primarily focused on increasing the energy efficiency, primarily by vibrational-induced dissociation. In work by Pietanza et al.[92–96], a lot of attention was paid to the coupling between the electron energy distribution function (EEDF) and the vibrational kinetics, as well as the different dissociation mechanism. Particular focus was given to the effect of superelastic vibrational collisions on the EEDF. In work by researchers of the Instituto de Plasmas e Fusão Nuclear the vibrational exchanges between the 72 lowest vibrational levels of ground state CO_2 in DC pulsed glow discharges, under low-excitation conditions, were studied in a theoretical and experimental investigation[97;98]. This group also proposed a new set of cross sections for CO_2 plasmas, which was validated by comparison with swarm data, obtained by solving the Boltzmann equation, with available

experimental data[99].

Also in our group, the influence of vibrational excitation and subsequent dissociation on the plasma kinetics has been studied in various plasma types, such as MW and GA plasmas, DBDs, and nanosecond pulsed discharges[28;70;74;83;100–105]. Recently, chemical kinetics models are focussing more on the effect of thermal dissociation in high temperature CO_2 plasmas[59;106–108], since this pathway can also lead to high energy efficient dissociation (see figure 1.6).

Next to 0D models, plasmas are increasingly being described by multi-dimensional models, ranging from 1D models[105] to 2D models[87;109]. Currently, such models exist for GA plasmas and APGDs. More research is needed to develop such models for MW and DBD plasmas.

1.7 Goal of this work

The aim of this work is to better understand how the CO_2 conversion and energy efficiency in vibrationally active non-equilibrium plasmas can be improved, with particular focus on the interplay between vibrational excitation and gas temperature. Through modeling the plasma chemistry, more insight is gathered in how this efficiency can be increased for different conditions.

In chapter 2, the theory that forms the basis of the 0D model is explained. The chemistry set and scaling laws that are required to scale the reactions for different vibrational levels are explained in chapter 3.

In chapter 4, we will study the effect of the supersonic flow field of a Laval nozzle on the chemical kinetics in the plasma. The supersonic flow is know to create a pressure and temperature drop that enhances the VT non-equilibrium and facilitates optimal conditions for vibrational-induced dissociation.

Since the rising gas temperature inside the plasma limits vibrational overpopulation and subsequent dissociation, the effect of pulsing to enhance the VT non-equilibrium will be studied in chapter 5.

In chapter 6, we will study the effect of thermal quenching the dissociation products on the overall CO_2 conversion and energy efficiency in cold and warm plasmas at different specific energy inputs. We will also compare the performance of vibrational-induced dissociation with that of thermal dissociation.

CHAPTER 2

General model description

2.1 Introduction

A plasma is a highly complex environment, consisting of many different species which can all interact with each other, and are also dependent on the influence from electromagnetic fields, fluid dynamics, and from thermodynamics.

In order to exactly describe the plasma, the position ($\boldsymbol{r}$) and velocity ($\boldsymbol{v}$) of every species should be known at a certain time (t). When describing N species, this will lead to 6N different solvable variables when describing the plasma in 3D space. While for small scale simulations, and at low species densities, this can lead to acceptable computational times, for large systems, or at high particle densities, this would require unrealistically high computational resources.

At higher particle densities and simulation regions, a fluid description can be used, in which the species densities are solved for, in stead of a description of the individual particles. This category ranges from zero-dimensional (0D) to three-dimensional (3D) models. In zero-dimensional models, the spatial dimensions are ignored, and the species densities are only calculated as a function of time. These models are usually very time efficient and are therefore well suited for large and detailed chemistry sets. Multi-dimensional models can include transport processes, but require the description of a limited chemistry set in order to keep the computational time acceptable.

In this thesis, we use a 0D fluid description of the plasma. The model applied for these studies is a zero-dimensional (0D) chemical kinetics model, using the code ZDPlasKin[110]. In chapter 4, 2D axisymetric flow calculations are also performed, from which the flow results are used as an input into the 0D model. In the next sections, an overview is given of the different equations, and how they are implemented in the modelling framework.

2.2 Boltzmann equation

When using a continuum description of the different plasma species, the non-equilibrium effects can be included by means of the Boltzmann equation. This equation describes the statistical distribution $f_\alpha(\boldsymbol{r}, \boldsymbol{v}, t)$ of the ensemble of particles of species α at a certain time t in phase space, where $\boldsymbol{r}$ is the position vector and $\boldsymbol{v}$ is the velocity vector. The general form of the Boltzmann equation is given by[111]:

$$\frac{\partial f_\alpha}{\partial t} + \boldsymbol{v} \cdot \frac{\partial f_\alpha}{\partial \boldsymbol{r}} + \boldsymbol{\gamma} \cdot \frac{\partial f_\alpha}{\partial \boldsymbol{v}} = (\frac{\delta f_\alpha}{\delta t})_c \tag{2.1}$$

with $\boldsymbol{\gamma}$ the acceleration vector, and $\left(\frac{\delta f_\alpha}{\delta t}\right)_{coll}$ the rate of change of f due to collisions.

It is computationally demanding to solve the Boltzmann equation for every species inside the plasma. Therefore, in our model, the Boltzmann equation is only solved for the electrons in order to calculate the electron energy distribution function (EEDF). Additional information will be given in section 2.4.

2.3 Conservation equations of moments of the Boltzmann equation

In a fluid description, the particles are described by their macroscopic variables, i.e. particle density, velocity and temperature. These macroscopic values do not depend on velocity, but only on position and time. The particle density n_α of species α at $(t, \boldsymbol{r})$ is defined as:

$$n_\alpha(t, \boldsymbol{r}) = \int f_\alpha(t, \boldsymbol{r}, \boldsymbol{v}) d\boldsymbol{v} \tag{2.2}$$

The mean value $< b(t, \boldsymbol{r}) >$ of a quantity b can also be calculated using the distribution function:

$$< b(t, \boldsymbol{r}) >= \frac{1}{n_\alpha(t, \boldsymbol{r})} \int b(t, \boldsymbol{r}, \boldsymbol{v}) f_\alpha(t, \boldsymbol{r}, \boldsymbol{v}) d\boldsymbol{v} \tag{2.3}$$

Eq. 2.3 can be used to calculate the macroscopic quantities that are related to the first three moments of the Boltzmann distribution function:

$$\zeta_\alpha(t, \boldsymbol{r}) = \int m_\alpha \boldsymbol{v}^i f_\alpha(t, \boldsymbol{r}, \boldsymbol{v}) d\boldsymbol{v} \qquad \text{for } i = 0..2 \tag{2.4}$$

For n=0, this results in the mass density $\rho_\alpha = m_\alpha n_\alpha$. For n=1, this gives $\rho_\alpha \boldsymbol{u}_\alpha$, with $\boldsymbol{u}_\alpha$ the average flow velocity. For n=2, this gives $\frac{1}{2}(3p + \rho_\alpha \boldsymbol{u}_\alpha^2)$, with p the pressure.

The conservation equations for mass density, momentum, and energy can then be found by calculating the same three moments of the Boltzmann equation (equation 2.1). In the next sections, an overview will be given of these conservation equations. For more detailed information of the derviation of these equations, we refer to the book of Bittencourt [111]

2.3.1 Conservation of mass

The continuity equation, or the conservation of mass equation, can be obtained by taking the zeroth order moment of the Boltzmann equation, namely m_α and integrating it over velocity space:

$$\frac{\partial \rho_\alpha}{\partial t} + \nabla \cdot (\rho_\alpha \boldsymbol{u}_\alpha) = S_\alpha \tag{2.5}$$

in which S_α is the mass density source. This mass density source comes from the collective contribution of the different chemical reactions, involving species α. This can be expressed as:

$$S_\alpha = m_\alpha \sum_j R_j [a^R_{\alpha j} - a^L_{\alpha j}] = m_\alpha \sum_j (k_j \prod_l n_l)[a^R_{\alpha j} - a^L_{\alpha j}] \tag{2.6}$$

in which index j refers to reaction j and index l refers to the different reactants of reaction j. a^R_{sj} and a^L_{sj} are the right- and left-hand side stoichiometric coefficients of species α, respectively, taking part in reaction j, k_j is the reaction rate coefficient, and $R_j = k_j \prod_l n_l$ is the reaction rate.

2.3.2 Conservation of momentum

The conservation of momentum equation is obtained by integrating the first order moment of the Boltzmann equation, namely $\mathrm{m}_\alpha \mathrm{v}_\alpha$, over velocity space:

$$\frac{\partial \rho_\alpha \boldsymbol{u}_\alpha}{\partial t} + \boldsymbol{\nabla}(\rho_\alpha \boldsymbol{u}_\alpha . \boldsymbol{u}_\alpha) = -\boldsymbol{\nabla} p_\alpha + \boldsymbol{A}_\alpha - \boldsymbol{u}_\alpha S^m_\alpha + n_\alpha \boldsymbol{F}_\alpha \tag{2.7}$$

where $\boldsymbol{A}_\alpha$ is the momentum transfer collision term and $\boldsymbol{F}_\alpha$ represents the different forces acting on species α. More detailed information about this equation can be found in Lieberman[112].

Eq. 2.7 is not solved in the 0D model. In the 2D flow simulations that are presented in Chapter 4, this equation is solved for the fluid as a whole under the form:

$$\rho \frac{\partial \boldsymbol{u}}{\partial t} + \rho(\boldsymbol{u}.\boldsymbol{\nabla})\boldsymbol{u} = \boldsymbol{\nabla}.\Big[-p\boldsymbol{I} + \boldsymbol{\tau} \Big] + \boldsymbol{F} \tag{2.8}$$

where ρ and $\boldsymbol{u}$ are the mass density and velocity vector of the fluid, $\boldsymbol{I}$ is the unity tensor, $\boldsymbol{F}$ the external force acting on the fluid, and $\boldsymbol{\tau}$ is the viscous stress tensor which is defined as:

$$\boldsymbol{\tau} = \mu\Big(\boldsymbol{\nabla u} + (\boldsymbol{\nabla u})^T\Big) - \frac{2}{3}\mu(\boldsymbol{\nabla u})\boldsymbol{I} \tag{2.9}$$

where μ is the dynamic viscosity. More details about the implementation of these equations can be found in Chapter 4.

2.3.3 Conservation of energy

The conservation of energy equation is obtained by integrating the second order moment of the Boltzmann equation, namely $m_\alpha v_\alpha^2$, over velocity space

$$\frac{\partial}{\partial t}\left(\frac{3}{2}p_\alpha\right) + \boldsymbol{\nabla}\left(\frac{3}{2}p_\alpha \boldsymbol{u}_\alpha\right) + p_\alpha \boldsymbol{\nabla}.\boldsymbol{u}_\alpha + \boldsymbol{\nabla}.\boldsymbol{q}_\alpha = M_\alpha - \boldsymbol{u}_\alpha.\boldsymbol{A}_\alpha + \frac{1}{2}u_\alpha^2 S_\alpha \quad (2.10)$$

where p_α represents the pressure, $\boldsymbol{u}_\alpha$ the velocity vector, $\boldsymbol{q}_\alpha$ the heat flux vector, M_α the rate of energy density change due to collisions, $\boldsymbol{A}_\alpha$ the momentum transfer collision term, and S_α the mass density source. In the next sections, we explain how these equations are incorporated in the 0D model.

2.4 Implementation in 0D model

2.4.1 Basic description of the 0D model

We use the code ZDPlasKin[110] to develop a zero-dimensional (0D) chemical kinetics model. Such a 0D model only describes the evolution of the plasma as a function of time, and does not consider any spatial dimensions. The plasma is thus considered homogeneous. This means that in the above equations $\partial/\partial \boldsymbol{r} = 0$. The model calculates the continuity equations for all species considered in the model:

$$\frac{dn_\alpha}{dt} = \sum_j R_j[a_{\alpha j}^R - a_{\alpha j}^L] = \sum_j (k_j \prod_l n_l)[a_{\alpha j}^R - a_{\alpha j}^L] \quad (2.11)$$

The plasmas under consideration are in non-local thermal equilibrium (non-LTE). This means that the electrons, that are primarily excited due to their lower mass, have a much higher temperature than the heavier species. These heavy species are assumed to be in thermal equilibrium with each other. Due to the importance of the electron heating, and the subsequent transfer of energy to the heavy particles in collisions, the distribution of the electron energy has a big impact on the plasma kinetics[92;93]. The ZDPlasKin framework couples a chemical kinetics solver to a two-term Boltzmann equation solver BOLSIG+[42], which calculates the electron energy distribution function (EEDF) F_0 (in $\mathrm{eV}^{\frac{-3}{2}}$). The mean electron energy ($\bar{\epsilon}$) is then calculated according to

$$\bar{\epsilon} = \int_0^\infty \epsilon^{3/2} F_0 d\epsilon \quad (2.12)$$

The rate coefficients (k_k) for the electron impact reactions are calculated using

a set of collision cross sections σ_k, using:

$$k_k = \sqrt{\frac{2e}{m_e}} \int_0^\infty \epsilon \sigma_k F_0 d\epsilon \tag{2.13}$$

with e the elementary charge, and m_e the electron mass.

The EEDF is regularly updated during the calculations, upon changes of the gas temperature, the electron density, the reduced electric field, or the density of species reacting with electrons.

For the heavy species, the Boltzmann equation is not solved. The rate coefficients that describe the reactions involving these species use analytical expressions that depend on the average gas temperature of these species. More information will be given in chapter 3.

In chapter 5 and 6, the gas temperature is calculated self-consistently according to

$$\sum_\alpha n_\alpha \frac{\gamma_\alpha}{\gamma_\alpha - 1} k_B \frac{dT_g}{dt} = P_{el} + \sum_j R_j \Delta H_j - P_{ext} \tag{2.14}$$

where $\gamma_\alpha = c_p/c_v$ is the ratio of specific heats of species α, P_{el} is the gas heating power density due to elastic electron-neutral collisions, ΔH_j the heat released (or consumed) in reaction j, and P_{ext} the power loss density due to exchanges with the surroundings. For CO_2, we only have to take into account the heat capacity due to translational and rotational degrees of freedom, as well as the vibrational symmetric mode levels that are not described by an individual species. More detail about the implementation can be found in ref. 104.

We will take the external cooling term to be[101;104]

$$P_{ext} = \frac{8\lambda}{R^2}(T_g - T_w) \tag{2.15}$$

in which λ is the gas thermal conductivity, and T_w is the wall temperature taken as 300 K. We take $\lambda(T_g) = (0.071 T_g - 2.33) \times 10^{-3} W m^{-1} K^{-1}$ following ref 104. In chapter 5 and 6 additional cooling terms are also added to examine the effect of higher and lower cooling. The details of the approach are described in the respective chapters.

2.4.2 Gas expansion

In this work, we follow the time-evolution of a volume element as it moves through a plasma reactor. The model starts with pure CO_2, mimicking the gas at the inlet of the reactor. At a certain time, the plasma is ignited. The added energy can either increase the gas temperature, lead to a change in the chemical

composition of the gas, or a combination of both. In order to keep the pressure constant, changes in gas temperature and chemical composition will allow the volume element to contract or expand, according to the ideal gas law. This effect can be taken into account by introducing a gas expansion factor, $\beta(t)$, which equals 1 at the start of the simulation, and drops when the gas expands. The factor is defined as:

$$\beta(t) = \frac{M(t=0)T_g(t=0)}{M(t)T_g(t)} \tag{2.16}$$

with M the total number of molecules and T_g the gas temperature. For example, if all CO_2 is dissociated into CO and $\frac{1}{2}O_2$, the initial number of molecules M(t=0) rises to $\frac{3}{2}$ M(t=0), and thus $\beta = \frac{2}{3}$, at constant gas temperature, because the volume expands to keep the pressure constant. Similarly, the expansion factor drops upon rising gas temperature. The electron density is not included in this expansion factor, as the ionization degree is too small.

This approach is used in chapter 5 and 6 where we consider incompressible flow. In chapter 4 compressible flow is considered. However, in this chapter, the plug-flow approximation is considered, which will be explained in section 2.4.5.

2.4.3 Plasma power

The plasma conditions are defined in the model by setting a certain ionization degree (d_i). The electron density (n_e) then equals $d_i \times N$ (with N the gas number density). At the same time, a constant reduced electric field E/N (with E the electric field) is set. The deposited power density (in eV/cm^{3}s) applied to the plasma is then calculated using Joule's law:

$$P_{dep,pl} = \sigma E^2 = \sigma N^2 \left(\frac{E}{N}\right)^2 \tag{2.17}$$

with σ the conductivity (in $\frac{C}{cmVs}$), given by $\sigma = en_e\mu_e$. The electron mobility μ_e is obtained from the Boltzmann solver, and e is the elementary charge.

The plasma is ignited by applying the power as described above. The plasma is sustained until the applied power reaches the value corresponding to a certain predefined SEI (in eV/molec.), defined as:

$$\text{SEI}(t) = \frac{\int_0^t \frac{P_{dep}(t)}{\beta(t)} dt}{N(t=0)} \tag{2.18}$$

The dependency between the SEI and the residence time is specific to the conditions under study. In reality, a similar SEI can be reached with different deposited power profiles, leading to a different deposited power density. When the

power density is lower, the residence time will increase. However, this situation will correspond to lower ionization degrees or reduced electric fields, and we decided to keep these fixed in this work, as characteristic plasma parameters. Also, in a 0D model, the plasma parameters are assumed to be homogeneous. In reality, localized power deposition can also lead to longer residence times for the same total SEI[64].

2.4.4 Post processing

The goal of the simulations is to obtain insight into conditions that provide maximum conversion and energy efficiency. The CO_2 conversion is calculated as

$$\chi(t)[\%] = \left[1 - \frac{N_{CO_2}(t)}{\beta(t) N_{CO_2}(t=0)}\right] \times 100\% \tag{2.19}$$

where N_{CO_2} is the total number density of all CO_2 molecules (i.e. the sum of the ground state and all vibrationally and electronically excited CO_2 molecules) at a given time t.

The energy efficiency is calculated as

$$\eta[\%] = \chi[\%] \frac{\Delta H^o}{\text{SEI}} \tag{2.20}$$

where $\Delta H^o = 2.93$ eV/molec. is the reaction enthalpy of the reaction $CO_2 \rightarrow CO + \frac{1}{2}O_2$ at the inlet temperature of 300 K.

Finally, we also calculate the vibrational temperature of CO_2, based on the population of the first asymmetric mode level:

$$T_v = \frac{-E_1}{ln\left(\frac{n_1}{n_0}\right)} \tag{2.21}$$

where E_1 is the energy of the first asymmetric mode level (3380 K), with n_1 its density, and n_0 the ground state density of CO_2.

2.4.5 Plug-flow approximation

While the model calculates the time evolution of the different species densities, the axial evolution can be obtained by calculating the velocity of the volume as it moves through a reactor. The considered volume element moves at an axial velocity u that is calculated from the conservation of mass flow rate

$$u = \frac{\dot{m}}{\rho A} \tag{2.22}$$

with $\dot{m}$ the mass flow rate, $\rho = \sum_j n_j M j$ the mass density of the gas, and A

the reactor tube cross-sectional area. Similarly as in equation 2.16, the volume expands when the temperature or the number of particles increases. In a reactor at constant pressure, this volume expansion will lead to a higher velocity. In that case, the velocity can be correlated to the gas expansion factor as:

$$\beta(t) = \frac{u(0)A(0)}{u(t)A(t)} \tag{2.23}$$

We want to note that in equation 2.16 the gas expands to keep the pressure constant. In chapter 4, varations in the pressure also exist. While this equation is then no longer valid, the effect of changing pressure is incorporated in equation 2.22.

In the plug flow approximation, the plasma will be turned on at position z_0. After a certain plasma length z_p the plasma is turned off. At any position z, the SEI then becomes

$$\text{SEI}(z) = \int_{z_0}^{z} \frac{1}{\Phi} \frac{T_{ref}}{p_{ref}} \frac{k_B}{e} \frac{1}{10^{-3}} A(z) P_{dep} dz \tag{2.24}$$

where Φ is the gas flow rate in standard litres per second, $T_{ref} = 273.15\ K$ and $p_{ref} = 101325\ Pa$ are the temperature and pressure at standard conditions, e is the elementary charge to convert J into eV, and k_B is the Boltzmann constant. The factor 10^{-3} comes from the conversion of $l = dm^3$ to m^3.

Using the plug-flow approximation, the conversion (χ) and energy efficiency (η) is obtained by substituting equation 2.23 in equation 2.19

$$\chi(z)[\%] = \left[1 - \frac{N_{CO_2}(z)u(z)A(z)}{N_{CO_2}(0)u(0)A(0)}\right] \times 100\% \tag{2.25}$$

$$\eta[\%] = \chi[\%] \frac{\Delta H^\circ}{\text{SEI}} \tag{2.26}$$

where $\Delta H^o = 2.93$ eV/molec., similarly as in equation 2.20. The chemistry set used as an input for the model will be described in more detail in the next chapter.

CHAPTER 3

CO_2 chemistry set and scaling laws

3.1 Introduction

The chemistry set used in this work underwent a series of updates, starting from the original set that was developed by Aerts et al.[102] and Kozák et al.[103;104]. This set was subsequently subjected to an extensive literature review of the containing reaction rate coefficients[113;114]. All of the sets that were included in these studies contained an extensive list of species and reactions. Since some of these species and reactions were of minor importance to the overall plasma behavior, Berthelot and Bogaerts reduced the chemistry set by removing the species of minor importance[101]. This set was also used in an extensive uncertainty analysis study[114], where it was argued that including more species had a negative impact on the model uncertainty, while they virtually had no influence on the model results. The chemistry set used in this work therefore keeps a close resemblance with the reduced chemistry set of Berthelot et al.[28;114].

3.2 Species considered

The species included in the chemistry sets are listed in Table 3.1-3.3. In Table 3.1, the species used in chapter 4 are shown. In Table 3.2, updates or additions to the species in table 3.1 are shown, which are used in chapter 5 and in chapter 6, while table 3.3 provides further updates or additions, used in chapter 6. In the added/changed species of table 3.2, applicable to the chemistry sets of chapters 5 and 6, the cross section set underwent an update based upon newly available literature. In the added species described in table 3.3, applicable to the chemistry set of chapter 6, more vibrational states are added for CO and O_2, as well as the O_2^+ ion due to the high conversion degrees reached in that work.

Given the importance of the vibrational levels in non-equilibrium plasmas, the vibrationally excited molecules are added as separate species in the model.

Table 3.1: Species described in the model.

Neutral ground states
CO_2, CO, O_2, O, C

Charged species
CO_2^+, CO^+, CO_4^+, O^-, O_2^-, CO_3^-, CO_4^-, e^-

Excited states	Associated energy [eV]	State[a]
$O_2[v_{1-4}]$	Anharmonic oscillator	
$CO[v_{1-10}]$	Anharmonic oscillator	
$CO_2[v_{1-21}]$	Anharmonic oscillator	(00n)
$CO_2[v_a]$	0.083	(010)
$CO_2[v_b]$	0.167	(020) + (100)
$CO_2[v_c]$	0.252	(030) + (110)
$CO_2[v_d]$	0.339	(040) + (120) + (200)
$CO_2[e_1]$	10.5	$(^1\Sigma_u^+)$ + $(^3\Pi_u)$ + $(^1\Pi_u)$
$O_2[e_1]$	0.98	$(a^1\Delta_g)$ + $(b^1\Sigma_g^+)$
$O_2[e_2]$	8.4	$(B^3\Sigma_u^-)$ + higher triplet states
$CO[e_1]$	6.22	$(a^3\Pi_r)$
$CO[e_2]$	7.9	$(A^1\Pi)$
$CO[e_3]$	13.5	$(a'^3\Sigma^+)$ + $(d^3\Delta_i)$ + $(e^3\Sigma^-)$ + $(b^3\Sigma^+)$
$CO[e_4]$	10.01	$(C^1\Sigma^+)$ + $(E^1\Pi)$ + $(B^1\Sigma^+)$ + $(I^1\Sigma^-)$ + $(D^1\Delta)$

[a] CO_2 electronic states designation from Grofulović et al.[99], O_2 and CO electronic states notation from Huber & Herzberg[115].

Table 3.2: Additional/updated species described in the model used in chapters 5 and 6.

Excited states	Associated energy [eV]	State
$O_2[e_1]$	0.98	$(a^1\Delta_g)$
$O_2[e_2]$	1.6	$(b^1\Sigma_g^+)$
$O_2[e_3]$	4.5	$(A^3\Sigma_u^+)$ + $(C^3\Delta_u)$ + $(c^1\Sigma_u^-)$
$O_2[e_4]$	9.7	radiative levels
$O_2[e_5]$	14.7	radiative levels
$CO[e_1]$	6.22	$(a^3\Pi_r)$
$CO[e_2]$	6.8	$(a'^3\Sigma^+)$
$CO[e_3]$	7.9	$(A^1\Pi)$
$CO[e_4]$	10.4	$(b^3\Sigma^+)$
$CO[e_5]$	10.6	$(C^1\Sigma^+)$ + $(E^1\Pi)$
$CO[e_6]$	13.5	$(d^3\Delta_i)$ + $(e^3\Sigma^-)$

Table 3.3: Additional/updated species described in the model used in chapter 6.

Charged species
O_2^+

Excited states	Associated energy [eV]	State
$O_2[v_{5-33}]$	Anharmonic oscillator	
$CO[v_{11-50}]$	Anharmonic oscillator	

3.2.1 Vibrational and electronic excited states

As was mentioned in section 1.4.2, the CO_2 molecule is characterized by three different vibrational modes; the symmetric stretch mode, the doubly degenerate symmetric bend mode, and the asymmetric stretch mode, characterized by quantum number v_1, v_2, and v_3, respectively. The energies of the vibrational levels can be calculated by the anharmonic oscillator approximation[116]:

$$\frac{E_{CO_2}}{hc} = \sum_i \omega_i \left(v_i + d_i/2\right) + \sum_{j \leq i} x_{ij} \left(v_i + d_i/2\right) \left(v_j + d_j/2\right) + x_{l_2 l_2} l_2^2 \qquad (3.1)$$

with ω_i, x_{ij}, and $x_{l_2 l_2}$ the spectroscopic constants determined by experiments, and $d_i = (d_1 d_2 d_3) = (121)$ the degeneracies of the different vibrational modes. In this work, the spectroscopic data from Suzuki[116] are used: w_1 = 1354.31 cm^{-1}, w_2 = 672.85 cm^{-1}, w_3 = 2396.32 cm^{-1}, w_1 = 1354.31 cm^{-1}, x_{11} = -2.93 cm^{-1}, x_{12} = -4.61 cm^{-1}, x_{13} = -19.82 cm^{-1}, x_{22} = 1.35 cm^{-1}, x_{23} = -12.31 cm^{-1}, x_{33} = -12.47 cm^{-1}. Eq. 3.1 enables us to calculate the energy of all vibrational levels. However, more than 10000 different levels exist that have an energy below the dissociation energy of CO_2 (i.e. 5.5 eV). Including them all in the chemistry set would lead to an equal number of coupled balance equations that need to be solved. Since this is computationally infeasible, we only include the vibrational levels that play an important role. Figure 3.1 compares all of the vibrational levels (a) with the vibrational levels that are included in the model (b). The model includes the first four grouped symmetric mode levels; v_a =(010), v_b = (020) + (100), v_c = (030) + (110), and v_d = (040) + (120) + (200). Next to the symmetric levels, the model contains 21 asymmetric mode levels; v_n = (00n) with n=1-21, up till the dissociation limit of CO_2. We justify taking a limited number of symmetric levels into account with the fact that the asymmetric vibrational mode levels are predominantly excited at the low electron temperatures of 1-3 eV[102], considered in this thesis, and they experience a very

fast vibrational-vibrational energy exchange[117]. In addition, the vibrational-translational relaxation rate constants of the asymmetric vibrational mode levels are much lower than those of the symmetric levels[117]. Hence, the asymmetric mode levels are more important for CO_2 dissociation.

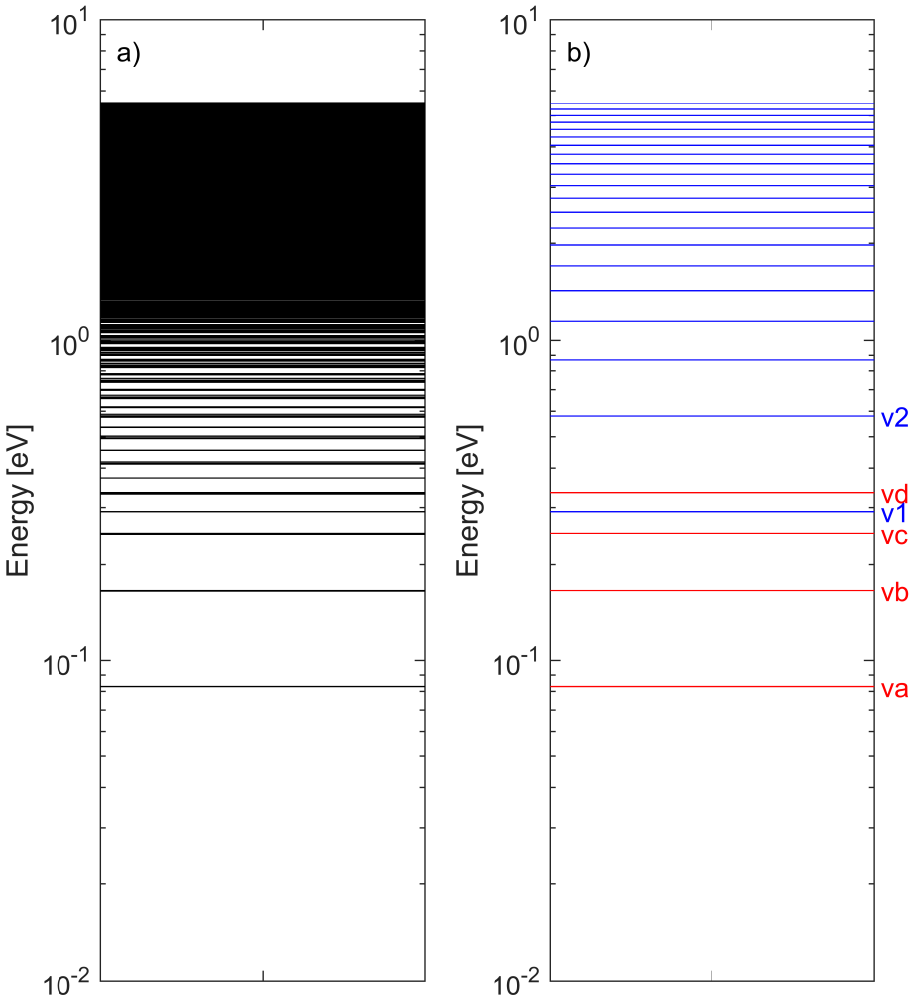

Figure 3.1: a) All vibrational levels of CO_2 up till the dissociation limit. b) Vibrational levels included in the model, with the symmetric grouped levels shown in red, and the asymmetric levels shown in blue.

For CO and O_2, 10 and 4 levels are taken into account in Chapter 4 and 5. In

these studies, the maximum achieved CO_2 conversion is low, and it was found that including more levels had no effect on the model outcome[101]. In Chapter 6, 50 and 33 levels are included, for CO and O_2 respectively, since the CO_2 conversion reaches much higher values in this study. The energy of the vibrational levels is calculated using the formula[118]:

$$\frac{E_{CO,O_2}}{hc} = \omega_e \left(v + 1/2\right) + \omega_e x_e \left(v + 1/2\right)^2 + \omega_e y_e \left(v + 1/2\right)^3 \tag{3.2}$$

where v is the vibrational quantum number, ω_e is the vibrational frequency, and x_e and y_e are the first and second anharmonicity coefficients. The values for ω_e and x_e are taken from the NIST database[119]. For CO, $\omega_e = 2169.81$ cm^{-1}, $x_e = 6.12 \times 10^{-3}$ cm^{-1} and $y_e = 0$, and for O_2, $\omega_e = 2169.81$ cm^{-1}, $x_e = 7.58 \times 10^{-3}$ cm^{-1}, and $y_e = 5.3 \times 10^{-5}$ cm^{-1}.

For CO_2, one electronic level, with an energy of 10.5 eV, is taken into account, due to lack of information on higher electronic excited states. The electronic level with an energy of 7 eV immediately results in dissociation[120]. For CO and O_2, initially 4 and 2 electronic levels are taken into account, respectively, in chapter 4, and later 6 and 5 levels are taken into account, in chapters 5 and 6[121;122].

3.3 Reactions included in the model

The set used in chapter 4 can be found in section A.1. The electron impact reactions are shown in Table A.1 and A.2. The reactions of Table A.1 are described by electron impact cross sections, found in the LXCat database[123], while the reactions in Table A.2 are described by rate coefficients, calculated with analytical expressions. The ion-ion reactions and ion-neutral reactions are shown in Table A.3. Table A.4 lists the neutral reactions, for which the rate coefficients are given in the form of Arrhenius expressions:

$$k(T_g) = AT_g^B exp\left(\frac{-E_a}{k_B T_g}\right) \tag{3.3}$$

where E_a is the activation energy, k_B is the Boltzmann constant, and A and B are reaction specific coefficients.

Finally, the neutral reactions involving vibrational energy transfer through VT and VV relaxation between different molecules are presented in Table A.5.

In later chapters (5 and 6), the chemistry set is updated (i.e. rate coefficients for reactions $CO_2 + O \leftrightarrow CO + O_2$ are slightly changed) by comparing the thermodynamic equilibrium conversion calculated by the model, with the theoretical thermodynamic equilibrium conversion. Also, the cross section set was updated. The changes made to the chemistry set are shown in section A.2. In chapter 6,

O_2^+, and a higher number of vibrational levels of CO and O_2 are added since at the conditions under study, high conversion degrees, i.e. high concentrations of CO and O_2, are obtained. The added or changed reactions are shown in section A.3.

The chosen reaction rate coefficients are subject to uncertainty. This uncertainty propagates to the model output. It was shown by Berthelot and Bogaerts that the uncertainty on certain important calculation results, such as the CO_2 conversion and vibrational population, can even reach 100%[114]. Nevertheless, this study also revealed that the trends predicted by the model are typically not affected by the uncertainty. In the modeling results, presented in this thesis, it is therefore more important to focus on the trends rather than the absolute values that are presented.

3.4 Scaling reactions including vibrational levels

Most of the rate coefficients and cross sections used in this work are generally known for the ground state or low vibrational level molecules. Scaling laws are used to scale these rate coefficients towards higher vibrational levels. In this study, we mostly follow the same approach as in previous work[28;100;101;103;104;113;114;124;125] to determine the various rate coefficients. The reactions that require scaling for higher vibrational levels are: electron impact reactions (Table A.1 and A.6), reactions involving vibrational exchange (VV and VT reactions, Table A.5 and A.11), and neutral reactions (Table A.4 and A.7).

3.4.1 Electron impact reactions

The cross sections for vibrational excitation are usually only known for reactions starting from ground state to the lower vibrational levels. We use the Fridman approximation to scale the excitation cross section σ_{nm} for the reaction involving the vibrationally excited molecule X: $X(v_n) + e^- \rightarrow X(v_m) + e^-$ from the know cross section σ_{01}, i.e. the cross section for excitation from the ground state to $X(v_1)$[37;103]:

$$\sigma_{nm}(\epsilon) = \frac{exp(\alpha(m-n-1))}{1+\beta n}\sigma_{01}(\epsilon + E_{01} - E_{nm}) \tag{3.4}$$

in which $E_{01} = E_1 - E_0$ and $E_{nm} = E_m - E_n$ are the energy differences between vibrational states 1 and 0 and states m and n, respectively, ϵ is the electron energy, and α and β are two scaling parameters. The values used in this work are given by Fridman[37]. For CO_2, $\alpha = 0.5$ and $\beta = 0$, for CO, $\alpha = 0.6$ and $\beta = 0$, and for O_2, $\alpha = 0.7$ and $\beta = 0$.

For excitations to bound states, like electronically excited states or ionization of a molecule, the process is likely to proceed through another vibrational excited level, according to the Frank-Condon principle. We therefore assume no effect of vibrational energy on these reactions, and the same cross sections as for the reactions from ground state are used. On the contrary, we assume that the vibrational excitation is effective in lowering the energy barrier for dissociation and dissociative ionization reactions. We therefore lower the threshold energy of the cross section by the vibrational energy of the level.

For all excitation reactions, the cross sections for the reverse de-excitation processes (i.e. superelastic collisions) are determined from the detailed balance principle.

3.4.2 Vibrational energy exchange reactions

Serveral theories exist to scale the rate coefficients of vibrational exchange reactions (VT relaxation, VV relaxation between the same molecules, and VV' relaxation between different molecules) to higher vibrational levels[97;103]. The theoretical models available can be put in three major categories; 1) first order perturbation theories (FOPT), 2) forced harmonic oscillator (FHO) models, and 3) quantum-classical trajectory (QCT) calculations. FOPTs are based on collinear collision models that may be suited to calculate transition probabilities for conditions where they are much smaller than unity[97]. The most popular FOPTs include the Schwartz–Slawsky–Herzfeld (SSH) theory[126] and the Sharma–Brau (SB) theory[127]. The SSH theory considers short-range repulsive forces to be effective in producing vibrational transitions, while the SB theory considers long-range repulsive forces[97;128]. This might lead to an overestimation of the reaction rates at higher temperatures for the SSH theory, while the SB theory might lead to an underestimation of the rates at higher temperatures. In general, these FOPTs are only valid at low to moderate temperatures, and they only cover single quantum transitions. However, these theories are very popular for their simplicity. While the forced harmonic oscillator theory, and quantum classical trajectory calculations are both more accurate theories, most of the calculations that have been performed with these theories concern diatomic molecules[129–132]. While efforts are being made to extend these theories for CO_2[133–135], no full set is yet available.

In this work, the SSH theory is used to scale the VV and VT relaxation rates. A detailed explanation of the application of this theory to the CO_2 chemistry set can be found in Kozák and Bogaerts[103], and Koelman et al.[113]. For VT relaxation, the scaling goes as follows:

$$k_{n,n-1} = k_{1,0} Z_n \frac{F(\gamma_n)}{F(\gamma_1)} \tag{3.5}$$

where $k_{n,n-1}$ is the rate constant for VT relaxation $X[v_n] \longrightarrow X[v_{n-1}]$ and $k_{1,0}$ is the basic rate constant for $X[v_1] \longrightarrow X$, with n being the vibrational number of molecule X. The scaling factor Z_n is expressed as:

$$Z_n = n \frac{1 - x_e}{1 - n x_e} \tag{3.6}$$

where x_e is the anharmonicity of the energy levels. The function F is given by:

$$F(\gamma_n) = \frac{1}{2} \left[3 - \exp(-\frac{2}{3}\gamma_n) \right] \exp(-\frac{2}{3}\gamma_n) \tag{3.7}$$

Finally, γ_n is a parameter measuring the adiabaticity of the reaction and is calculated as:

$$\gamma_n = \Big(\frac{\pi^2 \omega_n^2 \mu}{2\alpha^2 k_B T_g} \Big)^{1/2} \tag{3.8}$$

with $\omega_n = \Delta E/\hbar = |(E_n - E_{n-1})|/\hbar$ the energy over the reduced Plank constant, μ represents the reduced mass and α is a parameter of the exponential repulsive potential. The value of α is determined by using[126] $\alpha = 17.5/r_0$, with r_0 the radius parameter of the Lennard-Jones potential. The values of r_0 are taken from Kozák and Bogaerts[103]: 3.94 Å, 3.69 Å and 3.47 Å for CO_2, CO and O_2, respectively.

The scaling law to obtain rate coefficients for reactions involving vibrational exchange between two identical molecules (VV) and vibrational exchange between two different molecules (VV') is slightly different. The following scaling law is used for reactions $X[v_n] + X[v_{m-1}] \longrightarrow X[v_{n-1}] + X[v_m]$ and $X[v_n] + Y[v_{m-1}] \longrightarrow X[v_{n-1}] + Y[v_m]$:

$$k_{n,n-1}^{m-1,m} = k_{1,0}^{0,1} Z_n Z_m \frac{\gamma_{nm}}{\gamma_{11}} \tag{3.9}$$

γ_{nm} is calculated from equation (3.8), in which $\omega_n = |(E_n - E_{n-1})|/\hbar$ is replaced by $\omega_{nm} = |(E_n + E_{m-1} - E_{n-1} - E_m)|/\hbar$, and Z_m and Z_n are defined by equation (3.6)

3.4.3 Neutral reactions

In neutral reactions, the vibrational energy can be used to overcome the activation energy barrier. The neutral reaction rate coefficients for higher vibrational levels

can be expressed with the theoretical-informal approach[28;37]:

$$k(T_g, E_v) = f(T_g) \cdot A \cdot min\left[exp\left(\frac{-(E_a - \alpha E_{v_i})}{k_B T_g}\right), 1\right] \tag{3.10}$$

where T_g and T_v are the gas and vibrational temperatures, respectively, k_B is the Boltzmann constant, A the pre-exponential factor, E_a the activation energy, E_{v_i} the vibrational energy of each level i, and α a parameter that determines the efficiency with which the vibrational energy is used to overcome the activation energy barrier. When $\alpha E_{v_i} > E_a$, the reaction is considered to be barrierless, and the rate coefficient is equal to the pre-exponential factor. The efficiency α is calculated according to the Fridman-Macheret approximative α model[37]

$$\alpha = \frac{E_a}{2E_a - \Delta H^o} \tag{3.11}$$

where ΔH^o is the enthalpy of the reaction.

The pre-exponential factor and the activation energy are experimentally or theoretically determined (see details in tables A.4 and A.7). To calculate these two constants, no distinction is made between the different higher energetic states. The gas is viewed as a neutral ensemble. However, at higher gas temperatures, the higher vibrational levels are more populated, since their population is described by the Boltzmann distribution at equilibrium conditions:

$$\frac{N_{CO_2(v_i)}}{N_{CO_{2,tot}}} = \frac{exp\left(\frac{-E_{v_i}}{k_B T_g}\right)}{\sum_i exp\left(\frac{-E_{v_i}}{k_B T_g}\right)} \tag{3.12}$$

When considering these states separately, and using equation 3.10, the reaction rate at a given temperature and equilibrium conditions should be the same as when considering the total CO_2 gas as an ensemble and using a regular Arrhenius expression. To make both of these rates match, the following correction function $f(T_g)$ is added to equation 3.10:

$$f(T_g) = \left(\sum_i \frac{exp\left(\frac{-E_{v_i}}{k_B T_g}\right)}{\sum_j exp\left(\frac{-E_{v_j}}{k_B T_g}\right)} exp\left(\frac{\alpha E_{v_i}}{k_B T_g}\right)\right)^{-1} \tag{3.13}$$

This correction is only included in chapter 6 due to the high gas temperatures that are reached in that study.

3.5 Characteristic time scales of VV and VT relaxation and electron impact vibrational excitation

In addition to translational energy, vibrational energy can also be used to overcome the activation energy barrier of two main dissociation reactions (i.e. CO_2 + M $\rightarrow$ CO + O + M, and CO_2 + O $\rightarrow$ CO + O_2). Given the high activation energy barriers (E_a) of both reactions (i.e. E_a = 4.55 eV and E_a = 1.44 eV, respectively), the dissociation goes through the higher vibrational levels when the gas temperature is low[28;101]. In order to get high overpopulation, electron impact vibrational excitation and VV relaxation need to occur faster than VT relaxation. In figure 3.2, we plot the characteristic time scales for the following reactions as a function of gas temperature, in the range of interest for typical plasmas used for CO_2 conversion, and at a pressure of 100 mbar:

- e^- + CO_2 $\rightarrow$ e^- + CO_2(V1), as characteristic electron impact vibrational exciation (eV)
- CO_2 + CO_2(V1) $\rightarrow$ CO_2 + CO_2, as characteristic VT relaxation
- CO_2 + CO_2(V1) $\rightarrow$ CO_2(V1) + CO_2, as characteristic VV relaxation

The characteristic time scales for these reactions are defined as $\tau_{eV} = (n_e k_{0\rightarrow1}^{eV})^{-1}$, $\tau_{VT} = (n_{CO_2} k_{1\rightarrow0})^{-1}$, and $\tau_{VV} = (n_{CO_2} k_{1\rightarrow0}^{0\rightarrow1})^{-1}$, with $k_{0\rightarrow1}^{eV}$, $k_{1\rightarrow0}$, and $k_{1\rightarrow0}^{0\rightarrow1}$, the rate constants for eV, VT and VV processes, respectively, and with n_e, and n_{CO_2} the electron and CO_2 number densities, respectively. The rate constants for VV and VT relaxation are taken from table A.5, while the electron impact vibrational excitation rate constant is calculated based upon the cross section and a Maxwellian EEDF, with average electron energy of a CO_2 plasma at a reduced electric field of 50 Td, namely 0.9 eV[28]. We plot the eV characteristic time scale not only at an ionization degree of 10^{-6}, but also at 10^{-5} and 10^{-7}, as this value greatly affects the characteristic time.

We want to note that the characteristic time scale of VV and VT relaxation corresponds to the relaxation time of an excited CO_2(V1), while the characteristic time scale of the electron impact reaction represents the time at which one CO_2 molecule gets excited. Given that eV takes place before VT can take place, this does not mean that if the time scale of VT relaxation is shorter than that of the electron impact excitation, no vibrationally excited molecules will exist. Also, the reaction rate of electron impact excitation will still be higher at comparable time scales, because the gas predominantly contains CO_2 ground state molecules. Hence, this must be taken into account when comparing these different time scales.

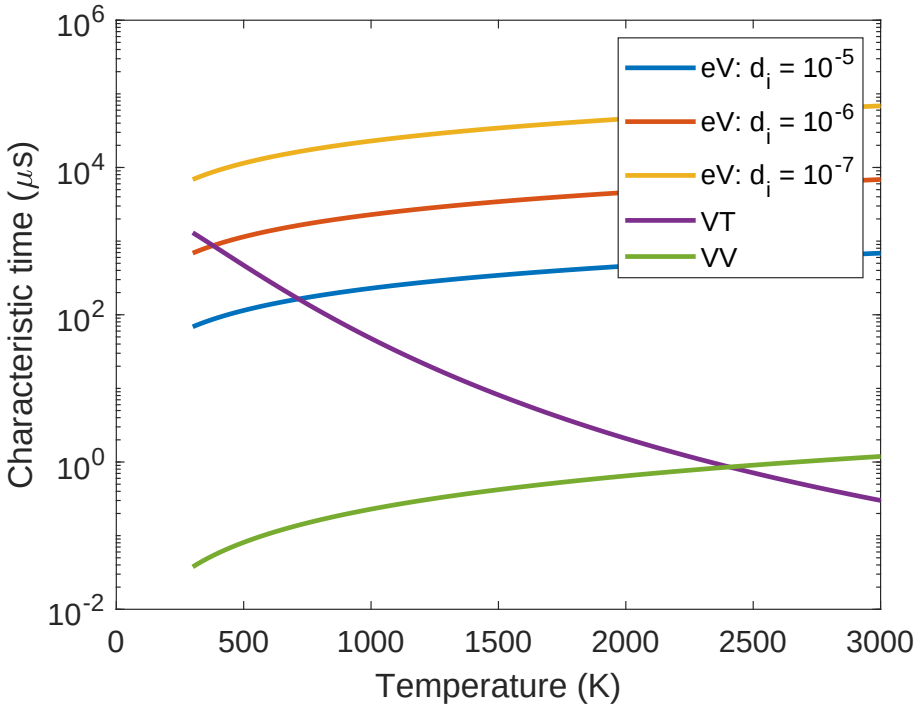

Figure 3.2: Characteristic time scales of electron impact vibrational excitation (eV) at three different ionization degrees (d_i) and a reduced electric field of 50 Td, and of VT and VV relaxation, as a function of gas temperature at a pressure of 100 mbar.

At 300 K, the characteristic time scale of VT relaxation (1.3 ms) is comparable to that of the electron impact vibrational excitation at $d_i = 10^{-6}$ (0.7 ms), while VV relaxation happens at a much shorter time scale (0.04 μs). This means that the rate of population of the higher vibrational levels, needed for energy-efficient CO_2 dissociation, is mainly limited by the electron impact vibrational excitation. This excitation process can be enhanced upon increasing ionization degree, which is logical, as there will be more electrons available for excitation. At a 10 times higher ionization degree (10^{-5}), the characteristic time scale of vibrational excitation decreases with the same factor 10. Similarly, an decrease in the ionization degree to 10^{-7} will increase the relaxation time.

The characteristic time scales of electron impact vibrational excitation and VV relaxation increase with gas temperature, while the characteristic time scale of VT relaxation decreases drastically, which is both detrimental for populating the higher vibrational levels, and thus for energy-efficient CO_2 conversion. At temperatures above 2400 K, VT relaxation becomes even faster than VV relaxation. We want to note that the characteristic time scale of electron impact vibrational

excitation changes with gas temperature, simply because the ionization degree is fixed and the gas density changes with gas temperature. For a constant electron density and electron temperature, the time scale would not change with gas temperature. To maximize the effect of vibrational-induced dissociation, the gas temperature thus needs to be close to room temperature, in combination with an as high as possible ionization degree, which is consistent with previous model calculations from our group[28]. The time scales, shown in figure 3.2, will be used to explain the trends in chapter 5.

CHAPTER 4

Microwave plasmas in supersonic flow

The results presented in this chapter were published in [124]:

- V. Vermeiren and A. Bogaerts. Supersonic Microwave Plasma: Potential and Limitations for Energy-Efficient CO_2 Conversion. *J. Phys. Chem. C*, 122(45):25869–25881, 2018. DOI: 10.1021/acs.jpcc.8b08498

4.1 Introduction

Berthelot and Bogaerts studied the effect of different discharge conditions on the energy efficiency and CO_2 conversion in microwave plasmas[101]. They concluded that lower pressures, higher power densities, and lower temperature had a beneficial effect on the efficiency of the dissociation process. The lower pressure and higher power densities lead to more vibrational excitation, which is beneficial for the conversion. A lower temperature results in more pronounced VV transfer with respect to VT transfer.

The requirement of low pressure and low temperature, however, poses challenges for industrial application of the technique. A microwave supersonic flow plasma can tackle these two issues. The maximum energy efficiency, reported to date, was in such a reactor[36]. In this setup, a pressure difference is applied over a converging-diverging nozzle. The adiabatic expansion of the nozzle cross section accelerates the flow to supersonic velocities. A first benefit of this type of reactor is that the acceleration to supersonic speed creates a pressure drop, from high pressure conditions ($\geq$ 1 bar) to intermediate pressure (around 100 mbar), the latter being more beneficial for energy-efficient conversion[29;37;101]. A second benefit is that the rapid increase in kinetic energy reduces the internal energy of the gas, thus lowering the temperature[136]. This allows the use of higher power densities, while staying at low temperatures, which is also beneficial for energy-efficient CO_2 conversion.

Even in the absence of electromagnetic coupling, the supersonic flow field can drive the overpopulation of the highly excited vibrational states, leading to dissociation of CO_2[37]. This effect of supersonic expansion on the non-equilibrium vibrational distribution function in CO_2 was theoretically studied by Peerenboom et al.[137] in a quasi 1D model, which includes 21 asymmetric mode vibrational levels and state-to-state vibrational kinetics. The model shows that supersonic expansion indeed has a beneficial effect on the population of the highest vibrational levels.

In this chapter, we present a combined supersonic flow model and chemical reaction kinetics model of a supersonic microwave CO_2 plasma in a converging-diverging nozzle geometry. The aim of this work is to study the effect of different characteristics of supersonic flow, e.g. pressure drop, and the shock wave, on the reaction kinetics. Based on this information, we will change the flow conditions in the model, in order to manipulate the flow field to examine the effect of the latter on the CO_2 conversion.

4.2 Computational details

The study consists of two separate parts. First, non-reactive flow simulations are performed in COMSOL multiphysics. A 2D axisymmetric high Mach flow number k/ϵ-model is used to calculate the flow for pure CO_2 at room temperature. This model combines the standard Reynolds Average Navier Stokes (RANS) k/ϵ-model with Euler's equations for inviscid flow, and will be explained in more detail in section 4.2.1. This model is chosen based upon its user-friendly nature, and the limited amount of computational resources and time needed to acquire results. Certain aspects of the flow behavior are not captured in our model in contrast to more complex simulations[138]. However, the effect of the approximations is not to an extent that will be relevant for this study.

Subsequently, a center cut line of the flow results is used as input in a zero-dimensional chemical kinetics model, described in more detail in section 4.2.2. The chemistry set used is presented in section 4.2.3. During the different simulations, the pressure and temperature will be fixed. The flow and plasma description are thus decoupled. The validity of this assumption, as well as other model approximations, will be discussed in more detail in section 4.2.4.

4.2.1 Flow model

The standard RANS k/ϵ-model is well known in computational fluid dynamics theory and can describe a wide range of turbulent flows[139]. It is a two-equation turbulence model that solves for the mass and momentum continuity partial differential equations:

$$\nabla \cdot (\rho \mathbf{u}_g) = 0 \tag{4.1}$$

$$\begin{aligned} \rho (\mathbf{u}_g \cdot \nabla) \mathbf{u}_g = \nabla \cdot \Big[& -p\mathbf{I} + (\mu + \mu_T) \left(\nabla \mathbf{u}_g + \nabla (\mathbf{u}_g)^T \right) \\ & + \frac{2}{3} (\mu + \mu_T) (\nabla \cdot \mathbf{u}_g) \mathbf{I} - \frac{2}{3} \rho k \mathbf{I} \Big] + \mathbf{F} \end{aligned} \tag{4.2}$$

where ρ stands for the gas density, $\mathbf{u}_g$ is the gas flow velocity vector, superscript T stands for transposition, p is the gas pressure, μ and μ_T are the dynamic and turbulent viscosity of the fluid, k is the turbulent kinetic energy, $\mathbf{I}$ is the unity tensor and $\mathbf{F}$ is the body force vector. Next to this, the turbulence is modelled by adding two additional equations that solve for the turbulent kinetic energy k, and the turbulent dissipation rate ϵ:

$$\rho (\mathbf{u}_g \cdot \nabla) k = \nabla \cdot \left[\left(\mu + \frac{\mu_T}{\sigma_k} \right) \nabla k \right] + P_k - \rho \epsilon \tag{4.3}$$

$$\rho\left(\mathbf{u}_g \cdot \nabla\right)\epsilon = \nabla \cdot \left[\left(\mu + \frac{\mu_T}{\sigma_\epsilon}\right)\nabla\epsilon\right] + C_{\epsilon 1}\frac{\epsilon}{k}P_k - C_{\epsilon 2}\rho\frac{\epsilon^2}{k} \tag{4.4}$$

Equation 4.3 and 4.4 calculate the transport of turbulent energy and its dissipation into heat (ϵ), respectively. P_k represents the production term for turbulent kinetic energy. σ_k, σ_ϵ, $C_{\epsilon 1}$, and $C_{\epsilon 2}$ are model constants which are experimentally determined[139].

Since all flow properties are coupled to each other, the number and combinations of boundary conditions that are needed for well posedness depend on the flow state[140]. In order to provide consistent inlet and outlet boundary conditions, the speed at which the different flow quantities propagate at the boundary needs to be known.

A plane wave analysis of the inviscid part of the flow is performed in order to apply a consistent number of boundary conditions, using the method described in detail in ref. 141. Inviscid flow is described by Euler's equations, which can be written as

$$\frac{\partial \mathbf{Q}}{\partial t} + \frac{\partial \mathbf{F}_j}{\partial \mathbf{Q}}\frac{\partial \mathbf{Q}}{\partial x_j} = 0 \tag{4.5}$$

where

$$\mathbf{Q} = \begin{bmatrix} \rho \\ u_i \\ p \end{bmatrix}$$

with $\mathbf{Q}$ the state vector to be solved for, $\mathbf{F}_j$ the flux vector and ρ, u_i and p the mass density, velocity components and pressure, respectively.

4.2.2 Plasma model

In this chapter, the plug flow approximation described in section 2.4.5 is used. The model uses the input values for pressure, temperature, and mass flow rate that were aqcuired from the flow model, to calculate the velocity from the conservation of mass flow rate (see equation 2.22). The model starts at the inlet ($z = 0$) with pure CO_2. The plasma is ignited at a certain axial position in the reactor. In the plasma region, two plasma parameters are fixed. The reduced electric field is fixed to a value of 50 Td, and the ionization degree to 10^{-6}, which are both typical values for CO_2 microwave plasmas[29;38].

We use a fixed value for the SEI, and apply a power deposition until the value for the SEI, calculated with equation 2.24,is reached at $z = z_0 + z_p$, with z_p the

plasma length, after which the power deposition drops to 0. This approach can be seen in figure 4.1, and was used in similar studies by our group[28;114]. The plasma length is calculated by the model, based on the SEI value used. This is preferable, since no experimental data are available on the plasma length in this type of reactor.

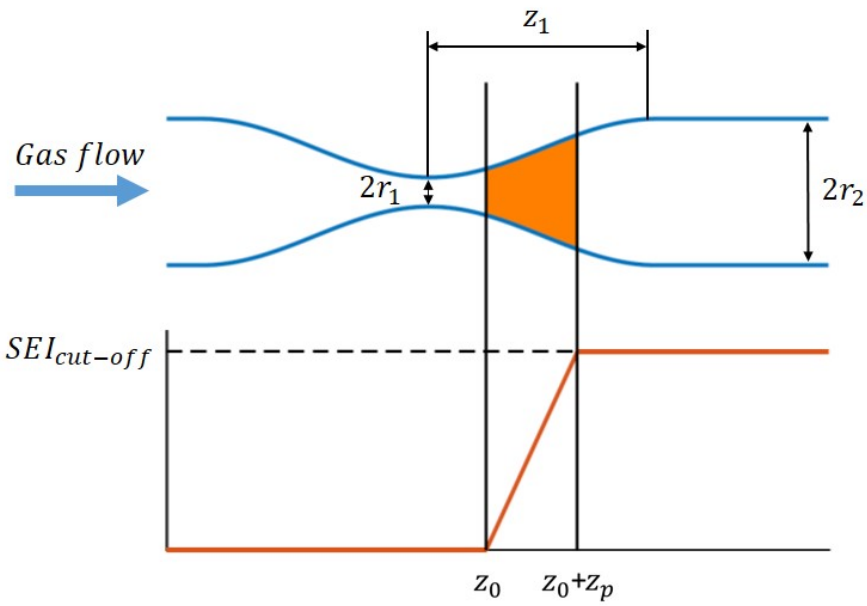

Figure 4.1: Schematic presentation of the Laval nozzle geometry (top) with plasma (orange) and specific energy input SEI (bottom) as a function of the axial distance in the geometry. The plasma starts at z_0 and continues until the cut-off value for the SEI is reached at $z_0 + z_p$, with z_p the plasma length.

4.2.3 Chemistry set

The species used in the chemistry set of this chapter are shown in table 3.1. The reactions are shown in the tables of section A.1. Tables A.1 and A.2 show the electron impact reactions, described by cross sections and analytical expressions, respectively. Tables A.3 and A.4 list the reactions involving ions, and the neutral-neutral reactions, respectively. The reactions in which vibrational energy is exchanged are shown in Table A.5.

4.2.4 Model approximations

Every model needs approximations, so here we would like to point out the validity of the approximations made in this work. First, the setup is studied with a 0D

model. This model is radially averaged and can thus not take into account any spatial gradients in the radial direction. In reality, a MW plasma can become contracted when operating at higher pressures[60;142], which can thus not be captured by our model. A 0D model is however still favourable, since it yields a detailed description of the plasma chemistry, needed to evaluate the CO_2 conversion and energy efficiency, within limited calculation time.

Further approximations are related to the temperature of the molecules. When a supersonic flow expands, internal energy is converted to kinetic energy in order to fuel the acceleration[136;143;144]. This acceleration happens adiabatically if no heat source is applied on the flow. The flow is then described by the isentropic flow relations between pressure, temperature and density for a perfect gas:

$$\frac{p}{p_t} = \left(\frac{\rho}{\rho_t}\right)^{\gamma} = \left(\frac{T}{T_t}\right)^{\frac{\gamma}{\gamma-1}} = \left(1 + \frac{\gamma-1}{2}M^2\right)^{-\frac{\gamma}{\gamma-1}} \tag{4.6}$$

where p, ρ, T are the static pressure, mass density, and temperature, respectively, and p_t, ρ_t, T_t the total pressure, mass density and temperature, $\gamma = c_p/c_v$ is the ratio of specific heats, and M the Mach number of the flow. The total pressure, mass density and temperature are those when the flow is isentropically brought to rest, i.e. when $M = 0$, and are assumed to stay constant when no heat is exchanged with the environment.

In the model, a temperature-dependent lookup table is used as input for the specific heat capacity at constant pressure (c_p), from which γ is calculated according to:

$$\gamma = \frac{c_p}{c_p - R_s} \tag{4.7}$$

with $R_s = 188.9\ J/(kg \cdot K)$ the specific gas constant of CO_2. In the supersonic region, the gas temperature decreases to fuel the acceleration. At low temperatures (< 300 K), the vibrational degrees of freedom are less easily excited, and therefore become less important in the calculation of γ. In the supersonic region, γ approaches 1.4, which is the ratio of specific heats that only includes the translational and rotational degrees of freedom in a linear molecule.

Given that the flow and the plasma are decoupled, the effect of the plasma on the flow is not included in this model. When a plasma is created in the supersonic region, the applied electrical energy can either dissociate the gas, or can be lost in gas heating. Gas expansion due to conversion can lead to an increase in the molar flow rate. In this chapter, however, the conversion is limited to a few percent (see section 4.3)), so the effect of the conversion on the flow will be low.

When heat is added to supersonic flow, the trends of the different physical parameters are quite different with respect to subsonic flow. Contrary to subsonic

flow, heat addition in supersonic flows will lead to a deceleration of the flow to lower Mach numbers[144]. Such flow with heat addition is called Rayleigh-line flow[144] and is described by a Rayleigh curve. The added heat will lead to both a temperature and pressure increase[144]. This phenomenon is very unfavourable for MW plasma-based CO_2 conversion[101]. The amount of heat can increase until a critical value for added heat is reached. At that point, the gas is decelerated to $M \approx 1$, after which the flow will be thermally choked[37;143;145;146], and a shock is generated. The critical heat (Q_{cr}) that can be added to a system, without thermally choking the flow, can be estimated by the formula:

$$Q_{cr} = c_p T_0 \left[\frac{(M^2-1)^2}{2(\gamma+1)M^2[1+(1/2)(\gamma-1)M^2]} \right] \tag{4.8}$$

with c_p the specific heat capacity, and T_0 the inlet nozzle gas temperature. The critical heat can be augmented by an increase of the inlet nozzle temperature T_0 or by reagents dilution in noble gases[146].

Eq. 4.8 is valid for constant area ducts. The deceleration of the flow, due to heat addition, can be countered by increasing the cross-sectional area of the discharge over the region in which the heat is added[146]. This phenomenon is called 'nozzle profiling' and can double the critical heat with a sixfold increase of the cross-sectional area[146]. However, since the 0D model does not take into account radial contraction of the plasma, the plasma length is shorter than it would be in a full 3D (or 2D cylindrically symmetric) calculation. Hence, the plasma length is only a few millimetres long (see section 4.3). The formula of the constant area duct (equation 4.8) can thus serve as a good estimate for our case, since a significant increase of the cross-sectional area over this distance is too complex and maybe impossible.

Figure 4.2 shows the critical heat as a function of Mach number. We can see that the critical heat rises with higher Mach numbers, until a maximum value of 0.1867 eV/molec. is reached at Mach ∞.

The heat that is added to the system, by the plasma, is $Q = (1-\eta)\times$ SEI. This heat will increase the total temperature, while the total pressure is unaffected. The static pressure and temperature will increase (i.e. closer to the total values) due to the deceleration of the Mach number (see equation 4.6). In this study, we use non-reactive flow results from COMSOL (i.e. without plasma) as input in a 0D plasma model. This means that the pressure and temperature remain fixed in the 0D model. Given that the total temperature (i.e. when the flow is at M = 0) remains at room temperature, we can assume that the reported energy efficiencies are maximum values of what can be achieved with this model, given that heat from the plasma would increase the total and static temperature and thus lower the energy efficiency[101]. To make sure that after the plasma is applied,

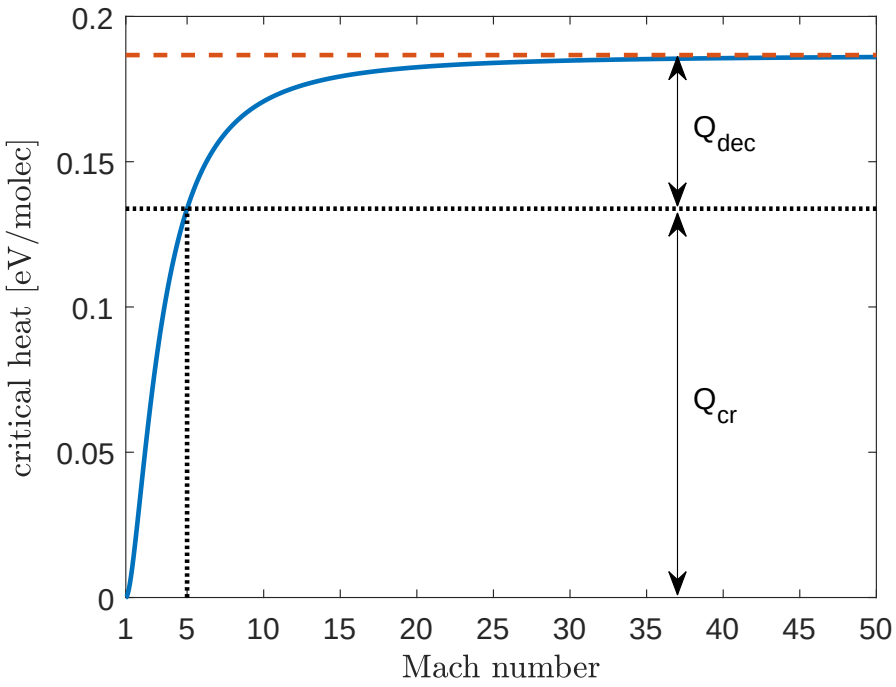

Figure 4.2: Critical heat before thermal choking of the flow occurs, as a function of Mach number (full line), with the maximum critical heat at high Mach numbers (dashed line) and the critical heat and the deceleration heat for an example at Mach = 5 (dotted line)

the static temperature and pressure conditions are still valid, we will assume that the heat from the plasma has decelerated a hypothetical initial flow with much higher Mach number to the one which we are using. The maximum deceleration heat for a certain Mach number can then be defined by:

$$Q_{dec}(M) = Q_{cr}(M_\infty) - Q_{cr}(M) \tag{4.9}$$

where the flow decelerates from Mach ∞ to the Mach number from the flow results. For example, if flow conditions are used in which the Mach number reaches 5, then the maximum heat that can be added is the heat that slowed the flow down from Mach ∞ to Mach 5, i.e. $Q_{dec}(5) = Q_{cr}(M_\infty) - Q_{cr}(5) = 0.1867 - 0.1338 = 0.0529$ eV/molec. The maximum deceleration heat, and the critical heat are displayed in figure 4.2 for the example of Mach = 5. In this study, we make sure that the SEI is always chosen as not to violate the criterion of equation 4.9. As mentioned above, the rising gas temperature due to the plasma can increase the molar flow rate. This effect is not taken into account in our flow model, because the plasma and flow model are decoupled. The magnitude

of this effect is unclear and will depend on the SEI and the energy efficiency of the conversion process.

Given that microwave CO_2 plasmas can be characterized by a high thermodynamic non-equilibrium, the effect of the supersonic flow on the rotational and vibrational temperature needs to be discussed. In this study, the rotational degrees of freedom are assumed to be in equilibrium with translation, and will not be separately described. This assumption is valid for microwave CO_2 plasmas[147] since the rotational-translational relaxation only slows down at very high gas temperatures[148]. We assume in this study that the vibrational temperature is also not affected by the supersonic expansion. Given that most of the energy for supersonic acceleration comes from translational energy, yielding a drop in gas temperature while the vibrational temperature remains constant, the non-equilibrium between these two is enhanced, leading to overpopulation of the vibrational levels with respect to the Boltzmann distribution[37;137]. This assumption is also used in vibrational collision studies of hypersonic flows[149;150].

4.3 Results and discussion

In section 4.3.1, we will illustrate the flow field results without plasma, i.e., for pure CO_2 at room temperature inlet conditions. In section 4.3.2 and 4.3.3, we will describe the evolution of the plasma through the reactor, with focus on the CO_2 dissociation and recombination mechanisms, and the evolution of the vibrational distribution function. In sections 4.3.4, 4.3.5, and 4.3.6, we will discuss in more detail the effect of plasma position, flow conditions, and power, on the overall energy efficiency and CO_2 conversion. Finally, in section 4.3.7, we will study the maximum theoretical energy efficiency for different inlet and outlet pressures.

4.3.1 Flow field results without plasma

The three parameters that define the geometry (see figure 4.1) are chosen to resemble the dimensions in which high energy efficiency is reported[36]: $r_1 = 0.4$ cm, $r_2 = 2$ cm, and $z_1 = 10$ cm. The inlet nozzle is slightly larger than reported in[36]. The flow results for an inlet pressure $p_{in} = 2$ bar and outlet pressure $p_{out} = 1$ bar are plotted in figure 4.3, illustrating the axial velocity profile, the Mach number, the static pressure and the static temperature. The results are only shown in the expansion region of the nozzle, where the supersonic acceleration affects these quantities. We discuss here one flow field case, for one geometry, inlet and outlet pressure, in detail, but additional flow results for different conditions and geometries (i.e. different values for z_1) can be found in appendix B.

The flow field consists of two distinct regions (depicted in figure 4.3(a)). First,

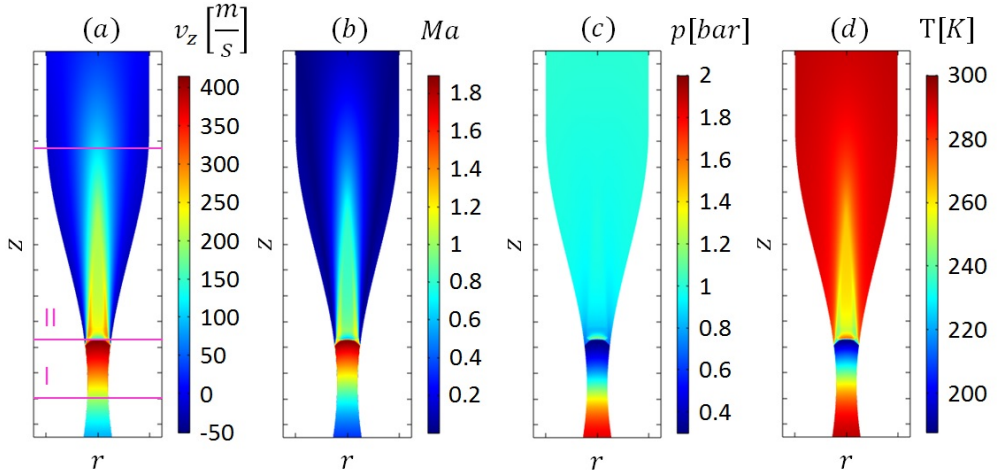

Figure 4.3: (a) Axial velocity magnitude (b) Mach number (c) static pressure and (d) static temperature in the case of $r_1 = 0.4$ cm, $r_2 = 2$ cm, $z_1 = 10$ cm, $p_{in} = 2$ bar, $p_{out} = 1$ bar.

the flow accelerates due to the nozzle expansion (region I), from an axial velocity of 6 m/s before the nozzle to 415 m/s (Figure 4.3(a)). This corresponds to a Mach number of 1.9 (Figure 4.3(b)). The static pressure exhibits a drop from 2 bar to 0.3 bar (Figure 4.3(c)), while the static temperature drops from 300 K to 187 K (Figure 4.3(d)).

The supersonic region I is followed by a discontinuous deceleration to sonic conditions, called a shock wave. This is characterized by a decrease in Mach number, and an increase in pressure and temperature. At the inlet pressure of 2 bar, the flow shows a single shock with bifurcated ends[151;152]. This shape is a result of boundary layer separation[151]. When the flow accelerates to a lower Mach number, the shock wave could exhibit a more curved shape[151].

The shock wave separates the supersonic region from the mixing region (region II in figure 4.3(a)). In this region the pressure increases monotonically to the outlet pressure of 1 bar. The same trend is observed in the axial velocity, Mach number, and temperature, where a gradual return to sonic conditions takes place.

It can be seen in figure 4.3(a) that a part of the axial velocity (close to the walls) is negative. There is indeed a small portion of the flow that recirculates along the walls, after the shock wave. This effect can not be taken into account in a 0D model, but is of no importance, given that the ideal plasma location lies in the supersonic region, before the shockwave.

When the flow in the supersonic region accelerates to higher Mach numbers, a third region forms between the supersonic region and the mixing region, called the shock train. The shock train is characterized by a sequence of shocks separat-

ing subsonic from supersonic regions[151]. After each shock, the flow accelerates again to supersonic velocities, after which it is decelerated by the following shock. The region is characterized by pressure and temperature oscillations. This can be seen in figure B.1 (region III), for an inlet pressure of $p_{in} = 4$ bar and outlet pressure of $p_{out} = 1$ bar, in which the flow accelerates to Mach 2.5. We want to note that in this case, the calculated minimum temperature of 141K is far below the desublimation point of CO_2 at the corresponding pressure of 0.2 bar, which is about 180 K[153]. In reality, cluster formation can occur in supersonic flow[154]. When a plasma is applied, the temperature will most likely stay above this desublimation point, so including this phenomenon in our model is not relevant for this study.

4.3.2 Main CO_2 dissociation and recombination mechanisms in the plasma and afterglow region

The mechanisms will be studied by looking at the so-called reduced reaction rates of the different processes (i.e., $100 \times R/N[\%/s]$, with R and N the reaction rates and the total gas density, respectively). This approach is chosen to take into account the change of total density through the reactor. The results can hence be interpreted as the percentage of CO_2 that is converted or recombined through these processes, with 100 $\%/s$ meaning that all CO_2 is converted in 1 second. Note that the values exceed far beyond 100 $\%/s$, since the residence time is in the order of μs.

Figure 4.4 (top) shows the main dissociation and recombination mechanisms, when applying an SEI of 0.2 eV/molec., in the supersonic flow region of a flow case with $p_{in} = 2$ bar and $p_{out} = 1$ bar, rendering M $\approx$ 1.9. The pressure variation as a function of position is illustrated in figure 4.4 (bottom). The plasma covers a domain of 1 mm (see purple rectangle in Figure 4.4), which corresponds to a residence time of 2.7 μs. The three main CO_2 dissociation mechanisms are electron impact dissociation (X4, blue curve), dissociation of ground-state and vibrationally excited CO_2 by collision with any molecule M (N1, red curve) and by reaction with an O radical (N2, yellow curve). The main recombination mechanism is recombination of CO with an O radical (N4, purple dotted curve).

At the start of the plasma, electron impact dissociation is the most prominent dissociation reaction. The reaction continues to be relevant in the entire plasma region, because of the abundance of free electrons, and drops to 0 at the end of the plasma. Vibrational-induced dissociation upon collision with any molecule (N1) becomes the most important dissociation mechanism at about 1/3 of the plasma length. The reason is that some time is required for the vibrational energy of CO_2 to climb the ladder up to the higher levels, from which dissociation can more

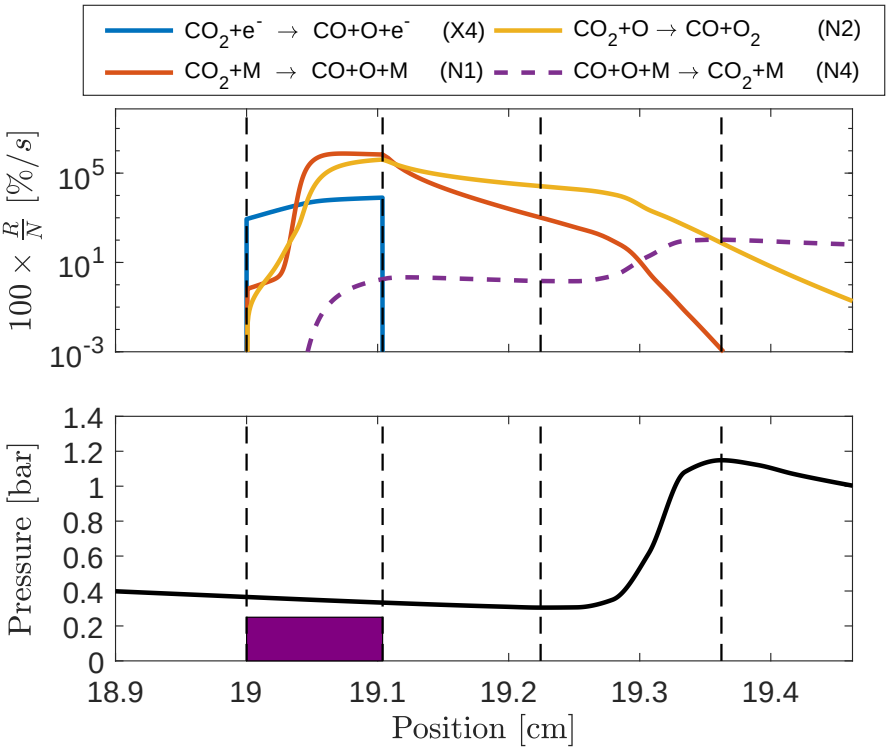

Figure 4.4: Top: Evolution of the main CO_2 dissociation and recombination mechanisms in the plasma and afterglow for the following conditions: SEI = 0.2 eV/molec., p_{in} = 2 bar, p_{out} = 1 bar, and geometry dimensions: r_1 = 0.4 cm, r_2 = 2 cm, z_1 = 10 cm. Bottom: Absolute pressure as a function of axial position with the plasma indicated as a purple rectangle.

easily take place. Given the high velocity, the gas travels some distance before this reaction becomes important. The same applies to dissociation by recombination with an O radical (N2), which even lags a little behind, since the O radicals first need to be produced by reaction (N1). At the same time, when the conversion rises in the plasma, recombination also becomes active, although the rate is much lower than for the dissociation reactions, given the low gas temperature.

As it takes some time for vibrational-induced dissociation to become a more active dissociation pathway, it is clear from these results that the short residence time (i.e. 2.7 μs) is also a limiting factor at this low SEI value. Indeed, after the high vibrational levels become more populated, the dissociation has little time to occur through this energetically favourable pathway. However, this could also be a result of working with a 0D model. In reality, radial contraction can increase the axial plasma length and thus the residence time, which would result in a greater importance of vibrational-induced dissociation, with respect to electron impact

dissociation, in the plasma. At this stage, it is not possible to quantify this effect. Furthermore, the residence time would also increase if the E/N (now set to 50 Td) or the ionization degree (now set to 10^{-6}) were lower. While reducing the ionization degree will have a negative impact on the energy efficiency, a reduction of the E/N has a positive impact[28].

In the afterglow, reactions N1 and N2 remain active, but the latter becomes the most dominant dissociation reaction. Both reactions are, however, quenched when the pressure increases in the shockwave region (between the lines at 19.22 cm and 19.36 cm). The most important recombination reaction (N4) shows an opposite trend. The reduced rate of this reaction remains the same in the afterglow, compared to the end of the plasma, but exhibits a pronounced rise in the shockwave region. After the shockwave, this reaction becomes more important than the dissociation reactions, which will limit the overall CO_2 conversion and energy efficiency.

4.3.3 Vibrational distribution function

In order to better understand the results of the previous section, we take a closer look at the evolution of the vibrational distribution function (VDF); see figure 4.5, for the same conditions as in figure 4.4. The three upper panels show VDFs, calculated at different axial positions, as indicated by the corresponding numbers in the plot of the pressure in the lower panel. At the plasma onset, the VDF shows no significant overpopulation of the vibrational levels, and is close to a Boltzmann distribution (no. 1). The vibrational temperature at that point is 237 K, while the gas temperature is 198 K. Since the supersonic acceleration increases the non-equilibrium between the gas temperature and the vibrational temperature, the value of the latter is slightly higher[137]. Very quickly, however, the vibrational levels get populated (no. 2-3), until the VDF reaches a stationary distribution (no. 4-7). This evolution explains the spatial delay in the rates of reactions N1 and N2, as displayed in figure 4.4. In the afterglow the VDF retains a high population of the higher vibrational levels (no. 8-10). However, in the shockwave, the pressure increases sharply from 305 mbar to about 1.15 bar over a distance of 1.4 mm, and the higher vibrational levels are depopulated (no. 11-14) due to VT relaxation and VV ladder downclimbing (see below). Right after the shockwave, the vibrational temperature is still high (1520 K). However, since the higher vibrational levels, from which dissociation occurs, are depopulated by VT relaxation and VV downclimbing, there is no more CO_2 dissociation at that position.

To understand what happens with the vibrational energy, we take a look at the main vibrational reaction mechanisms, namely VV and VT relaxation.

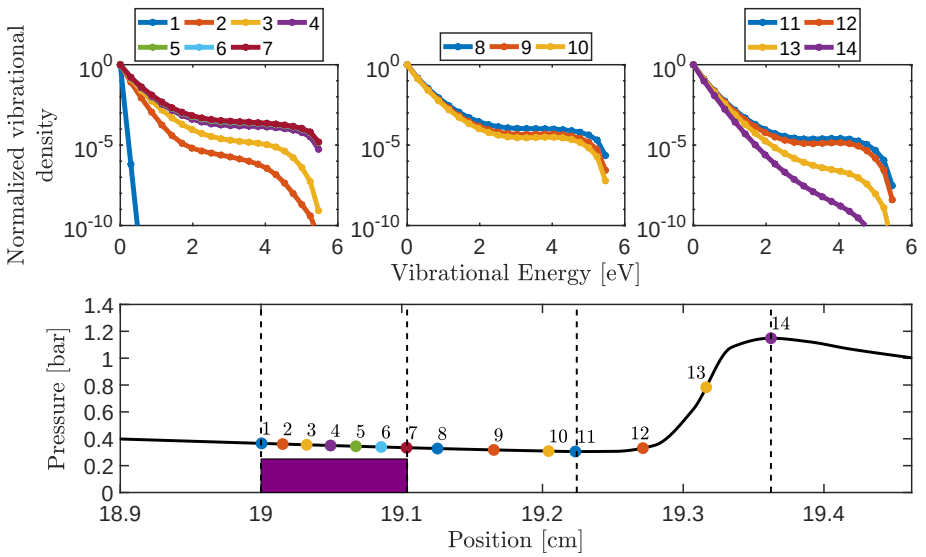

Figure 4.5: Evolution of the vibrational distribution function (VDF) for different axial positions as indicated on the pressure evolution in the lower panel, for the following conditions: SEI = 0.2 eV/molec., p_{in} = 2 bar, p_{out} = 1 bar, and geometry dimensions: r_1 = 0.4 cm, r_2 = 2 cm, z_1 = 10 cm.

Figure 4.6 shows the density averaged reaction rate for electron impact vibrational excitation (eV), VV relaxation (VV) and VT relaxation (VT), multiplied with the energy transfer of the different processes. For eV en VV (top panel), it can be interpreted as the energy that is transported up minus the energy transported down the vibrational ladder per second. For VT relaxation (middle panel) it is the energy lost to heat per second. This approach is chosen to give more weight to reactions with higher energy gains or losses.

To realize efficient vibrational-induced dissociation, the higher vibrational levels must be very quickly populated. At the start of the plasma, electron impact vibrational excitation is the only process that transports energy up the vibrational ladder (see figure 4.6, top panel). This process continues to transport energy up the vibrational ladder in the rest of the plasma. In the afterglow, this process obviously does not occur anymore. Initially, VV relaxation transports energy from the higher vibrational levels to lower vibrational levels in a ladder downclimbing process (see figure 4.6, top panel). This can be explained since most of the net energy from electron impact vibrational excitation goes to the second and third levels, and is partially returned to the first level in a ladder downclimbing process. This happens until the lower levels are sufficiently populated, and a stationary VDF is reached. More information about this can be found in appendix B (Figures B.2 and B.3). In the second half of the plasma region, there is VV ladder

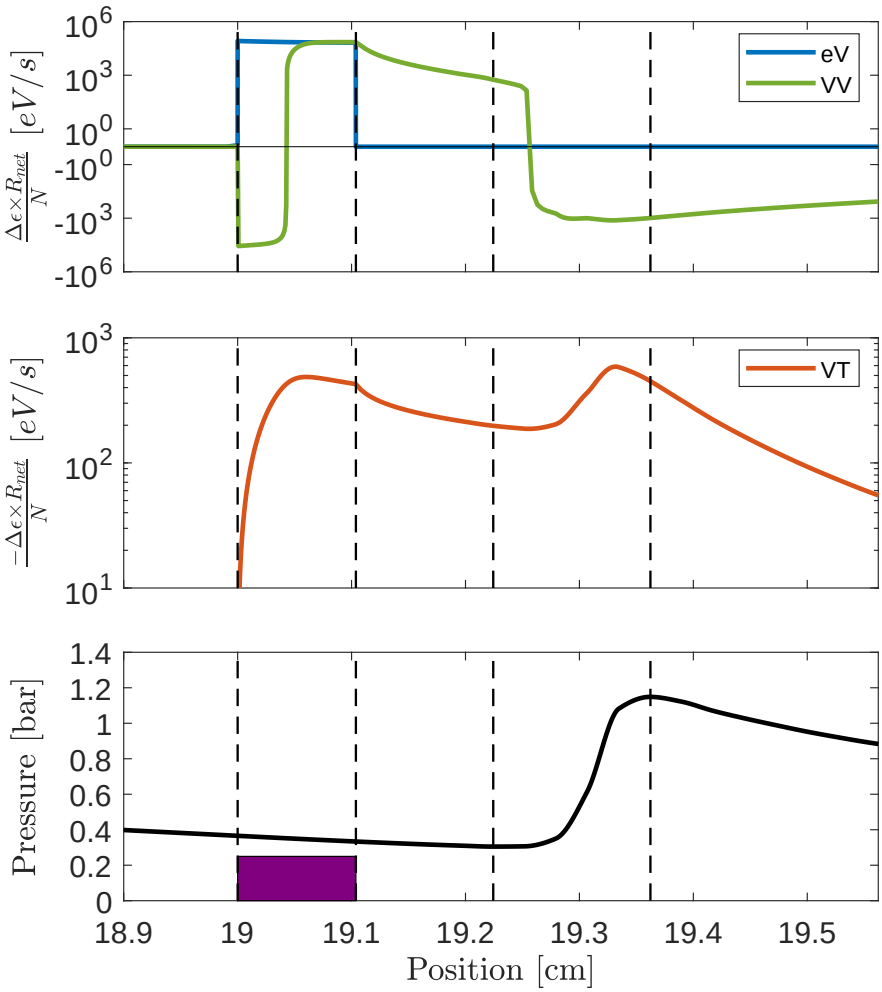

Figure 4.6: Evolution of electron impact vibrational excitation (eV, top panel), the VV relaxation (VV, top panel) and VT relaxation (VT, middle panel) through the plasma and afterglow, for the following conditions: SEI = 0.2 eV/molec., p_{in} = 2 bar, p_{out} = 1 bar, and geometry dimensions: r_1 = 0.4 cm, r_2 = 2 cm, z_1 = 10 cm. Bottom panel: Absolute pressure as a function of axial position with the plasma in purple rectangle.

climbing to the higher vibrational levels. This is continued in the afterglow, but the energy transported up the ladder gradually decreases, and reverses at some point (19.25 cm), so there is ladder downclimbing through the shockwave region.

The main vibrational energy loss, namely VT relaxation, rises in the plasma region (see figure 4.6, middle panel), due to the increasing vibrational overpopulation (cf. figure 4.5). In the afterglow, the VT energy loss slightly drops, but in the shockwave region, it rises again due to the rising pressure and temperature

(see figure 4.3).

It is clear that the depopulation of the higher vibrational levels, as shown in figure 4.5, is the result of VV ladder downclimbing and increased VT relaxation.

4.3.4 Effect of plasma position on the CO_2 conversion and energy efficiency

In the above results, the plasma was exactly located in the supersonic region. In this section, we will explore how changing the plasma position, by moving the position of the waveguide in the supersonic flow reactor, will affect the CO_2 conversion and corresponding energy efficiency. In figure 4.7 (top panel), we indicate different starting positions of the plasma region, keeping a fixed total SEI of 0.2 eV/molec. in a supersonic flow reactor with $r_1 = 0.4$ cm, $r_2 = 2$ cm, $z_1 = 10$ cm, at an inlet pressure of 2 bar and an outlet pressure of 1 bar (i.e., the same as in previous sections). In addition, the pressure evolution is shown. Note that the plasma lengths in the reactor are different, depending on the starting position, to keep the same SEI. While a larger reactor radius will result in a shorter axial plasma length, the plasma length seems more correlated with the pressure at which the plasma is ignited. Indeed, when the pressure is higher, the plasma length is shorter. This is a result of the higher power density applied to ignite a plasma with an ionization degree of 10^{-6}. In reality, axial and radial contraction of the plasma is observed at higher pressures[155], but so far this has not been studied in CO_2 microwave plasmas.

Figure 4.7 (bottom panel) shows the energy efficiency (left axis) and CO_2 conversion (right axis) for the different plasma positions, displayed in the top panel. The most energetically favourable position is coloured in green in the top panel. The energy efficiency increases from 20.5 % to 26.5 % when moving deeper into the supersonic region. The conversion rises accordingly from 1.4 % to 1.8 %. Note that the calculated energy efficiency and conversion are proportional to each other, as the SEI is kept constant here (see equation 2.26 above).

It can be seen that the most energetically favourable position (top panel) does not lie closest to the shockwave, where the pressure reaches its minimum. In fact, the energy efficiency is more than 1 % lower when the plasma lies directly in front of the shockwave. This is the result of the vibrational quenching effect due to the rising pressure in the shockwave (cf. figure 4.5 above), and the increasing importance of recombination, with respect to CO_2 dissociation (cf. figure 4.4 above). In contrast, when the plasma is generated somewhat before the shockwave, the dissociation reactions (N1, N2) continue to be important right after the plasma before the shockwave (see figure 4.4), and this has a beneficial effect on the overall conversion and energy efficiency.

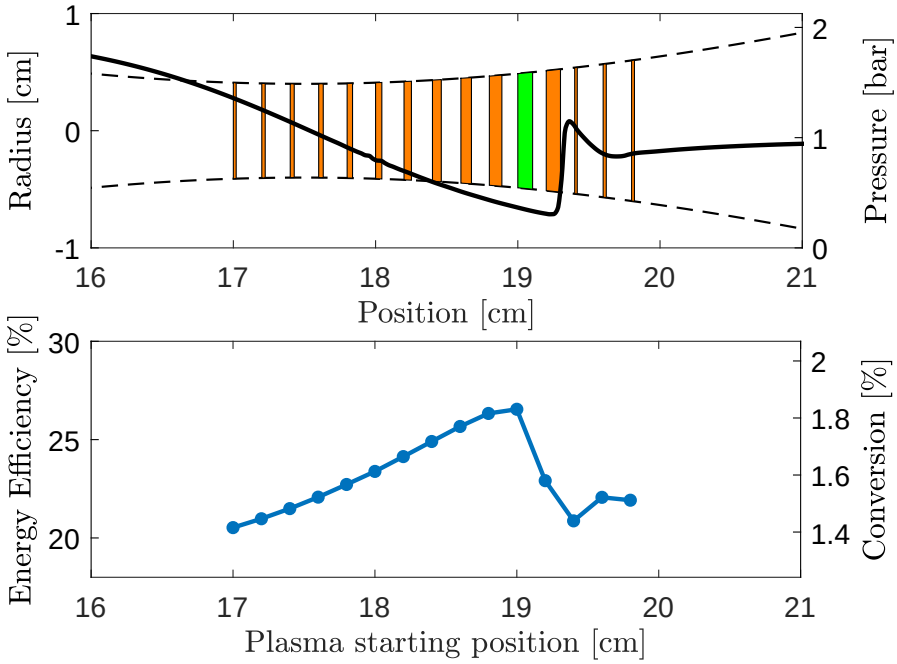

Figure 4.7: Top figure: Illustration of different plasma positions and plasma lengths as a function of the position in the reactor (dotted line), for which the CO_2 conversion and energy efficiency are calculated. Also shown is the pressure as a function of position in the reactor (full line). Bottom figure: Calculated energy efficiency and conversion for the different plasma positions indicated in the top figure.

Note that the results for energy efficiency and conversion were calculated in all cases with a fixed temperature profile, as obtained from the flow simulations (cf. figure 4.3). When the temperature would be calculated self-consistently, the energy efficiency and conversion, displayed in figure 4.7, would be somewhat lower.

4.3.5 Effect of flow conditions on the CO_2 conversion and energy efficiency

With a fixed geometry, the main parameters that can be modified to change the flow field are the inlet and outlet pressure. Their effect on the flow field parameters can be seen in detail in appendix B (Figures B.5 and B.6). Increasing the inlet pressure from 1 to 2 bar results in a lower temperature, a higher Mach number, and a lower minimum pressure. However, when the inlet pressure rises above 2 bar, the minimum pressure stays about the same, while the temperature keeps decreasing and the Mach number keeps increasing.

Reducing the outlet pressure also yields a higher maximum velocity, a higher Mach number, a lower minimum temperature, and in addition, the minimum pressure drops, in contrast to a rise in inlet pressure where the drop in minimum pressure stops at inlet pressures above 2 bar. For energy-efficient CO_2 conversion, the outlet pressure is thus an ideal parameter to tune the flow field to reach optimum conditions. In this way, the negative effects of plasma heating due to the deceleration, namely an increase in temperature and pressure (see section 4.2.4), can be countered. An increase in inlet pressure would not have the same desired effect, since the total pressure is increased, and a similar increase in added heat (and subsequent decrease in Mach number) would result in a faster rise of the absolute pressure in the pressure drop (see equation 4.6). This means that the inlet pressure is not an ideal parameter to tune the flow in order to counter the effect of increasing pressure, and will hence not be described in this section. The maximum energy efficiencies that can be reached when changing this parameter will, however, be studied in more detail in section 4.3.7.

Here, we present the effect of the flow fields on the CO_2 conversion and energy efficiency, by varying the outlet pressure. Since a lower outlet pressure will increase the Mach number of the flow (see appendix B), and in order to stay consistent with the upper limit of the added heat (see equation 4.9) we perform this study with an SEI of 0.15 eV/molec instead of 0.2 eV/molec.

Figure 4.8 shows the energy efficiency and conversion as a function of plasma position in the reactor, for three different outlet pressures (bottom panel). The pressure variation in these three cases is illustrated in the top panel. When the outlet pressure drops from 1 to 0.4 bar, the maximum energy efficiency increases from 20.46 % to 23.84 % (see bottom panel). When the outlet pressure is 1 bar, the minimum pressure is 307 mbar. The optimal plasma position for energy-efficient CO_2 conversion is then found between 19 cm (at a pressure of 365 mbar) and 19.08 cm (at a pressure of 342 mbar). When the outlet pressure is at 0.4 bar, the minimum pressure is 77 mbar. In this case, however, the highest energy efficiency is reached when the plasma is located between 19.8 cm (at a pressure of 180 mbar) and 19.95 cm (at a pressure of 158 mbar), hence much earlier than the shock wave position, compared to the case with outlet pressure of 1 bar. The reason is that the pressure for highest energy efficiency was found at pressures between 100 and 300 mbar[29;37;101]. Closer to the shockwave, where the minimum pressure of 77 mbar is reached, the energy efficiency is only 14.8%.

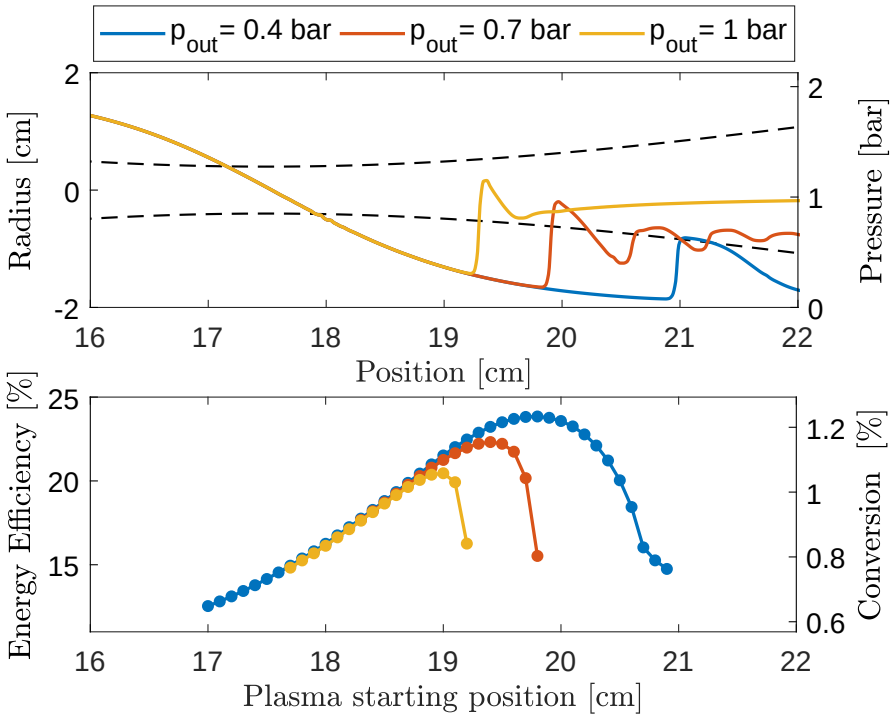

Figure 4.8: Top figure: Pressure distributions for three different values of outlet pressure (colored lines) as a function of position in the reactor (dotted lines). Bottom figure: Energy efficiency and CO_2 conversion as a function of the plasma position, for the same three different values of outlet pressure as in the top figure.

4.3.6 Effect of power on the CO_2 conversion and energy efficiency

When a high amount of heat is applied on a supersonic region, the flow needs to accelerate to higher Mach numbers, to avoid thermal choking of the flow (see figure 4.2). For that reason, it is interesting to study the effect of power on the dissociation pathways and the energy efficiency, since a lower amount of heat is then added to the flow, avoiding the initial acceleration to high Mach numbers. In this section, we will study these pathways for SEI of 0.05, 0.1, 0.15, and 0.2 eV/molec. We will not study the effect of higher SEI values, to avoid violating the maximum deceleration heat criterion (see equation 4.9). The energy efficiency and CO_2 conversion as a function of plasma starting position for the above mentioned SEI values are included in appendix B (Figure B.4). They show the same trends as presented in section 4.3.4. The values for the maximum energy efficiency are 0.06 %, 9.4 %, 20.52, and % 26.5 %, respectively. The maximum energy efficiency thus increases much faster than the SEI (or input power). It should be noted that

at higher SEI, a higher amount of heat is added to the flow, in spite of the higher energy efficiency. Indeed, $Q = (1 - \eta) \times SEI$ is 0.05, 0.0906 , 0.1192, and 0.1470 eV/molec., for the SEI values of 0.05, 0.1, 0.15, and 0.2 eV/molec., respectively. Note that if flow and plasma would be coupled together, this could have a negative impact on the VT-VV relaxation balance, which moves in favor of VT when the temperature increases, and this would decrease the relative contribution of N1 and N2 to the CO_2 dissociation, and hence lower the energy efficiency.

The plasma positions for highest energy efficiency for all four cases lie at the same position (see figure B.4). The Mach number at that position is 1.83. However, higher SEI values give higher decelerations, since they add more heat (see above). According to equation 4.9, the initial Mach numbers to end up with M = 1.83 are M = 3, M = 4.4, M = 6.1, and M = 12.8, respectively. A higher SEI thus requires a higher initial Mach number to counter the stronger deceleration.

The non-linear increase of the energy efficiency with increasing power (or SEI) is a result of the longer residence time. For SEI of 0.05, 0.1, 0.15, and 0.2 eV/molec., the residence time is 0.66 μs, 1.37 μs, 1.98 μs, and 2.7 μs, respectively. The residence time affects the relative contribution of the different dissociation processes, explained in more detail in section 4.3.2. These relative contributions are plotted in figure 4.9, for the four different SEI values. For SEI of 0.1, 0.15, and 0.2 eV/molec, the energetically efficient vibrational-induced dissociation processes (N1 and N2) contribute most to the overall dissociation. However, the relative contribution of N1 (with reaction enthalpy ΔH = 5.5 eV), is higher than the contribution of the most energetically favourable reaction N2 (with the lowest reaction enthalpy: ΔH = 0.35 eV). In an ideal case, these two reactions should have an equal relative contribution, so that the O atom created in N1 is used in N2[28]. The contribution of N2 increases from 26 % at SEI = 0.1 eV/molec. to 35 % at SEI = 0.2 eV/molec., which explains the higher energy efficiency (see above).

When the SEI is 0.05 eV/molec., the residence time is so short that there is not enough time for VV relaxation to populate the highest vibrational states. The dissociation is almost exclusively caused by electron impact dissociation, which is the least energy-efficient process (with ΔH = 7 eV), explaining the very low conversion and energy efficiency.

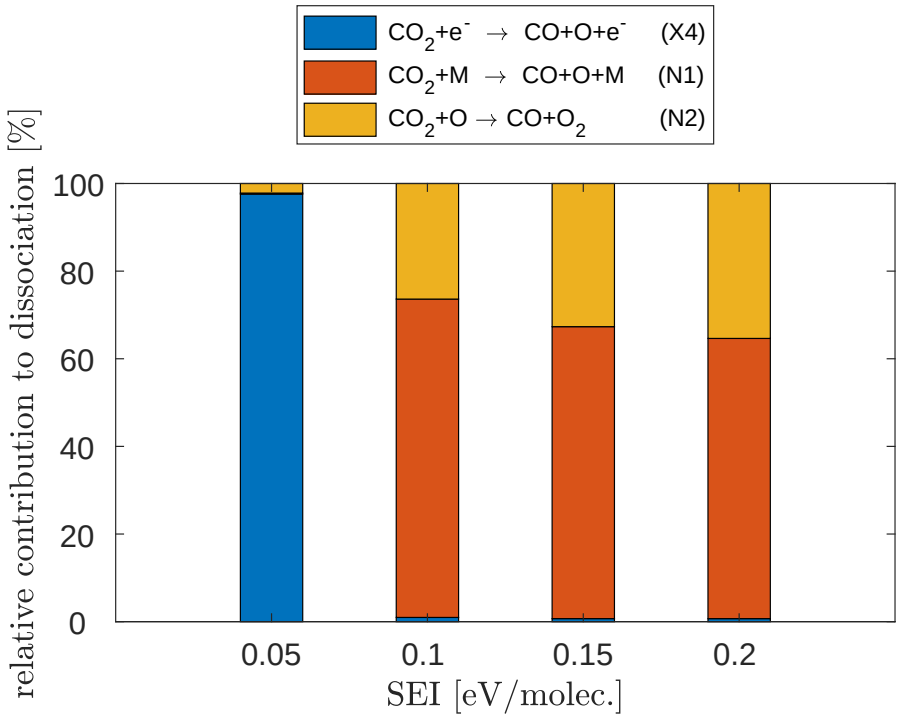

Figure 4.9: Relative contribution of the main CO_2 dissociation mechanisms at different SEI for the following conditions: $r_1 = 0.4$ cm, $r_2 = 2$ cm, $z_1 = 10$ cm, $p_{in} = 2$ bar, $p_{out} = 1$ bar.

4.3.7 Theoretical maximum energy efficiency for different inlet and outlet pressures

It is clear from section 4.3.6, that under the studied conditions, the two main limiting factors for high energy efficiency are the short residence time of the gas in the plasma region, and the maximum deceleration heat (see equation 4.9). In this section, we present the maximum calculated energy efficiency for supersonic conditions with different inlet and outlet pressures. Given that the temperature profile, used in this study, is without effect of plasma heating, and given that a higher temperature will negatively affect the energy efficiency of the system[101], the reported efficiencies should be considered as maximum values that are achieved with this model.

The maximum heat that can be added to a certain supersonic flow is according to the criterion, described in equation 4.9. This criterion is checked when applying different SEI values in the pressure drop region. The results are only taken into account if the criterion is not violated at any of the plasma starting positions. In principle, the plasma could be applied before the pressure drop, in which the

pressure drop serves as cooling for the afterglow[62], which has a beneficial effect on the energy efficiency[101]. It is also important to note that the conditions used in this section represent the flow conditions, assuming that the deceleration due to the plasma has already taken place, and not the initial conditions before applying the plasma (in accordance with equation 4.9). If these were initial conditions, the cases with a lower Mach flow number would have a lower allowed heat addition (see equation 4.8).

Figure 4.10 shows the maximum energy efficiency as a function of inlet pressure, at an outlet pressure of 1 bar. The colors of the bars represent the maximum SEI that can be applied at any position in the pressure drop, without violating the above mentioned criterion of maximum deceleration heat. At lower inlet pressures, the acceleration of the flow is limited (see appendix B). This means that a higher SEI can be applied to the system (see equation 4.9) to decelerate it from high initial Mach numbers. At higher inlet pressure, when the pressure difference between the inlet and the outlet increases, the acceleration of the flow becomes stronger, limiting the maximum SEI that can be applied to the flow. At an inlet pressure of 1.2 bar, the maximum energy efficiency is 27.4 %. As the inlet pressure increases, the maximum energy efficiency rises, until values of about 28 % are reached at inlet pressures of 1.7-2.4 bar. Note that this study is performed with stepwise increments of the SEI. Because higher energy efficiencies might exist at intermediate values of the SEI, error bars have been added, based on the value of the energy efficiency obtained at the applied SEI where the criterion of equation 4.9 is first broken. Since these higher SEI values lead to higher energy efficiencies, the error bars only point upwards. When the inlet pressure is further increased to 3.1 bar, the maximum energy efficiency decreases to 27.3 %, as explained below.

The initial rise of the maximum energy efficiency, when increasing the inlet pressure, can be explained by the fact that the higher Mach number in the pressure drop results in intermediate pressures that are favourable for CO_2 dissociation in MW plasmas[37;101]. The subsequent drop of the maximum energy efficiency upon further increasing the inlet pressure results from the limited SEI that can be applied in order to comply with the criterion of equation 4.9, which reduces the residence time and decreases the contribution of the most energetically favourable dissociation reactions (see section 4.3.2 and 4.3.6).

Figure 4.11 shows the maximum energy efficiency at different outlet pressures, while keeping the inlet pressure at 2 bar. At lower outlet pressures, the supersonic acceleration increases. This limits the maximum SEI that can be applied to the system (see equation 4.9), and subsequently shortens the residence time and the contribution of vibrational-induced dissociation (see section 4.3.2 and 4.3.6). The maximum energy efficiency also decreases with decreasing outlet pressure, since

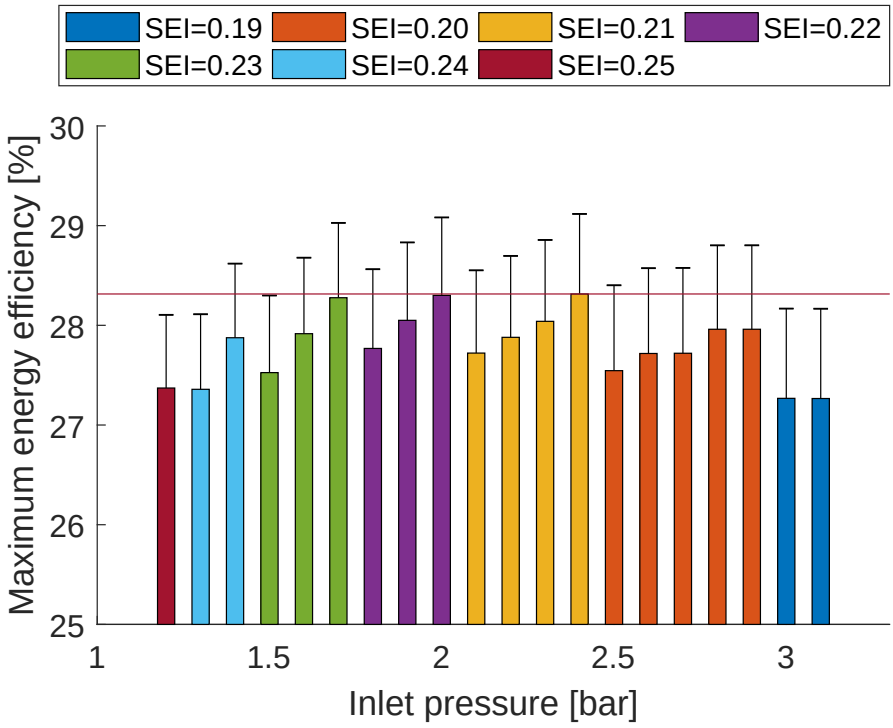

Figure 4.10: Maximum energy efficiencies as a function of inlet pressure, at an outlet pressure of 1 bar. The color legend gives the maximum SEI that can be applied for each case, assuming a deceleration from high Mach number flows. Error bars have been added to take into account the stepwise increase of the SEI, because higher energy efficiencies might exist at intermediate values of the SEI (see text).

the pressure in the pressure drop region was already at optimal conditions for the case of 2 bar inlet pressure (see figure 4.10).

From figures 4.10 and 4.11, it is clear that the maximum energy efficiency does not increase above 30 %. However, as mentioned above, the initial Mach number should be very high in order to apply these types of SEI. In literature, energy efficiencies for MW plasmas at supersonic flow conditions have been reported, in excess of 90%[36;37]. This is clearly much higher than predicted by our models. A number of reasons could explain this mismatch:

(i) The efficiency of vibrational-induced dissociation depends on the time scales of electron impact vibrational excitation, and subsequent VV or VT relaxation (see section 3.5). The cross section and reaction rate coefficients that describe these reactions are all characterized by an uncertainty. If electron impact vibrational excitation and VV relaxation would occur faster, or VT relaxation would occur slower, than they currently do in the model, higher efficiencies can

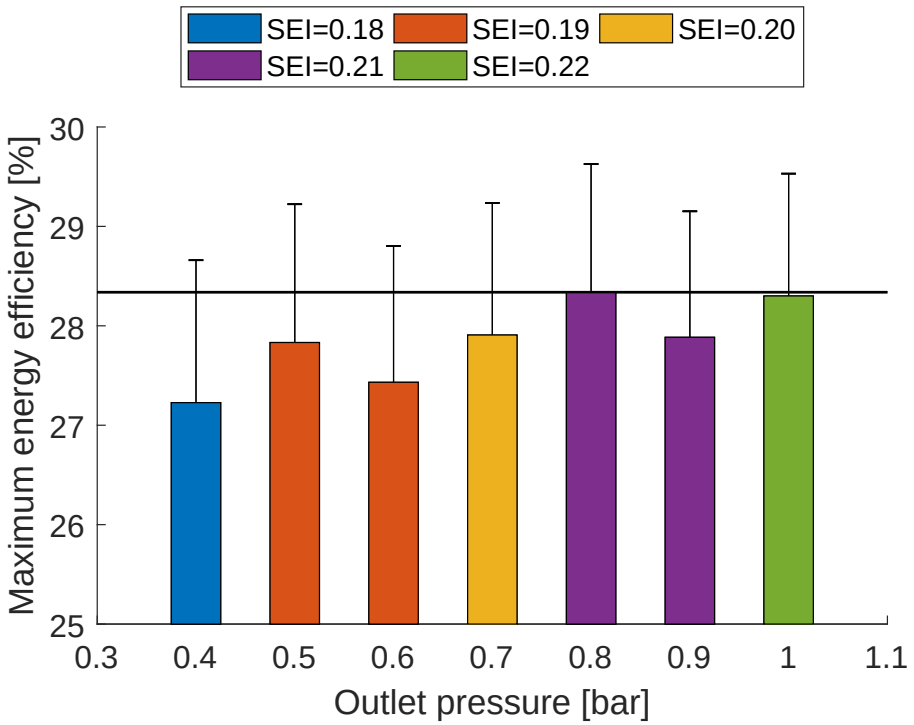

Figure 4.11: Maximum energy efficiency as a function of outlet pressure, at an inlet pressure of 2 bar. The color legend gives the maximum SEI that can be applied for each case, assuming a deceleration from high Mach number flows. Error bars have been added to take into account the stepwise increase of the SEI, because higher energy efficiencies might exist at intermediate values of the SEI (see text).

be obtained with this process.

(ii) As stated in section 4.2.4, nozzle profiling could increase the maximum critical heat that can be added to the system without thermal choking. When this effect is taken into account, it is possible to increase the amount of heat that can be added to the flow, and thus the SEI, probably resulting in a higher energy efficiency as well.

However, even when the energy efficiency would be underestimated in our model, the trends presented, and thus the message, will still be valid.

4.4 Conclusions

In this chapter, we used a combination of 2D fluid dynamics simulations of the gas flow and 0D chemical kinetics modelling of the plasma chemistry, to under-

stand the performance of a supersonic flow microwave plasma reactor for CO_2 conversion.

Adding heat to a supersonic flow slows it down until it chokes. In this study, the plasma that was ignited meets a criterion of maximum deceleration heat, for which the supersonic flow could in theory slow down from high Mach numbers to the Mach number at which the plasma is applied. This criterion limits the SEI to values below 0.24 eV/molec.

We studied the evolution of the different reaction mechanisms through the plasma and afterglow. At the start of the plasma, electron impact vibrational excitation is the main dissociation mechanism. The model predicts that there is a spatial delay for vibrational-induced dissociation to start, due to the high velocity of the gas, combined with the time it takes for the higher vibrational levels to get sufficiently populated. Due to the limited SEI, the residence time of the gas inside the plasma region is short. As a consequence, the vibrational-induced dissociation pathway does not have enough time to operate, hence limiting the energy efficiency of the conversion process. Vibrational induced dissociation still occurs in the immediate afterglow region, due to the continued overpopulation of the higher vibrational levels, but the rate is much lower than in the plasma. The higher vibrational levels are subsequently quenched by the shockwave, which leads to a rise in pressure and temperature, after which recombination becomes more important than CO_2 dissociation.

We studied how the energy efficiency and CO_2 conversion change when moving the applied power profile (from the waveguide) through the supersonic reactor. The energy efficiency increases when the power profile moves into the pressure drop of the supersonic region. However, the most energy-efficient power position does not lie closest to the shockwave, given the continued effect of vibrational-induced dissociation in the early afterglow.

One of the main parameters to tune the energy efficiency is the outlet pressure. By changing the outlet pressure, the temperature and pressure in the supersonic region can be modified. We illustrated that for an inlet pressure of 2 bar, the maximum energy efficiency and CO_2 conversion increase with decreasing outlet pressure. This can be explained by the more optimal pressure regime for efficient CO_2 dissociation[29;37;101], that was reached in the supersonic region at lower outlet pressures. However, the most favourable position moves further away from the position of minimum pressure.

The energy efficiency and CO_2 conversion increase upon higher input power. Indeed, the longer plasma residence time enhances the relative contribution from the most energetically favourable dissociation pathway (N1+N2), since the higher vibrational levels have more time to become populated.

Finally, we examined the maximum energy efficiency for different inlet and

outlet pressures. For an outlet pressure of 1 bar, a sufficiently high inlet pressure should be applied to create favourable pressure conditions in the supersonic region. However, a too high inlet pressure will increase the Mach number, limiting the SEI that can be applied, when decelerating from high initial Mach numbers. A lower SEI results in a shorter residence time, a shorter time for VV relaxation to take place, and hence a lower energy efficiency. This last phenomenon was also seen when reducing the outlet pressure, which increases the Mach number, allowing for a lower maximum SEI when coming from high initial Mach numbers, and hence a lower energy efficiency. The model predicts a maximum energy efficiency of 28.3 % at an inlet pressure of 2.4 bar, an outlet pressure of 1 bar, and a SEI of 0.21 eV/molec.

In conclusion, the model provides insight into the underlying mechanisms, as well as the limitations for the energy efficiency of supersonic MW plasmas used for CO_2 conversion. Under the studied conditions, these limitations include (i) the short residence time of the gas in the plasma region, limiting the time for sufficient population of the higher vibrational levels, which is important for energy-efficient CO_2 dissociation, (ii) the shockwave, resulting in a rise in pressure and temperature, which increases the rate of recombination and quenches the higher vibrational levels from which dissociation occurs, by a rise in VT relaxation and VV ladder downclimbing, and (iii) the maximum heat, and thus power or SEI, that can be added to the supersonic flow by the plasma, to avoid thermal choking, which for CO_2 lies at 0.1867 eV/molec. In literature, much higher energy efficiencies, up to 90 %, were reported[36], which could not be reproduced by our model. This might be caused by some inherent limitations of the 0D model, i.e. no radial contraction, or by the uncertainty on the vibrational excitation and relaxation rate coefficients. However, even with an underestimation of the energy efficiency, the trends presented in this work, and thus the message, will still be valid.

CHAPTER 5

Improving the energy efficiency through pulsing

The results presented in this chapter were published in [125]:

- V. Vermeiren and A. Bogaerts. Improving the Energy Efficiency of CO_2 Conversion in Nonequilibrium Plasmas through Pulsing. *J. Phys. Chem. C*, 123(29):17650–17665, 2019. DOI: 10.1021/acs.jpcc.9b02362

5.1 Introduction

As was mentioned in chapter 1, the efficiency of the ladder climbing is limited through the loss of vibrational energy in gas heating, in a process called vibrational-translational (VT) relaxation[28;37;38;101;103;104]. This VT relaxation process becomes more prominent at higher gas temperatures[28;104] causing even more gas heating (self-acceleration). For efficient vibrational-induced dissociation, it is therefore crucial that a strong non-equilibrium exists between the vibrational temperature and the gas temperature[28].

However, most MW and GA plasmas, especially at higher pressures and SEIs, are close to thermal equilibrium[29;54;64;74;101]. In this case, the vibrational distribution function (VDF) follows a Boltzmann distribution, without overpopulation of the higher vibrational levels[74;101]. At high gas temperatures ($\geq$ 2500 K) CO_2 conversion can occur through thermal dissociation, leading to a high CO_2 conversion and energy efficiency, as claimed in literature[29;39] and demonstrated in chapter 6. However, at temperatures of 1000-2000 K, the temperature is too low for thermal dissociation, and too high for efficient vibrational-induced dissociation.

Plasma power modulation through pulsing might be an interesting pathway to increase the vibrational-translational non-equilibrium. The main argument to indicate its potential lies in the characteristic timescales of the VV and VT processes. The timescale for VT relaxation is several orders of magnitude higher than for VV relaxation of the asymmetric mode of CO_2. By adjusting the plasma on-time accordingly, VT relaxation can thus be limited with respect to VV relaxation. Also, the characteristic timescale for VT relaxation decreases with increasing gas temperature, while that of VV relaxation increases (see figure 3.2). Given that the plasma is cooled between two consecutive pulses, the VT non-equilibrium can be enhanced in the next pulse, which has again a beneficial effect on the characteristic timescales of VV and VT relaxation. These timescales were discussed in more detail in section 3.5.

The effect of power modulation in CO_2 plasmas has predominantly been studied in DBDs[50;103;156;157]. While it is shown that the energy efficiency increases in the so-called 'burst mode' with respect to the usual AC mode[156], the electron temperature in a DBD is too high for efficient use of vibrational-induced dissociation[103].

Pulsed MW plasma experiments have been performed in CO_2 flows with N_2 admixtures by Silva et al.[55], at pressures of 1.33-13.33 mbar. The authors measured the vibrational temperature of the electronically excited states of the N_2 admixture through optical emission spectroscopy. They showed that this vibrational temperature was much higher than the gas temperature, leading them

to conclude that CO_2 dissociation could take place through vibrationally excited CO_2 levels. The work was continued by Britun et al.[57], who measured the conversions and energy efficiencies at different pulse repetition rates, reaching a maximum conversion of 23 % and energy efficiency of 33 %, at a pressure of 9.7 mbar, a pulse repetition rate of 0.5 kHz, a flow rate of 2.7 slm, and a duty cycle of 50%. The conversion and energy efficiency dropped upon rising pulse repetition rate, while keeping all the other conditions fixed. Furthermore, with a lower pulse repetition rate, when the energy efficiency was the highest, the vibrational temperature reached a maximum value, and dropped upon rising pulse repetition rate. However, a similar trend was also observed for the gas temperature.

Power modulation of CO_2 MW plasmas was also studied by van den Bekerom et al.[64] The energy efficiency increased with lower duty cycle and higher peak power, but the time in between the pulses was too short to allow for significant gas cooling, resulting in a close-to-thermal equilibrium, in which the vibrational-induced dissociation does not play an important role.

Although a strong effect of power modulation on the conversion and energy efficiency has been demonstrated experimentally, more insight is needed to determine its full potential. Therefore, in this chapter, we will examine the effect of different plasma on and off times on the conversion, energy efficiency, and the underlying mechanisms of CO_2 conversion. This will be done for a plasma where the gas temperature reaches a value that is high enough to diminish the vibrational-induced dissociation, but not high enough to create thermal dissociation.

5.2 Model description

5.2.1 Plasma model

In this chapter, we will describe the time evolution of a volume element moving through a plasma reactor (see sections 2.4.2 and 2.4.3). The model starts at t=0 with pure CO_2 and a Boltzmann vibrational distribution function (VDF). During the pulses, the plasma is ignited by applying a certain DC reduced electric field E/N (with E the electric field and N the gas number density) and by fixing the electron density (n_e) to a value determined by the ionization degree (d_i) $n_e = Nd_i$. During the interpulses, and in the afterglow, the electron density and reduced electric field are set to zero.

We choose a fixed pressure of 100 mbar, as it is representative for MW experiments yielding good energy efficiency[29;36;39]. During the plasma pulses, we fix the values of the ionization degree and reduced electric field to those that are typical in MW and GA plasmas, 10^{-6} and 50 Td[29;38;52]. These values show the

clearest potential of power modulation. For DBD plasmas, the ionization degree can reach values up to 10^{-4},[120] and they generally operate at reduced electric fields above 100 Td[38;43]. Therefore, later in this chapter, we will vary the ionization degree, and reduced electric field, to study their effect on the potential of pulsed power as well.

We apply a power deposition in a series of pulses, which will end when the total applied power reaches an SEI of 1 eV/molec. This SEI is chosen since the gas temperature reached in these simulations are high enough to diminish vibrational overpopulation, but not high enough to reach thermal dissociation. The latter will be discussed in more detail in chapter 6.

The gas temperature is calculated self-consistently in the model, using equation 2.14. We will take the external cooling term to be[101;104]

$$P_{ext} = \frac{8(\lambda + \lambda_{add})}{R^2}(T_g - T_w) \tag{5.1}$$

in which λ is the gas thermal conductivity, and T_w is the wall temperature taken as 300 K. We take $\lambda(T_g) = (0.071T_g - 2.33) \times 10^{-3} Wm^{-1}K^{-1}$ following[104]. More details of the procedure to obtain λ are explained in ref 104. R is the radius of the reactor, which is set to 7 mm[55;57]. We can add an additional thermal conductivity $\lambda_{add}[Wm^{-1}K^{-1}]$ to the equation, which can be changed manually to study the effect of additional cooling on the pulsing performance. Indeed, in reality, a higher thermal conductivity can be achieved in turbulent flow regimes[139], and this turbulent conductivity has been shown to exert a cooling effect on the plasma.[109].

5.2.2 Chemistry set

The chemistry set, used in this chapter, is mostly comprised of the same species and reactions as the one used in chapter 4, displayed in table 3.1, and the tables in section A.1, respectively. For this set, an update in cross section data has been performed, due to more recent cross section reviews. In addition, the rate coefficient of the dissociation reaction $CO_2 + O \leftrightarrow CO + O_2$ is changed so that the thermodynamic equilibrium conversion of the model more closely matches the theoretical thermodynamic equilibrium conversion. The updated species and reactions are displayed in table 3.2 and the tables in section A.2.

5.3 Results and discussion

In section 5.3.1, we will investigate the effect of different plasma pulse and interpulse times on the CO_2 conversion and energy efficiency, for a plasma at a

pressure of 100 mbar, a reduced electric field of 50 Td, and an ionization degree of 10^{-6}. Sections 5.3.2 and 5.3.3 will be dedicated to the time-evolution of the vibrational and gas temperature throughout the first pulse, and after the first pulse, respectively, for different values of t_{on}. In section 5.3.4, the average vibrational and gas temperature for the different cases will be compared to those of a continuous plasma. Next, the vibrational distribution function (VDF) will be tracked through the first pulse, after the first pulse, and at the end of the plasma, in section 5.3.5. In section 5.3.6, we will demonstrate the evolution of the most important dissociation and recombination mechanisms for the different plasma pulse and interpulse times, which will be linked to the results in section 5.3.1. Section 5.3.7 will discuss the effect of additional cooling on the energy efficiency dependence of the interpulse time. Finally, in section 5.3.8, we will study the effect of the pulsing potential at different ionization degrees and reduced electric fields.

5.3.1 Effect of pulsing on the energy efficiency and conversion

Figure 5.1 shows the CO_2 conversion (right y-axis) and energy efficiency (left y-axis) for different plasma pulse times (t_{on} = 1 μs, 10 μs, 40 μs, 60 μs, 100 μs) , and different interpulse times (t_{off} = 1 μs, 10 μs, 100 μs, 1 ms, 10 ms, 100 ms, 1 s) with an SEI of 1 eV/molec, at a reduced electric field of 50 Td and an ionization degree of 10^{-6}. The horizontal line corresponds to the conversion and energy efficiency of a continuous (non-pulsed) plasma at the same SEI. Note that the conversion and energy efficiency are linearly correlated, because the SEI is constant here (see equation 2.20). Therefore, in the following we will only focus on the values of energy efficiency, but the same discussion applies to the conversion.

The results show two separate trends of conversion and energy efficiency upon increasing interpulse time. At short pulse times (t_{on} = 1 and 10 μs), the energy efficiency reaches a maximum of 4.4 % and 8 %, respectively, at short interpulse times of t_{off} = 1 μs. These values are, however, lower than the energy efficiency for a continuous plasma (i.e., 8.7 %). When the interpulse time increases, the energy efficiency drops considerably. The drop is more pronounced for t_{on} = 1 μs, for which the values of the energy efficiency become negligible at interpulse times above t_{off} = 10 μs. For t_{on} = 10 μs, the energy efficiency increases again slightly at interpulse times greater than 10 ms.

For longer pulse times (t_{on} = 40, 60, and 100 μs), the energy efficiency at the shortest interpulse time (t_{off} = 1 μs) is 8.6%, 8.7% and 8.7%, respectively, hence very close to the energy efficiency of the continuous plasma. When the interpulse time increases, the energy efficiency initially decreases slightly, being

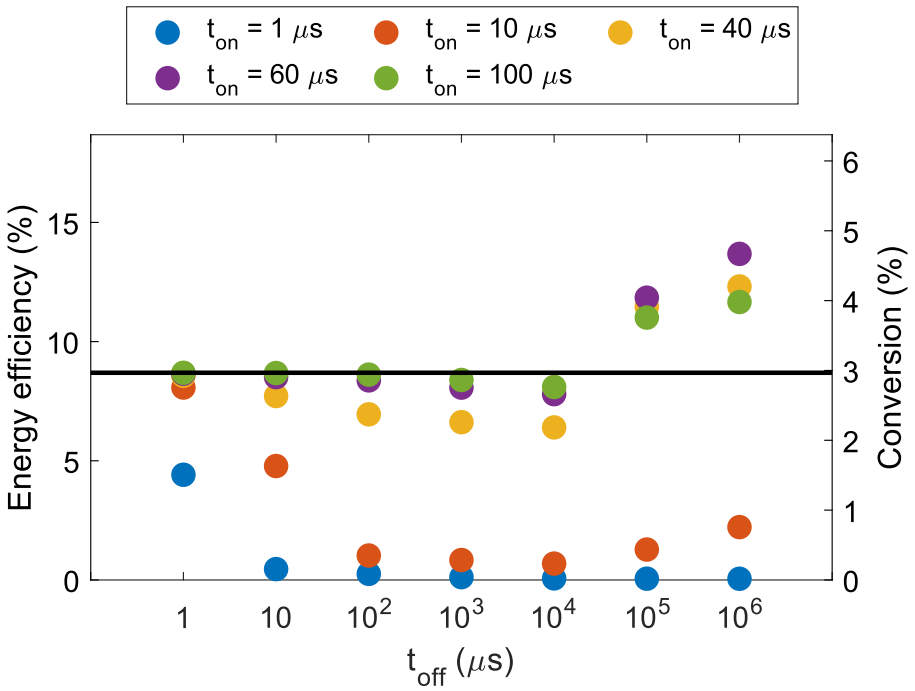

Figure 5.1: Energy efficiency and conversion as a function of interpulse time (t_{off}), for five different plasma on times (t_{on}), for an SEI of 1 eV/molec. The horizontal line represents the conversion and energy efficiency of a continuous plasma at the same SEI.

most pronounced for t_{on} = 40 μs. However, when applying an interpulse time of t_{off} = 100 ms, the energy efficiency for all three pulse times becomes larger than that of the continuous plasma. A maximum energy efficiency is reached at an interpulse time of t_{off} = 1 s, yielding values of 12.3%, 13.7%, and 11.7%, for t_{on} = 40, 60, and 100 μs, respectively. Hence, a maximum relative increase of 57% in both the conversion and energy efficiency, with respect to a continuous plasma, is observed for t_{on} = 60 μs and t_{off} = 1 s. However, we believe it is important to focus on the trends, rather than the absolute values of the efficiencies, as they can be affected by the uncertainties on the rate coefficients. In particular, the energy efficiency was shown to greatly depend on the uncertainty on the activation energy of the reaction $CO_2 + O \rightarrow CO + O_2$[28]. If the activation energy of this reaction would be lower, the energy efficiencies would be higher.

In summary, our model reveals that a short plasma pulse and interpulse time both have a negative effect on the CO_2 conversion and energy efficiency. Indeed, the plasma pulse time and interpulse time both need to be sufficiently long ($t_{on} \geq$ 40 μs, and $t_{off} \geq$ 100 ms) to ensure a higher conversion and energy efficiency than

in a continuous plasma. In the experiments conducted by Britun et al.[57], a higher energy efficiency was also found at lower pulse repetition rates. However, a quantitative comparison of the results cannot be performed, because the experiments were conducted at a lower pressure (27 mbar) and higher specific energy input (2 eV/molec.) than in our study. In the next sections, we will explain the above trends.

5.3.2 Time-evolution of the vibrational and gas temperature during the first pulse

To understand the results plotted in figure 5.1, we first take a look at the time-evolution of the vibrational and gas temperature during the first pulse, for different plasma pulse times, i.e., t_{on} = 10, 60, and 100 μs.

Given that the build-up of the vibrational and gas temperature is the same in the first pulse for all cases, we show the gas and vibrational temperature evolution through a continuous plasma in figure 5.2, but we indicate the end of the pulses for the three cases by vertical dashed lines.

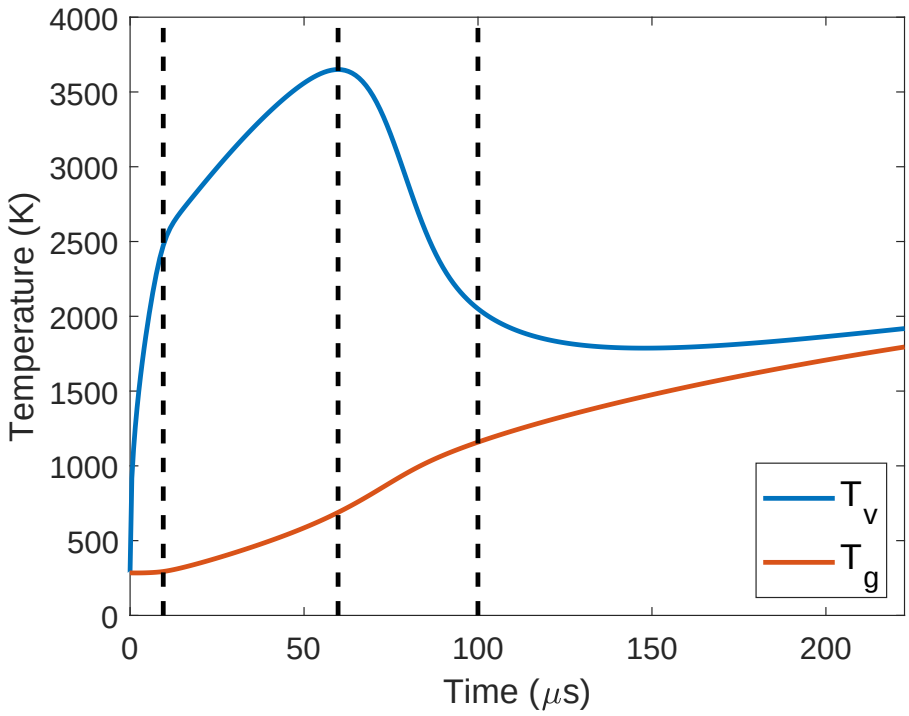

Figure 5.2: Time-evolution of vibrational temperature (blue line) and gas temperature (red line) during a continuous plasma. The vertical dashed lines indicate the end of the plasma pulses with t_{on} = 10, 60, and 100 μs.

At the start of the plasma (t=0), the vibrational temperature immediately

increases to a value of 2506 K after 10 μs, while the gas temperature does not significantly increase. This behavior is correlated with the long characteristic time scale of VT relaxation around 300 K (see figure 3.2), and the fact that the vibrational energy levels first need to be populated before they release their energy into heat by VT relaxation. Because of the low VT relaxation rate, the gas temperature does not significantly increase in this time frame.

After $10\mu s$, the gas temperature starts increasing monotonically until the end of the continuous plasma (i.e. when 1 eV/molec is reached). The vibrational temperature also continues to increase, but at a slower pace than before. It reaches a maximum value of 3650 K at t = 60 μs, with a corresponding gas temperature of 689 K. While the gas temperature keeps on increasing beyond that point, the vibrational temperature starts to drop until it reaches 2050 K at t = 100 μs, with a corresponding gas temperature of 1149 K. This can be correlated with the shorter characteristic time scale for VT relaxation with respect to electron impact vibrational excitation at this higher gas temperature (see figure 3.2). At the end of the continuous plasma (223 μs), the vibrational and gas temperature are nearly equal to each other (i.e. 1918 K vs 1795 K), indicating that there is no significant VT non-equilibrium anymore. The evolution of the vibrational and gas temperature, described by our model, follows the same trends as in the experiments by Klarenaar et al.[158]. Note that these experiments were conducted at a lower pressure (6.7 mbar), a lower ionization degree (10^{-7}), but a similar reduced electric field (60 Td). In section 5.3.8, we will demonstrate, however, that the evolution of the vibrational and gas temperature is similar at lower ionization degrees.

In summary, our model reveals that a plasma pulse time of 60 μs is ideal, at the conditions investigated, because at this time the vibrational temperature reaches its maximum. For shorter plasma pulses, the vibrational temperature does not have enough time to reach this maximum value. On the other hand, at longer pulse times, VT relaxation starts to dominate, due to the high gas temperature, causing a drop in vibrational temperature. This ideal plasma pulse time of 60 μs, to reach the highest vibrational temperature, corresponds with the plasma pulse time that provides the highest conversion and energy efficiency (figure 5.1), clearly indicating that a high vibrational temperature is required to reach the most energy-efficient CO_2 conversion.

5.3.3 Time-evolution of the vibrational and gas temperature after the first pulse

Figure 5.3 presents the vibrational and gas temperature as a function of time after the first pulse, for the three different plasma pulse times of figure 5.2 above,

i.e., t_{on} = 10, 60, and 100 μs, as well as the afterglow of the continuous plasma. The vibrational and gas temperature are shown in full and dotted blue line, with corresponding values on the left y-axis. In addition, the gas temperature is also plotted with a red full line on a smaller scale (right y-axis) to better illustrate the finer details of its time-evolution. The calculations are performed for a long interpulse time of 1 s, but to evaluate the VT non-equilibrium for different interpulse times, the latter are also indicated with vertical dashed lines in figure 5.3, with the values written in the x-axis.

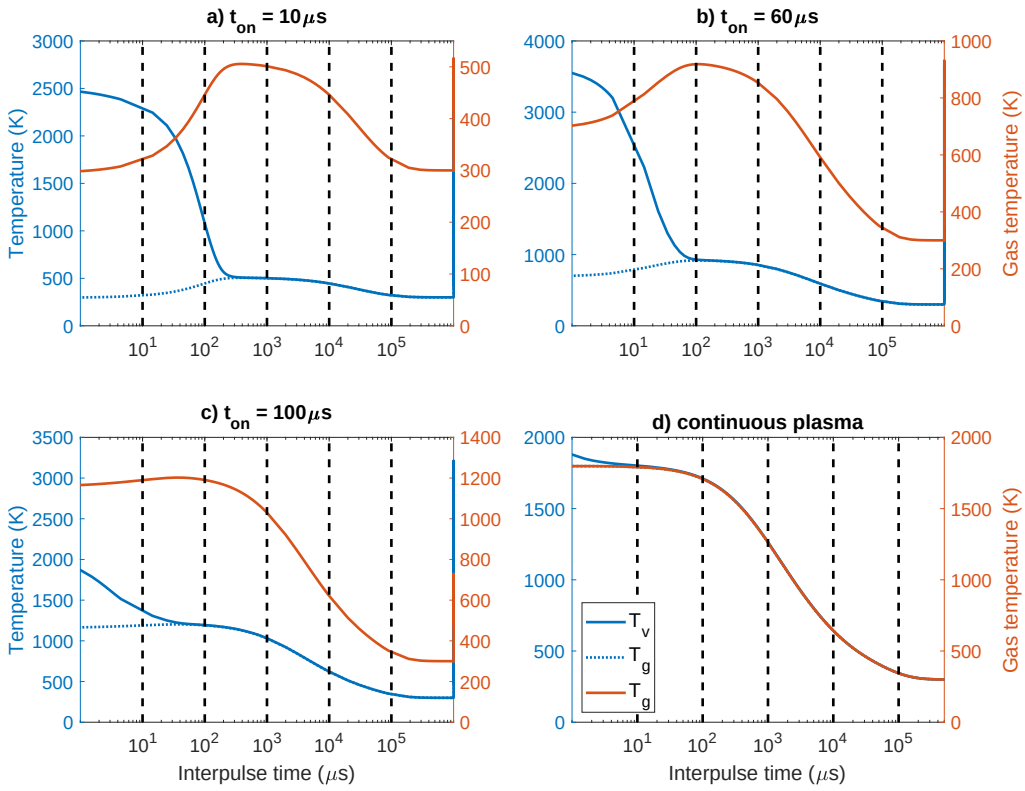

Figure 5.3: Time-evolution of the vibrational (full blue line - left y-axis) and gas temperature (full red line - right y-axis, as wel as blue dotted line - left y-axis, to directly compare to the vibrational temperature) after the first pulse, for the three different plasma pulses of figure 5.2, i.e. (a) t_{on} = 10 μs, (b) t_{on} = 60, and (c) t_{on} = 100 μs, and (d) the afterglow of a continuous plasma. To evaluate the VT non-equilibrium for different interpulse times, the latter are indicated in the figure with vertical dashed lines.

For all pulsed cases, a VT non-equilibrium exist at the end of the plasma pulse. This non-equilibrium is higher for the lower plasma pulse times (i.e. t_{on} = 10 μs and t_{on} = 60 μs). In between pulses, the vibrational temperature reduces quickly due to VT relaxation. The drop continues until the non-equilibrium

disappears. This happens after 10-100 μs and takes a longer time for cases in which the non-equilibrium was higher.

The vibrational energy is mostly lost in heating. This can be correlated by the increase in the gas temperature right after the pulse. This increase is again higher for cases with a higher vibrational temperature. This increase stops when the non-equilibrium disappears after 10-100 μs. In the case of the continuous plasma, the temperature does not increase after the plasma, because the vibrational and gas temperature are already close to equilibrium at the end of the plasma. Unlike the vibrational temperature, the gas temperature reduces much more slowly. It takes up to between 100 ms - 1 s to cool the gas down to room temperature.

In conclusion, figure 5.3 clearly illustrates that for the different plasma pulse times, and for interpulse times shorter than 100 μs, pulsing will further increase the gas temperature and reduce the vibrational temperature, which has a negative effect on the VT non-equilibrium, and hence on the vibrational-induced dissociation. At interpulse times shorter than 100 ms, the gas is still above room temperature when the next pulse would start, which should also be avoided to reach strong VT non-equilibrium in the next pulse. Only when the interpulse time is 100 ms or 1 s, the gas is cooled down sufficiently and the vibrational and gas temperature are both at room temperature. At these interpulse times, higher conversions and energy efficiencies are indeed found with respect to a continuous plasma (cf. figure 5.1 above).

5.3.4 Average vibrational and gas temperature during the pulses

In the previous section, we saw that between the pulses, the vibrational temperature reduced, while the gas temperature increased at small interpulse times, and decreased at longer interpulse times. These gains and losses are higher for shorter plasma pulses, since a higher amount of pulses are needed to reach the same SEI. For more details, see figure C.1 in the appendix, where the total vibrational and gas temperature gains and losses between the pulses are shown for different cases.

The vibrational temperature loss between the pulses needs to be compensated in subsequent pulses, which can affect the average vibrational temperature in the plasma. Figure 5.4 illustrates the average vibrational (blue) and gas temperature (red) during the plasma (i.e., averaged over all plasma pulse times), for different plasma pulse and interpulse times, as well as the corresponding values in the continuous plasma, depicted by the horizontal lines with similar colors. In order to compare these values of the average vibrational temperature to the energy efficiency, we include figure 5.5, which shows the energy efficiency (also depicted in figure 5.1) as a function of the average vibrational temperature, for all modelled cases.

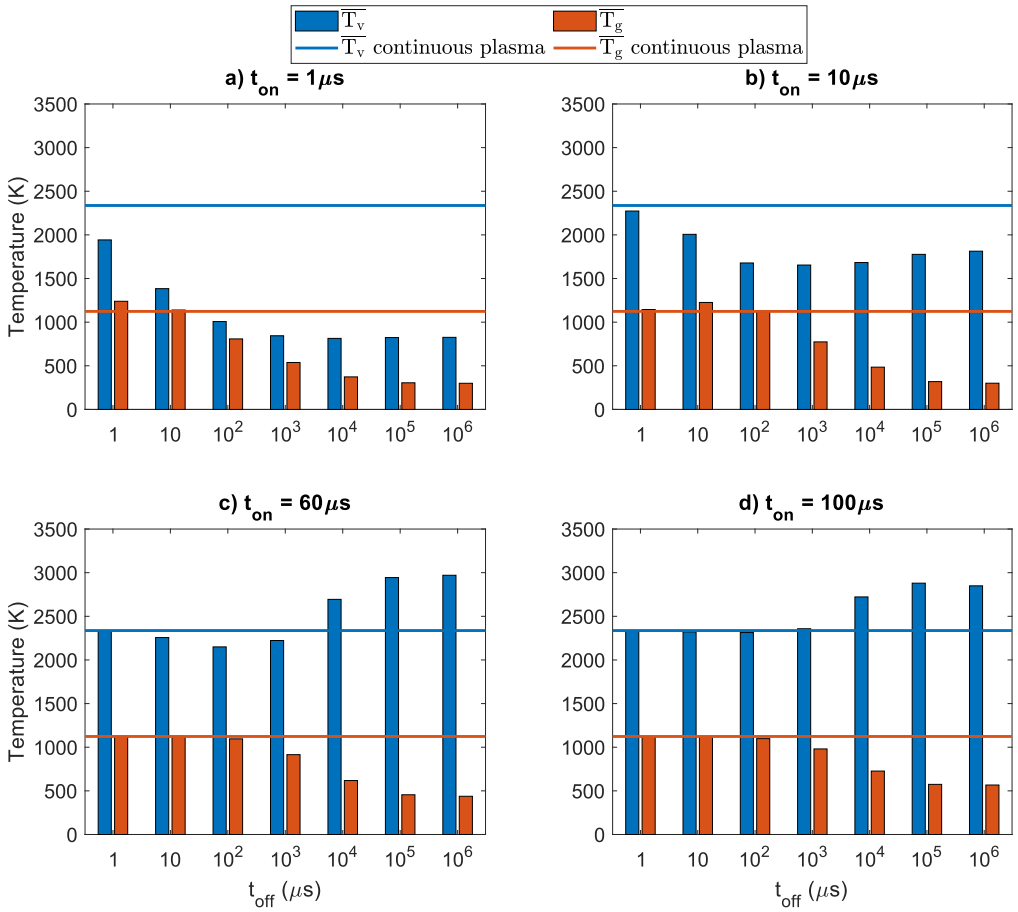

Figure 5.4: Average vibrational temperature (blue) and gas temperature (red), during the pulses, for different plasma pulse and interpulse times. The horizontal lines correspond to the values for the continuous plasma.

For short plasma pulse times, i.e. $t_{on} \leq 10$ μs, the vibrational and gas temperature are closest to the values of the continuous plasma (i.e. 2337 K and 1123 K, respectively) at short interpulse times. This is consistent to figure 5.3, where the vibrational temperature moderately decreased for short interpulses, while the gas temperature could slightly increase. Note that the rise in gas temperature after the first pulse does not lead to a higher average gas temperature, with respect to the continuous case. As the vibrational temperature is reduced, the rise in average gas temperature due to VT relaxation will be lower at the start of the next pulse. Also, later in the plasma, the gas temperature could be much higher, resulting in a stronger cooling between the pulses (see equation 5.1). At interpulse times above 0.1 s, we see that the average gas temperature reduces to 300 K, which is most beneficial for efficient vibrational-induced dissociation [28;101].

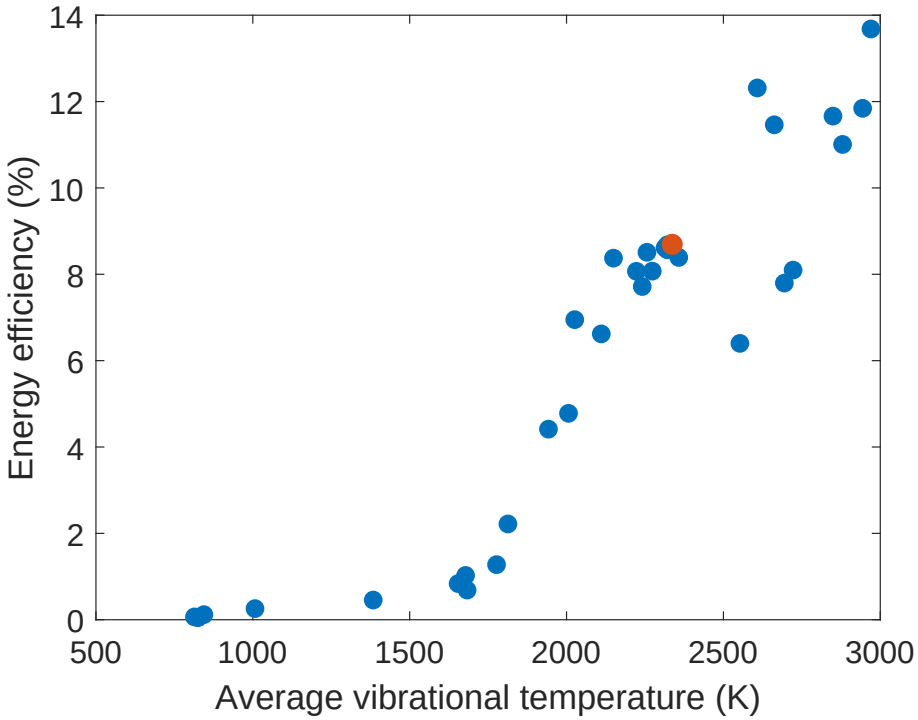

Figure 5.5: Energy efficiency as a function of the average vibrational temperature for different plasma pulse and interpulse times (blue), and for the continuous plasma (red).

However, the average vibrational temperature also reduces to 826 K for t_{on} = 1 μs and to 1813 K for t_{on} = 10 μs. While the low gas temperature allows for efficient vibrational excitation, the plasma pulse time is too short to reach higher values than those of the continuous plasma. For t_{on} = 10 μs, the vibrational temperature does start to increase again at t_{off} > 10 ms, explaining the small increase which is also noticed in figure 5.1.

For longer plasma pulse times (t_{on} = 60 and 100 μs), the vibrational and gas temperature are again close to the values of the continuous plasma at short interpulse times. Again, the interpulse time is too short to allow for significant vibrational and translational changes. At $t_{off} \geq 1$ ms, the average gas temperature starts to drop until it reaches an average value of 438 K and 567 K at and interpulse time of 1 s, for t_{on} = 60 and 100 μs, respectively. This temperature drop results in an increase of the average vibrational temperature. For $t_{on} \geq$ 10 ms, the average gas temperature is sufficiently reduced, which allows for the average value of the vibrational temperature to exceed the value of the continuous plasma to reach 2970 K and 2849 K at and interpulse time of 1 s for t_{on} = 60 and 100 μs, respectively. However, while the value of the vibrational temperature

exceeds the value of the continuous plasma for $t_{on} \geq 10$ ms, the energy efficiency only exceeds the one from the continuous plasma for $t_{on} \geq 100$ ms (see figure 5.1). In order to explain this, we take a look at the VDF in the next sections.

5.3.5 Effect of pulsing on the vibrational distribution function (VDF)

The vibrational temperature is a strong indicator for efficient vibrational-induced dissociation. However, it is only a measure of the population of the first vibrational level (see equation 2.21). As dissociation takes place from the higher vibrational levels of CO_2 [101], it is therefore also useful to study the vibrational distribution function (VDF) of the asymmetric stretch mode, which is the most important for CO_2 dissociation [101;103]. In the next sections, we will show the calculated VDFs at the end of the first pulse (for different plasma pulse times), after the first pulse (for a fixed plasma pulse time and different interpulse times), and at the end of the plasma. In each case, we will also plot the corresponding Boltzmann distribution functions at the vibrational temperature reached at these conditions, to evaluate the degree of vibrational overpopulation of the higher levels.

5.3.5.a VDF at the end of the first pulse

Similarly as what was mentioned in section 5.3.2 for the vibrational and gas temperature, the buildup of the VDFs during the first pulse is similar, for different plasma pulse times. The VDFs at the end of the first pulse, for different plasma pulse times (i.e. t = 1, 10, 60, and 100 μs) are displayed in figure 5.6. We also added t = 80 μs, which is relevant for later discussion. The Boltzmann distributions corresponding to the vibrational temperatures, at the different pulse times, are also shown in dotted lines, to evaluate the overpopulation of the higher vibrational levels with respect to this equilibrium distribution.

At a short plasma pulse time of 1 μs, the VDF starts getting populated. While the overpopulation with respect to the equilibrium Boltzmann distribution at T_v due to the short characteristic time scale of VV relaxation at temperatures around 300 K (0.04 μs; see figure 3.2), the time is still too short to reach a significant population of the higher levels. This population is much more significant at a plasma pulse time of 10 μs, at which a vibrational temperature of 2473 K is reached (see also figure 5.2). For a plasma pulse time of 60 μs, the vibrational temperature is 3650 K. The population of the higher vibrational levels is still strong, but this is most apparent for the intermediate levels, while the highest levels (V17-V21) are somewhat depleted with respect to t = 10 μs, due to the somewhat higher gas temperature (689 K), causing more VT relaxation.

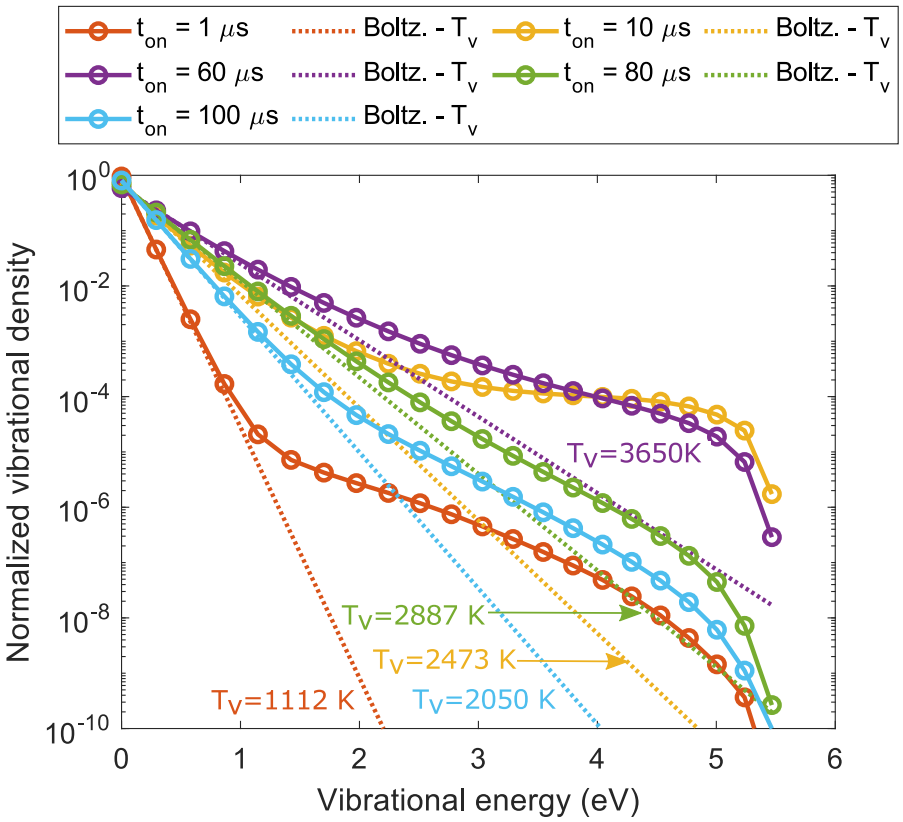

Figure 5.6: VDFs at the end of the first pulse, for four different plasma pulse times. The corresponding Boltzmann distribution functions at the vibrational temperature reached in these cases (cf. figure 5.2) are also plotted in the same color (with these vibrational temperatures indicated), to illustrate the degree of overpopulation of the higher vibrational levels with respect to this equilibrium distribution.

At a time of 80 μs, the gas temperature has increased to 956 K, and VT relaxation becomes more important (cf. shorter characteristic time scale; see figure 3.2). It can be seen that at t = 80 μs, the vibrational temperature reduces to 2887 K. While this vibrational temperature is higher than in the case of t = 10 μs (i.e. 2473 K), the overpopulation of the higher vibrational levels with respect to the Boltzmann distribution is considerably lower, which has a negative effect on the vibrational-induced dissociation.

For a plasma pulse time of 100 μs, the gas temperature has increased to 1149 K. While the vibrational temperature reduces to 2050 K, the higher vibrational levels get more depleted, with respect to 80 μs. However, this depletion is not as pronounced as compared to the depletion going from 60 μs to 80 μs.

5.3.5.b Relaxation of the VDF between two pulses

In figure 5.7, we show the VDF at the end of the first pulse (black curve), for a plasma pulse time t_{on} = 60 μs, and before the start of a new pulse, for four different interpulse times, i.e., t_{off} = 1 μs, 10 μs, 1 ms, and 1 s. The Boltzmann plots at the corresponding vibrational temperatures are also indicated, to evaluate the degree of overpopulation of the higher levels with respect to this equilibrium distribution.

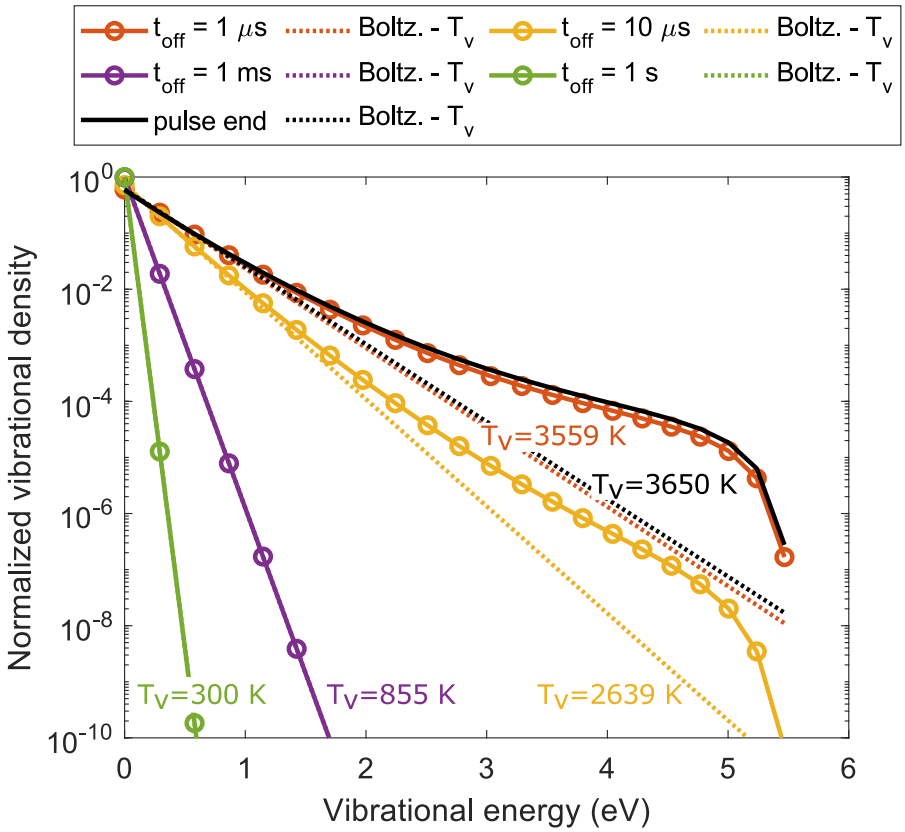

Figure 5.7: VDFs at the end of the first pulse, and before the start of the second pulse, for a plasma pulse time t_{on}= 60 μs, and for four different interpulse times. The corresponding equilibrium Boltzmann distribution at the vibrational temperature reached in these cases (cf. figure 5.3 b) are also plotted in the same color (with these vibrational temperatures indicated), to illustrate the degree of overpopulation of the higher vibrational levels with respect to this equilibrium distribution.

Figure 5.3 illustrated that the vibrational temperature quickly drops after the plasma pulse, and that a quasi-equilibrium with the gas temperature was reached at around t = 1 ms. This is also observed in the VDFs; see figure 5.7. At the end

of the plasma pulse with t_{on} = 60 μs, the higher levels of the VDF are strongly populated (cf. also figure 5.6). After 1 μs , the VDF still looks very similar to the one at the end of the pulse, and only a small relaxation is noticed. After 10 μs, the higher vibrational levels are clearly less populated. While the overpopulation with respect to the Boltzmann distribution is still significant, a faster relaxation is observed for the higher vibrational levels. Similarly as in figure 5.3, the VDF relaxes to its Boltzmann distribution after 1 ms. For longer interpulse times, the population of the VDF still decreases, since the vibrational and gas temperature, and corresponding Boltzmann distribution decrease.

5.3.5.c VDF at the end of the plasma

Previous sections only showed the VDF and the vibrational and gas temperature during and after the first pulse, but many consecutive pulses can occur. Therefore, we plot in figure 5.8 the VDFs at the end of the plasma (i.e. at the end of the last full pulse in case of more than two pulses, or when the predefined SEI of 1 eV/molec. is reached), for two different plasma pulse times (i.e., 1 and 60 μs) and in each case for four different interpulse times. For comparison, the VDF in case of a continuous plasma (when the SEI of 1eV/molec. is reached) is also illustrated. In addition, in each case, the corresponding Boltzmann distributions are also plotted at the indicated vibrational temperatures, to evaluate the degree of overpopulation of the higher vibrational levels with respect to this equilibrium distribution. In figure C.3 and C.4 of the SI, we also show the VDFs at half of the plasma (i.e., when an SEI of 0.5 eV/molec is reached), for t_{on}= 1 μs and 10 μs, and the VDFs at the end of the plasma, for t_{on}= 10 μs and 100 μs, for different interpulse times.

For both plasma pulse times, the VDFs at an interpulse time of 1 μs are virtually the same as the VDF in case of a continuous plasma, with a similar vibrational temperature. Indeed, the interpulse time is insufficient to cause significant relaxation of the VDF (see figure 5.7). With increasing interpulse time, the evolution of the VDF is different for the two plasma pulse times.

For a plasma pulse time of 1 μs and an interpulse time of 1 ms and above, the VDFs become underpopulated with respect to the continuous plasma. Indeed, the interpulse time is sufficiently long to cause relaxation of the VDF (see figure 5.7). However, the plasma pulse time is too short to get significant population of the higher vibrational levels (see figure 5.6). In figure 5.8, the difference is not large, given that the VDF of the continuous plasma is mostly thermalized as a result of the high gas temperature (1795 K). The underpopulation of the VDF is much more clear in figure C.3 of the SI, where the VDFs at half of the plasma are shown.

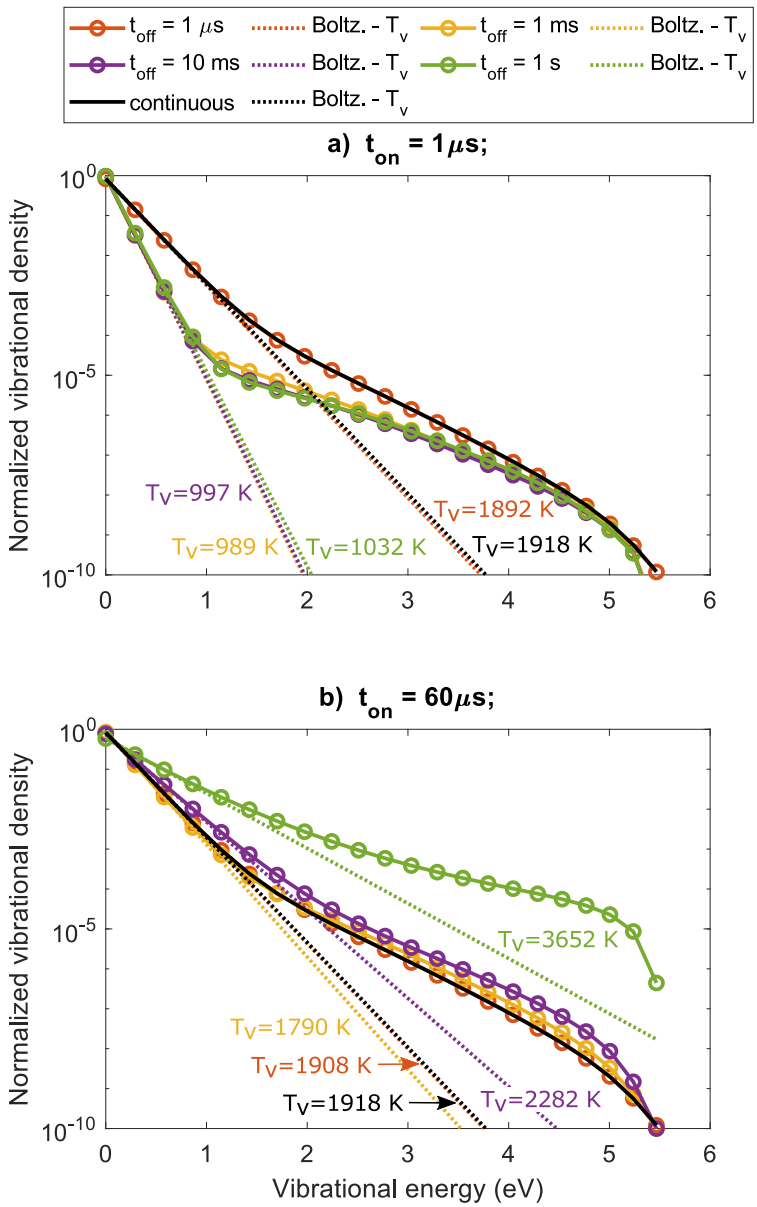

Figure 5.8: VDFs at the end of the plasma, for two different plasma pulse times, i.e., $t_{on} = 1$ μs (a, top panel), and $t_{on} = 60$ μs (b, bottom panels), and for different interpulse times (see legend), at a fixed SEI of 1 eV/molec. The VDF calculated for a continuous plasma (at the same SEI) is illustrated for comparison (black curves). The corresponding Boltzmann distribution functions at the indicated vibrational temperature (reached in each case at the end of the plasma) are also plotted in the same color, to illustrate the degree of overpopulation of the higher vibrational levels with respect to this equilibrium distribution.

For a plasma pulse time of 60 μs, the VDF starts getting more populated at higher interpulse times. At an interpulse time of 1 ms, a slight overpopulation of the higher vibrational levels is observed, compared to the VDF of the continuous plasma, despite the slightly lower vibrational temperature (1790 K). This can be correlated with the lower gas temperature (1404 K), allowing for a faster VV relaxation and a slower VT relaxation (see figure 3.2). For an interpulse time of 10 ms, the gas temperature is even lower (1043 K). However, it can be seen that while the vibrational temperature (2281 K) is higher than the continuous case , the population of the higher vibrational levels did not significantly increase. Indeed, while the first vibrational level gets excited, the gas temperature is still too high to allow for a fast overpopulation of the higher vibrational levels (cfr. lower characteristic time scale for VT at higher gas temperature, see figure 3.2), that were depleted during the interpulse (see figures 5.3 and 5.7). This results in a lower overpopulation of the VDF with respect to the equilibrium Boltzmann distribution at T_v (see figure 5.8 b). Note that a lower population of the higher vibrational levels, despite a similar vibrational temperature, was also noticed in figure 5.6 for t = 10 and 80 μs. In the latter case, the gas temperature reached 956 K, which is comparable to the gas temperature mentioned above (1043 K). The slightly higher overpopulation of the VDF for t_{on} = 60 μs and t_{off} = 10 ms, compared to the continuous plasma, is not enough to compensate for the vibrational energy loss between the pulses (see section C.2 in the appendix) and does not lead to higher energy efficiency.

When the interpulse time increases to t_{off} = 1 s, the gas temperature drops back to 300 K (see figure 5.3). This results in a larger characteristic time scale, and thus lower rate, for VT relaxation, and a faster VV relaxation. For a plasma pulse time of 60 μs, this results in a large overpopulation, with respect to the continuous plasma, that is again similar to the one in the first plasma pulse (see figure 5.6). Because at these conditions, higher energy efficiencies are found, it seems that the higher vibrational overpopulation is enough to compensate for the vibrational energy losses between the pulses (see section C.2 in the appendix).

In figure C.4 of the appendix, we show the VDFs at the end of the plasma, for plasma pulse time of 10 μs and 100 μs, for different interpulse times. As these plasma pulse times are long enough to reach significant overpopulation (see figure 5.6), the evolution of the VDFs with increasing interpulse time is similar to the evolution at a plasma pulse time of 60 μs. While the VDFs show a large overpopulation of the higher vibrational levels compared to the VDF of the continuous plasma, for both t_{on} = 10 μs, and t_{on} = 60 μs, at an interpulse time of 1 s, this only leads to a higher energy efficiency for the plasma pulse time of 60 μs (see figure 5.1). Indeed, due to the shorter plasma pulse time at t_{on} = 10 μs, the number of pulses is higher to reach the same SEI of 1 eV/molec, which

will increase the total amount of vibrational energy that is lost (see figure C.1 in the appendix). Because more vibrational energy is lost, there is less vibrational energy available for vibrational-induced dissociation. In the next section, we will discuss in more detail the dissociation mechanisms.

5.3.6 Effect of pulsing on the dissociation and recombination mechanisms

Now that we understand the effect of pulsing on the vibrational and gas temperature and on the shape of the VDF, we can investigate the effect of the different plasma pulse and interpulse times on the CO_2 dissociation and recombination mechanisms. In figure 5.9, we plot the percentage of CO_2 that is converted by electron impact dissociation (red), dissociation upon collision with a molecule M (blue), and upon collision with an O atom (yellow), as a function of interpulse time, for four different plasma pulse times. The most important recombination mechanism, i.e. recombination of CO and O (purple), is plotted as negative CO_2 conversion. The horizontal lines correspond to the conversion by these five mechanisms in a continuous plasma at the same SEI.

For t_{on}= 1 μs (figure 5.9 a), all three dissociation mechanisms have the highest CO_2 conversion at t_{off} = 1 μs. At this short interpulse time, the VDF does not relax significantly between two pulses (see figure 5.7), so there is still enough vibrational build-up through the plasma (see figure 5.8 a and figure C.3 in the appendix). This results in the largest contribution to dissociation from collisions of CO_2 with either a molecule M, or an atom O. Given the high activation energy barriers of these reactions[28], and the relatively low gas temperatures calculated in this work, the energy to overcome this barrier comes from the higher vibrational levels. This is also shown in figure C.5 of the appendix, where the contribution of the vibrational levels to the overall dissociation is shown.

When the interpulse time increases, the overpopulation of the higher vibrational levels is considerably lower (see figure 5.8 a and figure C.4 in the appendix), so vibrational-induced dissociation, upon collision with a molecule M or an atom O, becomes insignificant. Therefore, electron impact dissociation becomes the most important dissociation process, although its absolute value is also quite low and drops upon increasing interpulse time. This is because at the conditions under study (i.e. E/N = 50 Td), most of the electron energy goes into vibrational excitation of CO_2[28;102], and only a smaller portion goes into direct electron impact dissociation. For longer interpulse times, the VDF relaxes between two pulses (see figure 5.7), so more of the electron energy is needed at the start of the next pulse to repopulate the VDF, resulting in a lower contribution of electron impact dissociation to the conversion.

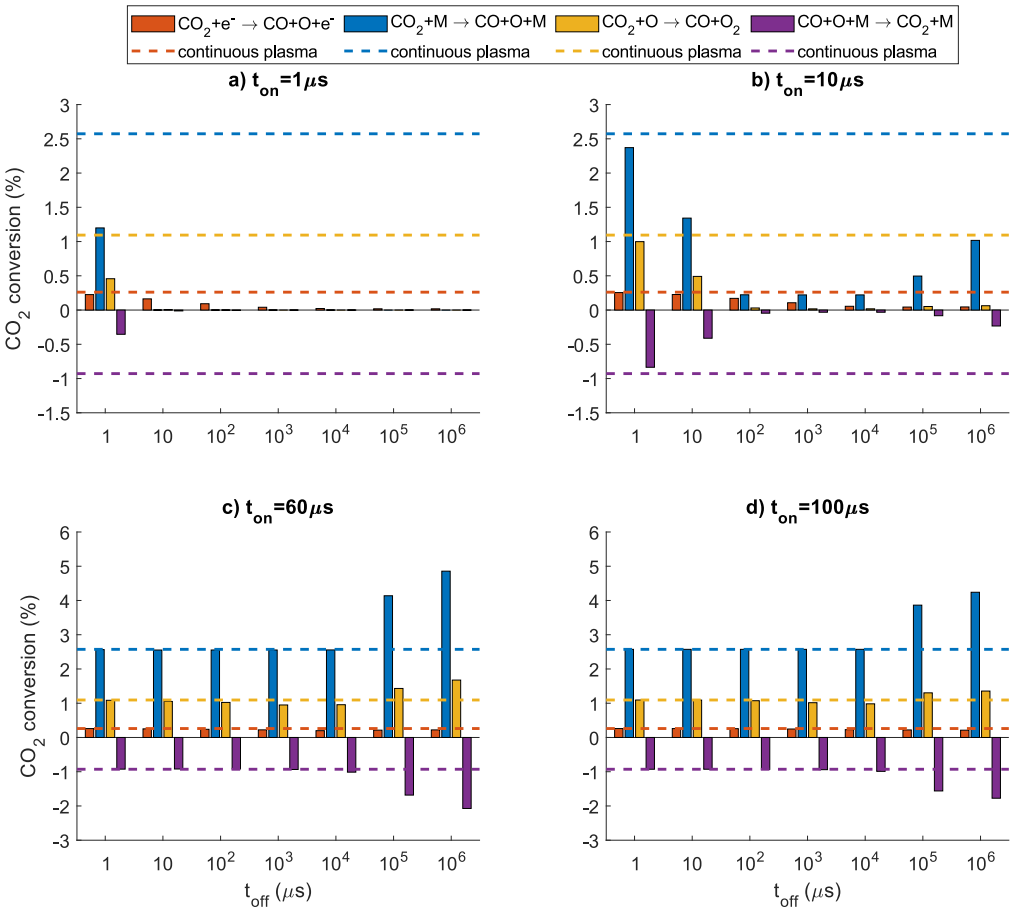

Figure 5.9: Percentage of converted CO_2 by the three main dissociation reactions: electron impact dissociation (red), dissociation upon collision with a molecule M (blue) and dissociation upon collision with an O atom (yellow). The major recombination reaction, forming CO_2 is also plotted (purple, negative value). The dashed lines represent the respective conversions and recombination for a continuous plasma at the same SEI of 1 eV/molec.

Because the dissociation mechanisms have a lower contribution than those of the continuous case for all interpulse times at t_{on}= 1 μs, the recombination reactions are also lower than in the continuous case for all interpulse times. The highest contribution from this reaction happens at short interpulse times, where the overall dissociation is highest.

For t_{on} =10 μs (figure 5.9 b), vibrational-induced dissociation (upon collision with either another molecule M or an O atom) is dominant for all interpulse times. Just like for t_{on} = 1 μs, the conversion reaches its maximum for short interpulse times (i.e. t_{off} = 1 μs), because the VDF is not drastically depleted

between the pulses at these short interpulse times. The conversion is higher than for $t_{on} = 1$ μs, since there are less pulses in total (for the same fixed SEI), and thus less overall vibrational energy loss (see figure C.1 of the appendix). When the interpulse time increases, all three dissociation mechanisms first yield less conversion, but above $t_{off} = 10$ ms, they again become more important. This is consistent with the increase in energy efficiency, observed in figure 5.1, and can be explained by the lower gas temperature, which allows for a higher population of the VDF near the end of the plasma, compared to a continuous plasma (see figure C.4 in the appendix). The contribution of electron impact dissociation is again quite small and drops upon longer interpulse times, like with $t_{on} = 1$ μs, for the same reason.

The recombination is high at short interpulse times, similarly to figure 5.9 (a). The recombination is slightly lower than in the continuous case, which can be correlated to the lower conversion.

It is clear from figure 5.9 (a,b) that these very short plasma pulse times yield a significantly lower conversion by all three processes than the continuous plasma, for all interpulse times, except for the shortest interpulse times, where the role of electron impact dissociation is comparable to that for a continuous plasma. This picture corresponds to figure 5.1, where the overall conversion and energy efficiency were lower than for the continuous plasma.

For $t_{on} = 60$ μs and $t_{on} = 100$ μs, the conversion by all three processes is comparable to the continuous plasma for $t_{off} \leq 10$ ms. When $t_{off} \geq 100$ ms, the conversion by vibrational-induced dissociation, upon collision with a molecule M or an atom O, becomes higher than that for the continuous plasma. This is correlated with the lower number of pulses, and hence lower total vibrational temperature loss (see figure C.1 in the appendix), at these plasma pulse times, combined with a significant overpopulation of the higher vibrational levels, with respect to the continuous plasma, close to the end of the plasma (see figure 5.8). Similarly to the conversion, the contribution of the recombination process follows that of the continuous plasma for short interpulse times. For longer interpulse times, the recombination becomes higher than that of the continuous case, which can be explained by the higher contribution of the dissociation mechanisms. However, the higher recombination is not enough to compensate for the increase in dissociation, thus explaining the higher conversion and energy efficiencies in figure 5.1.

5.3.7 Influence of cooling on the pulsing effect

From sections 5.3.3, 5.3.4, and 5.3.5, we concluded that the reduction of the gas temperature resulted in a higher average vibrational temperature, and a higher

overpopulation of the higher vibrational levels, which is beneficial for vibrational-induced dissociation (see section 5.3.6). Thus, we may conclude that a lower gas temperature has a beneficial effect on the dissociation, and therefore we investigate here the effect of additional wall cooling on the energy efficiency, for a plasma pulse time of $t_{on} = 60$ μs, and different interpulse times. This is illustrated in figure 5.10, for the standard case (no additional cooling: $\lambda_{add} = 0$), and three different cooling rates, defined by additional thermal conductivities, $\lambda_{add} = 0.01$, 0.1, and 1 $Wm^{-1}K^{-1}$ (see equation 5.1 above). For higher cooling rates, the improvement in energy efficiency with respect to a continuous plasma happens at shorter interpulse times. Indeed, for λ_{add} =0.1 $Wm^{-1}K^{-1}$, the energy efficiency already shows an improvement at $t_{off} = 10$ ms, while for λ_{add} =1 $Wm^{-1}K^{-1}$, this occurs at $t_{off} = 1$ ms already. This means that additional cooling can be used to tune the interpulse time at which the full potential of plasma pulsing can be exploited.

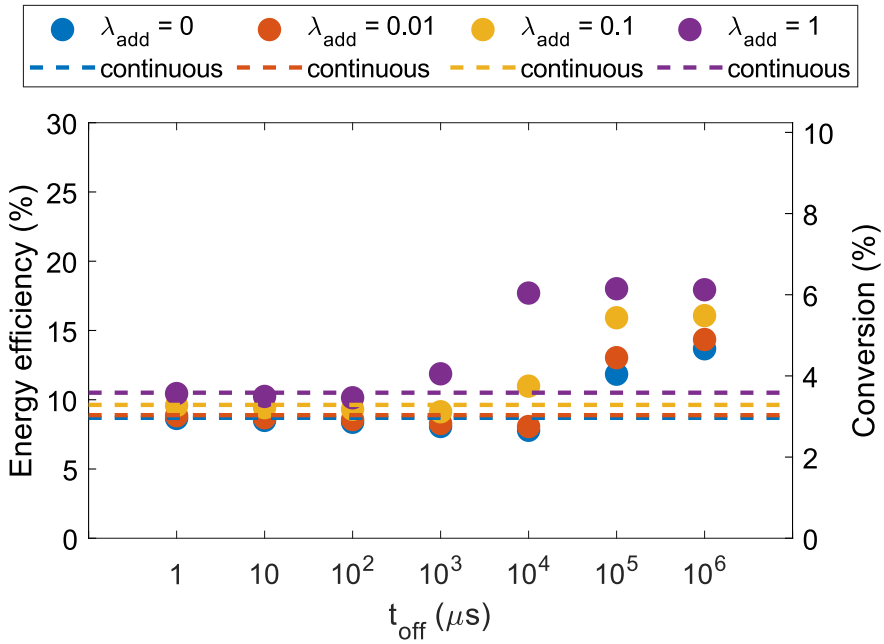

Figure 5.10: Energy efficiency and conversion as a function of interpulse time (t_{off}), for a plasma pulse time $t_{on} = 60$ μs, and for different cooling rates, as defined by the additional thermal conductivity, λ_{add} (in $Wm^{-1}K^{-1}$), besides the basic case (no additional cooling). The dashed horizontal lines correspond to the continuous plasma cases.

5.3.8 Influence of the ionization degree and reduced electric field on the pulsing effect

Up till now, we have only discussed the effect of pulsing at an ionization degree of 10^{-6} and a reduced electric field of 50 Td, which are characteristic for plasmas like MW and GA discharges[29;38;52]. In this section, we will evaluate the effect of the ionization degree and the reduced electric field on the potential of plasma pulsing. In figure 5.11, we vary the ionization degree between 2×10^{-7} and 10^{-5} at a reduced electric field of 50 Td. The blue bars are the energy efficiencies for a continuous plasma, while the red bars represent the maximum energy efficiency (evaluated for different plasma pulse and interpulse times) that can be added by pulsing. For ionization degrees of 5×10^{-7} and 10^{-6}, pulsing can indeed increase the energy efficiency of CO_2 dissociation, upon selecting the right values of plasma pulse and interpulse times (cf. figure 5.1). However, at both lower and higher ionization degrees, pulsing seems not to increase the energy efficiency, which can be explained as follows.

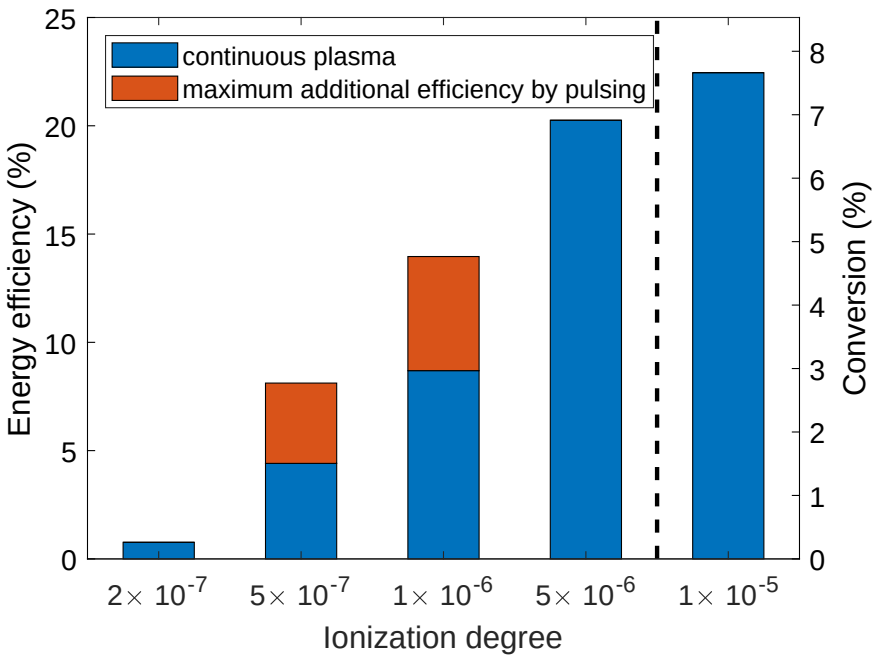

Figure 5.11: Energy efficiency and conversion of a continuous plasma (blue bars), and maximum additional energy efficiency caused by pulsing, for different ionization degrees, at an interpulse time of 1 s, and a reduced electric field of 50 Td. At ionization degrees higher than the dashed line, no thermalization of the vibrational temperature occurs for this total SEI.

The reason why the energy efficiency does not increase at the high ionization degree of 1×10^{-5} lies in the much faster rise of the vibrational temperature, with respect to the gas temperature, due to the shorter time scales of electron impact vibrational excitation (see figure 3.2). This is shown in figure C.6 of the appendix where the time-evolutions of the vibrational and gas temperature are plotted at different ionization degrees. Since the vibrational temperature rises much faster than the gas temperature, the latter does not reach high enough values to thermalize the vibrational temperature, which therefore increases until the end of the plasma. Since no thermalization of the vibrational temperature occurs during the continuous plasma, pulsing will not be able to increase the vibrational temperature, and will therefore not be able to improve the energy efficiency. For $d_i = 5 \times 10^{-6}$, thermalization does start to occur. However, the energy efficiency does not improve, as this thermalization happens closer to the end of the plasma, which prevents pulsing from improving the energy efficiency. In figure 5.11, ionization degrees higher than the dashed vertical line have a vibrational temperature increase until the end of the plasma.

At a low ionization degree of $d_i = 2 \times 10^{-7}$, the vibrational temperature does reach a maximum value, after which it thermalizes (see figure C.6 of the appendix). However, pulsing cannot increase the energy efficiency (see figure 5.11). This can be explained by the contribution of the different dissociation and recombination mechanisms, shown in figure 5.12 for different plasma pulse times, and an interpulse time of 1 s. At low ionization degrees, the characteristic time scale of electron impact vibrational excitation is much longer (see for $d_i = 10^{-7}$ in figure 3.2), resulting in a smaller contribution from vibrational-induced dissociation upon collision with a molecule M or an atom O. As can be seen in figure 5.12, electron impact dissociation becomes the most important dissociation mechanism. While pulsing increases the dissociation upon collision with a molecule M (see t_{on} = 100 - 1000 μs in figure 5.12), this rise is compensated by the negative effect of pulsing on electron impact dissociation (as was also seen in figure 5.9). The lower total contribution from these two reactions also lowers the dissociation upon collision with an atom O as well as the recombination, as they provide the O atoms for these reactions. The reduced contribution of electron impact dissociation and dissociation by collision with an atom O will therefore not lead to higher energy efficiencies, with respect to the continuous plasma.

When the reduced electric field increases, vibrational-induced dissociation becomes less important due to the lower amount of electron energy that goes to the vibrational modes[28]. Figure 5.13 illustrates the effect of the latter on the additional energy efficiency created by pulsing the plasma, for 100 Td and 150 Td. At a reduced electric field of 100 Td (corresponding to an electron temperature of about 2 eV), pulsing increases the energy efficiency at an ionization degree of $5 \times$

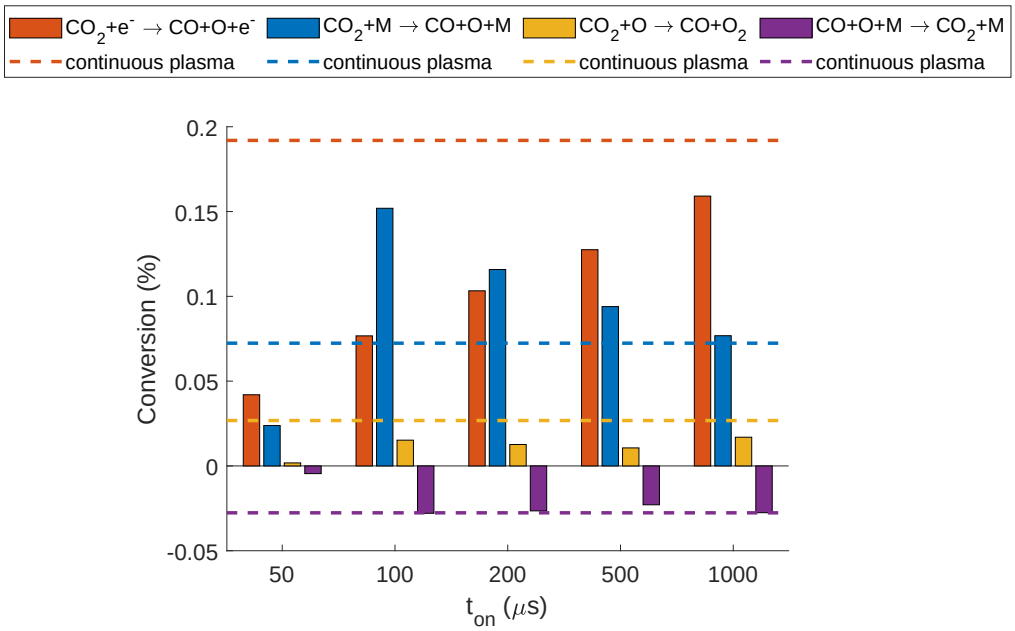

Figure 5.12: CO_2 conversion by the three main dissociation reactions: electron impact dissociation (red), dissociation upon collision with a molecule M (blue) and upon collision with an O atom (yellow), as well as the most important recombination reaction, for different plasma pulse times and an interpulse time of 1 s, a reduced electric field of 50 Td and an ionization degree of 2×10^{-7}. The dashed horizontal lines represent the respective conversions of a continuous plasma at the same SEI.

10^{-7} (see figure 5.13 a). At a reduced electric field of 150 Td (and corresponding electron temperature of 2.8 eV), the energy efficiency is only enhanced at an ionization degree of 5×10^{-8} and 10^{-7}. However, the increase is negligible.

For high and low ionization degrees, pulsing the plasma also does not lead to higher energy efficiency at higher reduced electric fields of 100 Td and 150 Td. Similar explanations as the ones that were given for a reduced electric field of 50 Td also apply. Indeed, at high ionization degrees, the vibrational temperature also increases until the end of the plasma (see figures C.7 and C.8 of the appendix), while at low ionization degrees, the negative effect of pulsing on the most prominent dissociation mechanism, i.e. electron impact dissociation, can not be compensated by the positive effect on the vibrational-induced dissociation by collision with a molecule M. This is shown in figures C.9 and C.10 of the appendix for $d_i = 10^{-7}$ at 100 Td and $d_i = 5 \times 10^{-8}$ at 150 Td, respectively.

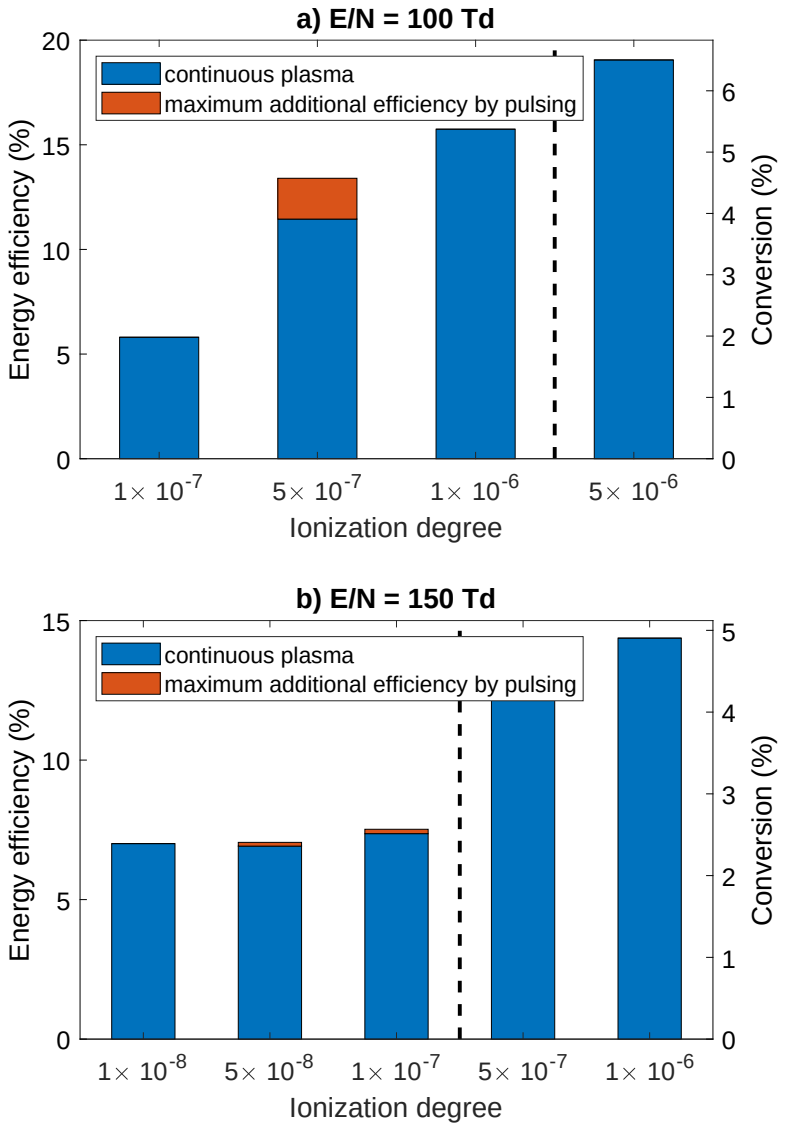

Figure 5.13: Energy efficiency and conversion of a continuous plasma (blue bars), and maximum additional energy efficiency, caused by pulsing, for different ionization degrees, at an interpulse time of 1 s, and for a reduced electric field of a) 100 Td, and b) 150 Td. At ionization degrees higher than the dashed line, no thermalization of the vibrational temperature occurs for this total SEI.

5.4 Conclusions

In this chapter, we have demonstrated the potential of plasma pulsing for improving the energy efficiency of CO_2 dissociation in a non-equilibrium plasma, by means of a 0D chemical kinetics model with self-consistent gas temperature calculation. At a reduced electric field of 50 Td, an ionization degree of 10^{-6}, and a total SEI of 1 eV/molec, our model predicts a drop in energy efficiency for short plasma pulse and interpulse times (i.e. $t_{on} \leq 10$ μs, and $t_{off} \leq 10$ ms), while an improvement in energy efficiency was calculated at longer plasma pulse and interpulse times.

To explain these results, we studied the vibrational and gas temperature evolution as a function of time during and after the pulse. The vibrational temperature quickly rises, but drops again after a maximum is reached, while the gas temperature rises more slowly, but shows a continuous increase during and even after the pulse, and only drops for long enough interpulse times. The plasma pulse time for which the highest energy efficiency was found (60 μs) corresponds to the time at which the vibrational temperature reaches its maximum. For shorter plasma pulse times, this maximum could not be reached, while at longer plasma pulse times, thermalization due to the high gas temperature results in a strong drop in vibrational temperature. This effect is correlated with the shorter characteristic time of VT relaxation at higher gas temperatures. At interpulse times above $t_{off} = 1$ ms, the vibrational and gas temperature reach an equilibrium, and both reach room temperature at $t_{off} = 1$ s. A maximum energy efficiency of 13.7% (compared to 8.7% for a continuous plasma at the same conditions) was obtained for a plasma pulse time $t_{on} = 60$ μs, and an interpulse time $t_{off} = 1$ s.

The effect of pulsing was also reflected in the evolution of the VDF. During the pulse, the higher vibrational levels start to get populated, but when the gas temperature becomes about 1000 K, the higher vibrational levels, which are needed for efficient vibrational-induced dissociation, start to get depleted. Hence, for plasma pulse times of 60 μs, the VDF is still overpopulated by the end of the pulse, but it quickly thermalizes after the pulse, and for interpulse times $t_{off} = 1$ ms, the VDF returns to a Boltzmann distribution, in equilibrium with the translational (gas) temperature.

We also compared the VDF at the end of the plasma (when the total SEI of 1 eV/molec was reached) for different plasma pulse and interpulse times. For short interpulse times, the VDF closely resembles that of a continuous plasma, which is nearly thermalized because of the higher gas temperature. However, for longer interpulse times, the reduction in gas temperature was enough to allow a considerable overpopulation of the vibrational levels with respect to the continuous plasma. This overpopulation was the highest for $t_{off} = 1$ s, at which the highest

energy efficiencies were found. However, the plasma pulse time needs to be long enough (ca. 60 μs), to fully exploit the beneficial effect of plasma pulsing, since the VDF needs this time to fully build up during the pulses, and a lower number of pulses reduces the losses of vibrational energy in between the pulses.

By evaluating the role of the various CO_2 dissociation processes, our model reveals that the higher energy efficiency upon pulsing (at long enough plasma pulse and interpulse times) is due to an increased contribution from vibrational-induced dissociation (mainly CO_2+M $\rightarrow$ CO+O+M, but also CO_2 + O $\rightarrow$ CO+O_2).

We also studied the effect of additional plasma cooling on the pulsing effect. Our model shows that for higher plasma cooling, the beneficial effects of pulsing already occur at shorter interpulse times, which is logical, as the gas temperature drops more quickly.

Finally, we evaluated the pulsing effect for different ionization degrees and reduced electric fields. At high ionization degrees, the vibrational temperature rises much faster than the gas temperature, resulting in higher energy efficiencies in a continuous plasma. Hence, as no thermalization of the vibrational levels occurs (due to the lower gas temperature), plasma pulsing cannot further improve the energy efficiency. At low ionization degrees and higher reduced electric fields, vibrational-induced dissociation is of lower importance, so pulsing has again no (or only a minor) effect on the energy efficiency. Therefore, our model reveals that pulsing can significantly enhance the energy efficiency for ionization degrees around 5×10^{-7} - 10^{-6}, and low reduced electric fields of about 50 Td and 100 Td.

In summary, our model provides interesting insights in how plasma pulsing can compensate for the negative effect of thermalization of the VDF, and how it can be used to increase the VT non-equilibrium in CO_2 plasmas, and thus to optimize the role of vibrational-induced dissociation.

We want to stress that the absolute values of conversion and energy efficiency in this work are subject to uncertainties, as a result of the uncertainties that exist on the rate coefficients. In addition, we want to note that the results only apply for a homogeneous plasma under the chosen external cooling term. At a lower external cooling, or when the plasma is radially contracted, leading to longer residence times, higher gas temperatures can be reached in the plasma. At these temperatures, thermal dissociation could become important. The results in this chapter only correspond to plasmas where thermal dissociation is not important, as pulsing will have a detrimental effect on this process. The effect of external cooling, and its effect on the plasma-based CO_2 dissociation will be discussed in more detail in the next chapter.

CHAPTER 6

The role of quenching in non-equilibrium plasmas

The results presented in this chapter were published in[108]:

- V. Vermeiren and A. Bogaerts. Plasma-Based CO_2 Conversion: To Quench or Not to Quench? *J. Phys. Chem. C*, 124(34):18401–18415, 2020. DOI: 10.1021/acs.jpcc.0c04257

6.1 Introduction

Over the last few years, research on CO_2 plasmas was largely focussed on increasing the VT non-equilibrium to reach higher energy efficiency of CO_2 conversion[28;56;92;93;97;103;158;159]. The aim was to enhance the vibrational temperature without (significantly) raising the gas temperature. However, in most experiments conducted with MW, APGD and GA discharges, the plasma appears to be in (or close to) thermal equilibrium, with the gas temperature (nearly) equal to the vibrational temperature[29;39;54;59;74;87;101].

These high gas temperatures (i.e. > 2500 K[39;60;63]) can even be reached at relatively low specific energy inputs (SEI), because the power input is localized in a limited gas volume[60;64;74] leading to a much higher local SEI[64]. This phenomenon is especially pronounced in APGD, GA and MW plasmas. In APGD and GA plasmas the contracted nature is inevitable, since the discharge is characterized by a plasma column that connects two electrodes[37;54;74]. In MW plasmas, the discharge is known to radially contract with increasing pressure, starting from around 100 mbar[58–60], in which the minimal plasma radius is equal to the skin depth[60].

The high temperatures[29;39;54;60;63;64;74] lead to significant thermal dissociation at the expense of vibrational-induced dissociation. The VDF exhibits a Boltzmann distribution, with no overpopulation of the higher vibrational levels, and the dissociation mainly occurs from the lower vibrational levels of CO_2[74;101]. While high energy efficiencies can be reached at these temperatures[39;59;74;107], the overall conversion starts to become constrained by the recombination reactions, mainly of CO with O_2 molecules, which become more important at higher temperatures[59;74;101].

A possible pathway to limit these recombination reactions at high gas temperatures is by quickly cooling the gas, thereby quenching the converted reaction products. Experimentally, this can be accomplished by a sharp temperature gradient between the plasma core and the surrounding gas[53;64]. In addition, the gas can be cooled by enhanced radial heat transport, achieved in turbulent flow regimes[59;109;139], or by supersonically accelerating the gas[62]. For high SEI plasmas, however, in which more than 0.19 eV/molec. goes to heat, this acceleration has to take place in the afterglow to prevent thermal choking of the flow[37;124].

Next to limiting the recombination reactions, and thus freezing of the reaction products (so-called ideal quenching), it is also possible to increase the CO_2 conversion upon quenching. This is called super-ideal quenching and happens when a VT non-equilibrium, created or enhanced by the sudden drop in gas temperature, promotes VV relaxation to the higher vibrational levels, and further enhances the dissociation reactions. More specifically, this can happen by the

reactions of vibrationally excited CO_2 molecules with any molecule (M), or with an O atom (i.e. $CO_2 + M \rightarrow CO + O + M$, or $CO_2 + O \rightarrow CO + O_2$).

Although it has been experimentally and theoretically demonstrated that high energy efficiencies for CO_2 conversion can be reached in warm plasmas at temperatures of 3000 K and above[29;39;63;64;74;107], and it is often stated that quenching is promising to reach higher energy efficiencies[37;59;62;64;101], more insight is needed to demonstrate its full potential. Therefore, we examine here the effect of quenching on the CO_2 conversion and energy efficiency for different plasma conditions. Furthermore, we compare the plasma conversion with purely thermal conversion, for the same power input, to elucidate the difference in performance, and to determine the actual role of thermal dissociation in plasma-based CO_2 conversion.

6.2 Model description

6.2.1 Plasma model

In this chapter, we follow the time-evolution of a volume element as it moves through a plasma reactor. The model starts with pure CO_2, mimicking the gas at the inlet of the reactor, and a Boltzmann vibrational distribution, corresponding to 300 K, i.e., the gas temperature at the inlet (see sections 2.4.2 and 2.4.3). At t=0, plasma power is applied to the gas (or thermal power when we use the model for pure thermal conversion; see below).

In order to compare the plasma performance with pure thermal simulations, we apply a heat source term with the same power deposition profile $P_{dep,th}$ as in the plasma case:

$$\frac{N_{th}}{\beta_{th}} P_{dep,th} = \frac{N_{pl}}{\beta_{pl}} P_{dep,pl} \tag{6.1}$$

with N_{th} and β_{th} being the total gas number density and expansion factor of the thermal simulation, respectively, and N_{pl} and β_{pl} for the plasma simulation.

At time t = 0 s, the plasma is ignited by applying the power as described above. The plasma is sustained until the applied power reaches the value corresponding to a certain predefined SEI (in eV/molec.).

We aim to study the effect of quenching at conditions of maximum CO_2 conversion and energy efficiency. This is typically achieved in MW plasmas at intermediate pressure[29;39]. We therefore assume a fixed pressure of 100 mbar.

The gas temperature is calculated self-consistently in the model, using equation 2.14. The heat exchange with the surroundings is particularly important in order to tune the VT (non) equilibrium effects. The external cooling term is

defined as[101;104]:

$$P_{ext} = \mathrm{c}\frac{8\lambda(T_g)}{R^2}(T_g - T_w) \tag{6.2}$$

where λ is the gas thermal conductivity, T_w is the wall temperature (assumed as 300 K), and the reactor radius R is set to 7 mm[55;57]. The gas thermal conductivity is calculated by[104]: $\lambda(T_g) = (0.071T_g - 2.33) \times 10^{-3} W m^{-1} K^{-1}$.

In order to study the effect of quenching on the CO_2 dissociation, we added a tuning constant c, to increase or decrease the cooling power (or thermal conductivity), which determines the gas temperature. Without quenching, c remains the same during the entire simulation. The gas can be quenched by reducing the gas temperature to 300 K (i.e. instantaneous quenching), or by increasing the cooling constant (i.e. c_1 before quenching and c_2 after quenching).

In reality, the cooling by thermal conductivity can be increased by gas flow turbulence[61;109]. A rise in thermal conductivity by a factor 100 (which is our model corresponds to c = 100) is quite feasible for CO_2 at room temperature. Indeed, while in our model, the thermal conductivity at 300 K is 0.019 W/(m*K), the effective thermal conductivity due to turbulence at 300 K was estimated to be 1-3 W/(m*K)[61], hence a factor (c=) 100 higher. The highest cooling constant in our model is c = 1000, which probably may only be realized upon mixing with a cold gas. However, the latter could also result in changes in the gas composition, but these effects are beyond the scope of our study. Indeed, our study is more conceptual.

6.2.2 Chemistry set

Similarly as in chapter 5, the foundation of the species and chemistry set are shown in table 3.1, and the tables in section A.1, respectively. In tables 3.2 and 3.3 updates and additions to the list of species are shown. Sections A.2 and A.3 present the modified or added reactions that apply to the chemistry set used in this chapter.

The main difference between the chemistry set used in the previous chapter and this one is that due to the higher conversion degree reached in this chapter, O_2^+ is added to the list of ions. Also, more vibrational levels of CO and O_2 are taken into account. For CO and O_2, 50 and 33 levels are taken into account, respectively. For O_2, these levels reach the dissociation limit, like the CO_2 vibrational levels of the asymmetric mode (see chapter 3). For CO, there are 63 levels up to the dissociation limit, but the levels above 50 were neglected, as they did not affect our results, due to the low vibrational excitation and strong VT relaxation, leading to a low population.

6.3 Results and discussion

All results are presented for a pressure of 100 mbar, which typically yields high energy efficiencies[38]. The ionization degree (d_i) is set to 10^{-6}, which can be considered as a lower value for diffuse microwave plasmas[60], but could also be applicable for glow discharge plasmas[160]. The reduced electric field (E/N) is set to 50 Td, as this is a value that ensures high vibrational excitation of the asymmetric mode levels of CO_2. We also present the results for an ionization degree (d_i) of 10^{-4} and E/N of 100 Td, to illustrate the behavior in a wider range of conditions.

6.3.1 Effect of cooling constant on the CO_2 conversion, gas and vibrational temperature during plasma

Figure 6.1 shows the time-evolution of the CO_2 conversion (left axis) and gas and vibrational temperature (right axis) for a plasma with SEI = 5 eV/molec., at weak (a) and strong (b) cooling, hence, representing a VT-equilibrium (or warm) plasma and a VT non-equilibrium (or cold) plasma, respectively. The vertical lines indicate the times at which an SEI of 1, 2, 3, and 4 eV/molec. is reached. Note that the residence time to reach a certain SEI in the cold plasma is shorter than in the warm plasma, as the gas density (N) is higher, requiring a higher electric field (and thus higher SEI) to reach an E/N of 50 Td.

At weak cooling (figure 6.1 (a)), a non-equilibrium between the vibrational and gas temperature arises at the start of the plasma, but quickly disappears, since the gas temperature rapidly rises, thus enhancing VT relaxation, so that the vibrational energy is lost to heat. At an SEI of 1 eV/molec., the vibrational and gas temperature are already in equilibrium. Van den Bekerom et al.[161] and Klarenaar et al.[158] also demonstrated experimentally for MW plasmas and glow discharge plasmas, respectively, that the non-equilibrium between vibrational and gas temperature is largest at the onset of plasma, after which it decreases when higher gas temperatures are reached. Exact comparison is not possible, as these experiments were performed at pressures of 25 mbar and 6.7 mbar, respectively.

The CO_2 conversion increases slowly at the plasma onset. It reaches 3.7 % at 1 eV/molec., and 8.6 % at 2 eV/molec., but then it rises much faster. At this time, the gas temperature has reached 3820 K, resulting in strong thermal dissociation of CO_2[74;107]. Thus, this high gas temperature is needed for significant conversion. At 5 eV/molec. a conversion of 84.6% is reached.

At strong cooling (figure 6.1 (b)), a non-equilibrium between vibrational and gas temperature exists for all shown SEI values, since VT relaxation is much less important at low gas temperatures. At an SEI of 1 eV/molec., the CO_2 conversion

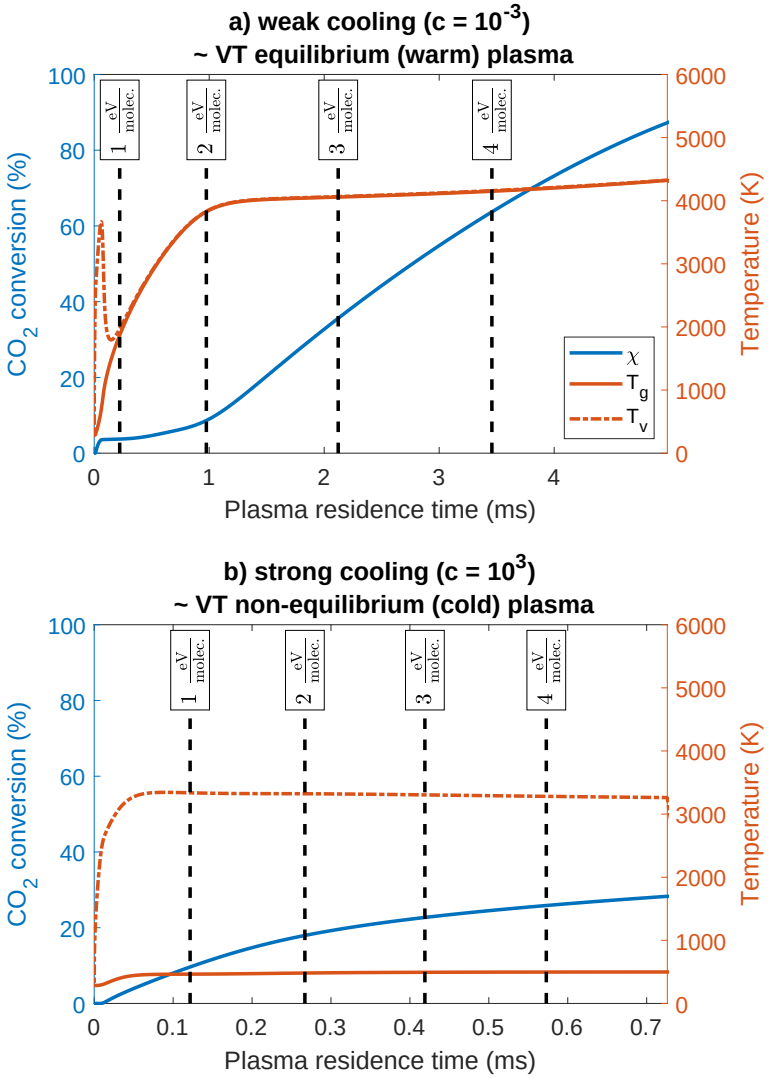

Figure 6.1: Time-evolution of the CO_2 conversion (left axis) and gas and vibrational temperature (right axis) for a plasma with SEI of 5 eV/molec., and for (a) weak cooling ($c = 10^{-3}$) and (b) strong cooling ($c = 10^3$), mimicking VT equilibrium (or warm) plasma and VT non-equilibrium (or cold) plasma, respectively. The time after which 1, 2, 3, and 4 eV/molec. of energy is supplied to the plasma is indicated with vertical dashed lines.

reaches 9.5 %, which is more than double of what was reached at the same SEI in figure 6.1 (a). However, when the SEI is higher than 2 eV/molec., the CO_2 conversion rises much more slowly than in figure 6.1 (a). At 5 eV/molec., a CO_2 conversion of 28.3 % is reached, hence much lower than in figure 6.1 (a). Thus, at SEI values below or equal to 1 eV/molec., cooling of the plasma is beneficial for

the conversion, consistent with previous studies performed by our group[28]. For SEI values of 2 eV/molec. and higher, cooling is detrimental, pointing towards the important role of thermal dissociation. This will be further elaborated in section 6.3.7.

6.3.2 CO_2 conversion and gas temperature in the afterglow of warm plasmas

In figure 6.2, we plot the time-evolution of the conversion and gas temperature in the afterglow of a plasma with SEI of 1, 2, 3, 4, and 5 eV/molec., at weak cooling ($c = 10^{-3}$), i.e., the afterglow of figure 6.1 (a), starting at the different vertical dashed lines.

The conversion continues to rise in the afterglow, due to thermal CO_2 dissociation. This is most obvious for larger SEI, and thus a higher gas temperature. Indeed, the system may not yet be in chemical equilibrium, because of the short residence time. At lower ionization degrees and reduced electric fields, when the residence time to reach these SEI values is longer, this equilibrium can already be reached inside the plasma.

Next to thermal dissociation, recombination is also important at high gas temperatures[101]. In the afterglow, the temperature slowly decreases as a function of time (figure 6.2 (b)), and around 10-100 ms (depending on the SEI) thermal dissociation becomes less important than recombination, so the CO_2 conversion starts to drop (figure 6.2 (a)). After ca. 2 s, the gas temperature has become low enough (ca. 1000-1500 K) for both recombination and dissociation to become unimportant. At that point, the conversion remains constant.

This figure clearly illustrates that when no additional cooling is applied in the afterglow, the CO_2 conversion, although being very high inside the plasma at high SEI values (even close to 100 %), eventually drops to low values ($\sim$ 20-25 %) after a few seconds, due to recombination reactions. To avoid this detrimental effect, we need to apply cooling in the afterglow, to quench the reaction products. This will be studied in the following sections.

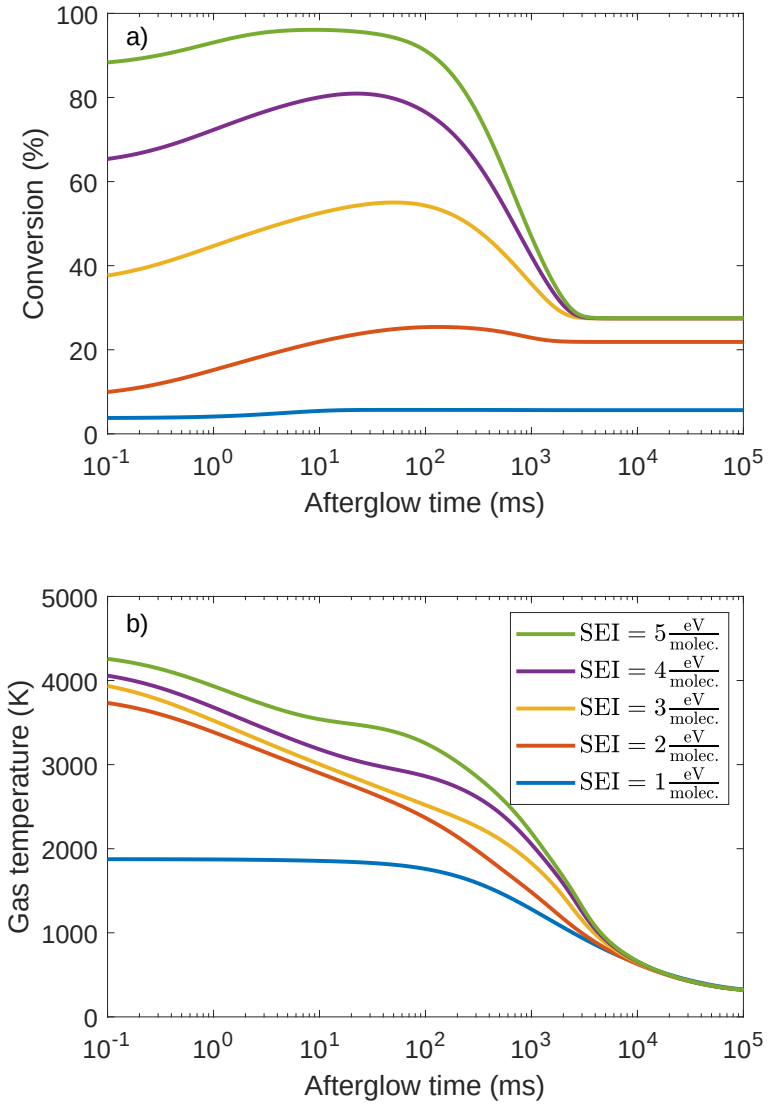

Figure 6.2: Time-evolution of the CO_2 conversion (a) and gas temperature (b) in the afterglow of a warm plasma with SEI of 1, 2, 3, 4, and 5 eV/molec., at weak cooling ($c = 10^{-3}$), when no additional cooling is applied in the afterglow.

6.3.3 Instantaneous quenching

Instantaneous quenching, i.e., quickly reducing the gas temperature to 300 K, can prevent the recombination. Indeed, at 300 K, thermal dissociation and recombination are not important, and the converted reaction products are "frozen".

We describe here the effect of instantaneous quenching, (i) at the plasma end, and (ii) in the afterglow, when the CO_2 conversion reaches its maximum without any quenching (see figure 6.2).

6.3.3.a Quenching after warm plasmas

In figure 6.3, we plot the time-evolution of the CO_2 conversion (top panels) and gas temperature (bottom panels) for a plasma with SEI of 0.5 eV/molec. (left panels) and 4 eV/molec. (right panels), at weak cooling ($c = 10^{-3}$). Note that a VT equilibrium exists at the plasma end with SEI of 4 eV/molec., but not at 0.5 eV/molec. (cf. figure 6.1 (a)).

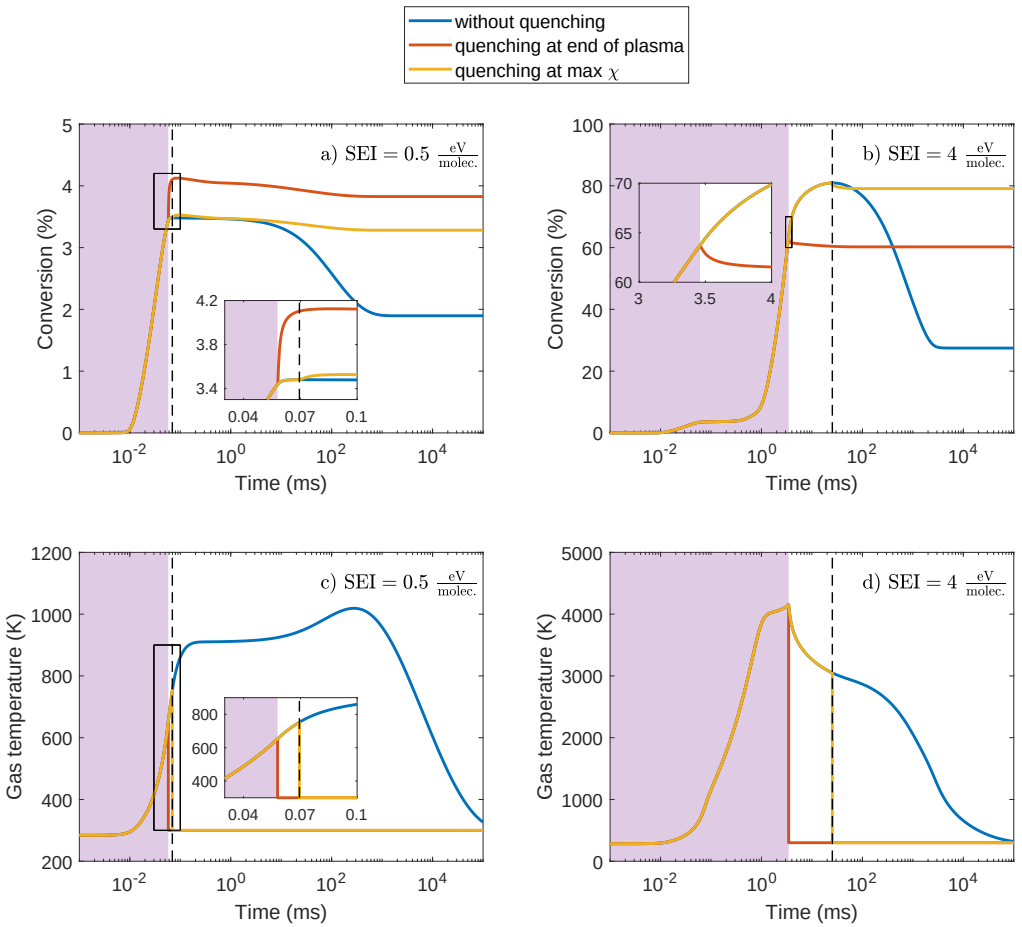

Figure 6.3: Time-evolution of the CO_2 conversion (a and b) and gas temperature (c and d) without quenching (blue curve) and with quenching at the plasma end (red curve) and at the maximum conversion in the afterglow (yellow curve) for a plasma with SEI of 0.5 eV/molec. (a and c) and 4 eV/molec. (b and d), at weak cooling ($c = 10^{-3}$). The purple area indicates the plasma, and the vertical dashed line shows where the conversion reaches a maximum in the afterglow without quenching. Note that the plasma with SEI of 0.5 eV/molec. is characterized by VT non-equilibrium, while SEI of 4 eV/molec. yields a VT equilibrium at the plasma end.

Quenching clearly leads to a higher final CO_2 conversion in all cases, but the ideal quenching moment is different for the plasma with high or low SEI.

For an SEI of 0.5 eV/molec. (figure 6.3 (a) and (c)), the optimal quenching moment is at the plasma end. The conversion increases rapidly after quenching, due to the VT non-equilibrium, enhanced by the fast drop in gas temperature. This is called "super-ideal quenching". Quenching at maximum conversion also yields a higher CO_2 conversion, but since the vibrational temperature drops quickly after switching off the plasma[125], the VT non-equilibrium, and thus the increase in conversion, is much smaller than when quenching at the plasma end (cf. yellow and red curve in figure 6.3 (a)).

For an SEI of 4 eV/molec., the optimal quenching moment is at maximum conversion. Since a chemical equilibrium is not yet reached at the plasma end, the conversion further increases after the plasma (see also figure 6.2). For both quenching cases, the CO_2 conversion remains more or less frozen (except for a small drop immediately after quenching). The VT non-equilibrium created by the drop in gas temperature is not enough to give a rise in conversion (i.e. super ideal quenching). The different trends in CO_2 conversion upon quenching, for the two SEI values, will be discussed more in depth in the following sections.

Next to the conversion, the energy efficiency is a good measure for effectiveness of quenching. Figure 6.4 summarizes both the conversion and energy efficiency as a function of SEI, without quenching (blue bars), and in case of quenching at the plasma end (red bars) and at maximum conversion (yellow bars).

For all SEI values, quenching at maximum conversion enhances the final conversion and energy efficiency, compared to no quenching. The rise is most pronounced for higher SEI values, where the conversion is most affected by a gradual drop in gas temperature (figure 6.2). Our model predicts a maximum final conversion of 90 %, for quenching at maximum conversion, at an SEI of 5 eV/molec., and a maximum energy efficiency of 58 %, again for quenching at maximum conversion, but at an SEI of 4 eV/molec.

Quenching at the plasma end only enhances the final conversion and energy efficiency for SEI below 1 eV/molec. and above 2 eV/molec. For SEI below 1 eV/molec., the VT non-equilibrium at the plasma end, further enhanced upon quenching, yields super-ideal quenching, see also figure 6.3 (a)). For SEI values of 1 and 2 eV/molec., the gas temperature at the plasma end is high enough to allow thermal CO_2 dissociation, but there is no significant drop in conversion in the afterglow due to gradual cooling (cf. figure 6.2 (a)), because the CO_2 conversion is limited, and thus the recombination reactions are not so important as for higher SEI values. Hence, quenching does not play such a big role in reducing the eventual drop in CO_2 conversion. For higher SEI values, the drop in CO_2 conversion is very pronounced (see figure 6.2 (a)), thus explaining why

quenching at the plasma end is again beneficial for SEI values above 2 eV/molec.

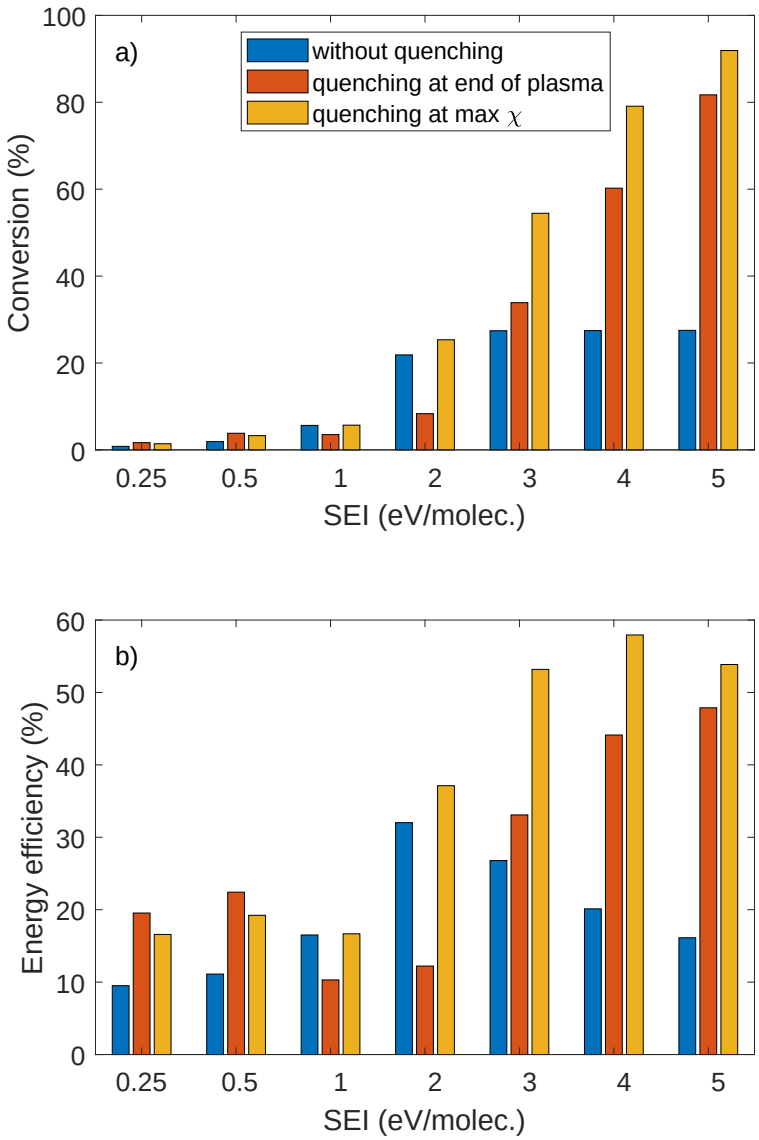

Figure 6.4: CO_2 conversion (a) and energy efficiency (b) as a function of SEI, without quenching (blue curve), and with quenching at the plasma end (red curve) and at maximum conversion (yellow curve), for warm plasma conditions (i.e. weak cooling; c = 10^{-3}). Note that an SEI of 0.25 and 0.5 eV/molec. yields a VT non-equilibrium plasma, while an SEI of 1 eV/molec. and higher results in a VT equilibrium plasma (cf figure 6.1 (a))

6.3.3.b Quenching after cold plasmas

When strong cooling (c = 10^3) is applied, the VT non-equilibrium does not disappear for higher SEIs (see figure 6.1 (b)). Figure 6.5 shows the effect of different quenching times on the evolution of the CO_2 conversion, for a cold plasma with SEI of 4 eV/molec.

In both cases, the CO_2 conversion slightly rises after quenching (i.e. super-ideal quenching; see inset in figure 6.5 (a)), but it is followed by a larger drop compared to without quenching. Hence, the final CO_2 conversion is lower for both quenching options than without quenching.

Comparing this situation to figure 6.3 (a), it seems that a VT non-equilibrium can enhance the CO_2 conversion, but for high SEI values, the conversion after plasma is higher, and more recombination can take place, resulting in a lower final CO_2 conversion. Only at low SEI values, non-equilibrium plasmas seem to benefit from quenching, yielding a clearly higher final CO_2 conversion (see figure 6.3 (a)).

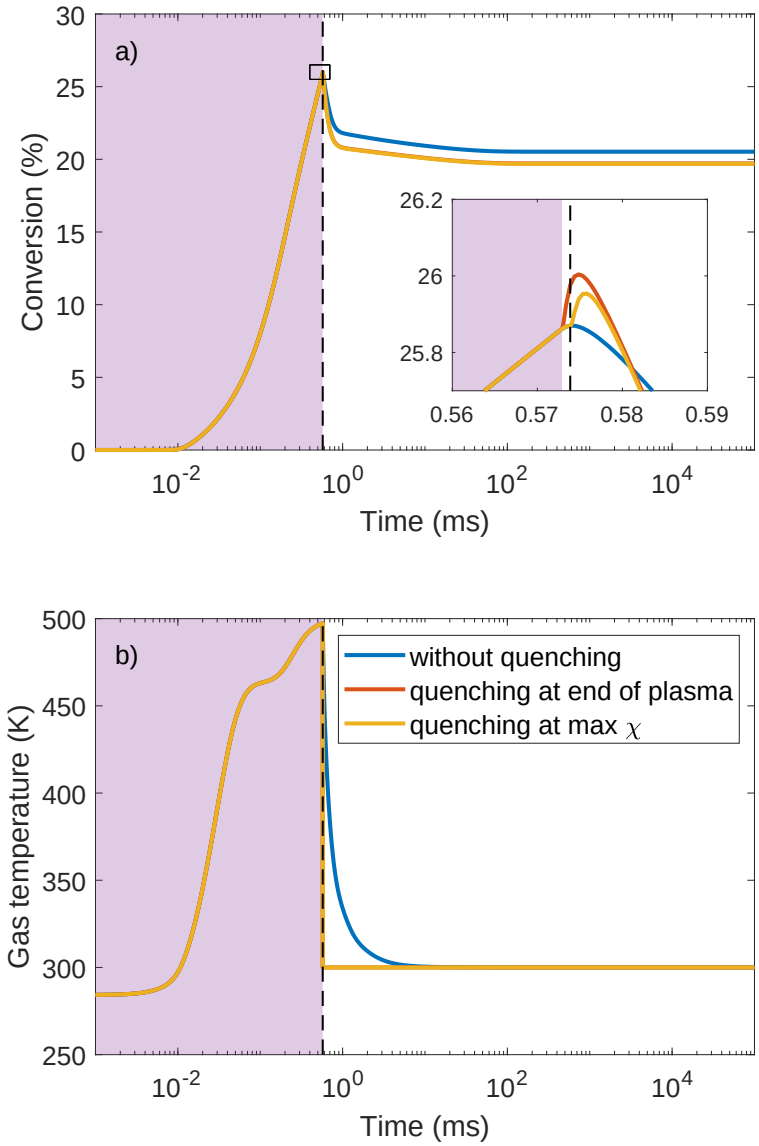

Figure 6.5: Time-evolution of the CO_2 conversion (a) and gas temperature (b) without quenching (blue curve), and with quenching at the plasma end (red curve) and at the maximum conversion (yellow curve), for a cold (VT non-equilibrium) plasma at SEI of 4 eV/molec. (strong cooling, c = 10^3). The purple area indicates the plasma, and the vertical dashed line shows where the conversion reaches a maximum in the afterglow without quenching.

6.3.4 Effect of instantaneous quenching on the dissociation and recombination rates

To explain the different behavior of instantaneous quenching at low and high SEI, we now discuss its effect on the dissociation and recombination rates, both for a plasma with low and high SEI (0.5 and 4 eV/molec.), characterized by VT non-equilibrium and equilibrium at the plasma end, respectively. Figs. 6.6 and 6.7 show the total contribution of the three most important dissociation reactions (reaction X4 in Table A.1, and reaction N1 and N2 in Table A.4 and A.7) and recombination reactions (N4 and N5 in Table A.4 and A.7), to the CO_2 conversion, plotted as positive and negative conversion. For both cases, the quenching moment that provides maximum CO_2 conversion (i.e. quenching at the plasma end for an SEI of 0.5 eV/molec., and quenching at maximum conversion in the afterglow for an SEI of 4 eV/molec., respectively) will be compared with the non-quenched case. Figure D.1 and D.2 in the appendix show the corresponding time-evolution of these rates after quenching, while figure D.3 and D.4 show the evolution of the O radical density after quenching.

Figure 6.6 illustrates that the dissociation rates increase upon quenching, as well as the recombination rate by reaction N5. However, due to the low conversion degree (3-4%), little CO and O_2 are present, and this reaction is not important. The main reason for the higher final CO_2 conversion is the lower contribution from recombination reaction N4, due to the faster drop in O radical density, shown in figure D.3 from the appendix.

Figure 6.7 illustrates that dissociation reactions N1 and N2, as well as recombination reactions N4 and N5, are all reduced. The reduction is most drastic for N2 and N5. Note that for these two reactions, the conversion value is higher than 100 % in the case without quenching, since on average, CO_2 dissociates and recombines multiple times, but the overall net conversion is of course not above 100 %. Due to the stronger reduction in recombination rate, the final CO_2 conversion increases, as also observed in figure 6.3 (b) (yellow vs blue curve). However, figure D.2 of the appendix shows that upon quenching, both recombination reactions see a fast but short increase, with respect to the non-quenched case. This can be correlated with the short decrease in CO_2 conversion, that is noticed when quenching (see yellow vs blue curve in figure 6.3 (b)).

In appendix D , we show the time-evolution of the dissociation and recombination rates (figure D.5), and the contribution of these reactions to the overall CO_2 conversion (figure D.6), for a non-equilibrium cold plasma with SEI of 4 eV/molec. (i.e., strong cooling, c = 10^3) corresponding to figure 6.5, in case of quenching at the plasma end. Quenching again enhances the dissociation reactions and recombination reaction N5, similar to figs. 6.6 and D.1 of the appendix

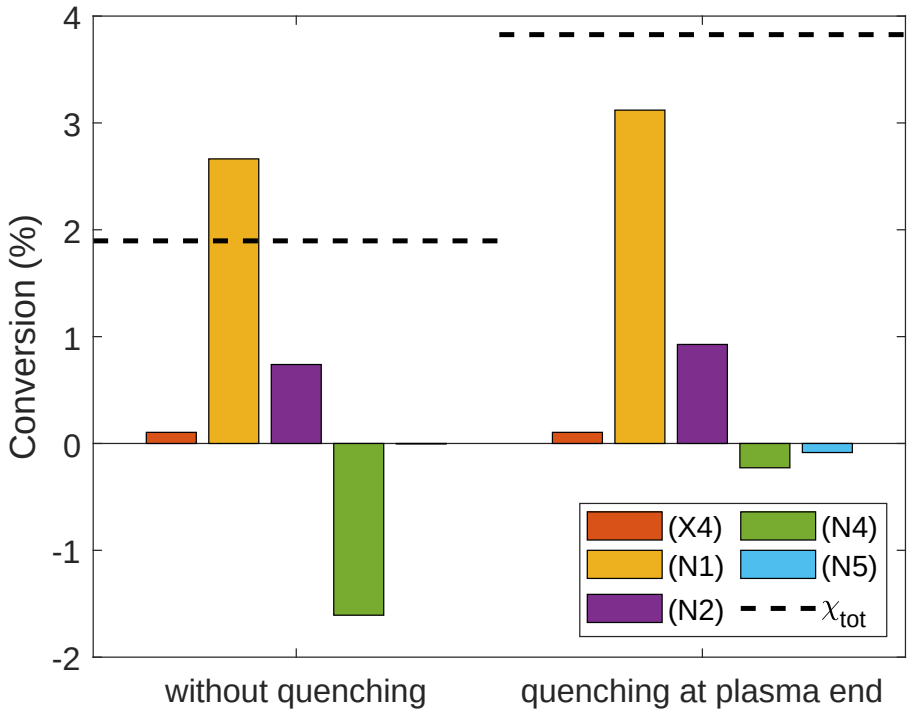

Figure 6.6: Total contribution of the dissociation and recombination reactions to the conversion for a warm VT non-equilibrium plasma with SEI of 0.5 eV/molec. that is quenched at the plasma end (right), and that was subjected to weak cooling (c = 10^{-3}). The case without quenching (left) is shown as a reference. The horizontal dashed lines indicate the final CO_2 conversion. Besides the major dissociation reactions (N1, N2), also electron impact dissociation (X4; see Table S.1 in SI) has a minor contribution.

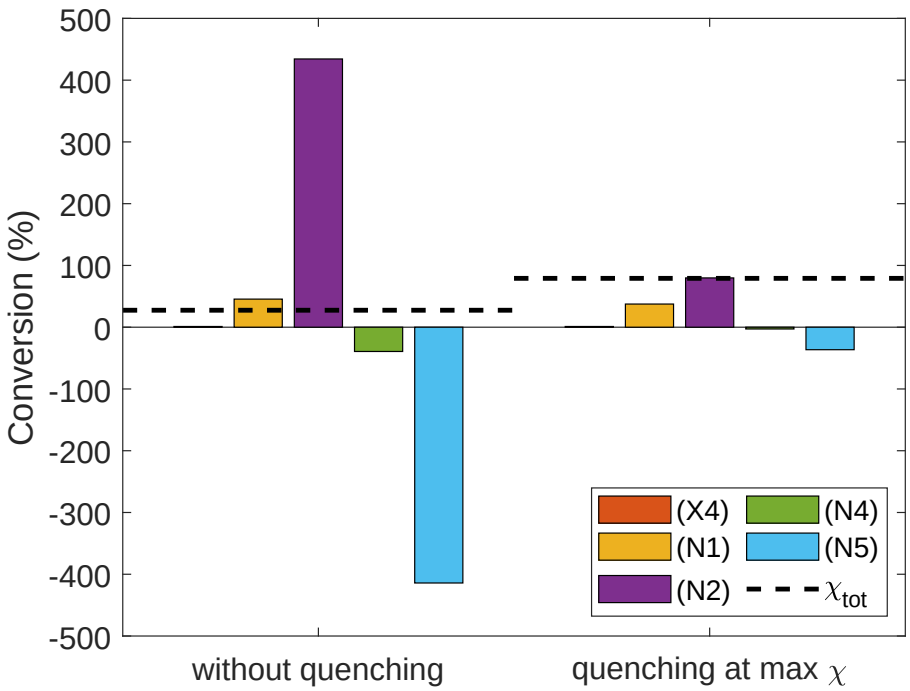

Figure 6.7: Total contribution of the dissociation and recombination reactions to the conversion for an equilibrium plasma with SEI of 4 eV/molec. that is quenched at maximum conversion (right), and that was subjected to weak cooling (c = 10^{-3}). The case without quenching (left) is shown as a reference. The horizontal dashed lines indicate the final CO_2 conversion. In contrast to the non-equilibrium plasma of figure 6.6, electron impact dissociation (X4) has a negligible contribution to the final CO_2 conversion.

(i.e., VT non-equilibrium warm plasma at SEI of 0.5 eV/molec). However, since the CO_2 conversion is higher than at SEI of 0.5 eV/molec., the recombination reactions are more important, and the rise in recombination reaction N5 happens over a longer time, resulting in an overall drop in CO_2 conversion, as indeed observed in figure 6.5.

6.3.5 Effect of instantaneous quenching on the VDFs of CO_2, CO and O_2

The dissociation reactions N1 and N2, and the recombination reaction N5 all have a high activation energy (see Table A.4 and A.7 of the appendix). At low gas temperatures, i.e., after quenching, these reactions can only take place if the molecules have sufficient vibrational energy to overcome the activation energy. Therefore, figures 6.8 and 6.9 illustrate the VDFs of CO_2, CO and O_2 at different times after quenching, for a VT non-equilibrium warm plasma with SEI of 0.5 eV/molec. that is quenched at the plasma end (cf. figure 6.6, figure D.1 in the appendix, and red curve in figure 6.3 (a)), and an equilibrium warm plasma with SEI of 4 eV/molec. that is quenched at maximum conversion (cf. figure 6.7, figure D.2, and yellow curve in figure 6.3 (b)), respectively.

In figure 6.8, right before quenching (i.e. at the plasma end), the higher vibrational levels of all three molecules already have a large overpopulation; see red curve; note that this time point is not indicated in the upper panel, because of the logarithmic x-axis. This is consistent with the VT non-equilibrium for SEI below 1 eV/molec. in figure 6.1 (a). Upon quenching, the drop in gas temperature results in a faster VV relaxation, and a slower VT relaxation, leading to a higher population of the higher vibrational levels of CO_2, enabling the dissociation reactions N1 and N2. On the other hand, the strong vibrational overpopulation of CO and O_2 also enables the recombination reaction N5 (see figure 6.6 and figure D.1 in the appendix). Due to the low conversion degree, CO_2 is the dominant molecule in the mixture, and the rise in N1 and N2, fuelled by the overpopulation of the higher vibrational levels of CO_2, is dominant over the rise in recombination reaction N5. However, the VDF of CO_2 depopulates much faster than those of CO and O_2, explaining why the fast increase in conversion is followed by a slow drop (point 2, purple curve in figure 6.8, and figure D.1 in the appendix). After 1 ms (time-point 3, green curve in figure 6.8), the higher vibrational levels of CO and O_2 exhibit no overpopulation anymore, and the recombination reaction N5 is no longer important (figure D.1 in the appendix). The resulting drop in CO_2 conversion is a result of reaction N4, which has a low activation energy, and does not need vibrational energy to take place.

In figure 6.9, the VDFs of the three molecules follow the Boltzmann distribu-

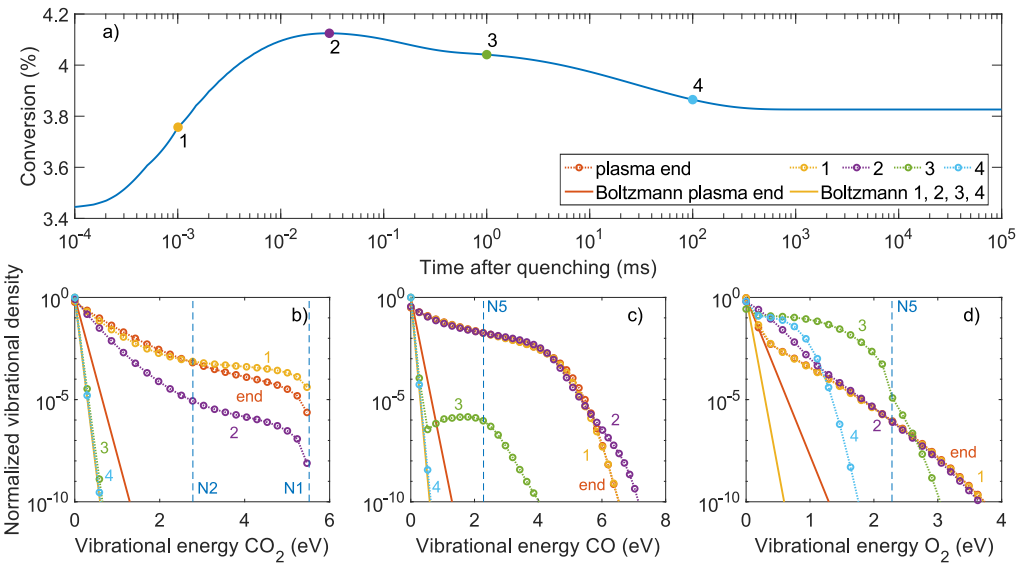

Figure 6.8: VDFs of CO_2, CO, and O_2 (bottom panels; b-d), and their corresponding Boltzmann distributions, at the end of a warm plasma with SEI of 0.5 eV/molec. (VT non-equilibrium, weak cooling, c = 10^{-3}) (red), and for different times after instantaneous quenching at the plasma end (1 to 4). The different time points are indicated on a plot of the conversion as a function of time (top panel; a). The vertical dashed lines in the bottom panels show the vibrational activation energies (E_a/α) of the dissociation reactions (N1 and N2) (b) and recombination reaction (N5) (c,d).

tion, since VT equilibrium was established at the plasma end (figure 6.1 (a)), and quenching occurs some time after the plasma. Due to the high gas temperature, the distribution of the higher vibrational levels is elevated, but not overpopulated compared to a Boltzmann distribution. Right after quenching, the Boltzmann distribution drops due to the drop in gas temperature, but the VDFs remain close to the Boltzmann distributions before quenching (see yellow curves; time point 1 in figure 6.9). A VT non-equilibrium is therefore created by quenching. Similar to figure 6.8, the higher levels of CO_2 are somewhat overpopulated due to the increased VV relaxation. While the vibrational temperature, after quenching, of about 3050 K is very similar to the vibrational temperature of figure 6.8 (i.e. 3500 K), the overpopulation of the higher and intermediate levels is much lower. Indeed, due to the much lower population of these levels in figure 6.9, VV relaxation requires a longer time to significantly populate the higher vibrational levels, since the energy has to come from the lowest levels. This gives more time for VT relaxation to depopulate the VDF. Also, the conversion degree is much higher, so there is less CO_2 to dissociate, and the recombination reactions are

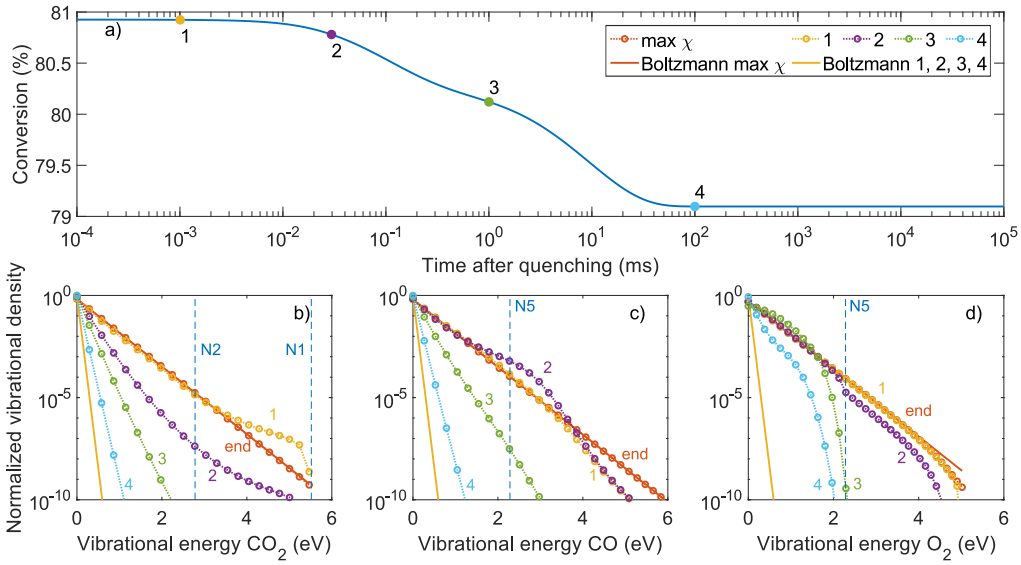

Figure 6.9: VDFs of CO_2, CO, and O_2 (bottom panels; b-d), and their corresponding Boltzmann distributions, at the end of a warm plasma with SEI of 4 eV/molec. (VT equilibrium, weak cooling; c = 10^{-3}) (red), and for different times after instantaneous quenching at maximum conversion (1 to 4). The different time points are indicated on a plot of the conversion as a function of time (top panel; a). The vertical dashed lines in the bottom panels show the vibrational activation energies (E_a/α) of the dissociation reactions (N1 and N2) (b) and recombination reaction (N5) (c,d).

more prominent (figure D.2 in the appendix), counteracting the eventual rise in CO_2 dissociation, yielding a net drop in conversion (upper panel of figure 6.9). Similarly to figure 6.8, the VDFs of CO and O_2 remain populated for a longer time, so recombination reaction N5 is active for a longer time (time point 2, purple curves, and figure D.2 in the appendix). Due to the higher concentration of CO and O_2, this results in a higher recombination, and a bigger drop in CO_2 conversion with respect to figure 6.8.

For completeness, figure D.7 in the appendix illustrates the VDFs of CO_2, CO, and O_2 for a VT non-equilibrium cold plasma at SEI of 4 eV/molec. (i.e. strong cooling; c = 10^3), that is quenched at the plasma end (cf. red curve in figure 6.5).

6.3.6 Effect of different quenching cooling rates

In previous sections, we discussed the effect of instantaneous quenching. This is the ideal case, but in reality, the gas cooling will not be instantaneous. Therefore, we discuss here the effect of different cooling rates (i.e. different cooling constants

c_2 in equation 6.2) on the CO_2 conversion, for warm plasmas, i.e. weak initial cooling ($c_1 = 10^{-3}$).

Figure 6.10 illustrates the time-evolution of the CO_2 conversion and gas temperature in the afterglow, for different cooling rates, for a warm non-equilibrium plasma with SEI of 0.5 eV/molec. that is quenched at the plasma end (cf. figure 6.3 (a)).

Without quenching (i.e., weak cooling in the afterglow; $c_2 = c_1 = 10^{-3}$), the gas temperature continues to rise in the afterglow (up to about 0.3 s) due to VT relaxation and recombination reactions.

Upon increasing c_2, the gas temperature drops faster (cf. figure 6.10 (b)). Hence, recombination becomes less important, resulting in a higher final CO_2 conversion (cf. figure 6.10 (a)). For a cooling constant $c_2 \geq 10^4$, the gas temperature reduces to 300 K within 10 μs (or less), and super-ideal quenching becomes apparent (cf. figure 6.10). Without quenching ($c_2 = c_1$), VT relaxation quickly depopulates the highest vibrational levels in the afterglow. Figure D.8 in the appendix shows that the VDF of CO_2 is in equilibrium within 100 μs after the plasma end. If the cooling rate is high enough ($c_2 \geq 10^4$), the gas temperature drops faster than the VDF can relax. This limits the drop in, or even enhances, the overpopulation of the higher vibrational levels of CO_2, thus increasing the dissociation rates, as the CO_2 vibrational energy can overcome the high activation energy of the dissociation reactions N1 and N2.

Figure 6.11 depicts the time-evolution of the CO_2 conversion and gas temperature in the afterglow, for different cooling constants, for a VT equilibrium warm plasma with SEI of 4 eV/molec. that is quenched at maximum conversion (cf. figure 6.3 (b)).

In this case, the gas temperature gets high enough to allow for thermal dissociation of CO_2, even after the plasma end. However, due to slow gas cooling, the recombination reactions reduce the CO_2 conversion significantly (cf. figure 6.11 (a,b)). Upon higher cooling rate, the final CO_2 conversion increases. Note that the maximum conversion is not reached with maximum cooling rate. Indeed, when the cooling constant rises from 100 to 1000, the conversion slightly decreases (see inset in figure 6.11 (a)). This is due to VV relaxation that populates the higher vibrational levels of CO and O_2 at lower gas temperatures (figure 6.9), so that they can overcome the high activation energy of the recombination reaction N5. The effect is however minor, and in general, we can conclude that for warm plasma conditions (i.e. weak initial cooling) higher cooling rates yield a higher final CO_2 conversion, either due to super-ideal quenching, further enhancing the CO_2 conversion (figure 6.10) or simply by freezing the CO_2 conversion, because the recombination reactions become negligible at low gas temperatures (figure 6.11).

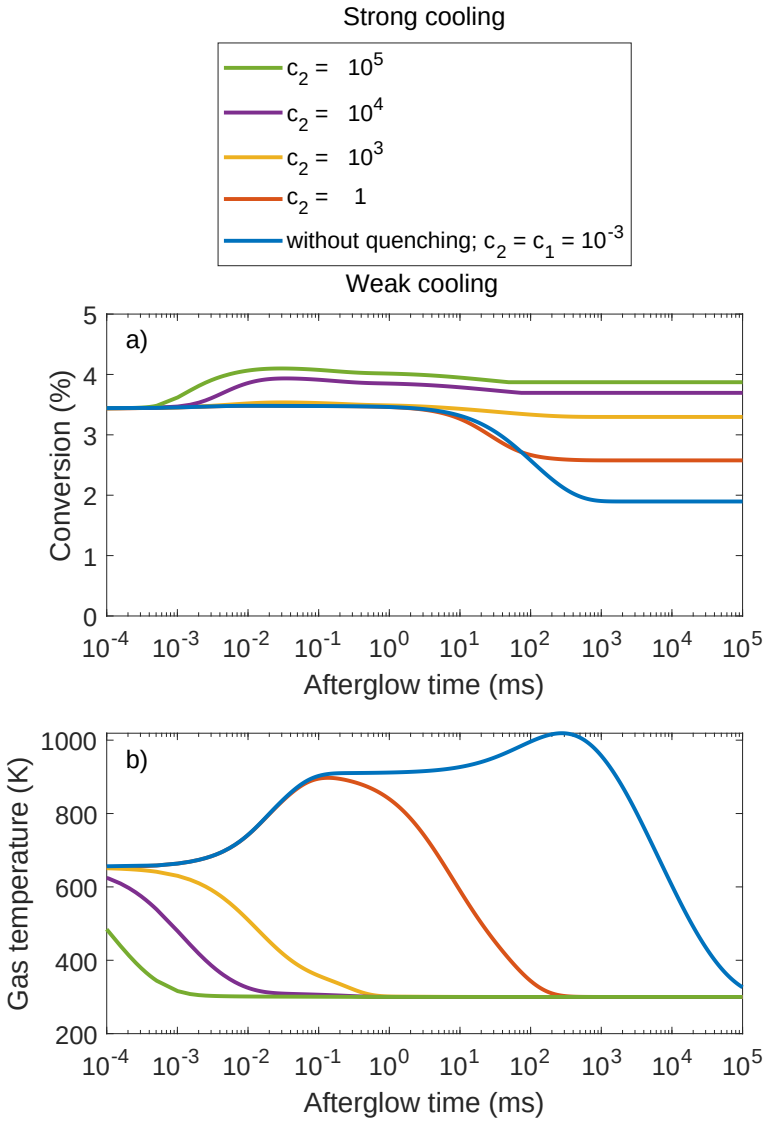

Figure 6.10: Time-evolution of the CO_2 conversion (a) and gas temperature (b), for different cooling rates in the afterglow, for a VT non-equilibrium plasma with SEI of 0.5 eV/molec. that is quenched at the plasma end. The plasma is initially subjected to weak cooling ($c_1 = 10^{-3}$), i.e. warm plasma. The cooling constants c_2 in the afterglow are indicated in the legend.

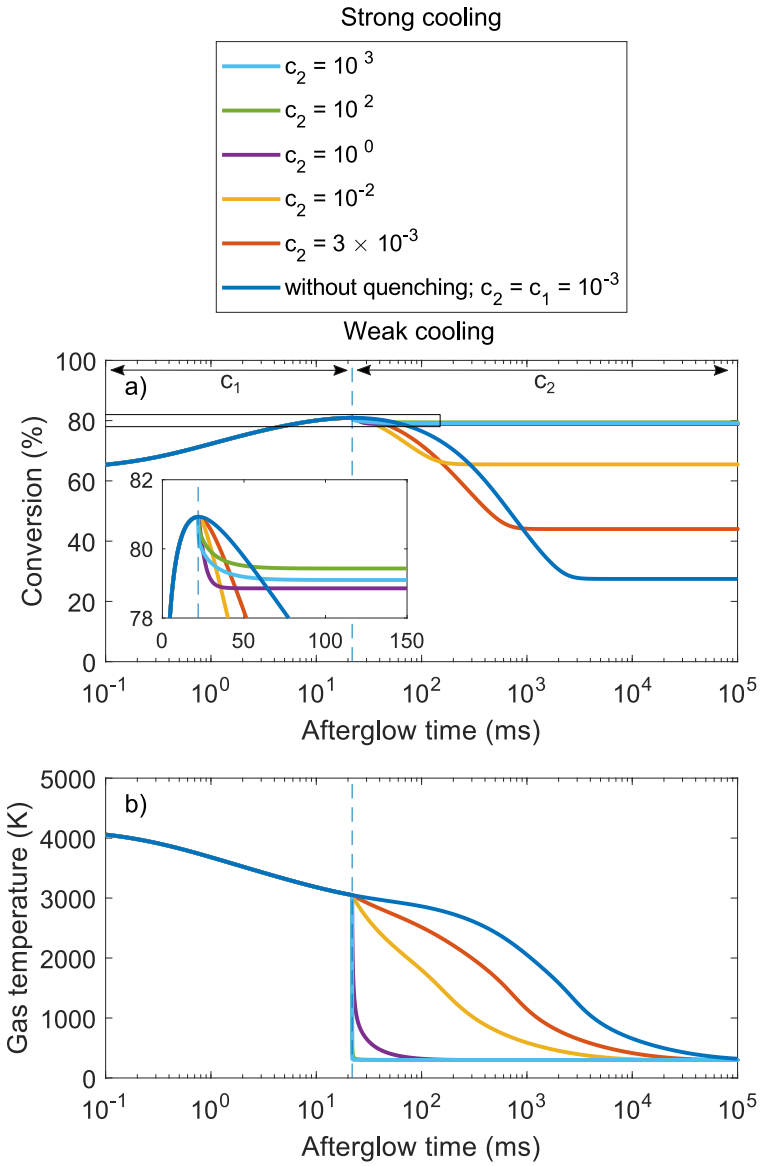

Figure 6.11: Time-evolution of the CO_2 conversion (a) and gas temperature (b), for different cooling rates, for a VT equilibrium plasma with SEI of 4 eV/molec. that is quenched at maximum CO_2 conversion. The plasma is initially subjected to weak cooling ($c_1 = 10^{-3}$), i.e. warm plasma. The cooling constants c_2 in the afterglow are indicated in the legend.

6.3.7 Comparison of plasma-based and thermal CO_2 conversion at different SEI values and gas temperatures, and effect of instantaneous quenching

Figure 6.12 illustrates the CO_2 conversion and energy efficiency as a function of SEI for a warm plasma (c = 10^{-3}), as well as for the purely thermal process, in which the same power is applied as heat, as explained in section 6.2.1, both with and without quenching at maximum CO_2 conversion. The maximum gas temperature in both cases is shown on the right axis.

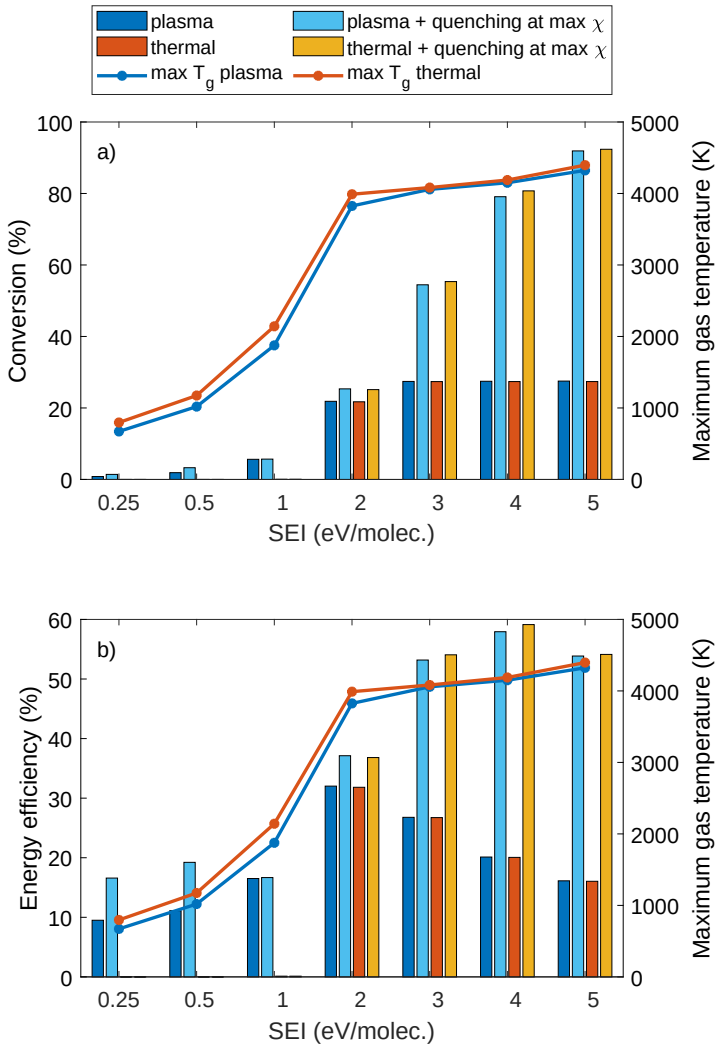

Figure 6.12: CO_2 conversion (a; left axis) and energy efficiency (b; left axis) and maximum gas temperature (right axis) as a function of SEI, for a warm plasma (i.e. weak cooling; c = 10^{-3}) and pure thermal conversion, with and without quenching at maximum conversion.

For SEI values $\leq$ 1 eV/molec., the maximum gas temperature is too low for thermal dissociation of CO_2. The thermal process therefore shows negligible conversion, while the plasma process exhibits a conversion of about 0.8-5.6 %, corresponding to an energy efficiency of 9.5 – 16.5 %, mostly attributed to vibrational-induced dissociation, but also electron impact dissociation.

For SEI $\geq$ 2 eV/molec., the conversion and energy efficiency of the thermal process rise, and they are similar to the plasma process, both with and without quenching. In addition, the maximum gas temperatures are also very comparable, due to the high VT relaxation that results in a VT equilibrium (see figure 6.1). Upon quenching, a similar behavior takes place because in both cases a VT non-equilibrium is created, since the VDF is "frozen" in its Boltzmann distribution from right before quenching (see figure 6.9). Similarly as in the plasma quenching case, the conversion degree slightly drops due to the higher concentration of CO and O_2, promoting a higher recombination (see figs. 6.3 b and 6.9). However, at high SEI, the conversion and energy efficiency of the quenched thermal case perform slightly better than that of the plasma case. This is because the power goes directly to the neutral species, while in the plasma case, inefficient processes like electron impact dissociation still play a role (see figs. 6.6 and 6.7). Without quenching, the final CO_2 conversion remains constant at 27-28 %, due to the slow cooling, which promotes recombination reactions.

In figure 6.13, we plot the CO_2 conversion and energy efficiency (left axis) as a function of cooling constant (c), i.e., mimicking warm and cold plasmas at different temperatures (see curves and right axis), for plasma-based and thermal conversion, both with an SEI of 4 eV/molec, and both without quenching and for instantaneous quenching at maximum conversion (i.e., the gas temperature drops immediately to 300 K).

At weak cooling (c = 10^{-3}), corresponding to a maximum gas temperature of 4150-4200 K, quenching reaches the highest conversion of 79 % and 81 %, corresponding to an energy efficiency of 58% and 59%, for the plasma and purely thermal case, respectively. At these high temperatures, the conversion is mostly thermal. The difference between quenching and no quenching is also high, since the slow drop in gas temperature without quenching is detrimental for the conversion (see also figure 6.2). With increasing cooling constant c, the maximum gas temperature decreases, leading to lower thermal conversion. Also the difference with and without quenching decreases, as the higher afterglow cooling also leaves less time for recombination. Note that the higher conversion is already significant for moderate cooling (c = 0.01 vs 10^{-3}), corresponding to low reduction in the maximum gas temperature, as the recombination in the afterglow typically occurs over a long time (order of 1 s; see figure 6.2). When the cooling c reaches 1, the maximum gas temperature is around 2500 K, which is too

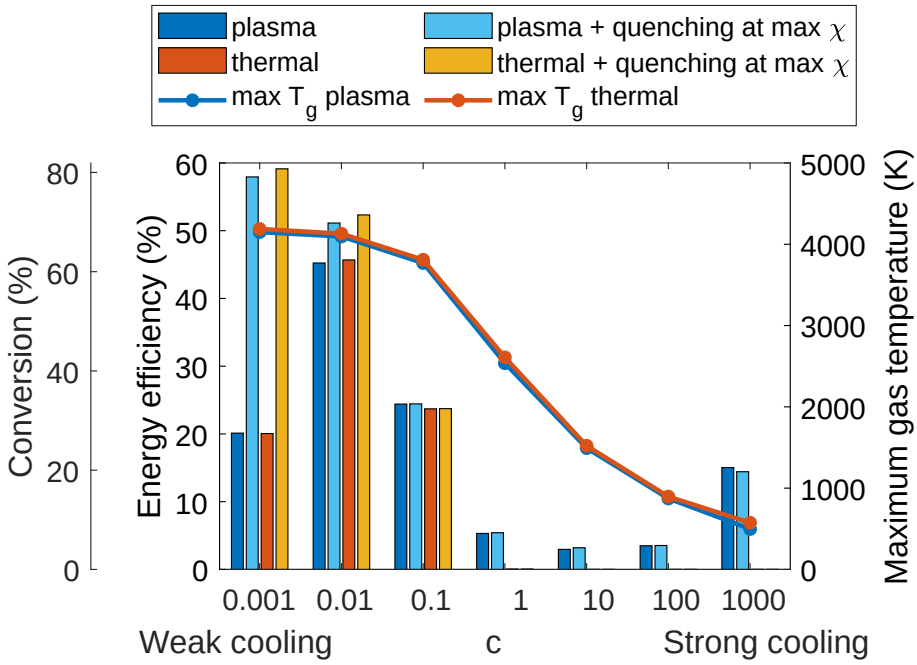

Figure 6.13: Energy efficiency and CO_2 conversion (left axis), and maximum gas temperature (right axis) as a function of cooling constant c for the plasma and purely thermal process, with SEI of 4 eV/molec., without quenching and with instantaneous quenching at maximum conversion.

low for (substantial) thermal dissociation. Therefore, the thermal CO_2 conversion and energy efficiency become negligible. The plasma-based CO_2 conversion and energy efficiency also drop. Indeed, while the gas temperature is too low for substantial thermal dissociation, it is still high enough for considerable VT relaxation, which prevents an efficient vibrational-induced dissociation. This VT relaxation becomes less important upon even stronger cooling, leading to higher vibrational-induced dissociation, and a subsequent rise in final CO_2 conversion and energy efficiency, for $c \geq 100$. These conditions correspond to cold VT non-equilibrium plasmas, where quenching does not enhance the CO_2 conversion or energy efficiency (cf. figure 5).

It must be realized that the exact values of conversion and energy efficiency are subject to uncertainties, as mentioned in section 6.2.2, and should thus be considered with caution, but the trends predicted by the model, for the effect of quenching and the comparison between plasma-based and thermal conversion should be reliable. Indeed, our modeling results are in reasonable agreement with the model of Kotov and Koelman, predicting maximum energy efficiencies of about 40 % at 4 eV/molec. in MW plasmas at comparable pressure[107],

and also stressing the dominant role of thermal conversion. den Harder et al.[29] and Bongers et al.[39] reported experimental energy efficiencies up to 48 % for gas temperatures between 3500-4000 K, at intermediate pressure. In addition, experiments revealed that quenching in the afterglow can enhance the energy efficiency to values around 50 %[39;62]. However, exact comparison with these experimental results is difficult, due to possible deviations in pressure, ionization degree and reduced electric field, and because of limitations to the 0D model[162], like not describing transport phenomena, and assuming spatial homogeneity. These transport phenomena might play an eminent role in facilitating the quenching process[59].

6.3.8 Quenching at higher ionization degree

In the previous sections, we considered an ionization degree of 10^{-6}. In contracted MW plasmas, the ionization degree can be much higher, up to 10^{-4}.[60] Therefore, we show here the evolution of the CO_2 conversion and energy efficiency as a function of SEI, for an ionization degree of 10^{-4}. The reduced electric field is kept at 50 Td.

In figure 6.14 we plot the conversion and energy efficiency (left axis) as a function of SEI, for the plasma and thermal process, at low cooling (c = 10^{-3}). The gas is instantaneously quenched at maximum conversion, and the maximum gas temperature is shown for both cases (right axis). When comparing figure 6.14 with figure 6.12, we can see that the conversion and energy efficiency are slightly higher at this higher ionization degree for SEI values $\leq$ 2 eV/molec. For SEI values $\leq$ 1 eV/molec. the temperature is too low for thermal conversion. Even at 2 eV/molec., the plasma-based conversion and energy efficiency are higher than for thermal conversion, both with and without quenching, since a higher ionization degree results in more electron impact reactions, including more electron impact vibrational excitation, and consequently also in more vibrational-induced dissociation[28]. Similar to the lower ionization degree of 10^{-6}, the highest conversions and energy efficiencies are again found for the higher SEI values (see also figure 6.12). Note also that the maximum gas temperature for these higher SEIs is larger than for a lower ionization degree (see figure 6.12). This is also observed in experiments[78].

For an SEI of 3-5 eV/molec., the conversions and energy efficiencies are very similar for plasma and thermal conversion, both with and without quenching. However, the maximum gas temperature is much lower for the plasma process than for the thermal process. This is because more energy goes to the vibrational levels at higher ionization degree, resulting in more vibrational-induced dissociation. Despite the difference in maximum gas temperature, and the fact that more

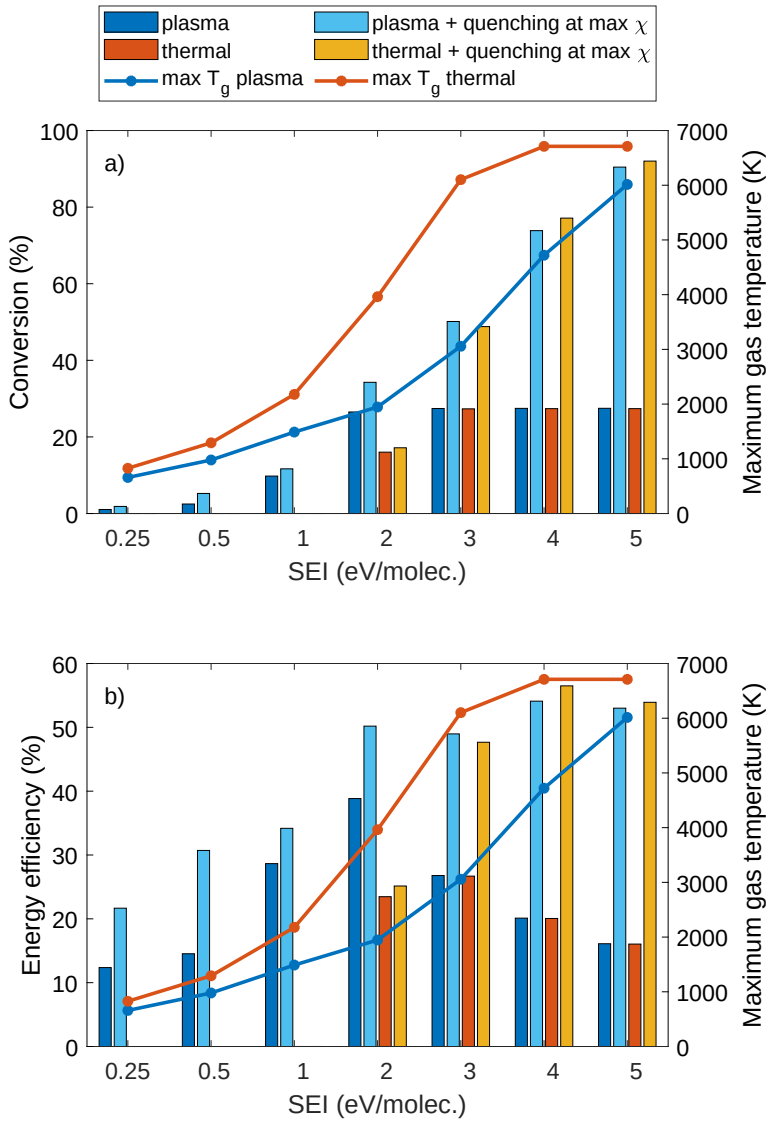

Figure 6.14: CO_2 conversion (a; left axis) and energy efficiency (b; left axis) and maximum gas temperature (right axis) as a function of SEI for the plasma and purely thermal process, with and without quenching, for an ionization degree of 10^{-4}, and weak cooling (c = 10^{-3}). The reduced electric field is 50 Td.

of the plasma-based CO_2 conversion takes place through vibrational-induced dissociation, the final CO_2 conversion and hence energy efficiency are similar for the plasma and thermal process. The energy efficiencies at these higher SEI values are very similar to the ones at lower ionization degree (see figure 6.12).

6.3.9 Quenching at higher reduced electric field

All previous results were obtained for a reduced electric field of 50 Td. As this value may be quite low for practical MW plasmas, we present here the evolution of CO_2 conversion and energy efficiency as a function of SEI, for a reduced electric field of 100 Td, again for a low cooling (c = 10^{-3}), and an ionization degree of 10^{-6}, and for both the plasma and thermal process, with and without quenching (instantaneous quenching at maximum conversion). The maximum gas temperature is shown for both cases on the right axis.

Figure 6.15 shows a similar evolution with increasing SEI as at lower E/N (see figure 6.12). At low SEI values (SEI = 0.25 – 1 eV/molec.), the plasma exhibits a low conversion and energy efficiency, and there is no thermal dissociation. At SEI = 2 eV/molec. the plasma process is less efficient than the thermal process, both with and without quenching. The same applies to higher SEI values upon quenching. This is because the higher reduced electric field makes electron impact dissociation more prominent, but the latter is less energetically favourably, explaining the lower energy efficiency than for pure thermal conversion. At higher SEI values (SEI = 3 – 5 eV/molec.), the plasma and thermal process without quenching become equally efficient, because the slow drop in gas temperature reduces the CO_2 conversion to a value of 27-28 %.

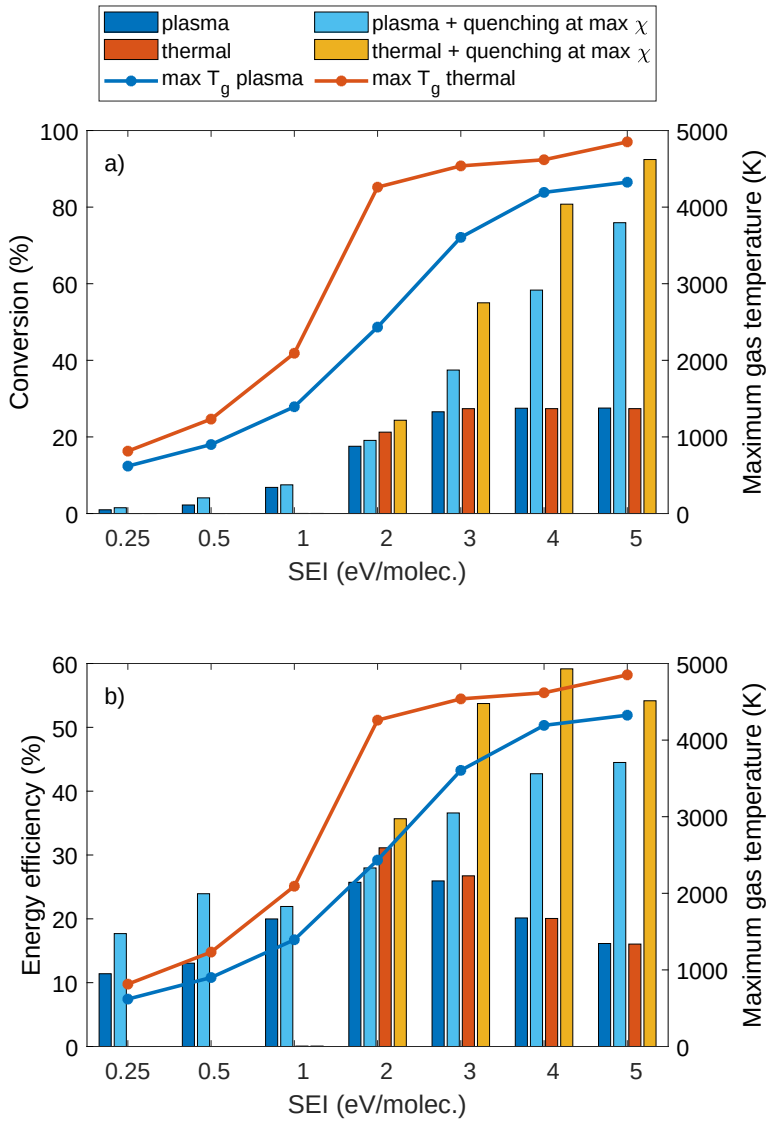

Figure 6.15: CO_2 conversion (a; left axis) and energy efficiency (b; left axis) and maximum gas temperature (right axis) as a function of SEI for the plasma and purely thermal process, with and without quenching, for an reduced electric field of 100 Td, and weak cooling (c = 10^{-3}). The ionization degree is 10^{-6}.

6.4 Conclusions

In this chapter, we demonstrated the potential of quenching for plasma-based CO_2 conversion, by means of chemical kinetics modelling. We consider so-called warm plasmas at a pressure of 100 mbar, an ionization degree of 10^{-6} and a reduced electric field of 50 Td, but our model predicts that the trends are the

same at higher ionization degree (10^{-4}) and reduced electric field (100 Td).

We calculated the gas and vibrational temperature, and the CO_2 conversion, as a function of time in the plasma, at weak and strong cooling, mimicking warm and cold plasma conditions, respectively. At weak cooling, high conversion degrees were reached for large SEI values (i.e., up to 96 % at SEI = 5 eV/molec.), due to the high gas temperature ($\sim$ 4000 K), leading to VT equilibrium and thus thermal conversion. However, without additional cooling in the afterglow, the conversion drops dramatically, due to the backward (recombination) reactions, leading to a low overall CO_2 conversion of 27 – 28 %.

We examined the effect of quenching for warm and cold plasma conditions, and we explained the results based on the dissociation and recombination reactions and the VDFs of the CO_2, CO and O_2 molecules. For warm plasma conditions at low SEI, yielding VT non-equilibrium, our model predicts it is best to quench at the plasma end. In this case, quenching can even further enhance the dissociation by the reactions ($CO_2 + M \rightarrow CO + O + M$ and $CO_2 + O \rightarrow CO + O_2$), due to the overpopulation of the CO_2 vibrational levels, which helps to overcome the activation energy of these reactions. This process is called "super-ideal quenching". For cold plasma conditions at high SEI, which also result in VT non-equilibrium, quenching also enhances the dissociation, but it promotes the recombination reactions even more, leading to a lower final CO_2 conversion. For warm plasma conditions at high SEI, yielding VT equilibrium, the high gas temperature enhances the CO_2 conversion even after the plasma, so it is more favourable to quench at maximum conversion. Upon fast quenching, both dissociation and recombination reactions stop, so the CO_2 conversion is frozen, leading to a much higher final CO_2 conversion and overall energy efficiency than without quenching (even up to a factor three enhancement).

We also evaluated the effect of different cooling rates in the afterglow, demonstrating overall the importance of fast cooling, although at high SEI values we also have to account for overpopulation of the higher vibrational levels of CO, which can overcome the activation energy of the recombination reaction, therefore leading to more recombination, resulting in a slight drop in the overall conversion.

Finally, we compared the performance of plasma-based CO_2 conversion with purely thermal conversion, for different SEI values and for warm (i.e. low cooling) and cold (i.e. high cooling) plasmas, as well as the effect of quenching, on both the CO_2 conversion and energy efficiency. For warm plasmas at SEI $\geq$ 2 eV/molec., yielding gas temperatures of 3000-4000 K, the plasma-based conversion is mostly thermal, and quenching can enhance the conversion and energy efficiency by up to a factor three. For low SEI plasmas at lower temperatures, when thermal conversion is negligible, the overall conversion and energy efficiency are quite low, and in addition, quenching becomes less efficient. For cold plasmas in VT non-

equilibrium at high SEI, quenching can even decrease the final CO_2 conversion.

In summary, our model provides interesting insights in how quenching can improve the CO_2 conversion and energy efficiency for various plasma conditions and cooling conditions. We showed that the highest conversion and energy efficiency can be reached for thermal conversion, at high gas temperatures in the plasma, followed by fast quenching. Such quenching can be realized when expanding the flow after the plasma, as demonstrated experimentally[39;62], but it may also be accomplished by mixing with a cold gas. In addition, the quenching might be combined with heat recovery, for preheating the gas entering the plasma reactor, so that less plasma power is wasted for gas heating, and all the power could be used for the conversion process.

Summary

There is a broad consensus in the scientific community that increased antropogenic emissions of greenhouse gases are responsible for an increase in the average global temperature. This global warming is correlated with extreme weather phenomena like droughts, floods and hurricanes. The most prominent greenhouse gas that is emitted is carbon dioxide, which is mostly the result of the combustion of fossil fuels. In order to tackle this problem, a shift to a carbon-neutral economy is needed. Since the energy sector is a major contributor to the emission of CO_2, due to its use of fossil fuels, a transition to more renewable sources of energy production is needed. However, one of the major drawbacks of the most important renewable energy sources is their intermittency. Therefore, large efforts are being directed to finding good energy storage technologies. A possible pathway is to use the excess renewable energy to dissociate CO_2 into CO and $\frac{1}{2}O_2$. The CO can be combined with H_2 to synthesise hydrocarbons in the Fischer-Tropsch process.

Plasma technology is interesting for this purpose, because it can easily convert electrical energy to chemical energy. The high thermodynamic non-equilibrium between the electron temperature and gas temperature in the plasma allows for endothermic reactions to take place without the need to first heat up the gas, thus lowering the energy cost with respect to pure thermal processes. In addition, a significant portion of the energy is put into the vibrational levels of CO_2. This vibrational energy can then be transferred to the higher vibrational levels, until the bond breaking energy, from which dissociation can take place. While this is a promising dissociation pathway, it is limited by the rise in gas temperature. At higher gas temperatures, thermal dissociation becomes more important at the expense of vibrational induced dissociation. In order to facilitate industrial application of plasma-based CO_2 dissociation, more insight is needed into the effect of vibrational-induced and thermal dissociation on the CO_2 conversion and energy efficiency, and how they can be improved. In this thesis, a chemical

kinetics model is used to reveal the underlying chemistry in order to get insight into how the efficiency of the dissociation process can be increased.

Chapter 1 gives a short overview of the problem of global warming, the different energy storage technologies that exist, and the different plasma reactors that are used for CO_2 dissociation, along with their maximum reported conversion and energy efficiencies. In chapter 2, the theory that forms the basis of the 0D model is explained. The chemistry set and scaling laws that are required to scale the reactions for different vibrational levels are explained in chapter 3.

In chapter 4 the effect of supersonic flow on the energy efficiency and CO_2 conversion is studied in a combined flow and plasma chemical kinetics model of a microwave CO_2 plasma in a Laval nozzle setup. In this study, the effects of the flow field on the different dissociation and recombination mechanisms, the vibrational distribution, and the vibrational transfer mechanism are discussed. In addition, the effect of experimental parameters, like position of power deposition, outlet pressure, and specific energy input, on the CO_2 conversion and energy efficiency is examined. The short residence time of the gas in the plasma region, the shockwave, and the maximum critical heat, and thus energy, that can be added to the flow to avoid thermal choking are the main obstacles to reaching high energy efficiencies.

In chapter 5 it is examined how pulsing can improve the VT non-equilibrium and lead to higher energy efficiency and CO_2 conversion. It is shown that higher energy efficiencies can be reached by correctly tuning the plasma pulse and interpulse times. The ideal plasma pulse time corresponds to the time needed to reach the highest vibrational temperature. The highest energy efficiencies are obtained with long interpulse times, i.e. ≥ 0.1 s, in which the gas temperature can entirely drop to room temperature. Furthermore, additional cooling of the reactor walls can already give higher energy efficiencies at shorter interpulse times. In this chapter, it is also shown that pulsing is detrimental for electron impact dissociation. Pulsing can not improve the efficiency for plasmas at low ionization degrees or high reduced electric fields, where this process is most dominant. The pulsing can also not improve the efficiency if the vibrational temperature reaches its maximum close to the end of the plasma.

Finally, in chapter 6, the effect of cooling/quenching during and after the plasma is investigated for warm (i.e. with low external cooling) and cold (i.e. with high external cooling) plasmas at different SEIs. For warm plasmas at low specific energy input (SEI $\sim$ 0.5 eV/molec.), it is best to quench at the plasma end, while for high SEI plasmas (SEI $\sim$ 4 eV/molec.), quenching at maximum conversion is better. For low SEI plasmas, quenching can even increase the conversion beyond the dissociation in the plasma, known as super-ideal quenching. To better understand the effects of quenching at different plasma conditions, we

study the dissociation and recombination rates, as well as the vibrational distribution function (VDF) of CO_2, CO, and O_2. When a high vibrational-translational (VT) non-equilibrium exists at the moment of quenching, the dissociation and recombination reaction rates both increase. Depending on the conversion degree at the moment of quenching, this can lead to a net increase or decrease of CO_2 conversion. In general, however, and certainly for warm plasmas at high temperature, quenching after the plasma helps to prevent recombination reactions and clearly enhances the final CO_2 conversion. We also investigate the effect of different quenching cooling rates on the CO_2 conversion and energy efficiency. Finally, we compare plasma-based conversion to purely thermal conversion. For warm plasmas with typical temperature above 2500 K, the conversion is roughly thermal.

In summary, the results obtained in this thesis give a better insight in the underlying mechanisms of plasma-based CO_2 conversion. They give valuable suggestions into how the CO_2 conversion and energy efficiency can be increased for cold to warm plasmas. These insights will be useful for future experimental research.

Samenvatting

Er bestaat een brede consensus in de wetenschappelijke gemeenschap over de bijdrage van verhoogde antropogene emissies van broeikasgassen aan de stijging van de gemiddelde temperatuur op aarde. Deze opwarming van de aarde is sterk gecorreleerd aan extreme weersverschijnselen zoals droogtes, overstromingen en orkanen. Het meest uitgestoten broeikasgas is koolstofdioxide, dat voornamelijk voortkomt uit de verbranding van fossiele brandstoffen. Om dit probleem aan te pakken is een verschuiving naar een koolstofneutrale economie nodig. Aangezien de energiesector een belangrijke bijdrage levert aan de uitstoot van CO_2, door het gebruik van fossiele brandstoffen, is een transitie naar meer hernieuwbare energiebronnen nodig. Een van de grootste nadelen van de belangrijkste hernieuwbare energiebronnen is echter hun periodieke werking. Dit is de aanleiding tot grote inspanningen in de zoektocht naar goede technologieën voor energieopslag. Een mogelijke manier is om het overschot aan hernieuwbare energie te gebruiken om de CO_2 te dissociëren in CO en $\frac{1}{2}O_2$. Het CO kan dan worden gecombineerd met H_2 om koolwaterstoffen te synthetiseren in het Fischer-Tropsch-proces.

Een interessante piste om dit overschot aan hernieuwbare energie om te zetten, is plasmatechnologie, aangezien plasmas eenvoudig elektrische energie kunnen omzetten in chemische energie. Het groot thermodynamisch onevenwicht tussen de elektronentemperatuur en de gastemperatuur in het plasma zorgt ervoor dat endothermische reacties kunnen plaatsvinden, zonder dat het gas eerst volledig opgewarmd moet worden, waardoor de totale energiekost drastisch verlaagd wordt t.o.v bij thermische processen. Bovendien wordt een significante hoeveelheid van de energie overgedragen aan de vibrationele niveau's van CO_2. Deze vibrationele energie kan dan verder worden overgedragen aan hoger-gelegen vibrationele niveaus, tot de bindingsenergie bereikt wordt en dus dissociatie plaatsvindt. Hoewel dit een veelbelovend pad naar dissociatie is, wordt het gelimiteerd door een stijging in de gastemperatuur. Bij hoge gastemperatuur wordt thermische dissociatie namelijk belangrijker ten koste van vibrationeel-geinduceerde. Om het

gebruik van plasma-gebaseerde CO_2 conversie als industriële toepassing eenvoudiger te maken, is meer inzicht nodig in het effect van vibrationeel-geinduceerde en thermische dissociatie op de CO_2 conversie en energie-efficiëntie, en hoe beiden verhoogd kunnen worden. Deze thesis hanteert een chemisch kinetisch model om de onderliggende chemie te onthullen, om meer inzicht te krijgen in hoe de efficiëntie van het dissociatieproces kan verbeterd worden.

Hoofdstuk 1 behandelt kort de problematiek rond de opwarming van de aarde, de verschillende technieken die bestaan voor energie-opslag, en de verschillende plasmareactoren die aangewend worden voor CO_2 dissociatie, alsook de maximale conversie en energie-efficiëntie die ermee bereikt werden. Hoofdstuk 2 bevat de theorie die aan de basis ligt van het 0D model. De chemieset en schalingswetten, nodig om de reacties voor verschillende vibrationele niveaus te schalen, worden besproken in hoofdstuk 3.

In hoofdstuk 4 wordt het effect van supersonische gasstroom op de energie-efficiëntie en CO_2 conversie bestudeerd, door een gasstroom- en plasma-chemisch kinetisch model van een microgolf CO_2 plasma te combineren in een Laval straalbuis opstelling. Deze studie behandelt de effecten van het stroomveld op verschillende dissociatie en recombinatie mechanismen, op de vibrationele verdeling, en op de vibrationele transfer-mechanismen. Ook het effect van experimentele parameters, zoals de positie van het vermogen, de uitlaat-druk en de specifieke energie-input op de CO_2 conversie en energie-efficiëntie worden bestudeerd. De grootste obstakels in het bereiken van hoge energie-efficiënties zijn de korte verblijftijd van het gas in het plasma, de schokgolf en de maximale kritische warmte, en dus energie, die kunnen toegevoegd worden aan de gasstroom, zonder thermisch verstikken.

Hoofdstuk 5 bespreekt hoe een gepulst plasma het VT onevenwicht kan verbeteren, resulterend in een hogere conversie en energie-efficiëntie. Wanneer de plasma pulstijd en de interpuls tijd correct op elkaar worden afgestemd, kunnen hogere energie-efficiënties bekomen worden. De ideale plasma pulstijd correspondeert daarbij met de tijd nodig om de hoogste vibrationele temperatuur te bereiken. De hoogste energie-efficiënties worden bereikt met lange interpulstijden, namelijk ≥ 0.1 s, waarbij de gastemperatuur volledig terug tot kamertemperatuur kan dalen. Bovendien kunnen door bijkomstig koelen van de reactorwanden al hogere energie-efficiënties bekomen worden wanneer korte interpulstijden gebruikt worden. In dit hoofdstuk wordt ook aangetoond dat pulsen nadelig is voor elektron-impact-dissociatie. Een gepulst plasma kan de efficiëntie niet verhogen bij lage ionizatie-graden of hoge gereduceerde elektrische velden, waar dit process het meest dominante dissociatiemechanisme is. Een gepulst plasma heeft ook geen verhoging van de efficiëntie tot gevolg als de vibrationele temperatuur zijn maximum bereikt naar het einde van het plasma toe.

Tenslotte behandelt hoofdstuk 6 het effect van koelen/*quenchen* gedurende en na het plasma voor warme en koude plasma's (d.w.z. respectievelijk met lage en hoge externe koeling), bij verschillende SEIs. Voor warme plasmas met een lage specifieke energie input (SEI $\sim$ 0.5 eV/molec.), is het best om te *quenchen* aan het plasma einde, terwijl het voor plasmas met een hoge specifieke energie input (SEI $\sim$ 4 eV/molec.) best is om te *quenchen* zodra de maximale conversie bereikt wordt. Voor plasmas met een lage SEI kan *quenchen* zelfs de conversie verhogen tot boven het niveau van dissociatie in het plasma, gekend als super-ideaal *quenchen*. Om de effecten van *quenchen* bij verschillende plasma condities beter te begrijpen, bestuderen we de dissociatie en recombinatie reactiesnelheden, net als de VDF (vibrationele distributie functie) van CO_2, CO, and O_2. Als op het moment van *quenchen* een groot VT onevenwicht bestaat, zullen zowel de dissocatie als de recombinatie reactiesnelheden verhogen. Afhankelijk van de graad van conversie op het moment van *quenchen*, kan dit zowel een stijging als een daling van de CO_2 conversioe tot gevolg hebben. Desalniettemin geldt algemeen, en vooral voor warme plasmas bij hoge temperaturen, dat *quenchen* na het plasma recombinatiereacties verhindert en dus de finale CO_2 conversie verhoogt. We hebben ook het effect van verschillende afkoelsnelheden op de CO_2 conversie en de energie-efficiëntie bestudeerd. Tenslotte hebben we de plasma-gebaseerde conversie vergeleken met puur thermische conversies, en gezien dat de conversie voor warme plasmas, met typische temperaturen hoger dan 2500 K, voornamelijk termisch verloopt.

Samengevat geven de resultaten in deze thesis een beter inzicht in de onderliggende mechanismen van plasma-gebaseerde CO_2 conversie. Er worden suggesties gegeven in hoe de CO_2 conversie en energie-efficiëntie verhoogd kunnen worden voor koude tot warme plasmas. Deze inzichten zijn waardevol voor toekomstig experimenteel onderzoek.

General conclusions and future outlook

In this thesis, we used a 0D modeling to investigate how the energy efficiency of CO_2 conversion can be improved in vibrationally active non-equilibrium plasmas varying from cold to warm plasma conditions. In cold plasma conditions, vibrational-induced dissociation is maximally effective. With increasing gas temperature, the effect of vibrational-induced dissociation diminishes due to a more prominent VT relaxation. This can already occur at gas temperatures between 1000-2000 K. These temperatures are also too low for thermal dissociation. At temperatures above 2000 K, thermal dissociation becomes more important, and vibrational-induced dissociation hardly plays any role.

Both in chapter 4 and 6 the effect of cold plasma conditions on the CO_2 conversion was examined. In the first, low SEI plasmas were applied to a supersonic flow gas. This low SEI requirement was necessary to avoid thermal choking of the gas. However, due to the low SEI, the residence time was too short to allow for significant vibrational-induced dissociation. With maximum energy efficiency predicted of about 30%, the model was unable to reproduce the high energy efficiencies reported by Asisov et al.[36]. However, these values have since not been reproduced. In chapter 6, the effect of cold plasma conditions, accompanied with quenching was examined for higher SEI plasma that were subjected to a high initial wall cooling. These conditions did not yield high CO_2 conversions and energy efficiencies that were reached for warm plasma conditions. The values could also not be increased by quenching.

In chapter 5, we demonstrated how pulsing can increase the energy efficiency of CO_2 conversion for plasmas with gas temperatures too high for vibrational-induced dissociation, but not high enough for thermal dissociation. When tuning the plasma pulse time to match the time at which the vibrational temperature would reach a maximum value, and allowing enough time between pulses to fully reduce the gas temperature to room temperature, a significant increase in VT non-equilibrium, and therefore also vibrational-induced dissociation, could be

realized. However, the efficiencies reached in this work are again much lower than the thermal efficiencies.

While the results for cold and intermediate temperature (i.e. $\leq$ 2000 K) plasmas give valuable suggestions into how the efficiency can be increased, those efficiencies are inferior to the ones that were reported for warm plasmas with high SEI in chapter 6. By reducing the wall cooling, high temperatures of 2500-7000 K can be reached, at which thermal dissociation becomes important. At those temperatures, high conversion degrees in excess of 80 % were shown for SEIs of 4 and 5 eV/molec. However, it was also shown that quenching the reaction products was crucial to maintaining the high thermal conversion degrees. With quenching, efficiencies up to 58% can be reached for plasmas with an SEI of 4 eV/molec.

The model results shown in this thesis provide interesting insight for future experimental and theoretical investigation. The results are however dependent on the reliability of the cross sections, reaction rate coefficients, and used scaling laws. Indeed, the CO_2 chemistry sets used in this thesis consist out of more than 2000 reactions. The uncertainty on these reactions negatively affects the uncertainty on the model results. In general, the model would greatly benefit from additional experimental verification of these rate coefficients, with particular attention for the reactions to which scaling laws are applied.

In addition, the model would also benefit from research into the improvement of the applied scaling theories. This is especially important for VV and VT relaxation rate coefficients where the scaling of the coefficients through more complex semi-classical and quantum models should be further investigated. This would make the rate coefficients more reliable for higher temperatures and vibrational levels.

One of the major approximations of studying the plasma chemistry with a 0D model is that no transport phenomena are included. While multi-dimensional CO_2 plasma models are already used for GAP[72] and APGD[87] plasmas, more research is needed to develop such models for MW plasmas and DBDs. These models can give more information about spatial distribution of the plasma and its parameters, as well as the residence time. In addition, the effect of flow on the plasma should be studied, which would be of particular interest in complex or supersonic flows.

List of publications and conference contributions

List of publications

- I. Belov, V. Vermeiren, S. Paulussen, and A. Bogaerts. Carbon Dioxide Dissociation in a Microwave Plasma Reactor Operating in a Wide Pressure Range and Different Gas Inlet Configurations. *J. CO_2 Util.*, 24:386–397, 2018. DOI: 10.1016/j.jcou.2017.12.009

- V. Vermeiren and A. Bogaerts. Supersonic Microwave Plasma: Potential and Limitations for Energy-Efficient CO_2 Conversion. *J. Phys. Chem. C*, 122(45):25869–25881, 2018. DOI: 10.1021/acs.jpcc.8b08498

- V. Vermeiren and A. Bogaerts. Improving the Energy Efficiency of CO_2 Conversion in Nonequilibrium Plasmas through Pulsing. *J. Phys. Chem. C*, 123(29):17650–17665, 2019. DOI: 10.1021/acs.jpcc.9b02362

- S. Van Alphen, V. Vermeiren, T. Butterworth, et al. Power Pulsing To Maximize Vibrational Excitation Efficiency in N_2 Microwave Plasma: A Combined Experimental and Computational Study. *J. Phys. Chem. C*, 124(3):1765–1779, 2020. DOI: 10.1021/acs.jpcc.9b06053

- V. Vermeiren and A. Bogaerts. Plasma-Based CO_2 Conversion: To Quench or Not to Quench? *J. Phys. Chem. C*, 124(34):18401–18415, 2020. DOI: 10.1021/acs.jpcc.0c04257

List of conference contributions

- V. Vermeiren and A. Bogaerts, A computational study of the plasma-flow interplay in a reverse vortex microwave discharge for CO_2 conversion , 69^{th}

Annual Gaseous Electronics Conference, October 10-14, 2016, Bochum, Germany: Poster presentation.

- V. Vermeiren and A. Bogaerts, A computational chemical kinetics study of a supersonic microwave plasma for CO_2 dissociation, 33^{th} International Conference on Phenomena in Ionized Gases, July 9-14, 2017, Estoril, Portugal: Oral presentation.

APPENDIX A

Chemistry sets

A.1 Chemistry set 1

The chemistry set in this section is used in Chapter 4.

Table A.1: Electron impact reactions calculated with cross section data, using the calculated EEDF, as explained in section 2.4, as well as the references where the data are adopted from.

No.	Reaction	Ref	Note*
(X1)[a]	$e^- + CO_2 \rightarrow 2e^- + CO_2^+$	164	
(X2)[b]	$e^- + CO_2 \rightarrow 2e^- + O + CO^+$	164	
(X3)[b]	$e^- + CO_2 \rightarrow O^- + CO$	164	
(X4)[b]	$e^- + CO_2 \rightarrow e^- + O + CO$	164	
(X5)[a]	$e^- + CO_2 \rightarrow e^- + CO_2[e_1]$	164	
(X6)[c]	$e^- + CO_2 \leftrightarrow e^- + CO[v_i]$	164	i=a,b,c,d
(X7)[c]	$e^- + CO_2[v_i] \leftrightarrow e^- + CO_2[v_j]$	164	i=0:5,j=(i+1):21
(X8)[b]	$e^- + CO \rightarrow 2e^- + CO^+$	165	
(X9)[b]	$e^- + CO \rightarrow C + O^-$	166	
(X9bis)[b]	$e^- + CO \rightarrow e^- + C + O$	121	
(X10)[a]	$e^- + CO \rightarrow e^- + CO[e_x]$	121	x=1-4
(X11)[c]	$e^- + CO \rightarrow e^- + CO[v_i]$	121	i=1-10
(X12)[b]	$e^- + O_2 \rightarrow e^- + O + O$	167	
(X12M)[a]	$e^- + O_2 + M \rightarrow e^- + O_2^- + M$	167	
(X13)[b]	$e^- + O_2 \rightarrow O + O^-$	167	
(X14)[c]	$e^- + O_2 \leftrightarrow e^- + O_2[v_i]$	167	i=1,2,3
(X15)[a]	$e^- + O_2 \leftrightarrow e^- + O_2[e_x]$	167	x=1,2

a) Same cross section also used for v_i (i = the various vibrationally excited levels)
b) Cross section also used for v_i, modified by lowering the energy threshold by the energy of the excited state of v_i
c) Cross section for the various levels (i,j) scaled and shifted using Fridman's approximation from the $(0 \rightarrow 1)$ cross-section
* v_0 is ground state

Table A.2: Electron impact reactions using analytical expressions for the rate coefficients, given in m^3/s and m^6/s, for two-body and three-body reactions, respectively, as well as the references where the data are adopted from. T_g and T_e are given in K and eV, respectively.

No.	Reaction	Rate coefficient	Reference
(E1a)	$e^- + CO_2^+ \rightarrow CO(v_1) + O$	$1 \times 10^{-11} T_e^{-0.5} T_g^{-1}$	168;169
(E1b)	$e^- + CO_2^+ \rightarrow C + O_2$	$1 \times 10^{-11} T_e^{-0.5} T_g^{-1}$	170
(E2)[a]	$e^- + CO_4^+ \rightarrow CO_2 + O_2$	$1.61 \times 10^{-13} T_e^{-0.5}$	170
(E3)	$e^- + CO^+ \rightarrow C + O$	$3.46 \times 10^{-14} T_e^{-0.48}$	171;172
(E4)[a]	$e^- + O + M \rightarrow O^- + M$	1×10^{-43}	169

[a] The primary source was not accessible

Table A.3: Ion-ion and ion-neutral reactions, as well as the references where the data are adopted from. The rate coefficients are given in m^3/s and m^6/s, for two-body and three-body reactions, respectively. T_g is given in K.

No.	Reaction	Rate coefficient	Reference
(I1)	$CO_2 + CO^+ \rightarrow CO_2^+ + CO$	1.0×10^{-15}	173;174
(I2a)[b]	$CO_2 + O^- + CO_2 \rightarrow CO_3^- + CO_2$	1.5×10^{-40}	173;175
(I2b)[b]	$CO_2 + O^- + CO \rightarrow CO_3^- + CO$	1.5×10^{-40}	173;175
(I2c)	$CO_2 + O^- + O_2 \rightarrow CO_3^- + O_2$	3.1×10^{-40}	173;175
(I3)	$CO_2 + O_2^- + M \rightarrow CO_4^- + M$	4.7×10^{-41}	173;175
(I4)	$CO + O^- \rightarrow CO_2 + e$	5.5×10^{-16}	173;176
(I5)	$CO + CO_3^- \rightarrow 2CO_2 + e$	5×10^{-19}	177
(I6)[a]	$CO_3^- + CO_2^+ \rightarrow 2CO_2 v_b + O$	5×10^{-13}	169
(I7)[a]	$CO_4^- + CO_2^+ \rightarrow 2CO_2 v_b + O_2$	5×10^{-13}	169
(I8)[a]	$O_2^- + CO_2^+ \rightarrow CO_2 v_1 + O_2 + O$	6×10^{-13}	169
(I9)	$CO_3^- + O \rightarrow CO_2 + O_2^-$	8×10^{-17}	178
(I10a)[a]	$CO_4^- + O \rightarrow CO_3^- + O_2$	1.12×10^{-16}	173
(I10b)[a]	$CO_4^- + O \rightarrow CO_2 + O_2 + O^-$	1.4×10^{-17}	173
(I11)	$O + O^- \rightarrow O_2 + e$	2.3×10^{-16}	179
(I12)[a]	$O + O_2^- \rightarrow O_2 + O^-$	1.5×10^{-16}	173
(I13)	$O_2^- + M \rightarrow O_2 + M + e$	$2.7 \times 10^{-16}(\frac{T_g}{300})^{0.5} exp(-5590/T_g)$	180;181
(I14)[c]	$O^- + M \rightarrow O + M + e$	$2.3 \times 10^{-15} exp(-26000/T_g)$	181–183

[a] The primary source was not accessible

[b] The rate coefficient of $CO_2 + O^- + He \rightarrow CO_3^- + He$ was used, due to the lack of further information.

[c] For usual values of gas temperature, i.e. $T_g \ll 26000$ K, the rate coefficient is very low, as pointed out by Gudmundsson[184].

Table A.4: Neutral-neutral reactions, as well as the references where the data are adopted from. The rate coefficients are given in m^3/s and m^6/s, for two-body and three-body reactions, respectively. T_g is given in K. The α parameter determines the effectiveness of lowering the activation energy for reactions involving vibrationally excited levels of the molecules (see details in section 3.4.3 and ref 37).

No.	Reaction	Rate coefficient	α	References
(N1)	$CO_2 + M \rightarrow CO + O + M$	$6.06 \times 10^{-16} exp(-52525/T_g)$	0.82	185
(N2)	$CO_2 + O \rightarrow CO + O_2$	$2.8 \times 10^{-17} exp(-16400/T_g)$	0.57	186
(N3)	$CO_2 + C \rightarrow 2CO$	$< 10^{-21}$	n.a.	187
(N4)[a]	$CO + O + M \rightarrow CO_2 + M$	$8.3 \times 10^{-46} exp(-1510/T_g)$	0.0	188;189
(N5)	$O_2 + CO \rightarrow CO_2 + O$	$4.2 \times 10^{-18} exp(-24000/T_g)$	0.5	189
(N6)	$O_2 + C \rightarrow CO + O$	$1.99 \times 10^{-16} exp(-2010/T_g)$	0.0	190
(N7)	$O + C + M \rightarrow CO + M$	$2.14 \times 10^{-41} (\frac{T_g}{300})^{-3.08} exp(-2144/T_g)$	n.a.	189;191
(N8)	$O + O + M \rightarrow O_2 + M$	$5.2 \times 10^{-47} exp(900/T_g)$	n.a.	189;191
(N9)	$O_2 + M \rightarrow O + O + M$	$3.0 \times 10^{-12} \frac{1}{T_g} exp(-59380/T_g)$	0.0	189;191

[a] Multiply by 7, 3 or 12 for M= CO_2, CO or O_2 respectively.

Table A.5: Neutral reactions between vibrationally excited molecules, as well as the references where the data are adopted from. The rate coefficients are given in m^3/s and m^6/s, for two-body and three-body reactions, respectively. T_g is given in K.

No.	Reaction	Rate coefficient	References
(V1)	$CO_2 v_a + M \rightarrow CO_2 + M$	$7.14 \times 10^{-14}\, exp(-177\, T_g^{-1/3} + 451\, T_g^{-2/3})$	117;192;193
(V2a)	$CO_2 v_1 + M \rightarrow CO_2 v_a + M$	$4.25 \times 10^{-7}\, exp(-407\, T_g^{-1/3} + 824\, T_g^{-2/3})$	117;194;195
(V2b)	$CO_2 v_1 + M \rightarrow CO_2 v_b + M$	$8.57 \times 10^{-7}\, exp(-404\, T_g^{-1/3} + 1096\, T_g^{-2/3})$	117;194;195
(V2c)	$CO_2 v_1 + M \rightarrow CO_2 v_c + M$	$1.43 \times 10^{-7}\, exp(-252\, T_g^{-1/3} + 685\, T_g^{-2/3})$	117;194;195
(V3)	$CO v_1 + M \rightarrow CO + M$	$1.0 \times 10^{-18}\, T_g\, exp(-150.7\, T_g^{-1/3})$	196
(V4)	$O_2 v_1 + M \rightarrow O_2 + M$	$1.3 \times 10^{-14}\, exp(-158.7\, T_g^{-1/3})$	117;193
(V5)	$CO_2 v_1 + CO_2 \rightarrow CO_2 v_a + CO_2 v_b$	$1.06 \times 10^{-11}\, exp(-242\, T_g^{-1/3} + 633\, T_g^{-2/3})$	117;194;195
(V6)	$CO_2 v_1 + CO_2 \rightarrow CO_2 + CO_2 v_1$	$1.32 \times 10^{-16}\, (\frac{T_g}{300})^{0.5}\, \frac{250}{T_g}$	197;198
(V7)	$CO v_1 + CO \rightarrow CO + CO v_1$	$3.4 \times 10^{-16} (\frac{T_g}{300})^{0.5}\, (1.64 \times 10^{-6}\, T_g + \frac{1.61}{T_g})$	199;200
(V8)	$CO_2 v_1 + CO \rightarrow CO_2 + CO v_1$	$4.8 \times 10^{-12}\, exp(-153\, T_g^{-1/3})$	117;194

A.2 Changes to the chemistry set 1

In this chemistry set, the cross section set was updated based on more recent available literature (see table A.6). Also, in order to have the thermodynamic equilibrium CO_2 conversion, calculated by the model, match more closely with

the values of equilibrium thermal dissociation, the two neutral reactions were changed (see table A.7). These changes apply to the results in chapter 5 and 6.

Table A.6: Updated electron impact reactions calculated with cross sections, using the calculated EEDF, as explained in section 2.4, as well as the references where the data are adopted from. These cross sections are used in chapter 5 and 6.

No.	Reaction	Ref	Note*
(X1)[a]	$e^- + CO_2 \rightarrow 2e^- + CO_2^+$	99	
(X2)[b]	$e^- + CO_2 \rightarrow 2e^- + O + CO^+$	99	
(X3)[b]	$e^- + CO_2 \rightarrow O^- + CO$	99	
(X4)[b]	$e^- + CO_2 \rightarrow e^- + O + CO$	99	
(X5)[a]	$e^- + CO_2 \rightarrow e^- + CO_2[e_1]$	99	
(X6)[c]	$e^- + CO_2 \leftrightarrow e^- + CO_2[v_i]$	164	i=a,b,c,d
(X7)[c]	$e^- + CO_2[v_i] \leftrightarrow e^- + CO_2[v_j]$	164	i=0:20,j=(i+1):21
(X8)[b]	$e^- + CO \rightarrow 2e^- + CO^+$	201	
(X9)[b]	$e^- + CO \rightarrow C + O^-$	201	
(X9bis)[b]	$e^- + CO \rightarrow e^- + C + O$	201	
(X10)[a]	$e^- + CO \rightarrow e^- + CO[e_x]$	121	x=1-6
(X11)[c]	$e^- + CO[v_i] \leftrightarrow e^- + CO[v_j]$	121	i=0:9;j=(i+1):10
(X12)[b]	$e^- + O_2 \rightarrow e^- + O + O$	122	
(X12M)[a]	$e^- + O_2 + M \rightarrow e^- + O_2^- + M$	167	
(X13)[b]	$e^- + O_2 \rightarrow O + O^-$	122	
(X14)[c]	$e^- + O_2[v_i] \leftrightarrow e^- + O_2[v_j]$	122	i=0:3;j=(i+1):4
(X15)[a]	$e^- + O_2 \leftrightarrow e^- + O_2[e_x]$	122	x=1-5

a) Same cross section also used for v_i (i = the various vibrationally excited levels)
b) Cross section also used for v_i, modified by lowering the energy threshold by the energy of the excited state of v_i
c) Cross section for the various levels (i,j) scaled and shifted using Fridman's approximation from the $(0 \rightarrow 1)$ cross-section
* v_0 is ground state

Table A.7: Updated neutral-neutral reactions, as well as the references where the data are adopted from. The rate coefficients are given in m^3/s . T_g is given in K. The α parameter determines the effectiveness of lowering the activation energy for reactions involving vibrationally excited levels of the molecules (see details in 37;103). These rate coefficients are used in chapter 5 and 6.

No.	Reaction	Rate coefficient	α	References
(N2)	$CO_2 + O \rightarrow CO + O_2$	$7.95 \times 10^{-18} exp(-18161/T_g)$	0.57	202
(N5)	$O_2 + CO \rightarrow CO_2 + O$	$3.99 \times 10^{-20} exp(-15275/T_g)$	0.5	203

A.3 Changes to the chemistry set 2

In Chapter 6, more vibrational levels of CO and O_2 were added, as well as the O_2^+ ion. The following reactions are therefore changed/added:

Table A.8: Updated/added electron impact reactions calculated with cross sections, using the calculated electron energy distribution function (EEDF), as explained in section 2.4, as well as the references where the data are adopted from. These cross sections are used in chapter 6.

No.	Reaction	Ref	Note*
(X11)[a]	$e^- + CO[v_i] \leftrightarrow e^- + CO[v_j]$	121	i=0:4;j=(i+1):50
(X11b)[a]	$e^- + CO[v_i] \leftrightarrow e^- + CO[v_j]$	121	i=5:49;j=i+1
(X14)[a]	$e^- + O_2[v_i] \leftrightarrow e^- + O_2[v_j]$	122	i=0:5;j=(i+1):33
(X14b)[a]	$e^- + O_2[v_i] \leftrightarrow e^- + O_2[v_j]$	122	i=6:32;j=i+1
(X16)[b]	$e^- + O_2 \rightarrow 2e^- + O_2^+$	122	

a) Cross section for the various levels (i,j) scaled and shifted using Fridman's approximation from the $(0 \rightarrow 1)$ cross-section
b) Cross section also used for $CO_2 v_i$, modified by lowering the energy threshold by the energy of the excited state of $CO_2 v_i$
* v_0 is ground state

Table A.9: Added electron impact reactions using analytical expressions for the rate coefficients, given in m^3/s and m^6/s, for two-body and three-body reactions, respectively, as well as the references where the data are adopted from. T_g and T_e are given in K and eV, respectively. These rate coefficients are used in chapter 6.

No.	Reaction	Rate coefficient	Reference
(E5)	$e^- + O_2^+ + M \rightarrow O_2 + M$	1×10^{-38}	204
(E6)	$e^- + O_2^+ \rightarrow O + O$	$6.46 \times 10^{-11} T_e^{-0.5} T_g^{-0.5}$	67

Table A.10: Added ion-ion and ion-neutral reactions, as well as the references where the data are adopted from. The rate coefficients are given in m^3/s and m^6/s, for two-body and three-body reactions, respectively. T_g is given in K. These rate coefficients are used in chapter 6.

No.	Reaction	Rate coefficient	Reference
(I15)	$O_2^+ + CO_2 + M \rightarrow CO_4^+ + M$	2.3×10^{-41}	170
(I16)	$O_2^+ + C \rightarrow CO^+ + O$	5.2×10^{-17}	205
(I17)	$CO_2^+ + O \rightarrow CO + O_2^+$	1.6×10^{-16}	205
(I18)	$CO_2^+ + O_2 \rightarrow CO_2 + O_2^+$	5.3×10^{-17}	205
(I19)	$CO^+ + O_2 \rightarrow CO + O_2^+$	1.2×10^{-16}	205
(I20)	$O_2^+ + CO_3^- \rightarrow CO_2 + O_2 + O$	3.0×10^{-13}	204
(I21)	$O_2^+ + CO_4^- \rightarrow CO_2 + O_2 + O_2$	3.0×10^{-13}	204
(I22)	$O_2^- + O_2^+ \rightarrow O_2 + O_2$	2.0×10^{-13}	206
(I23)	$O_2^- + O_2^+ \rightarrow O_2 + O + O$	4.2×10^{-13}	204
(I24)	$O_2^- + O_2^+ + M \rightarrow O_2 + O_2 + M$	2.0×10^{-37}	67
(I25)	$O_2^+ + O^- \rightarrow O_2 + O$	1.0×10^{-13}	204
(I26)	$O_2^+ + O^- \rightarrow O + O + O$	2.6×10^{-14}	206

Table A.11: Added neutral reactions between vibrationally excited molecules, as well as the references where the data are adopted from. The rate coefficients are given in m^3/s and m^6/s, for two-body and three-body reactions, respectively. T_g is given in K. These rate coefficients are used in chapter 6.

No.	Reaction	Rate coefficient	References
(V9)	$O_2[v_1] + O_2 \rightarrow O_2 + O_2[v_1]$	$0.9 \times 10^{-20}(\frac{T_g}{300})^{1.5}$	196
(V10)	$CO[v_1] + O_2 \rightarrow CO + O_2[v_1]$	$1.06 \times 10^{-12}\, exp(-306\, T_g^{-1/3} + 1226\, T_g^{-2/3})$	117

APPENDIX B

Supersonic microwave plasmas

B.1 Flow results for an inlet pressure of 4 bar

Figure B.1 shows the flow results at a higher inlet pressure than presented in chapter 4, namely 4 bar, and an outlet pressure of 1 bar. The results show the formation of a third distinct region (III), called the shock train, that forms between the supersonic and the mixing region. The shock train is characterized by a sequence of shocks separating subsonic from supersonic regions[151]. After each shock, the flow accelerates again to supersonic velocities, after which it is decelerated by the following shock. The region is characterized by pressure and temperature oscillations.

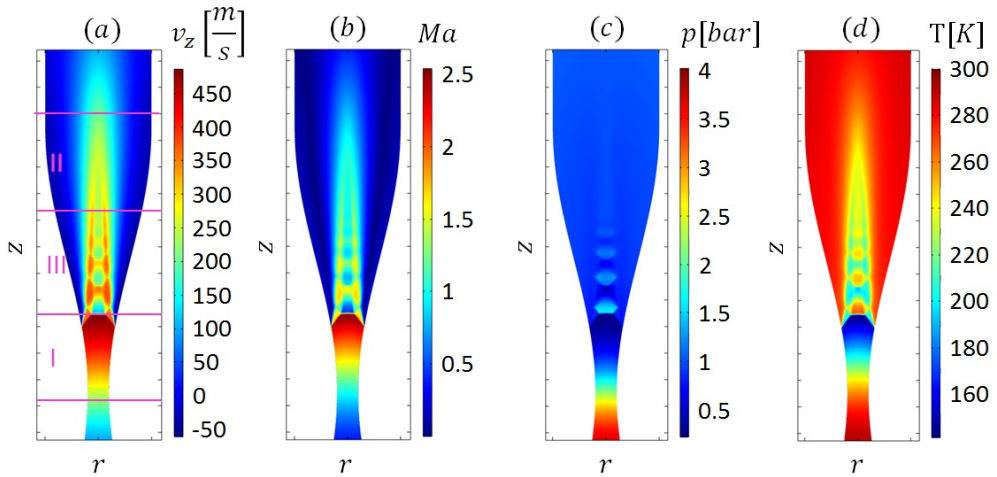

Figure B.1: (a) Axial velocity magnitude, (b) Mach number, (c) static pressure and (d) static temperature in the case of $r_1 = 0.4$ cm, $r_2 = 2$ cm, $z_1 = 10$ cm, $p_{in} = 4$ bar, $p_{out} = 1$ bar.

B.2 Vibrational energy transfer

In figure 4.6, it was shown that in the beginning of the plasma, VV relaxation transports energy from the higher vibrational levels to lower vibrational levels in a ladder downclimbing process. The explanation for this lies in the fact that CO_2(V2) receives more energy from the electrons than CO_2(V1). This can be seen in figure B.2, where the rate of electron energy loss to the lowest vibrational levels upon excitation from ground state CO_2 is shown. Next to the fact that more electron energy goes to the second level of the asymmetric vibrational mode instead of the first level, the density of the latter can be further depleted by electron impact vibrational excitation from that level to the higher vibrational levels.

The VV energy transfer reacts to this non-equilibrium between the first and the second vibrational level. In figure B.3, it can be seen that the first vibrational level is strongly populated by VV relaxation.

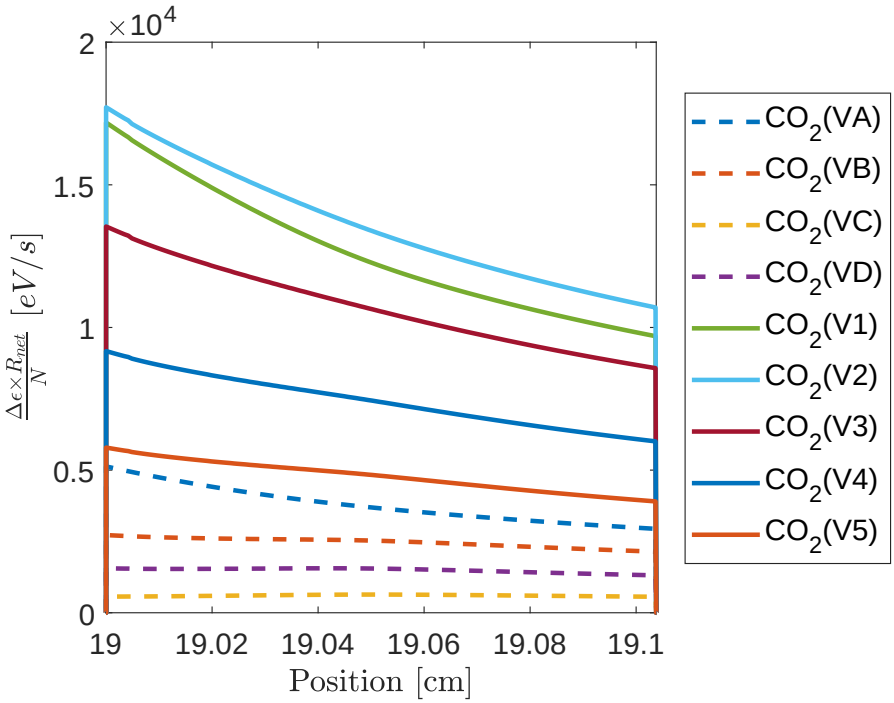

Figure B.2: Electron energy loss to the different vibrational levels from ground state CO_2 inside the plasma, which ranges from z=19 to z=19.1 cm (cf. Figure 4.6), with SEI = 0.2 eV/molec. The other conditions are: $r_1 = 0.4$ cm, $r_2 = 2$ cm, $z_1 = 10$ cm, $p_{in} = 2$ bar, $p_{out} = 1$ bar

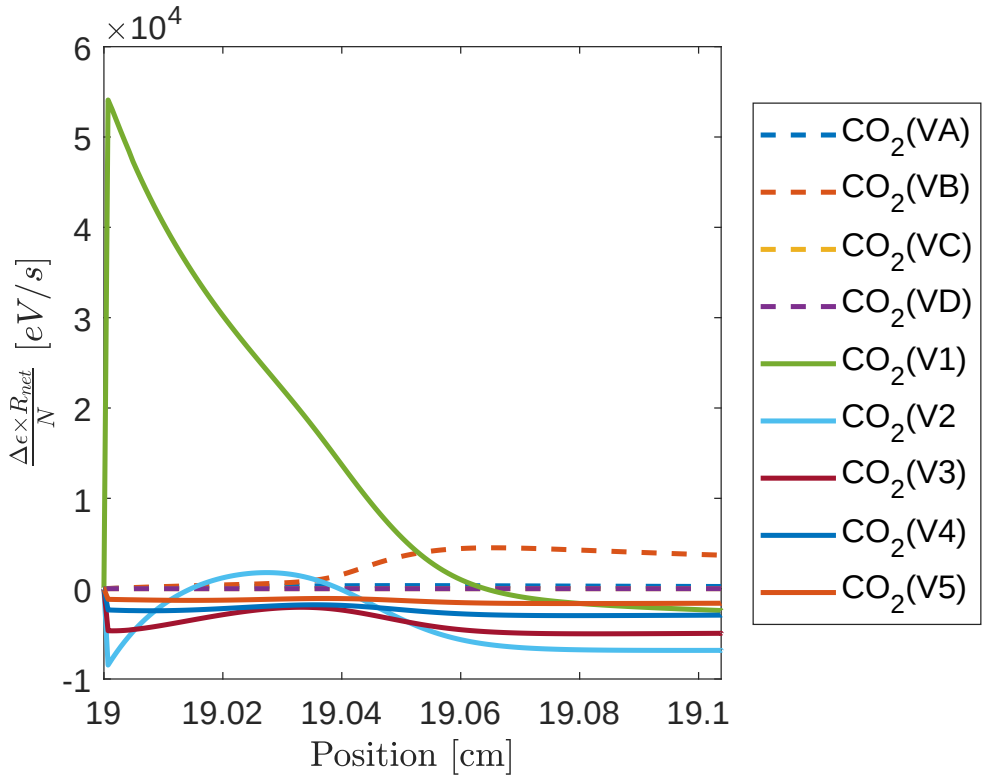

Figure B.3: Energy transfer to the different levels in VV relaxation from the other levels, inside the plasma, ranging from z=19 to z=19.1 cm, with SEI = 0.2 eV/molec. The other conditions are: $r_1 = 0.4$ cm, $r_2 = 2$ cm, $z_1 = 10$ cm, $p_{in} = 2$ bar, $p_{out} = 1$ bar.

B.3 Effect of the power on the energy efficiency

In figure B.4 we show the energy efficiency and conversion as a function of the plasma position in the reactor, at three different SEI values, namely 0.05, 0.1, 0.15, and 0.2 eV/molec. The energy efficiency shows the same trend in the four different cases.

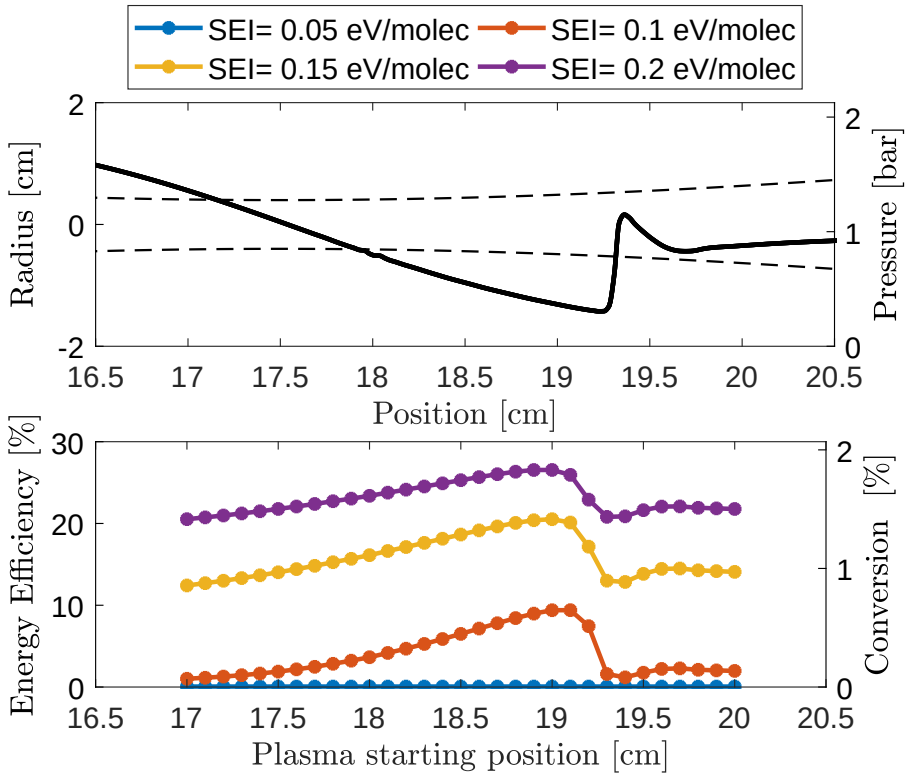

Figure B.4: Conversion and energy efficiency (bottom panel) as a function of plasma position in the reactor, for four different SEI values. The other conditions are: $r_1 = 0.4$ cm, $r_2 = 2$ cm, $z_1 = 10$ cm, $p_{in} = 4$ bar, $p_{out} = 1$ bar. The radius of the reactor (dashed line) and pressure (full line) are plotted in the top panel.

B.4 Flow results for different inlet pressures

Figure B.5 shows the evolution of the Mach number (top panel), pressure (middle panel) and temperature (bottom panel) for different inlet pressures, and an outlet pressure of 1 bar. With increasing inlet pressure, the maximum Mach number increases, and the minimum temperature decreases. In addition, the pressure minimum in the supersonic region decreases when the inlet pressure rises from 1.2 bar to 2 bar. A further increase of the inlet pressure does not change the minimum pressure, since the total pressure increases as well, requiring a higher Mach number to reach the same pressure in the supersonic region. The position of the pressure minimum, however, shifts a bit to later in the supersonic reactor.

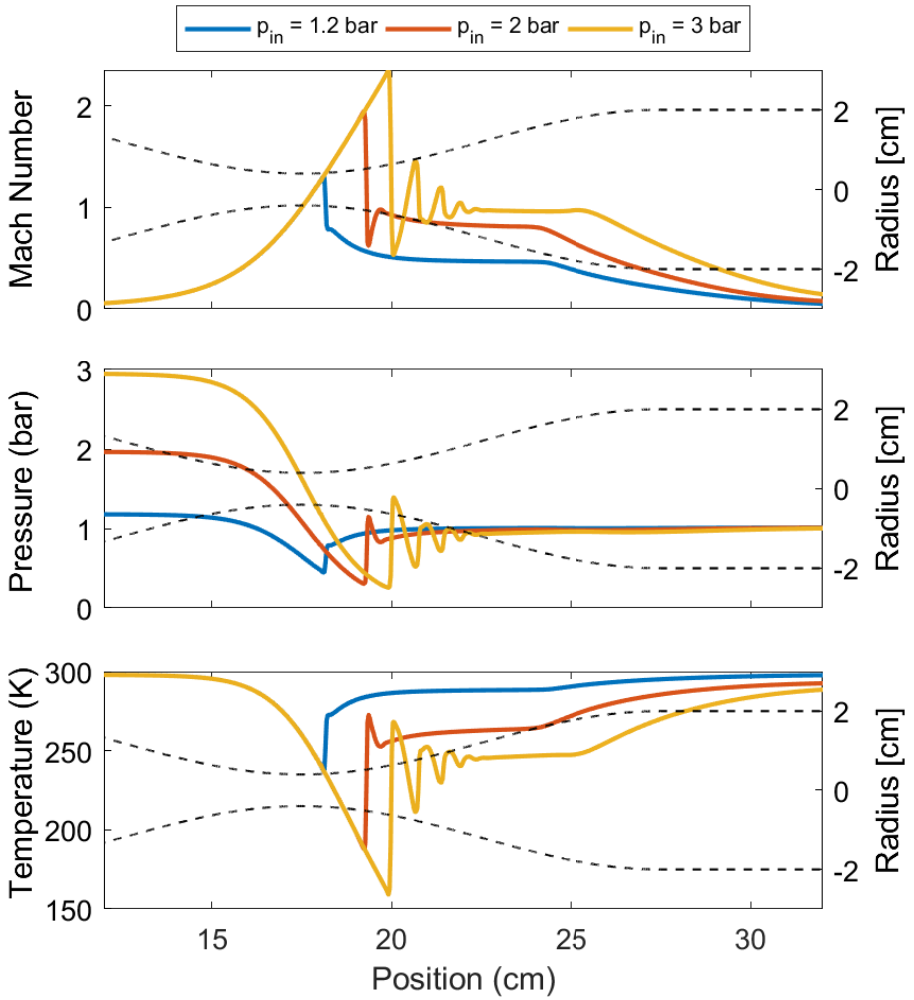

Figure B.5: Mach number (top panel), pressure (middle panel) and temperature (bottom panel) as a function of position for different inlet pressures. The radius of the geometry is given in dashed lines.

B.5 Flow results for different outlet pressures

Figure B.6 shows the evolution of the Mach number (top panel), pressure (middle panel) and temperature (bottom panel) for different outlet pressures, at an inlet pressure of 2 bar. A lower outlet pressure increases the Mach number, decreases the pressure, and decreases the temperature in the supersonic region. This makes the outlet pressure one of the main parameters to compensate for the decrease in Mach number, increase in temperature, and increase in pressure upon heat addition of the plasma.

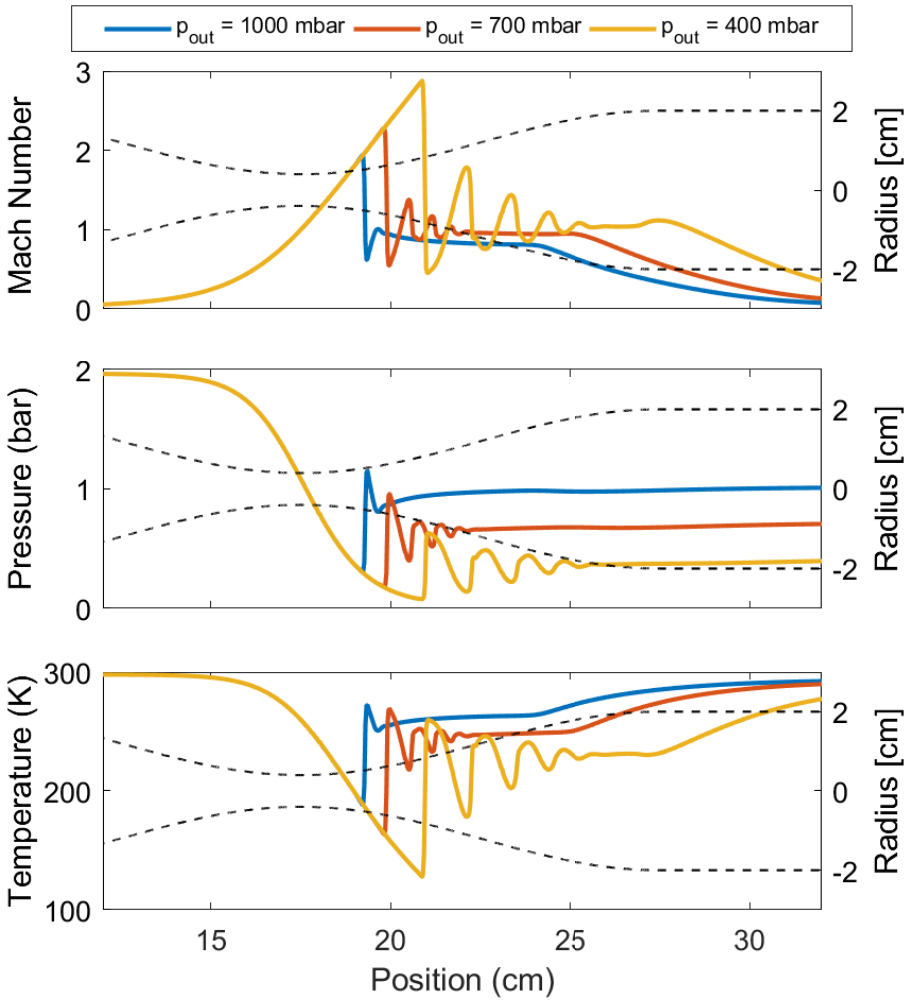

Figure B.6: Mach number (top panel), pressure (middle panel) and temperature (bottom panel) as a function of position for different outlet pressures. The radius of the geometry is given in dashed lines.

B.6 Flow results for different geometries

Figure B.7 shows the evolution of the Mach number (top panel), pressure (middle panel) and temperature (bottom panel) for different values of z_1, at an inlet pressure of 2 bar and an outlet pressure of 1 bar. The supersonic region is elongated when the z_1 parameter is increased. The values of the parameters increase or decrease to the same local minima or maxima.

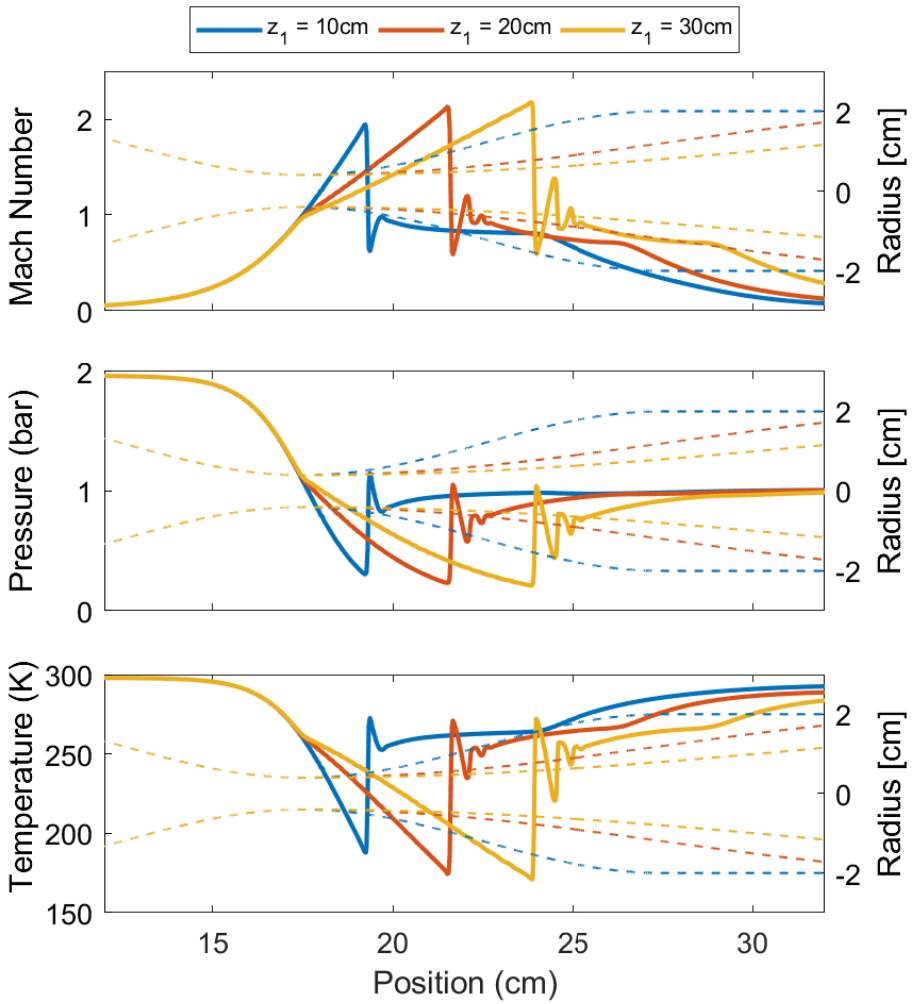

Figure B.7: Mach number (top panel), pressure (middle panel) and temperature (bottom panel) as a function of position for different z_1. The radius of the geometries is given in dashed lines.

APPENDIX C

Improving the energy efficiency through pulsing

C.1 Total vibrational and gas temperature gains or losses between the pulses

In order to get a more efficient vibrational-induced dissociation, the non-equilibrium between the vibrational and gas temperature needs to be enhanced [28]. We therefore present in figure C.1 the total loss or gain of the vibrational and gas temperature between the pulses ($\sum \Delta T_v$ and $\sum \Delta T_g$) for different plasma pulse and interpulse times. Positive $\sum \Delta T_v$ and $\sum \Delta T_g$ represent a total gain in vibrational and gas temperature between the pulses, while negative values correspond to a loss in temperature.

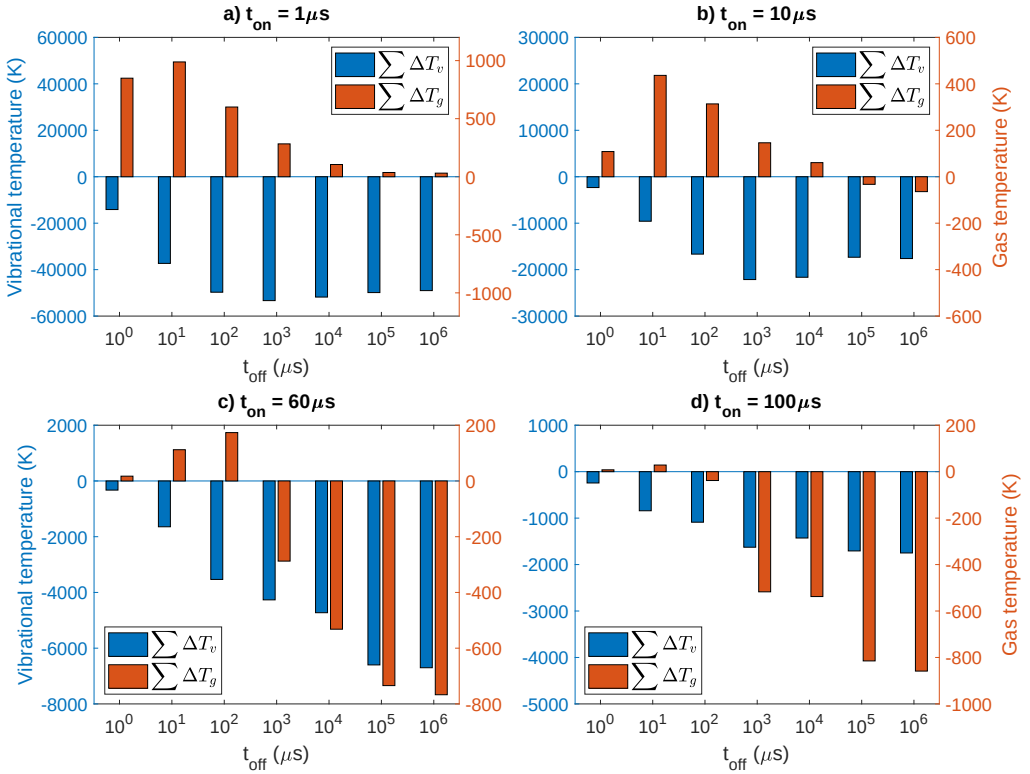

Figure C.1: Total temperature gain and loss between the pulses as a function of the interpulse time, for four different plasma pulse times, i.e., t_{on} = 1 μs, 10 μs, 60 μs, and 100 μs.

Figure C.1 shows similar trends in the evolution of $\sum \Delta T_v$ and $\sum \Delta T_g$. At short interpulse times, the vibrational temperature loss is minimal, which is beneficial, but the gas temperature increases between the pulses. This is consistent with figure 5.3, where at small interpulse times, VT relaxation made the vibrational temperature relax and the gas temperature increase. The total gain in gas

temperature is most pronounced at t_{off} = 10 μs, with a total gas temperature rise of 989 K, 436 K, 112 K, and 29 K, for t_{on} = 1, 10, 60, and 100 μs, respectively. We want to note that the gas temperature gain is highest at a shorter interpulse time than in figure 5.3, where the maximum was reached at (or above) 100 μs. This can be explained by the continued rise of the gas temperature after the first pulse, which can lead to an increased cooling (see equation 5.1).

At longer interpulse times, the vibrational temperature loss is higher, which is detrimental, but there is also a loss in gas temperature for all cases, except for t_{on} = 1 μs. However, the positive value here is negligible, because for such a short plasma pulse time, the gas temperature does not increase during the plasma, but after. This is also consistent with figure 5.3 (for a higher plasma pulse time of t_{on} = 10 μs), in which we can see that gas temperature is close-to room temperature at the end of the pulse, and returns to room temperature at an interpulse time of t_{off} = 1 s.

Finally, when comparing figure C.1 (a-d), we can conclude that the total vibrational temperature (or energy) loss is much larger for short plasma pulse times, because of the many pulses (and thus also interpulses) to reach the same total SEI. It is important to realize that the vibrational energy lost during these many interpulses needs to be regained during the next plasma pulse, thus explaining why short plasma pulses, especially in combination with long interpulse times, yield a low energy efficiency (cf. figure 5.1).

C.2 Temporal evolution of the gas temperature

In figure C.2, we show the evolution of the gas temperature from the initial time t_0 until the plasma end time t_{end} (when the total fixed SEI of 1 eV/molec. is reached), for four different plasma pulse times (t_{on} = 1, 10, 60, and 100 μs) and five different interpulse times (t_{off} = 10 μs, 100 μs, 1 ms, 10 ms, 1 s). For comparison, we also plot the gas temperature evolution for the continuous plasma with the same SEI. The x-axis represents the time from the start of the first pulse to the end of the last pulse. However, because the total time is different for different plasma pulse and interpulse times, to reach the same SEI, the reader should not compare different points on the x-axis, since they can represent different total times.

For all of the plasma pulse times, a longer interpulse time yields a lower maximum gas temperature, since there is more cooling. Moreover, the maximum gas temperature is lower than in the continuous plasma for all plasma pulse and interpulse times. At t_{off} = 1 s, the gas temperature completely drops to room temperature. With increasing plasma pulse times, it can be seen that the gas maximum for a given interpulse time increases.

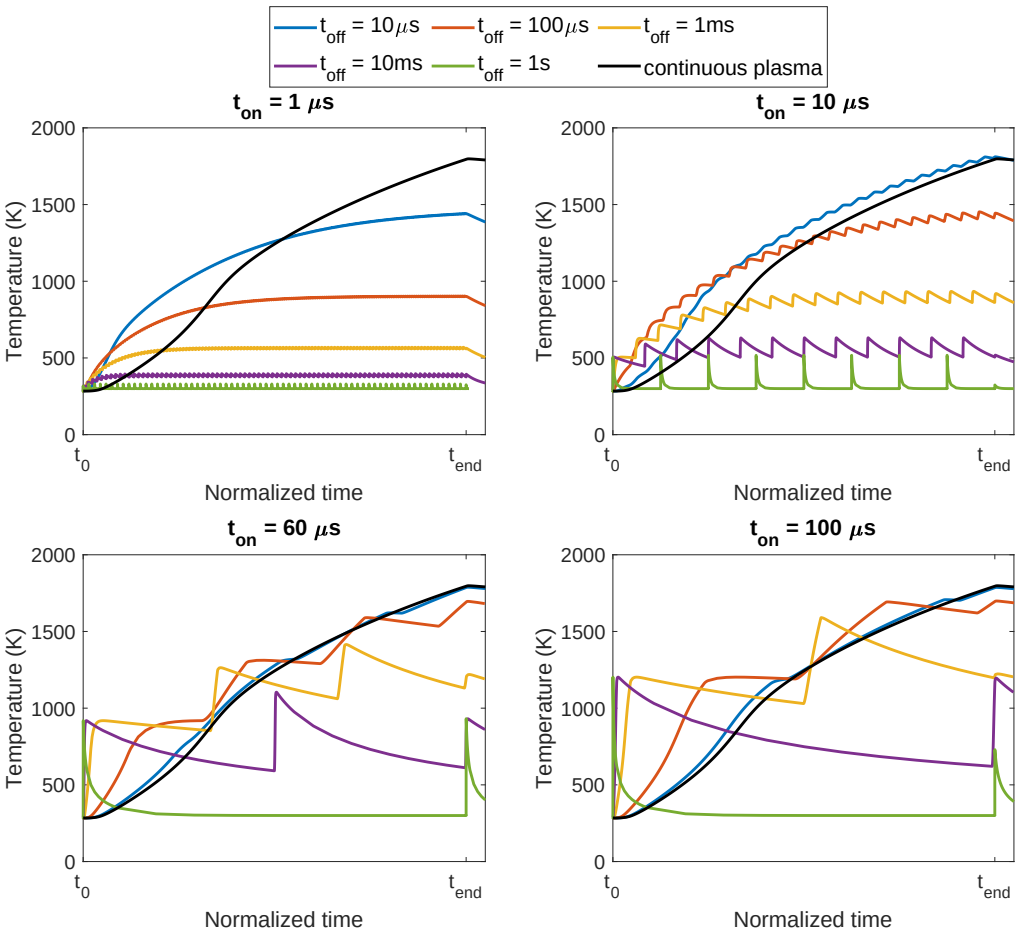

Figure C.2: Time-evolution of the gas temperature between the start of the first pulse and the end of the last pulse, for different plasma pulse times and interpulse times. t_{end} is defined by the time when the total fixed SEI of 1 eV/molec. is reached. For comparison, the gas temperature in the continuous plasma, for the same SEI, is also plotted (black curves).

C.3 VDF halfway the plasma

Figure C.3 illustrates the VDFs halfway of the plasma, i.e., when half of the SEI (thus 0.5 eV/molec) is deposited. For $t_{on} = 60$ μs and $t_{on} = 100$ μs, this happens in the first pulse, so we only show the VDFs for shorter plasma pulses, i.e., $t_{on} = 1$ μs and $t_{on} = 10$ μs. We also compare with the VDF in the continuous plasma, and with the Boltzmann plots at the corresponding vibrational temperatures. For $t_{on} = 1$ μs (panel a), the VDFs are always lower than in the continuous plasma, and they are most populated for short interpulse times, when there is limited time for relaxation. At longer interpulse times, the VDF completely relaxes in between

the pulses, and the pulse time is too short to reach significant population of the vibrational levels. At $t_{on} = 10$ μs, the VDF coincides with the continuous plasma at short interpulse times, but it is depleted for longer interpulse times. However, due to the low gas temperature at $t_{off} = 1$ s, the characteristic time scales of the VV relaxation is low, while that of the VT relaxation is high, resulting again in a fast and pronounced overpopulation of the higher vibrational levels, so the VDF becomes again very similar to that of a continuous plasma.

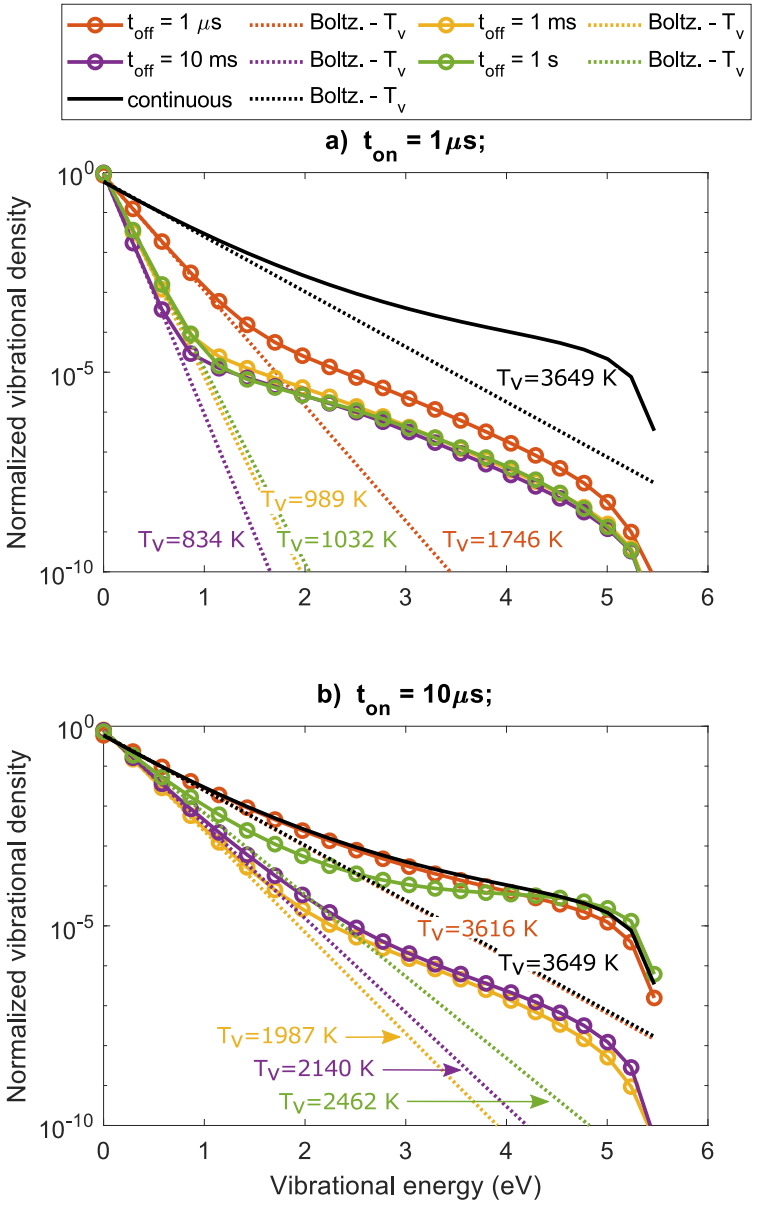

Figure C.3: VDFs halfway the plasma, i.e., when half of the SEI is deposited (0.5 eV/molec), for $t_{on} = 1$ μs (a, top panel), and for $t_{on} = 10$ μs (b, bottom panel), and for four different interpulse times. The VDF in the continuous plasma is also plotted (black curve), as well as the Boltzmann plots for each case at the corresponding vibrational temperatures.

C.4 VDF at the end of the plasma

In figure C.4, we plot the VDFs at the end of the plasma, for t_{on} = 10 μs and t_{on} = 100 μs. They should be compared with the VDFs for t_{on} = 1 and 60 μs, plotted in figure 5.8.

For t_{on} = 10 μs and t_{on} = 100 μs, the VDFs at the end of the plasma, for different interpulse times look very similar to the VDFs for 60 μs. The VDF at the end of the plasma coincides with the one of the continuous plasma for short interpulse times (1 μs to 1 ms), but it reaches a higher population for longer interpulse times, similar to t_{on} = 60 μs (see figure 5.8). However, while both plasma pulse time show a large overpopulation of the VDF at t_{off} = 1 s, the energy efficiency with respect to t_{on} = 60 μs remains lower. Indeed, for t_{on} = 10 μs, the short plasma pulse time enhances the vibrational temperature loss due to pulsing (see figure S1). Also, while the overpopulation at the end of the pulse is high, the overpopulation does not last long enough for vibrational-induced dissociation. For t_{on} = 100 μs, there are two pulses to reach the SEI of 1 eV/molec. at t_{off} = 1 s. However, during a significant portion of the first pulse, the VDF was thermalized, so our model predicts lower energy efficiencies for these conditions than for t_{on} = 60 μs (see figure 5.1).

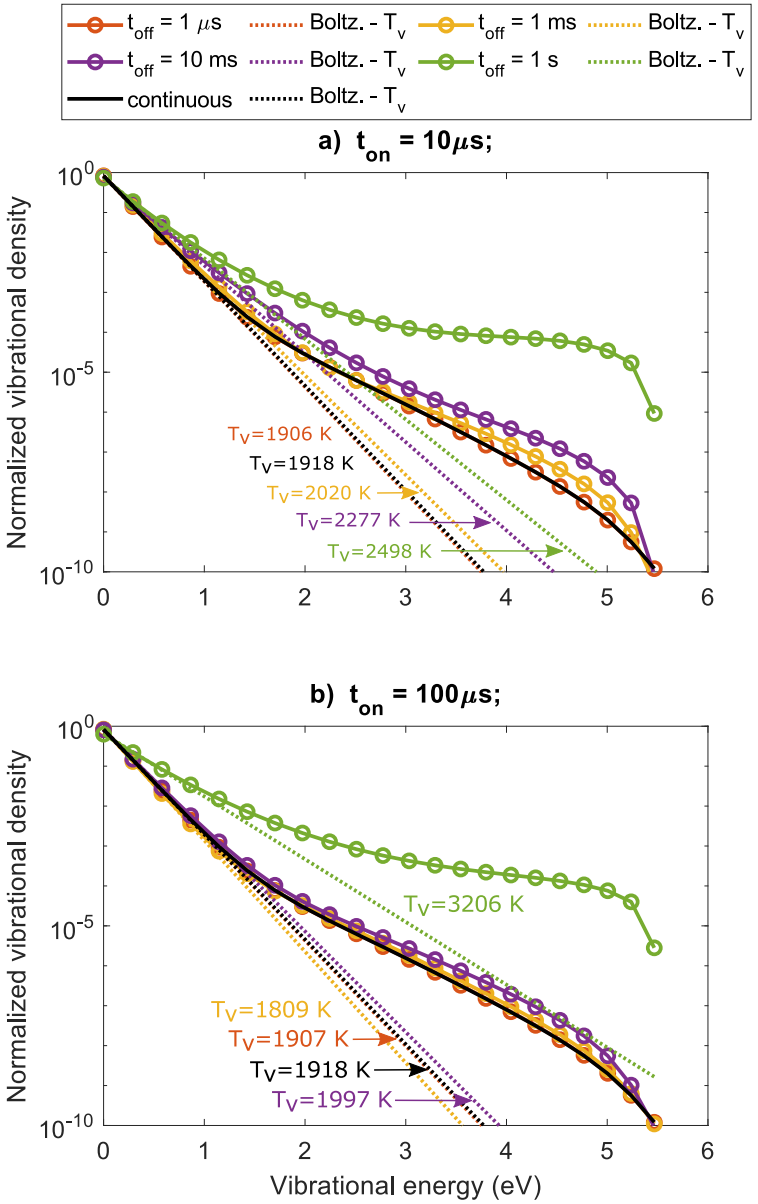

Figure C.4: VDFs at the end of the plasma, for $t_{on} = 10$ μs (a, top panel), and $t_{on} = 100$ μs (b, bottom panel) for four different interpulse times. The VDF in the continuous plasma is also plotted (black curve), as well as the Boltzmann plots for each case at the corresponding vibrational temperatures.

C.5 Relative contribution of the individual vibrational levels to the dissociation

In figure C.5, we show the relative contribution to dissociation from the different vibrational levels, for a plasma pulse time t_{on} = 1 μs (a, top panel), and t_{on} = 60 μs (b, bottom panel), at a short (t_{off} = 1 μs), and a long (t_{off} = 1 s) interpulse time. For long plasma pulse or short interpulse times (i.e. t_{on} = 60 μs or t_{off} = 1 μs), dissociation mainly takes place from the higher vibrational levels. The largest contribution comes from CO_2(V10), CO_2(V20) and CO_2(V21), with a contribution of about 4 %, 5 % and 67 %, respectively. These levels have the highest contribution, since their vibrational energy, i.e. 2.78 eV, 5.24 and 5.5 eV, lies close to the activation energy (E_a) divided by alpha of the two main vibrational-induced dissociation reactions (N1), with E_a/α = 5.5 eV, and (N2), with E_a/α = 2.77 eV. For more information, see ref. 28. In figure 5.9, we can see that these reactions indeed have the largest contribution to the dissociation.

The high vibrational levels do not contribute to a higher dissociation in case of a short plasma pulse and a long interpulse time (i.e. t_{on} = 1 μs and t_{off} = 1 s). In sections 5.3.3 - 5.3.5, it was discussed that these conditions had a negative effect on the vibrational temperature, and on the overpopulation of the higher vibrational levels. In that case, the main contribution to the dissociation came from electron impact dissociation (see figure 5.9).

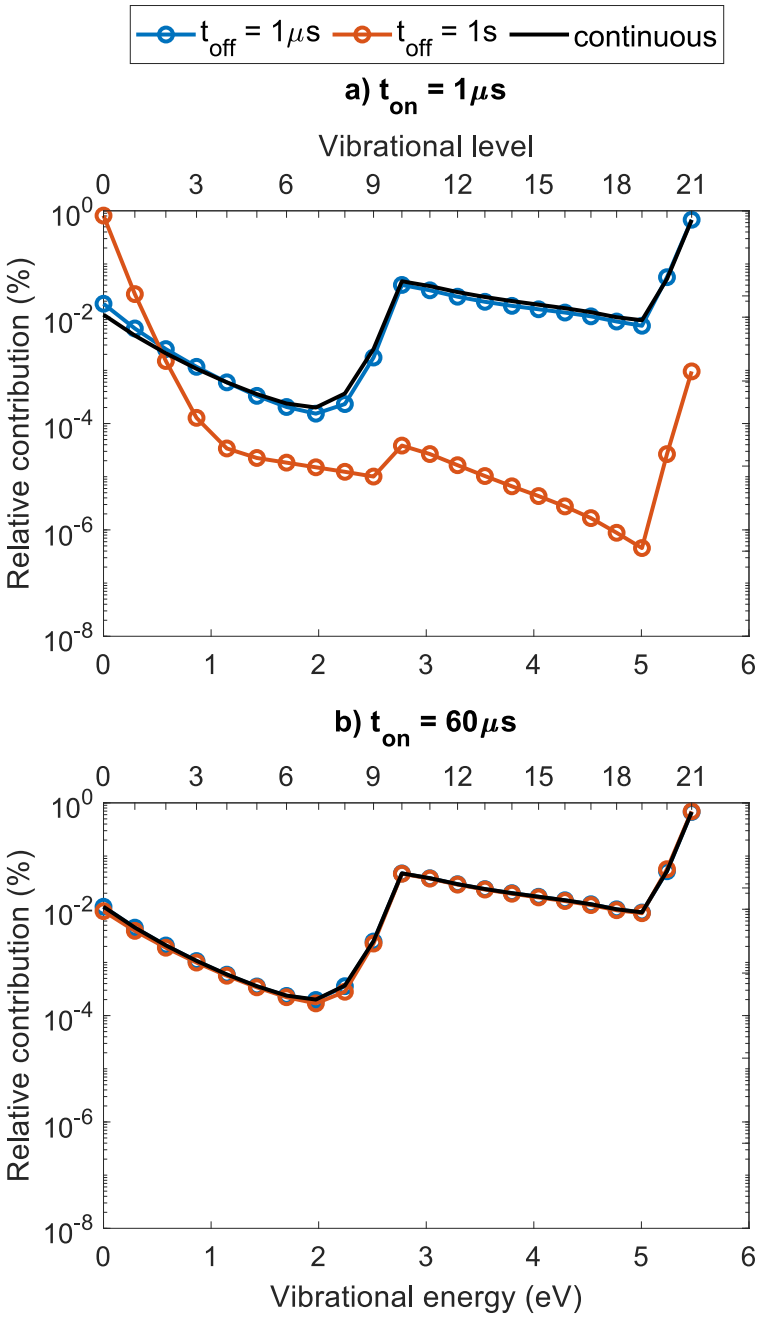

Figure C.5: Relative contribution of the vibrational levels to the overall dissociation, for $t_{on} = 1$ μs (a, top panel), and $t_{on} = 60$ μs (b, bottom panel), for interpulse times $t_{off} = 1$ μs and 1 s, a reduced electric field of 50 Td, an ionization degree of 10^{-6}, and a pressure of 100 mbar.

C.6 Time-evolution of the vibrational and gas temperature in a continuous plasma for different ionization degrees and reduced electric fields

Figures C.6-C.8 show the time-evolution of the vibrational and gas temperature in a continuous plasma, for different ionization degrees, and for reduced electric fields of 50 Td, 100 Td and 150 Td, respectively. The end time is different in each case, as it is defined by the time when the total fixed SEI of 1 eV/molec. is reached. At low ionization degrees, the vibrational temperature reaches a maximum value early in time, but this maximum shifts to later times upon higher ionization degree. This is correlated with the lower characteristic time scale of electron impact vibrational excitation with higher ionization degree, as was shown in figure 3.2. At an ionization degree of 5×10^{-6} and higher, the maximum value is reached close to or at the end of the plasma (i.e., when the SEI of 1 eV/molec. is reached). For these conditions, pulsing will not increase the energy efficiency, because the loss of vibrational energy between the pulses will not be compensated by a higher vibrational temperature. This is true for a reduced electric field of 50 and 100 Td (figures S6 and S7). At 150 Td, this is already the case for an ionization degree of 5×10^{-7} (figure C.8).

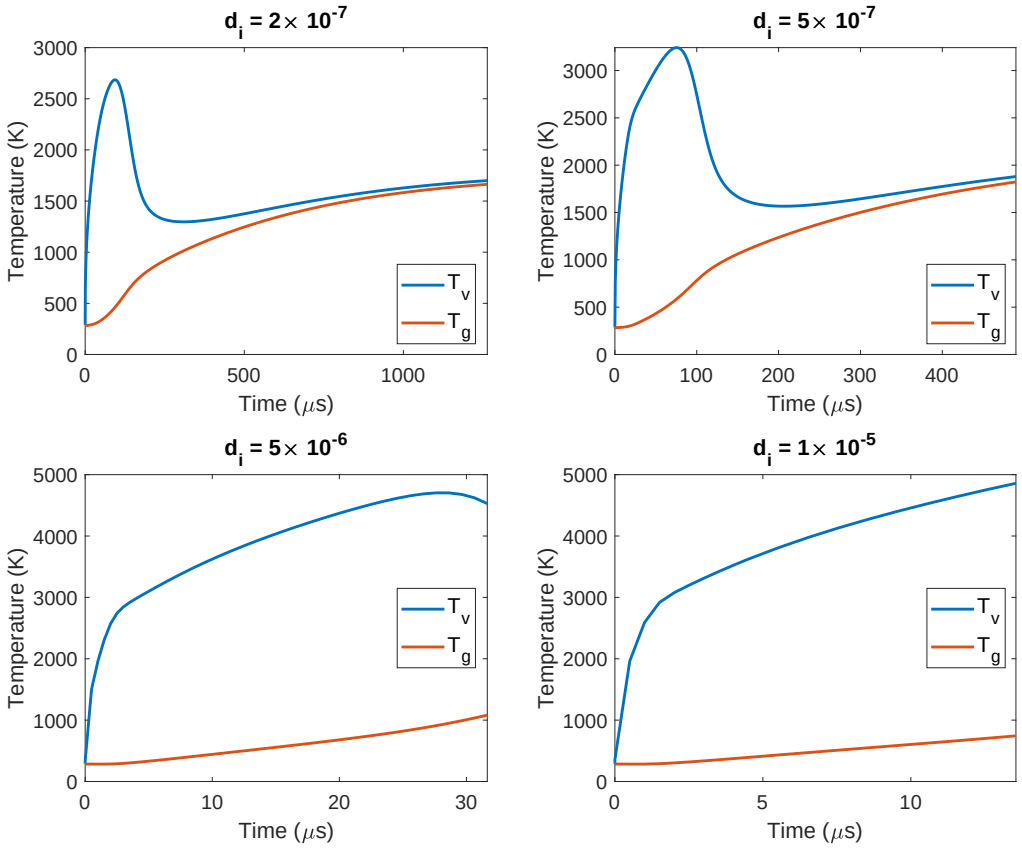

Figure C.6: Time-evolution of the vibrational and gas temperature in a continuous plasma for different ionization degrees, and a reduced electric field of 50 Td.

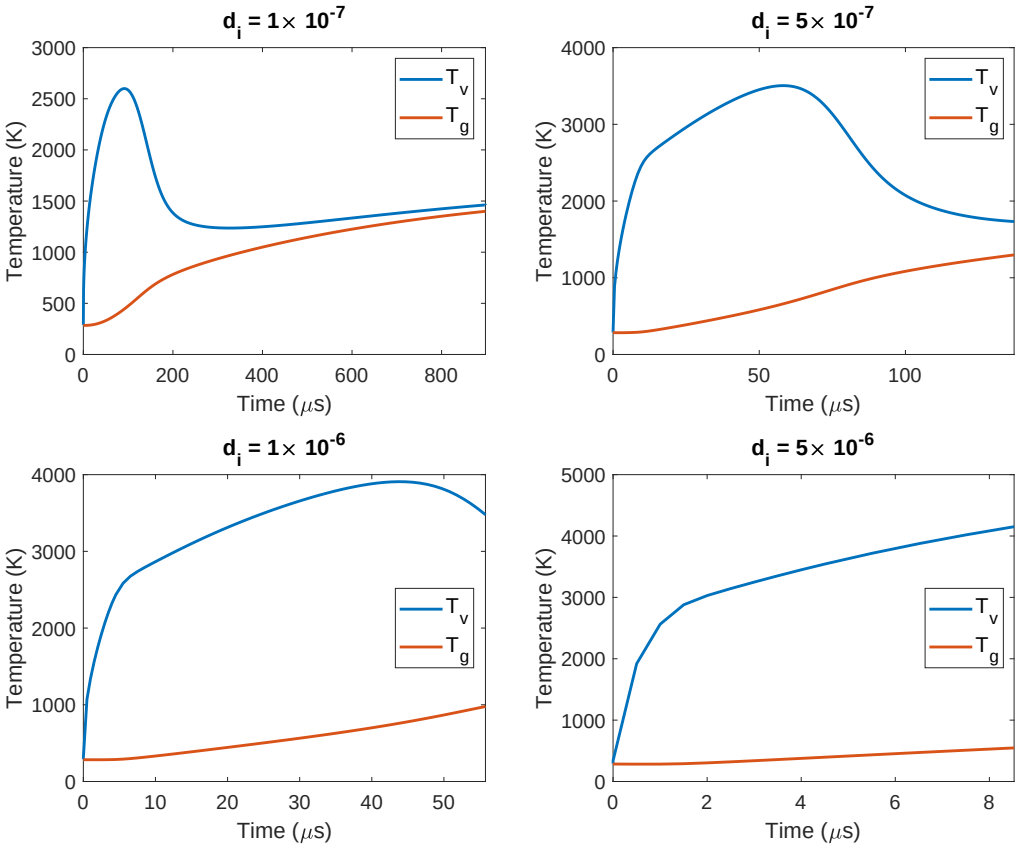

Figure C.7: Time-evolution of the vibrational and gas temperature in a continuous plasma for different ionization degrees, and a reduced electric field of 100 Td.

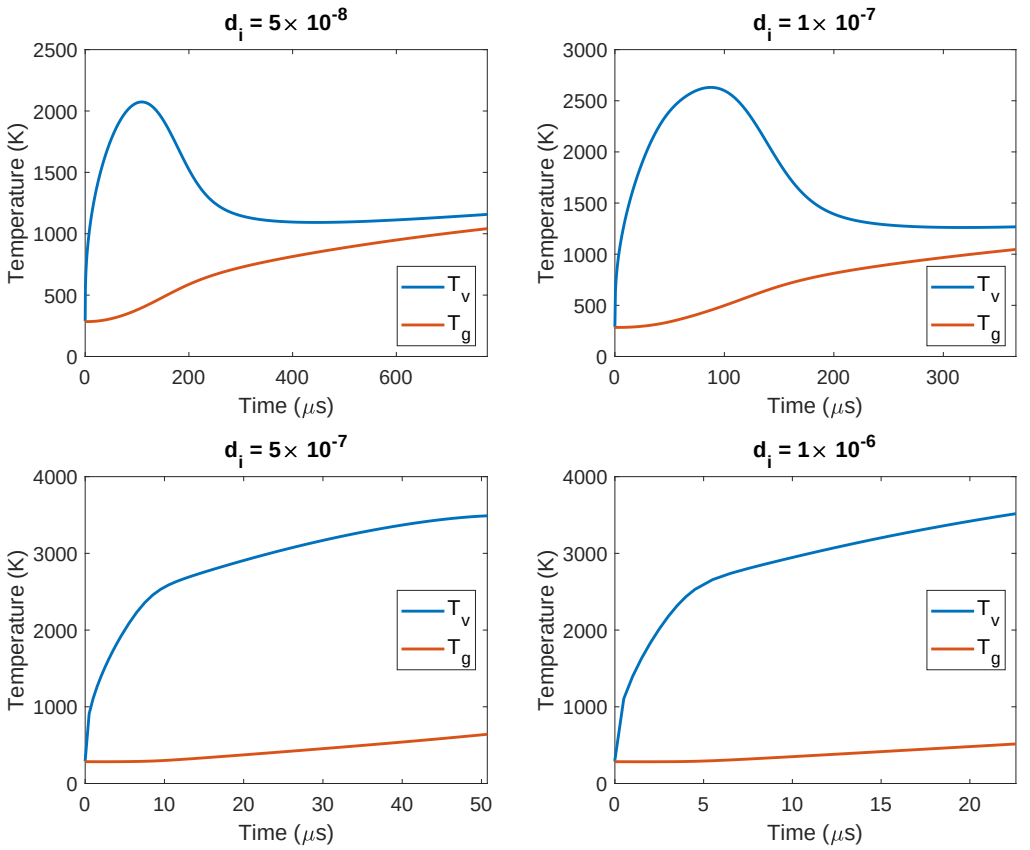

Figure C.8: Time-evolution of the vibrational and gas temperature in a continuous plasma for different ionization degrees, and a reduced electric field of 150 Td.

C.7 Dissociation mechanisms for different reduced electric fields at a low ionization degree

In figure 5.11 and 5.12, it was shown that at a low ionization degree of 2×10^{-7}, and a reduced electric field of 50 Td, pulsing did not improve the energy efficiency. It was seen in figure 13 that the electron impact dissociation became the most prominent dissociation mechanism. While pulsing did increase the vibrational-induced dissociation by collision of CO_2 with a molecule M, the negative impact on electron impact dissociation compensated for this increase, leading to an overall lower energy efficiency in a pulsed regime.

Upon increasing reduced electric field, electron impact dissociation becomes more important[28], so similar trends are observed in figures C.9 and C.10 for a reduced electric field of 100 Td (with $d_i = 10^{-7}$) and 150 Td (with $d_i = 5 \times 10^{-8}$) , respectively, where no or negligible improvement of the energy efficiency by pulsing is noticed (see figure 5.12). In both figures, it can be seen that the contribution to dissociation by collision with a molecule M becomes very small. Hence, the negative effect of pulsing on electron impact dissociation is not compensated by a positive impact on the dissociation by collision with a molecule M. However, it can be seen that with decreasing contribution from the dissociation mechanisms, the contribution from the most important recombination mechanism also decreases. This results in a negligible improvement for E/N = 150 Td and $d_i = 5 \times 10^{-8}$ in figure 5.13.

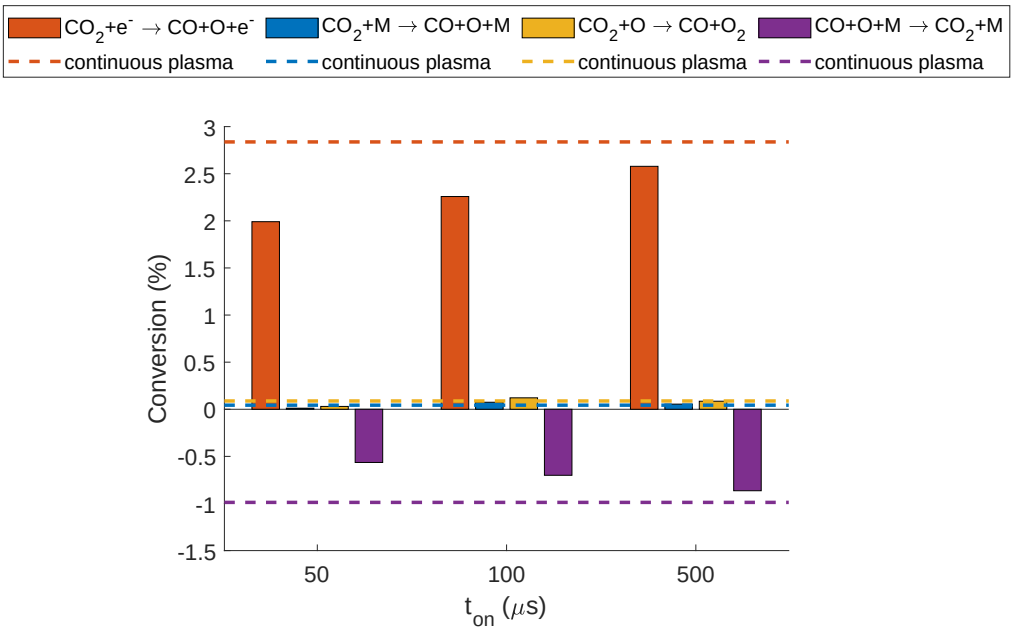

Figure C.9: CO_2 conversion by the three main dissociation reactions: electron impact dissociation (red), dissociation upon collision with a molecule M (blue) and upon collision with an O atom (yellow), as well as the most important recombination reaction, for different plasma pulse times and an interpulse time of 1 s, a reduced electric field of 100 Td and an ionization degree of 10^{-7}. The dashed horizontal lines represent the respective conversions of a continuous plasma at the same SEI.

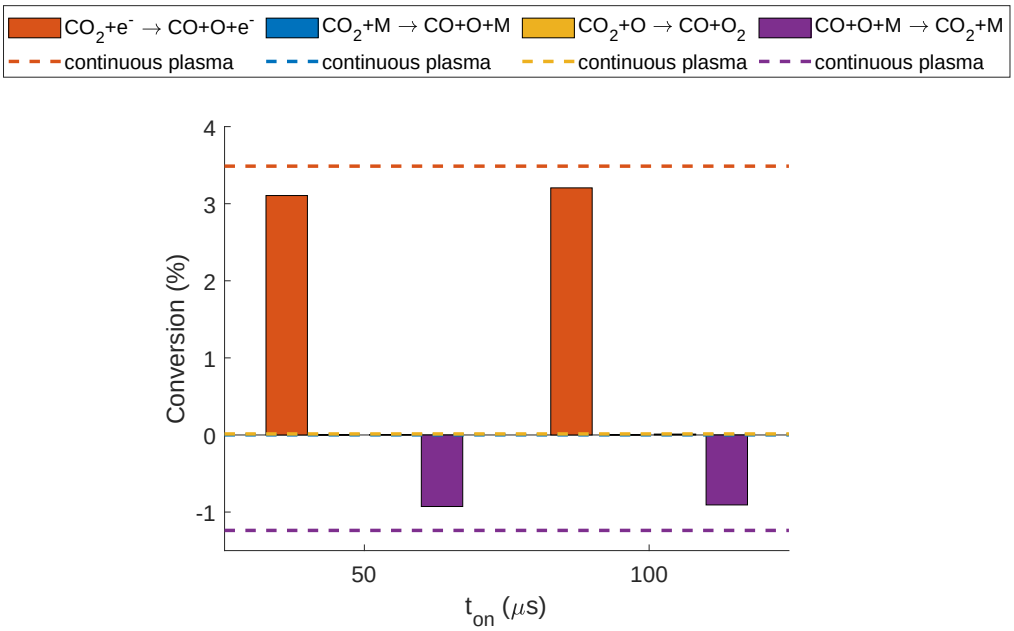

Figure C.10: CO_2 conversion by the three main dissociation reactions: electron impact dissociation (red), dissociation upon collision with a molecule M (blue) and upon collision with an O atom (yellow), as well as the most important recombination reaction, for different plasma pulse times and an interpulse time of 1 s, a reduced electric field of 150 Td and an ionization degree of 5×10^{-8}. The dashed horizontal lines represent the respective conversions of a continuous plasma at the same SEI.

APPENDIX D

The role of quenching in non-equilibrium plasmas

D.1 Effect of instantaneous quenching on the evolution of the dissociation and recombination rates for a plasma subjected to low cooling

Figure D.1 and D.2 illustrate the rates of the two most important dissociation reactions (reaction N1 and N2 of Tables A.4 and A.7) and recombination reactions (N4 and N5 of Tables A.4 and A.7), as a function of time after quenching, for VT non-equilibrium plasma conditions with SEI of 0.5 eV/molec. (figure D.1) and VT equilibrium plasma conditions with SEI of 4 eV/molec. (figure D.2), i.e., the conditions of figure 6.3. The dissociation and recombination rates with and without quenching are plotted in full and dashed lines, respectively. Because the reaction rates are subject to changes in the gas volume (i.e. due to changes in the gas temperature or chemical composition), we plot the expansion-corrected rates (i.e. R_i/β).

For a warm VT non-equilibrium plasma with SEI of 0.5 eV/molec., figure D.1 (a) demonstrates that the dissociation rates of CO_2 upon collision with any molecule M (N1), or with an O atom (N2) both increase due to quenching. Figure D.1 (b) indicates a rise for the recombination rate of CO and O_2 (N5), but a drop for the recombination rate of CO and O (N4), and the latter rate also drops faster in time. In addition, the dissociation rates are initially much higher than the recombination rates, but they drop fast starting from 0.01 ms, while the recombination rates last longer in time (up to 1 – 10 ms). This explains the sharp increase followed by a gradual drop in CO_2 conversion upon quenching, depicted in figure 6.3 (a) .

For a warm VT equilibrium plasma with SEI of 4 eV/molec., figure D.2 (a) shows a drastic drop of both dissociation rates upon quenching at maximum conversion. In addition, without quenching, both rates are much higher for a longer time. Indeed, the gas temperature remains much higher for a longer time, providing enough energy for both dissociation reactions to take place, while upon quenching, the gas temperature drops dramatically, thereby inhibiting both dissociation reactions. Furthermore, because of the VT equilibrium at the moment of quenching, there is also not enough vibrational energy to overcome the activation energy of these reactions. This is explained in more detail in section 6.3.5. The recombination reactions also stay high for a longer time without quenching, similar to the dissociation reactions, due to the high gas temperature. In addition, the CO_2 conversion is much higher at this high temperature (cf. figure 6.3 (a,b)), in contrast to figure D.1. This makes that both recombination reactions N4 and N5 (i.e. recombination of CO with O and O_2, respectively) are more important than in figure D.1, and comparable to the dissociation reactions (see figure D.2).

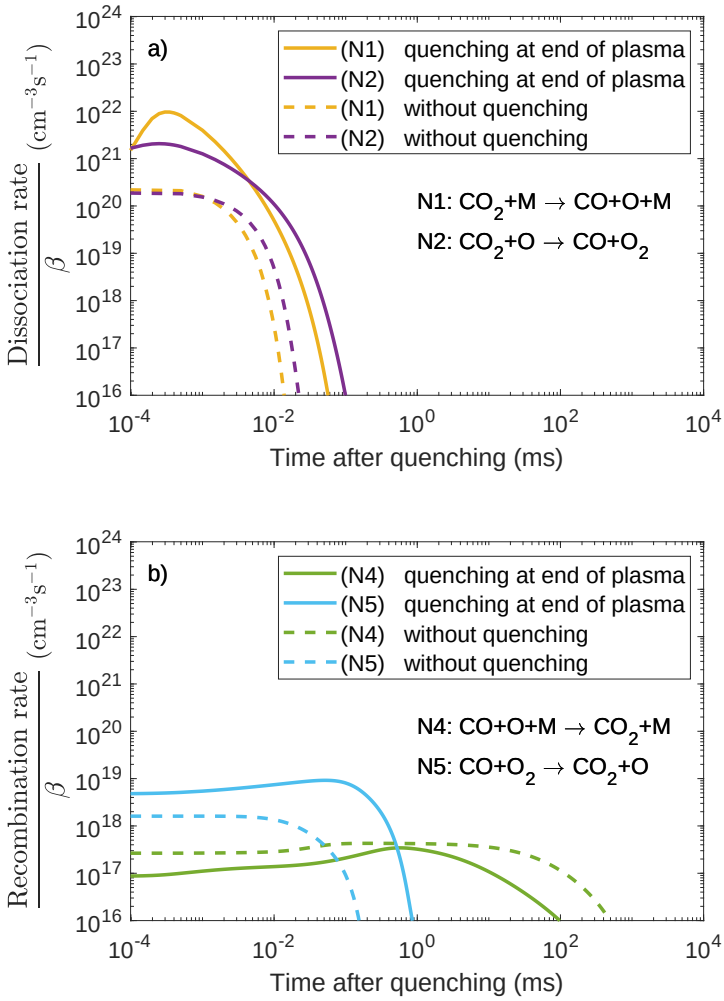

Figure D.1: Expansion-corrected dissociation (a) and recombination (b) rates for a warm VT non-equilibrium plasma at SEI of 0.5 eV/molec. (weak cooling c $= 10^{-3}$), for instantaneous quenching at the end of the plasma (full lines) and without quenching (dashed lines).

With the slowly decreasing gas temperature the dissociation reactions drop faster than the recombination reactions, and the conversion drastically decreases (see figure 6.2 (a,b)). Upon quenching, both recombination rates slightly increase, but they also drop earlier in time than without quenching; see figure D.2 (b). The rise in reaction rates is in contrast to the drop of the dissociation rates (figure D.2 (a)), which is especially striking for reaction N5, as it is also characterized by a high activation energy, just like both dissociation reactions N1 and N2. This opposite behavior will be explained in more detail in section 6.3.5, when studying the VDFs. Combined with the drop in dissociation rates, this initial rise in

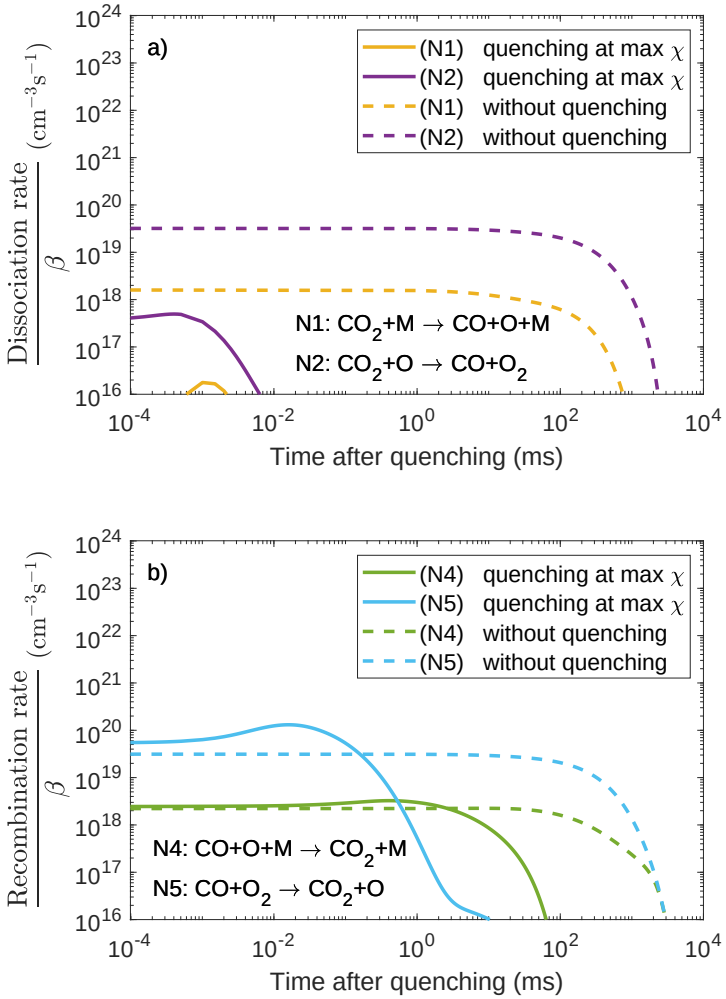

Figure D.2: Expansion-corrected dissociation (a) and recombination (b) rates for a VT equilibrium plasma at SEI of 4 eV/molec. (weak cooling; c = 10^{-3}), for instantaneous quenching at maximum CO_2 conversion (full lines) and without quenching (dashed lines).

recombination rates, followed by a fast decrease, results in a small but steep drop in CO_2 conversion upon quenching (cf. figure 6.3 (b), yellow curve), after which the CO_2 conversion is "frozen", as was obvious from figure 6.3 (b).

D.2 Effect of instantaneous quenching on the O atom density

Figure D.1 and D.2 showed the dissociation and recombination reaction rates as a function of time, for a plasma with SEI of 0.5 and 4 eV/molec., quenched at the

end of the plasma, and at the time of maximum conversion, respectively. Their behavior as a function of time, and upon quenching, could be explained from the VDFs, except for reaction N4 (i.e. CO + O + M $\rightarrow$ CO_2 + M, see Table S4), which does not have a high activation energy, in contrast to dissociation reactions N1 and N2, and recombination reaction N5. However, its behavior can be explained from the O atom density, as illustrated in figure D.3 and D.4. Indeed, it is clear that the evolution of reaction N4 in figure D.2 and D.1 follows the evolution of the O atom density. Both for a plasma with SEI of 0.5 and 4 eV/molec., subject to weak cooling (c = 10^{-3}), we observe from figures D.3 and D.4 that instantaneously quenching leads to a faster drop in the O atom density.

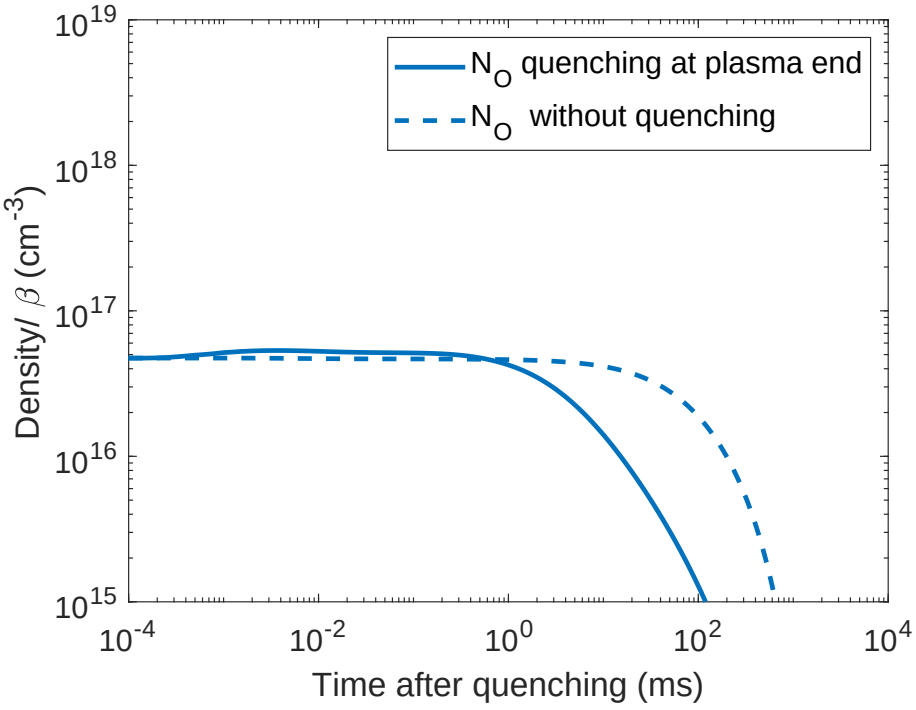

Figure D.3: Time-evolution of the expansion-corrected O atom density for a warm plasma with SEI of 0.5 eV/molec. that is instantaneously quenched at the end of the plasma (full lines) and without quenching (dashed lines).

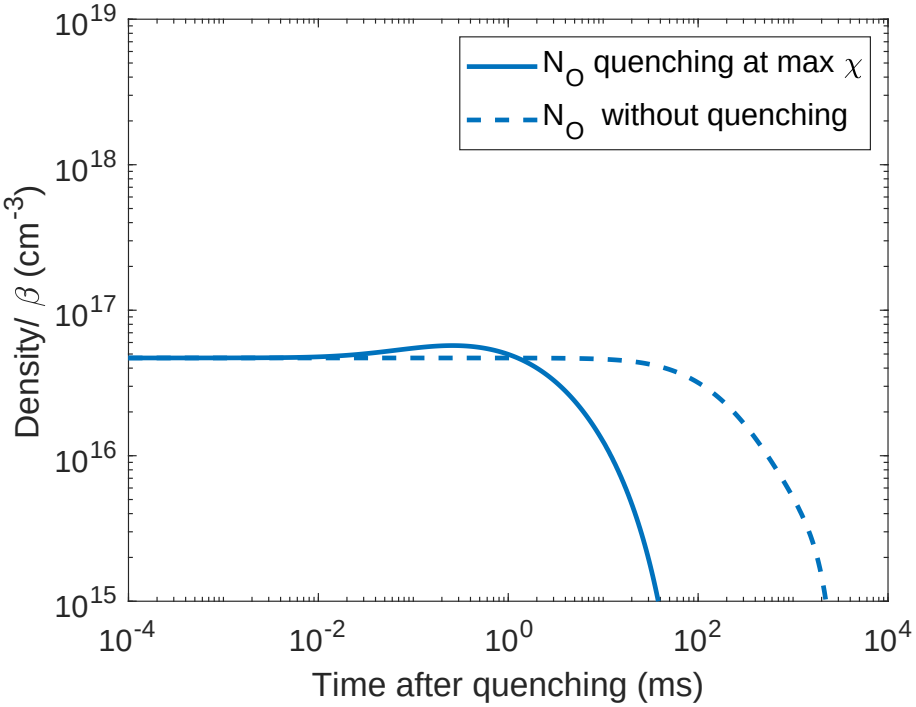

Figure D.4: Time-evolution of the expansion-corrected O atom density for a warm plasma with SEI of 4 eV/molec. that is instantaneously quenched at maximum conversion (full lines) and without quenching (dashed lines).

D.3 Effect of instantaneous quenching on the dissociation and recombination rates for a plasma subjected to strong cooling

In figure D.2 and D.1, we illustrated the effect of instantaneous quenching on the expansion-corrected dissociation and recombination rates for a plasma with SEI of 0.5 eV/molec. and 4 eV/molec. subject to weak cooling ($c = 10^{-3}$). In figure D.5 we show the same, but for a plasma with SEI of 4 eV/molec. subject to strong cooling ($c = 10^{3}$), hence a cold plasma at VT non-equilibrium conditions, that is quenched at the end of the plasma (full lines), and without quenching (dashed lines), for comparison. This corresponds to the conditions of figure 6.5.

Figure 6.5 showed that the CO_2 conversion slightly increased after quenching (i.e. super-ideal quenching), followed by an immediate drop. Figure D.5 indicates that shortly after quenching, the dissociation rates go up, but they drop quickly in time. The rate of the most important recombination reaction N5 also rises upon quenching, and extends over a longer time-scale than for the dissociation reactions. Due to the high conversion degree, the rise in this recombination

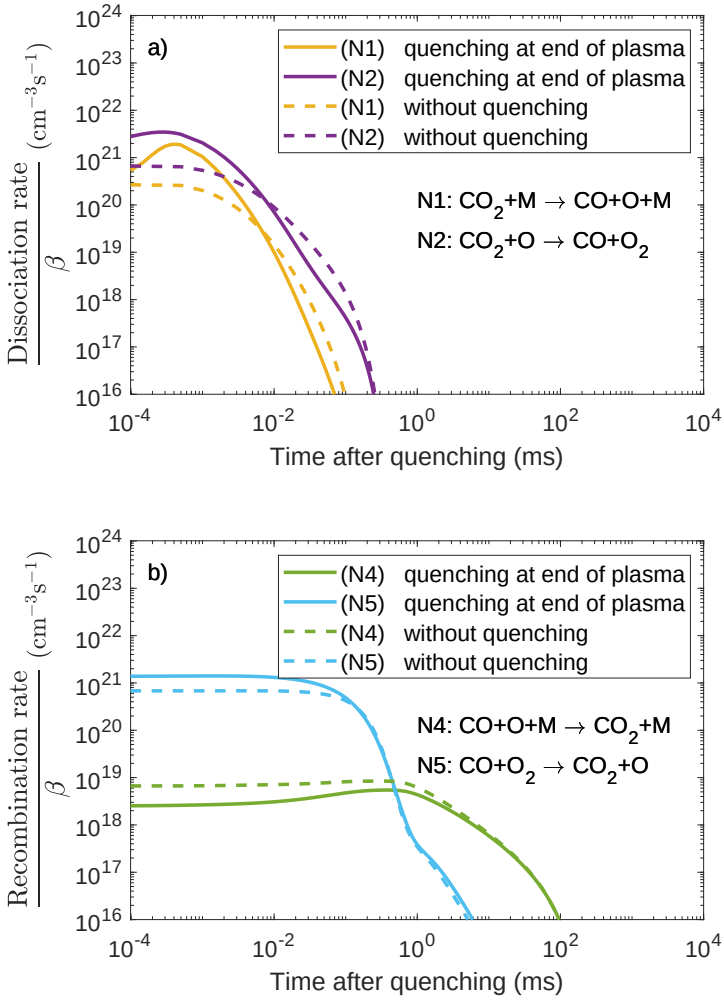

Figure D.5: Expansion-corrected dissociation (a) and recombination (b) rates for a VT non-equilibrium (cold) plasma with SEI of 4 eV/molec. (strong cooling; c = 10^3), for instantaneous quenching at the end of the plasma (full lines) and without quenching (dashed lines).

reaction is predominant, and reduces the CO_2 conversion after the first increase. This explains why the final CO_2 conversion is lower than without quenching (see figure 6.5).

Figure D.6 depicts the total dissociation and recombination, with and without quenching, for the same conditions as in figure D.5. Upon quenching, the contribution of the main recombination mechanism N5 indeed slightly increases, resulting in a somewhat lower final CO_2 conversion, depicted in figure 6.5.

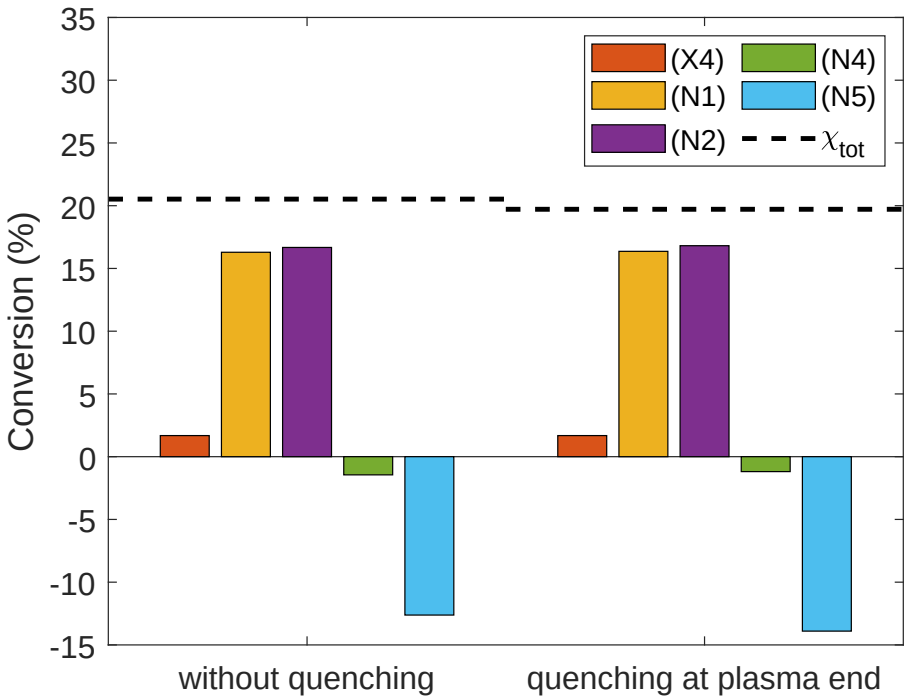

Figure D.6: Total contribution of the dissociation and recombination reactions to the conversion for a VT non-equilibrium (cold) plasma with SEI of 4 eV/molec. that is quenched at the end of the plasma (right), and that was subjected to strong cooling (c = 10^3). The case without quenching (left) is shown as a reference. The horizontal dashed lines indicate the final CO_2 conversion. Besides the major dissociation reactions (N1, N2), also electron impact dissociation (X4; see Table A.6) has a minor contribution.

D.4 Effect of instantaneous quenching on the VDFs of CO_2, CO, and O_2 for a plasma subjected to strong cooling

In figure 6.8, we plotted the VDFs of CO_2, CO, and O_2 after quenching at the end of the plasma, for a plasma subject to weak cooling. In figure D.7 we plot the same, but for a plasma with SEI of 4 eV/molec., that was subject to strong cooling (i.e. c = 10^3, cf. red curve in figure 6.5).

At the end of the plasma, the VDFs of all three molecules are highly populated. After quenching, the VDF of CO_2 relaxes very fast, while the VDFs of CO and O_2 remain populated for a longer time (see time-point 2 in figure D.7). Due to the low gas temperature, VV relaxation populates these higher levels more than in the case without quenching. This explains why recombination reaction

N5 becomes more important (cf. figure D.5 and D.6).

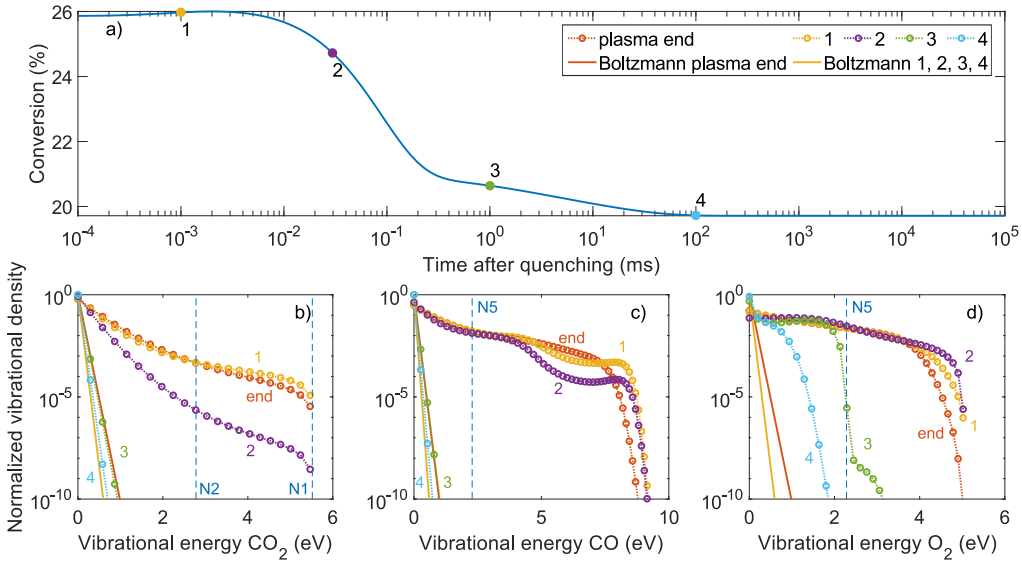

Figure D.7: VDFs of CO_2, CO, and O_2 (bottom panels; b-d), and their corresponding Boltzmann distributions, at the end of a cold plasma with SEI of 4 eV/molec. (VT non-equilibrium, strong cooling, c = 10^3) (red), and for different times after instantaneous quenching at the end of the plasma (1 to 4). The different time points are indicated on a plot of the conversion as a function of time (top panel; a). The vertical dashed lines in the bottom panels show the vibrational activation energies (E_a/α) of the dissociation reactions (N1 and N2) (b) and recombination reaction (N5) (c,d).

D.5 Relaxation time of the CO_2 VDF at low SEI

In figure 6.10, we observed that the CO_2 conversion of a plasma with 0.5 eV/molec., subject to weak cooling (c = 10^{-3}), could only drastically be enhanced upon quenching, when the gas temperature dropped to 300 K within less than 10 μs. To explain this, we plot in figure D.8 the evolution of the VDF at the end of the plasma and at several time-points in the afterglow, without quenching. At the end of the plasma, the VDF is clearly overpopulated, as was also clear from figure 6.8. After 1 μs in the afterglow, the VDF is still the same, but it drops quickly, and at 100 μs, it is relaxed to a Boltzmann distribution. This demonstrates that, in order to keep a significant overpopulation of the VDF, the gas temperature needs to drop faster than the relaxation of the VDF, hence within 10 μs.

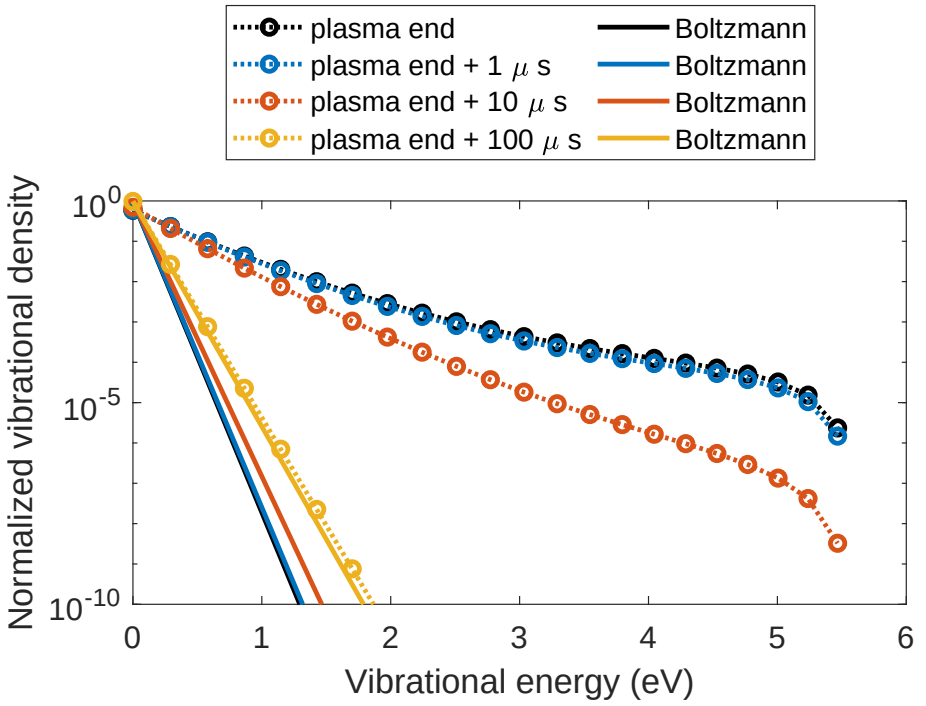

Figure D.8: VDF of CO_2 at the end of the plasma and at several time-points in the afterglow, without quenching, for a plasma with SEI of 0.5 eV/molec., subject to weak cooling ($c = 10^{-3}$), indicating that the VDF relaxes to a Boltzmann distribution in less than 100 μs after the end of the plasma.

Bibliography

[1] P. Breeze. The Carbon Cycle and Atmospheric Warming. In *Electricity Generation and the Environment*, pages 13–21. Elsevier, 2017. DOI: 10.1016/B978-0-08-101044-0.00002-0.

[2] R. Tuckett. *Greenhouse gases.* Elsevier Inc., 3 edition, 2019. DOI: 10.1016/B978-0-12-409547-2.14031-4.

[3] N. G. Loeb, B. A. Wielicki, D. R. Doelling, et al. Toward Optimal Closure of the Earth's Top-of-Atmosphere Radiation Budget. *J. Clim.*, 22(3):748–766, 2009. DOI: 10.1175/2008JCLI2637.1.

[4] K. E. Trenberth, J. T. Fasullo, and J. Kiehl. Earth's global energy budget. *Bull. Am. Meteorol. Soc.*, 90(3):311–323, 2009. DOI: 10.1175/2008BAMS2634.1.

[5] The NASA Earth's Energy Budget Poster, https://science-edu.larc.nasa.gov/energy_budget, Data retrieved: 08/04/2020.

[6] J. R. Flemming. *Historical Perspectives on Climate Change.* Oxford University Press, New York, USA, 1998.

[7] J. Tyndall. On the absorption and radiation of heat by gases and vapours, and on the physical connection. *Philos. Mag.*, 22:277–302, 1861.

[8] G. S. Callendar. The artificial production of carbon dioxide and its influence on temperature. *Q. J. R. Meteorol. Soc.*, 64(275):223–240, 1938. DOI: 10.1002/qj.49706427503.

[9] M. Crippa, G. Oreggioni, D. Guizzardi, et al. Jrc science for policy report: Fossil co_2 and ghg emissions of all world countries. Technical report, Joint Research Centre, European Commission, 2019.

[10] IPCC 2013, Fifth Assesment Report: Climate Change 2013 Synthesis Report, www.ipcc.ch.

[11] J. Cook, D. Nuccitelli, S. A. Green, et al. Quantifying the consensus on anthropogenic global warming in the scientific literature. *Environ. Res. Lett.*, 8(2), 2013. DOI: 10.1088/1748-9326/8/2/024024.

[12] The Paris Agreement, https://unfccc.int/process-and-meetings/the-paris-agreement/the-paris-agreement, Data retrieved: 08/04/2020.

[13] NASA Global Climate Change: Vital Signs of the Planet,http://climate.nasa.gov, Data retrieved: 08/04/2020.

[14] IPCC 2018, Special report: Global Warming of 1.5 °C, www.ipcc.ch.

[15] S. J. Davis, N. S. Lewis, M. Shaner, et al. Net-zero emissions energy systems. *Science*, 360(6396), 2018. DOI: 10.1126/science.aas9793.

[16] M. Jarre, M. Noussan, and A. Poggio. Operational analysis of natural gas combined cycle CHP plants: Energy performance and pollutant emissions. *Appl. Therm. Eng.*, 100(2016):304–314, 2016. DOI: 10.1016/j.applthermaleng.2016.02.040.

[17] Q. Wang, X. Chen, A. N. Jha, and H. Rogers. Natural gas from shale formation - The evolution, evidences and challenges of shale gas revolution in United States. *Renewable Sustainable Energy Rev.*, 30:1–28, 2014. DOI: 10.1016/j.rser.2013.08.065.

[18] X. Luo, J. Wang, M. Dooner, and J. Clarke. Overview of current development in electrical energy storage technologies and the application potential in power system operation. *Appl. Energy*, 137:511–536, 2015. DOI: 10.1016/j.apenergy.2014.09.081.

[19] M. C. Argyrou, P. Christodoulides, and S. A. Kalogirou. Energy storage for electricity generation and related processes: Technologies appraisal and grid scale applications. *Renewable Sustainable Energy Rev.*, 94:804–821, 2018. DOI: 10.1016/j.rser.2018.06.044.

[20] D. O. Akinyele and R. K. Rayudu. Review of energy storage technologies for sustainable power networks. *Sustainable Energy Technol. Assess.*, 8:74–91, 2014. DOI: 10.1016/j.seta.2014.07.004.

[21] H. Zhao, Q. Wu, S. Hu, H. Xu, and C. N. Rasmussen. Review of energy storage system for wind power integration support. *Appl. Energy*, 137:545–553, 2015. DOI: 10.1016/j.apenergy.2014.04.103.

[22] M. Aneke and M. Wang. Energy storage technologies and real life applications – A state of the art review. *Appl. Energy*, 179:350–377, 2016. DOI: 10.1016/j.apenergy.2016.06.097.

[23] J. A. Martens, A. Bogaerts, N. De Kimpe, et al. The Chemical Route to a Carbon Dioxide Neutral World. *ChemSusChem*, 10(6):1039–1055, 2017. DOI: 10.1002/cssc.201601051.

[24] A. de Klerk. Transport Fuel: Biomass-, Coal-, Gas- and Waste-to-Liquids Processes. In *Future Energy*, pages 199–226. Elsevier, 2020. DOI: 10.1016/B978-0-08-102886-5.00010-4.

[25] M. E. Dry. The Fischer–Tropsch process: 1950–2000. *Catal. Today*, 71(3-4):227–241, 2002. DOI: 10.1016/S0920-5861(01)00453-9.

[26] the Hydrogen Council. Path to hydrogen competitiveness: A cost perspective. Technical report, 2020.

[27] G. Glenk and S. Reichelstein. Economics of converting renewable power to hydrogen. *Nat. Energy*, 4(3):216–222, 2019. DOI: 10.1038/s41560-019-0326-1.

[28] A. Berthelot and A. Bogaerts. Pinpointing Energy Losses in CO_2 Plasmas - Effect on CO_2 Conversion. *J. CO_2 Util.*, 24:479–499, 2018. DOI: 10.1016/j.jcou.2018.02.011.

[29] N. den Harder, D. C. M. van den Bekerom, R. S. Al, et al. Homogeneous CO_2 Conversion by Microwave Plasma: Wave Propagation and Diagnostics. *Plasma Processes Polym.*, 14(6):1600120, 2017. DOI: 10.1002/ppap.201600120.

[30] C. K. N. Patel. Continuous-wave laser action on vibrational-rotational transitions of co_2. *Phys. Rev.*, 136:A1187–A1193, 1964. DOI: 10.1103/PhysRev.136.A1187.

[31] A. Cenian, A. Chernukho, V. Borodin, and G. Śliwiński. Modeling of Plasma-Chemical Reactions in Gas Mixture of CO_2 Lasers I. Gas Decomposition in Pure CO_2 Glow Discharge. *Contrib. Plasma Phys.*, 34(1):25–37, 1994. DOI: 10.1002/ctpp.2150340105.

[32] K. K. Corvin and S. J. B. Corrigan. Dissociation of Carbon Dioxide in the Positive Column of a Glow Discharge. *J. Chem. Phys.*, 50(6):2570–2574, 1969. DOI: 10.1063/1.1671416.

[33] A. Cenian, A. Chernukho, and V. Borodin. Modeling of Plasma-Chemical Reactions in Gas Mixture of CO_2 lasers. II. Theoretical Model and its Verification. *Contrib. Plasma Phys.*, 35(3):273–296, 1995. DOI: 10.1002/ctpp.2150350309.

[34] C. Leys, C. van Egmond, and E. Desoppere. Dissociation levels in fast-axial-flow CO_2 lasers: A quantitative model. *J. Appl. Phys.*, 78(4):2265–2269, 1995. DOI: 10.1063/1.360143.

[35] V. Guerra, T. Silva, P. Ogloblina, et al. The case for in situ resource utilisation for oxygen production on Mars by non-equilibrium plasmas. *Plasma Sources Sci. Technol.*, 26(11):11LT01, 2017. DOI: 10.1088/1361-6595/aa8dcc.

[36] R. I. Asisov, A. K. Vakar, V. K. Jivotov, et al. Non-Equilibrium Plasma-Chemical Process of CO_2 Decomposition in a Supersonic Microwave Discharge. *Proc. USSR Acad. Sci.*, 271(1):94–98, 1983.

[37] A. Fridman. *Plasma Chemistry*. Cambridge University Press, New York, USA, 2008.

[38] R. Snoeckx and A. Bogaerts. Plasma Technology - a Novel Solution for CO_2 Conversion? *Chem. Soc. Rev.*, 46(19):5805–5863, 2017. DOI: 10.1039/C6CS00066E.

[39] W. Bongers, H. Bouwmeester, B. Wolf, et al. Plasma-driven dissociation of CO_2 for fuel synthesis. *Plasma Processes Polym.*, 14(6):1600126, 2017. DOI: 10.1002/ppap.201600126.

[40] E. Gomez, D. A. Rani, C. Cheeseman, et al. Thermal plasma technology for the treatment of wastes: A critical review. *J. Hazard. Mater.*, 161(2-3):614–626, 2009. DOI: 10.1016/j.jhazmat.2008.04.017.

[41] Y. Itikawa. Cross Sections for Electron Collisions With Carbon Dioxide. *J. Phys. Chem. Ref. Data*, 31(3):749–767, 2002. DOI: 10.1063/1.1481879.

[42] G. J. M. Hagelaar and L. C. Pitchford. Solving the Boltzmann Equation to Obtain Electron Transport Coefficients and Rate Coefficients for Fluid Models. *Plasma Sources Sci. Technol.*, 14(4):722–733, 2005. DOI: 10.1088/0963-0252/14/4/011.

[43] A. Bogaerts, T. Kozák, K. van Laer, and R. Snoeckx. Plasma-based Conversion of CO_2 : Current Status and Future Challenges. *Faraday Discuss.*, 183:217–232, 2015. DOI: 10.1039/C5FD00053J.

[44] D. Mei, X. Zhu, Y.-L. He, J. D. Yan, and X. Tu. Plasma-Assisted Conversion of CO_2 in a Dielectric Barrier Discharge Reactor: Understanding the Effect of Packing Materials. *Plasma Sources Sci. Technol.*, 24(1):015011, 2014. DOI: 10.1088/0963-0252/24/1/015011.

[45] D. Mei and X. Tu. Atmospheric Pressure Non-Thermal Plasma Activation of CO_2 in a Packed-Bed Dielectric Barrier Discharge Reactor. *ChemPhysChem*, 18(22):3253–3259, 2017. DOI: 10.1002/cphc.201700752.

[46] I. Belov, S. Paulussen, and A. Bogaerts. Appearance of a Conductive Carbonaceous Coating in a CO_2 Dielectric Barrier Discharge and its Influence on the Electrical Properties and the Conversion Efficiency. *Plasma Sources Sci. Technol.*, 25(1):015023, 2016. DOI: 10.1088/0963-0252/25/1/015023.

[47] Y. Uytdenhouwen, S. Van Alphen, I. Michielsen, et al. A Packed-bed DBD Micro Plasma Reactor for CO_2 Dissociation: Does Size Matter? *Chem. Eng. J.*, 348:557–568, 2018. DOI: 10.1016/j.cej.2018.04.210.

[48] I. Michielsen, Y. Uytdenhouwen, J. Pype, et al. CO_2 Dissociation in a Packed Bed DBD Reactor: First Steps Towards a Better Understanding of Plasma Catalysis. *Chem. Eng. J.*, 326:477–488, 2017. DOI: 10.1016/j.cej.2017.05.177.

[49] Q. Yu, M. Kong, T. Liu, J. Fei, and X. Zheng. Characteristics of the Decomposition of CO_2 in a Dielectric Packed-Bed Plasma Reactor. *Plasma Chem. Plasma Process.*, 32(1):153–163, 2012. DOI: 10.1007/s11090-011-9335-y.

[50] S. Paulussen, B. Verheyde, X. Tu, et al. Conversion of Carbon Dioxide to Value-Added Chemicals in Atmospheric Pressure Dielectric Barrier Discharges. *Plasma Sources Sci. Technol.*, 19(3):034015 1–6, 2010. DOI: 10.1088/0963-0252/19/3/034015.

[51] R. Aerts, W. Somers, and A. Bogaerts. Carbon Dioxide Splitting in a Dielectric Barrier Discharge Plasma: A Combined Experimental and Computational Study. *ChemSusChem*, 8(4):702–716, 2015. DOI: 10.1002/cssc.201402818.

[52] W. Wang, D. Mei, X. Tu, and A. Bogaerts. Gliding Arc Plasma for CO_2 Conversion: Better Insights by a Combined Experimental and Modelling Approach. *Chem. Eng. J.*, 330:11–25, 2017. DOI: 10.1016/j.cej.2017.07.133.

[53] T. Nunnally, K. Gutsol, A. Rabinovich, et al. Dissociation of CO_2 in a Low Current Gliding Arc Plasmatron. *J. Phys. D: Appl. Phys.*, 44(27):274009, 2011. DOI: 10.1088/0022-3727/44/27/274009.

[54] M. Ramakers, G. Trenchev, S. Heijkers, W. Wang, and A. Bogaerts. Gliding Arc Plasmatron: Providing an Alternative Method for Carbon Dioxide Conversion. *ChemSusChem*, 10(12):2642–2652, 2017. DOI: 10.1002/cssc.201700589.

[55] T. Silva, N. Britun, T. Godfroid, and R. Snyders. Optical Characterization of a Microwave Pulsed Discharge used for Dissociation of CO_2. *Plasma Sources Sci. Technol.*, 23(2):025009, 2014. DOI: 10.1088/0963-0252/23/2/025009.

[56] T. Silva, N. Britun, T. Godfroid, J. van der Mullen, and R. Snyders. Study of Ar and Ar-CO_2 Microwave Surfaguide Discharges by Optical Spectroscopy. *J. Appl. Phys.*, 119(17):173302, 2016. DOI: 10.1063/1.4947520.

[57] N. Britun, T. Silva, G. Chen, et al. Plasma-assisted CO_2 Conversion: Optimizing Performance via Microwave Power Modulation. *J. Phys. D: Appl. Phys.*, 51(14):144002, 2018. DOI: 10.1088/1361-6463/aab1ad.

[58] A. J. Wolf, T. W. H. Righart, F. J. J. Peeters, W. A. Bongers, and M. C. M. van de Sanden. Implications of thermo-chemical instability on the contracted modes in CO_2 microwave plasmas. *Plasma Sources Sci. Technol.*, 29(2):025005, 2020. DOI: 10.1088/1361-6595/ab5eca.

[59] A. J. Wolf, F. J. J. Peeters, P. W. C. Groen, W. A. Bongers, and M. C. M. van de Sanden. CO_2 Conversion in Nonuniform Discharges: Disentangling Dissociation and Recombination Mechanisms. *J. Phys. Chem. C*, 124(31):16806–16819, 2020. DOI: 10.1021/acs.jpcc.0c03637.

[60] A. J. Wolf, T. W. H. Righart, F. J. J. Peeters, et al. Characterization of CO_2 microwave plasma based on the phenomenon of skin-depth-limited contraction. *Plasma Sources Sci. Technol.*, 28(11):115022, 2019. DOI: 10.1088/1361-6595/ab4e61.

[61] I. Belov, V. Vermeiren, S. Paulussen, and A. Bogaerts. Carbon Dioxide Dissociation in a Microwave Plasma Reactor Operating in a Wide Pressure Range and Different Gas Inlet Configurations. *J. CO_2 Util.*, 24:386–397, 2018. DOI: 10.1016/j.jcou.2017.12.009.

[62] A. P. H. Goede. CO_2 neutral fuels. *EPJ Web of Conferences*, 189:00010, 2018. DOI: 10.1051/epjconf/201818900010.

[63] G. J. van Rooij, D. C. M. van den Bekerom, N. den Harder, et al. Taming microwave plasma to beat thermodynamics in CO_2 dissociation. *Faraday Discuss.*, 183:233–248, 2015. DOI: 10.1039/C5FD00045A.

[64] D. C. M. van den Bekerom, J. M. P. Linares, T. Verreycken, et al. The Importance of Thermal Dissociation in CO_2 Microwave Discharges Investigated by Power Pulsing and Rotational Raman Scattering. *Plasma Sources Sci. Technol.*, 28(5):055015, 2019. DOI: 10.1088/1361-6595/aaf519.

[65] C. Tendero, C. Tixier, P. Tristant, J. Desmaison, and P. Leprince. Atmospheric pressure plasmas: A review. *Spectrochim. Acta, Part B*, 61(1):2–30, 2006. DOI: 10.1016/j.sab.2005.10.003.

[66] A. Bogaerts, E. Neyts, R. Gijbels, and J. van der Mullen. Gas discharge plasmas and their applications. *Spectrochim. Acta, Part B*, 57(4):609–658, 2002. DOI: 10.1016/S0584-8547(01)00406-2.

[67] B. Eliasson, M. Hirth, and U. Kogelschatz. Ozone synthesis from oxygen in dielectric barrier discharges. *J. Phys. D: Appl. Phys.*, 20(11):1421–1437, 1987. DOI: 10.1088/0022-3727/20/11/010.

[68] U. Kogelschatz, B. Eliasson, and W. Egli. From ozone generators to flat television screens: history and future potential of dielectric-barrier discharges. *Pure Appl. Chem.*, 71(10):1819–1828, 1999. DOI: 10.1351/pac199971101819.

[69] I. Michielsen, Y. Uytdenhouwen, A. Bogaerts, and V. Meynen. Altering Conversion and Product Selectivity of Dry Reforming of Methane in a Dielectric Barrier Discharge by Changing the Dielectric Packing Material. *Catalysts*, 9(1):51, 2019. DOI: 10.3390/catal9010051.

[70] S. Sun, H. Wang, D. Mei, X. Tu, and A. Bogaerts. CO_2 conversion in a gliding arc plasma: Performance improvement based on chemical reaction modeling. *J. CO_2 Util.*, 17:220–234, 2017. DOI: 10.1016/j.jcou.2016.12.009.

[71] H. Zhang, L. Li, X. Li, et al. Warm plasma activation of CO_2 in a rotating gliding arc discharge reactor. *J. CO_2 Util.*, 27:472–479, 2018. DOI: 10.1016/j.jcou.2018.08.020.

[72] G. Trenchev, S. Kolev, and A. Bogaerts. A 3D model of a reverse vortex flow gliding arc reactor. *Plasma Sources Sci. Technol.*, 25(3):035014, 2016. DOI: 10.1088/0963-0252/25/3/035014.

[73] M. Ramakers, J. A. Medrano, G. Trenchev, F. Gallucci, and A. Bogaerts. Revealing the arc dynamics in a gliding arc plasmatron: a better insight to improve CO_2 conversion. *Plasma Sources Sci. Technol.*, 26(12):125002, 2017. DOI: 10.1088/1361-6595/aa9531.

[74] S. Heijkers and A. Bogaerts. CO_2 Conversion in a Gliding Arc Plasmatron: Elucidating the Chemistry through Kinetic Modeling. *J. Phys. Chem. C*, 121(41):22644–22655, 2017. DOI: 10.1021/acs.jpcc.7b06524.

[75] R. Sorrentino. *Microwave and RF Engineering.* John Wiley & Sons, Ltd, United Kingdom, 2010.

[76] V. Georgieva, A. Berthelot, T. Silva, et al. Understanding Microwave Surface-Wave Sustained Plasmas at Intermediate Pressure by 2D Modeling and Experiments. *Plasma Processes Polym.*, 14(4-5):1600185, 2017. DOI: 10.1002/ppap.201600185.

[77] M. Moisan and Z. Zakrzewski. Plasma sources based on the propagation of electromagnetic surface waves. *J. Phys. D: Appl. Phys.*, 24(7):1025–1048, 1991. DOI: 10.1088/0022-3727/24/7/001.

[78] P. W. C. Groen, A. J. Wolf, T. W. H. Righart, et al. Numerical model for the determination of the reduced electric field in a CO_2 microwave plasma derived by the principle of impedance matching. *Plasma Sources Sci. Technol.*, 28(7):075016, 2019. DOI: 10.1088/1361-6595/ab1ca1.

[79] T. Silva. *CO_2 decomposition and related processes in microwave discharges studied by optical diagnostic methods.* PhD thesis, Université de Mons, 2015.

[80] M. S. Moss, K. Yanallah, R. W. K. Allen, and F. Pontiga. An Investigation of CO_2 Splitting Using Nanosecond Pulsed Corona Discharge: Effect of Argon Addition on CO_2 Conversion and Energy Efficiency. *Plasma Sources Sci. Technol.*, 26:035009, 2017. DOI: 10.1088/1361-6595/aa5b1d.

[81] L. M. Martini, N. Gatti, G. Dilecce, M. Scotoni, and P. Tosi. Laser Induced Fluorescence in Nanosecond Repetitively Pulsed Discharges for CO_2 Conversion. *Plasma Phys. Controlled Fusion*, 60(1):014016, 2018. DOI: 10.1088/1361-6587/aa8bed.

[82] L. M. Martini, S. Lovascio, G. Dilecce, and P. Tosi. Time-Resolved CO_2 Dissociation in a Nanosecond Pulsed Discharge. *Plasma Chem. Plasma Process.*, 38(4):707–718, 2018. DOI: 10.1007/s11090-018-9893-3.

[83] S. Heijkers, L. M. Martini, G. Dilecce, P. Tosi, and A. Bogaerts. Nanosecond Pulsed Discharge for CO_2 Conversion: Kinetic Modeling To Elucidate the Chemistry and Improve the Performance. *J. Phys. Chem. C*, 123(19):12104–12116, 2019. DOI: 10.1021/acs.jpcc.9b01543.

[84] G. Horváth, J. D. Skalný, and N. J. Mason. FTIR Study of Decomposition of Carbon Dioxide in DC Corona Discharges. *J. Phys. D: Appl. Phys.*, 41(22):225207, 2008. DOI: 10.1088/0022-3727/41/22/225207.

[85] Y. Wen and X. Jiang. Decomposition of CO_2 Using Pulsed Corona Discharges Combined with Catalyst. *Plasma Chem. Plasma Process.*, 21(4):665–678, 2001. DOI: 10.1023/A:1012011420757.

[86] J.-Y. Wang, G.-G. Xia, A. Huang, et al. CO_2 Decomposition Using Glow Discharge Plasmas. *J. Catal.*, 185(1):152–159, 1999. DOI: 10.1006/jcat.1999.2499.

[87] G. Trenchev, A. Nikiforov, W. Wang, S. Kolev, and A. Bogaerts. Atmospheric Pressure Glow Discharge for CO_2 Conversion: Model-based Exploration of the Optimum Reactor Configuration. *Chem. Eng. J.*, 362:830–841, 2019. DOI: 10.1016/j.cej.2019.01.091.

[88] A. Ozkan, A. Bogaerts, and F. Reniers. Routes to increase the conversion and the energy efficiency in the splitting of CO_2 by a dielectric barrier discharge. *J. Phys. D: Appl. Phys.*, 50(8):084004, 2017. DOI: 10.1088/1361-6463/aa562c.

[89] S. C. Kim, M. S. Lim, and Y. N. Chun. Reduction Characteristics of Carbon Dioxide Using a Plasmatron. *Plasma Chem. Plasma Process.*, 34(1):125–143, 2014. DOI: 10.1007/s11090-013-9499-8.

[90] A. Indarto, D. R. Yang, J. W. Choi, H. Lee, and H. K. Song. Gliding Arc Plasma Processing of CO_2 Conversion. *J. Hazard. Mater.*, 146(1-2):309–315, 2007. DOI: 10.1016/j.jhazmat.2006.12.023.

[91] L. F. Spencer and a. D. Gallimore. CO_2 dissociation in an atmospheric pressure plasma/catalyst system: a study of efficiency. *Plasma Sources Sci. Technol.*, 22(1):015019, 2012. DOI: 10.1088/0963-0252/22/1/015019.

[92] L. D. Pietanza, G. Colonna, G. D'Ammando, a. Laricchiuta, and M. Capitelli. Vibrational Excitation and Dissociation Mechanisms of CO_2 under Non-Equilibrium Discharge and Post-Discharge Conditions. *Plasma Sources Sci. Technol.*, 24(4):042002, 2015. DOI: 10.1088/0963-0252/24/4/042002.

[93] L. D. Pietanza, G. Colonna, G. D'Ammando, A. Laricchiuta, and M. Capitelli. Electron Energy Distribution Functions and Fractional Power Transfer in "Cold" and Excited CO_2 Discharge and Post Discharge Conditions. *Phys. Plasma*, 23(1), 2016. DOI: 10.1063/1.4940782.

[94] L. D. Pietanza, G. Colonna, G. D'Ammando, A. Laricchiuta, and M. Capitelli. Non Equilibrium Vibrational Assisted Dissociation and Ionization Mechanisms in Cold CO_2 Plasmas. *Chem. Phys.*, 468:44–52, 2016. DOI: 10.1016/j.chemphys.2016.01.007.

[95] L. D. Pietanza, G. Colonna, V. Laporta, et al. Influence of Electron Molecule Resonant Vibrational Collisions over the Symmetric Mode and Direct Excitation-Dissociation Cross Sections of CO_2 on the Electron Energy Distribution Function and Dissociation Mechanisms in Cold Pure CO_2 Plasmas. *J. Phys. Chem. A*, 120(17):2614–2628, 2016. DOI: 10.1021/acs.jpca.6b01154.

[96] L. D. Pietanza, G. Colonna, G. D'Ammando, and M. Capitelli. Time-Dependent Coupling of Electron Energy Distribution Function, Vibrational Kinetics of the Asymmetric Mode of CO_2 and Dissociation, Ionization and Electronic Excitation Kinetics under Discharge and Post-Discharge Conditions. *Plasma Phys. Controlled Fusion*, 59(1):014035, 2017. DOI: 10.1088/0741-3335/59/1/014035.

[97] T. Silva, M. Grofulović, B. L. M. Klarenaar, et al. Kinetic study of low-temperature CO_2 plasmas under non-equilibrium conditions. I. Relaxation of vibrational energy. *Plasma Sources Sci. Technol.*, 27(1):015019, 2018. DOI: 10.1088/1361-6595/aaa56a.

[98] M. Grofulović, T. Silva, B. L. M. Klarenaar, et al. Kinetic study of CO_2 plasmas under non-equilibrium conditions. II. Input of vibrational energy. *Plasma Sources Sci. Technol.*, 27(11):115009, 2018. DOI: 10.1088/1361-6595/aadb60.

[99] M. Grofulović, L. L. Alves, and V. Guerra. Electron-Neutral Scattering Cross Sections for CO_2: a Complete and Consistent Set and an Assessment of Dissociation. *J. Phys. D: Appl. Phys.*, 49:395207, 2016. DOI: 10.1088/0022-3727/49/39/395207.

[100] A. Berthelot and A. Bogaerts. Modeling of Plasma-Based CO_2 Conversion: Lumping of the Vibrational Levels. *Plasma Sources Sci. Technol.*, 25(4):045022, 2016. DOI: 10.1088/0963-0252/25/4/045022.

[101] A. Berthelot and A. Bogaerts. Modeling of CO_2 Splitting in a Microwave Plasma: How to Improve the Conversion and Energy Efficiency. *J. Phys. Chem. C*, 121(15):8236–8251, 2017. DOI: 10.1021/acs.jpcc.6b12840.

[102] R. Aerts, T. Martens, and A. Bogaerts. Influence of Vibrational States on CO_2 Splitting by Dielectric Barrier Discharges. *J. Phys. Chem. C*, 116(44):23257–23273, 2012. DOI: 10.1021/jp307525t.

[103] T. Kozák and A. Bogaerts. Splitting of CO_2 by Vibrational Excitation in Non-Equilibrium Plasmas: a Reaction Kinetics Model. *Plasma Sources Sci. Technol.*, 23(4):045004, 2014. DOI: 10.1088/0963-0252/23/4/045004.

[104] T. Kozák and A. Bogaerts. Evaluation of the Energy Efficiency of CO_2 Conversion in Microwave Discharges using a Reaction Kinetics Model. *Plasma Sources Sci. Technol.*, 24(1):015024, 2015. DOI: 10.1088/0963-0252/24/1/015024.

[105] W. Wang, A. Berthelot, S. Kolev, X. Tu, and A. Bogaerts. CO_2 Conversion in a Gliding Arc Plasma: 1D Cylindrical Discharge Model. *Plasma Sources Sci. Technol.*, 25(6):065012, 2016. DOI: 10.1088/0963-0252/25/6/065012.

[106] L. D. Pietanza, G. Colonna, and M. Capitelli. Kinetics versus thermodynamics on CO_2 dissociation in high temperature microwave discharges. *Plasma Sources Sci. Technol.*, 29(3):035022, 2020. DOI: 10.1088/1361-6595/ab6e5a.

[107] V. Kotov and P. M. J. Koelman. Plug flow reactor model of the plasma chemical conversion of CO_2. *Plasma Sources Sci. Technol.*, 28(9):095002, 2019. DOI: 10.1088/1361-6595/ab3774.

[108] V. Vermeiren and A. Bogaerts. Plasma-Based CO_2 Conversion: To Quench or Not to Quench? *J. Phys. Chem. C*, 124(34):18401–18415, 2020. DOI: 10.1021/acs.jpcc.0c04257.

[109] G. Trenchev, S. Kolev, W. Wang, M. Ramakers, and A. Bogaerts. CO_2 Conversion in a Gliding Arc Plasmatron: Multidimensional Modeling for Improved Efficiency. *J. Phys. Chem. C*, 121(44):24470–24479, 2017. DOI: 10.1021/acs.jpcc.7b08511.

[110] S. Pancheshnyi, B. Eismann, G. Hagelaar, and L. Pitchford. Zdplaskin, 2008.

[111] J. A. Bittencourt. *Fundamentals of Plasma Physics*. Springer New York, New York, NY, USA, 2004. DOI: 10.1007/978-1-4757-4030-1.

[112] M. A. Lieberman and A. J. Lichtenberg. *Principles of Plasma Discharges and Materials Processing*. John Wiley & Sons, Inc., Hoboken, NJ, USA, 2005. DOI: 10.1002/0471724254.

[113] P. Koelman, S. Heijkers, S. Tadayon Mousavi, et al. A Comprehensive Chemical Model for the Splitting of CO_2 in Non-Equilibrium Plasmas. *Plasma Processes Polym.*, 14(4-5):1600155, 2017. DOI: 10.1002/ppap.201600155.

[114] A. Berthelot and A. Bogaerts. Modeling of CO_2 Plasma: Effect of Uncertainties in the Plasma Chemistry. *Plasma Sources Sci. Technol.*, 26(11):115002, 2017. DOI: 10.1088/1361-6595/aa8ffb.

[115] K. P. Huber and G. Herzberg. *Molecular Spectra and Molecular Structure IV. Constant of diatomic molecules*. New York, NY, USA, 1979.

[116] I. Suzuki. General Anharmonic Force Constants of Carbon Dioxide. *J. Mol. Spectrosc.*, 25(4):479–500, 1968. DOI: 10.1016/S0022-2852(68)80018-9.

[117] J. A. Blauer and G. R. Gilmore. A Survey of Vibrational Relaxation Rate Data for Processes Important to CO_2-N_2-H_2O Infrared Plume Radiation. Technical report afrpl-tr-73-57, Ultrasystems, Inc., 1973.

[118] G. Herzberg. *Molecular Spectra and Molecular Structure: Spectra of Diatomic Molecules*, volume 1. Van Nostrand, New York, USA, 1950.

[119] NIST Chemistry WebBook, NIST Standard Reference Database Number 69 Constants of Diatomic Molecules, retrieved 4 December 2013.

[120] A. Bogaerts, W. Wang, A. Berthelot, and V. Guerra. Modeling Plasma-Based CO_2 Conversion : Crucial Role of the Dissociation Cross Section. *Plasma Sources Sci. Technol.*, 25:1–23, 2016. DOI: 10.1088/0963-0252/25/5/055016.

[121] J. E. Land. Electron Scattering Cross Sections for Momentum Transfer and Inelastic Excitation in Carbon Monoxide. *J. Appl. Phys.*, 49(12):5716–5721, 1978. DOI: 10.1063/1.324589.

[122] L. L. Alves. The IST-LISBON database on LXCat. *J. Phys.: Conf. Ser.*, 565(1):012007, 2014. DOI: 10.1088/1742-6596/565/1/012007.

[123] L. C. Pitchford, L. L. Alves, K. Bartschat, et al. LXCat: an Open-Access, Web-Based Platform for Data Needed for Modeling Low Temperature Plasmas. *Plasma Processes Polym.*, 14(1-2):1600098, 2017. DOI: 10.1002/ppap.201600098.

[124] V. Vermeiren and A. Bogaerts. Supersonic Microwave Plasma: Potential and Limitations for Energy-Efficient CO_2 Conversion. *J. Phys. Chem. C*, 122(45):25869–25881, 2018. DOI: 10.1021/acs.jpcc.8b08498.

[125] V. Vermeiren and A. Bogaerts. Improving the Energy Efficiency of CO_2 Conversion in Nonequilibrium Plasmas through Pulsing. *J. Phys. Chem. C*, 123(29):17650–17665, 2019. DOI: 10.1021/acs.jpcc.9b02362.

[126] R. N. Schwartz, Z. I. Slawsky, and K. F. Herzfeld. Calculation of Vibrational Relaxation Times in Gases. *J. Chem. Phys.*, 20(10):1591–1599, 1952. DOI: 10.1063/1.1700221.

[127] R. D. Sharma and C. A. Brau. Energy Transfer in Near-Resonant Molecular Collisions due to Long-Range Forces with Application to Transfer of Vibrational Energy from ν_3 Mode of CO_2 to N_2. *J. Chem. Phys.*, 50(2):924–930, 1969. DOI: 10.1063/1.1671145.

[128] V. Joly and A. Roblin. Vibrational relaxation of CO_2 (m, n^l, p) in a CO_2-N_2 mixture. Part 1: Survey of available data. *Aerosp. Sci. Technol.*, 3(4):229–238, 1999. DOI: 10.1016/S1270-9638(99)80045-5.

[129] I. V. Adamovich and J. W. Rich. Three-dimensional nonperturbative analytic model of vibrational energy transfer in atom–molecule collisions. *J. Chem. Phys.*, 109(18):7711–7724, 1998. DOI: 10.1063/1.477417.

[130] I. V. Adamovich, S. O. Macheret, J. W. Rich, and C. E. Treanor. Vibrational energy transfer rates using a forced harmonic oscillator model. *J. Thermophys Heat Transfer*, 12(1):57–65, 1998. DOI: 10.2514/2.6302.

[131] G. Billing Sørensen. Semiclassical three-dimensional model for vibrational energy transfer in diatomic molecules. *Chem. Phys.*, 5(2):244–254, 1974. DOI: 10.1016/0301-0104(74)80022-4.

[132] G. D. Billing and E. Fisher. VV and VT rate coefficients in N_2 by a quantum-classical model. *Chem. Phys.*, 43(3):395–401, 1979. DOI: 10.1016/0301-0104(79)85207-6.

[133] L. da Silva, M. J. Vargas, and J. Loureiro. Stellar co_2 version 2: A database for vibrationally-specific excitation and dissociation rates for carbon dioxide. Technical report, Instituto de Plasmas e Fusão Nuclear, Instituto Superior Técnico, Lisboa, Portugal, 2018.

[134] A. Lombardi, N. Faginas-Lago, L. Pacifici, and G. Grossi. Energy transfer upon collision of selectively excited CO_2 molecules: State-to-state cross sections and probabilities for modeling of atmospheres and gaseous flows. *J. Chem. Phys.*, 143(3):034307, 2015. DOI: 10.1063/1.4926880.

[135] M. Bartolomei, F. Pirani, A. Laganà, and A. Lombardi. A full dimensional grid empowered simulation of the $CO_2 + CO_2$ processes. *J. Comput. Chem.*, 33(22):1806–1819, 2012. DOI: 10.1002/jcc.23010.

[136] P. K. Kundu and I. M. Cohen. *Buoyancy-Driven Exchange Flow Through Small Openings in Horizontal Partitions*. Elsevier, San Diego, USA, 1990.

[137] K. Peerenboom, M. Khaji, and G. Degrez. Pooling through Cooling: Creating Optimal Vibrational Non-Equilibrium in CO_2 by Supersonic Expansion. *J. Phys. D: Appl. Phys.*, 50(19):195201, 2017. DOI: 10.1088/1361-6463/aa695e.

[138] J. F. Quaatz, M. Giglmaier, S. Hickel, and N. A. Adams. Large-Eddy Simulation of a Pseudo-Shock System in a Laval Nozzle. *Int. J. Heat Fluid Flow*, 49:108–115, 2014. DOI: 10.1016/j.ijheatfluidflow.2014.05.006.

[139] D. C. Wilcox. *Turbulence Modeling for CFD*. DCW industries Inc., La Canada, USA, 3 edition, 2006.

[140] T. Poinsot and D. Veynante. *Theoretical and Numerical Combustion*. Edwards Inc., Philadelphia, USA, 2005.

[141] J. Larsson. *Numerical Simulation of Turbulent Flows for Turbine Blade Heat Transfer Applications*. PhD thesis, Chalmers University of Technology, 1998.

[142] Y. Kabouzi, M. D. Calzada, M. Moisan, K. C. Tran, and C. Trassy. Radial Contraction of Microwave-Sustained Plasma Columns at Atmospheric Pressure. *J. Appl. Phys.*, 91(3):1008–1019, 2002. DOI: 10.1063/1.1425078.

[143] A. H. Shapiro. *The Dynamics and Thermodynamics of Compressible Fluid Flow*, volume 1. John Wiley & Sons, 1953.

[144] J. D. Anderson. *Modern compressible flow*. Number 1976. McGraw-Hill Publishing company, New York, USA, 1990.

[145] P. P. Wegener and D. J. Cagliostro. Periodic Nozzle Flow with Heat Addition. *Combust. Sci. Technol.*, 6(5):269–277, 1973. DOI: 10.1080/00102207308952329.

[146] A. Fridman and L. A. Kennedy. *Plasma Physics and Engineering: Second edition*. CRC Press, Boca Raton, USA, 2011.

[147] P. J. Bruggeman, N. Sadeghi, D. C. Schram, and V. Linss. Gas Temperature Determination from Rotational Lines in Non-Equilibrium Plasmas: a review. *Plasma Sources Sci. Technol.*, 23(2):023001, 2014. DOI: 10.1088/0963-0252/23/2/023001.

[148] C. Park. The limits of two-temperature kinetic model in air. In *48th AIAA Aerospace Sciences Meeting Including the New Horizons Forum and Aerospace Exposition*, pages 1–13, Reston, Virigina, 2010. American Institute of Aeronautics and Astronautics. DOI: 10.2514/6.2010-911.

[149] A. Munafó, M. Panesi, R. Jaffe, T. Magin, and A. Lani. Vibrational State to State Kinetics in Expanding and Compressing Nitrogen Flows. pages 1–24. American Institute of Aeronautics and Astronautics, 2010. DOI: 10.2514/6.2010-4335.

[150] A. Munafò, M. Panesi, R. L. Jaffe, et al. QCT-Based Vibrational Collisional Models Applied to Nonequilibrium Nozzle Flows. *Eur. Phys. J. D*, 66(7):188, 2012. DOI: 10.1140/epjd/e2012-30079-3.

[151] K. Matsuo, Y. Miyazato, and H.-d. Kim. Shock train and pseudo-shock phenomena in internal gas flows. *Prog. Aerosp. Sci.*, 35(1):33–100, 1999. DOI: 10.1016/S0376-0421(98)00011-6.

[152] T. Ikui, K. Matsuo, and M. Nagai. The Mechanism of Pseudo-Shock Waves. *Bulletin of JSME*, 17(108):731–739, 1974. DOI: 10.1299/jsme1958.17.731.

[153] C. R. Barber. The Sublimation Temperature of Carbon Dioxide. *Br. J. Appl. Phys.*, 17(3):391–397, 1966. DOI: 10.1088/0508-3443/17/3/312.

[154] O. F. Hagena and W. Obert. Cluster Formation in Expanding Supersonic Jets: Effect of Pressure, Temperature, Nozzle Size, and Test Gas. *J. Chem. Phys.*, 56(5):1793–1802, 1972. DOI: 10.1063/1.1677455.

[155] E. A. D. Carbone, S. Hübner, J. M. Palomares, and J. J. A. M. van der Mullen. The Radial Contraction of Argon Microwave Plasmas Studied by Thomson Scattering. *J. Phys. D: Appl. Phys.*, 45(34):345203, 2012. DOI: 10.1088/0022-3727/45/34/345203.

[156] A. Ozkan, T. Dufour, T. Silva, et al. DBD in Burst Mode: Solution for more Efficient CO_2 Conversion? *Plasma Sources Sci. Technol.*, 25(5):055005, 2016. DOI: 10.1088/0963-0252/25/5/055005.

[157] A. Ozkan, T. Dufour, T. Silva, et al. The Influence of Power and Frequency on the Filamentary Behavior of a Flowing DBD - Application to the splitting of CO_2. *Plasma Sources Sci. Technol.*, 25(2):025013, 2016. DOI: 10.1088/0963-0252/25/2/025013.

[158] B. L. M. Klarenaar, R. Engeln, D. C. M. van den Bekerom, et al. Time Evolution of Vibrational Temperatures in a CO_2 Glow Discharge Measured with Infrared Absorption Spectroscopy. *Plasma Sources Sci. Technol.*, 26(11):115008, 2017. DOI: 10.1088/1361-6595/aa902e.

[159] B. L. M. Klarenaar, A. S. Morillo-Candas, M. Grofulović, et al. Excitation and relaxation of the asymmetric stretch mode of CO_2 in a pulsed glow discharge. *Plasma Sources Sci. Technol.*, 28(3):035011, 2019. DOI: 10.1088/1361-6595/aada5e.

[160] R. G. Buser and J. J. Sullivan. Initial Processes in CO_2 Glow Discharges. *J. Appl. Phys.*, 41(2):472–479, 1970. DOI: 10.1063/1.1658700.

[161] D. C. M. van den Bekerom, A. van de Steeg, M. C. M. van de Sanden, and G. J. van Rooij. Mode resolved heating dynamics in pulsed microwave CO_2 plasma from laser Raman scattering. *J. Phys. D: Appl. Phys.*, 53(5):054002, 2020. DOI: 10.1088/1361-6463/ab5311.

[162] A. Hurlbatt, A. R. Gibson, S. Schröter, et al. Concepts, Capabilities, and Limitations of Global Models: A Review. *Plasma Processes Polym.*, 14(1-2):1600138, 2017. DOI: 10.1002/ppap.201600138.

[163] S. Van Alphen, V. Vermeiren, T. Butterworth, et al. Power Pulsing To Maximize Vibrational Excitation Efficiency in N_2 Microwave Plasma: A Combined Experimental and Computational Study. *J. Phys. Chem. C*, 124(3):1765–1779, 2020. DOI: 10.1021/acs.jpcc.9b06053.

[164] A. V. Phelps. Phelps Database from www.lxcat.net (retrieved September 4, 2014).

[165] C. Tian and C. R. Vidal. Cross Sections of the Electron Impact Dissociative Ionization of CO, CH_4 and C_2H_2. *J. Phys. B: At. Mol. Opt. Phys.*, 31(4):895–909, 1998. DOI: 10.1088/0953-4075/31/4/031.

[166] D. Rapp and D. D. Briglia. Total Cross Sections for Ionization and Attachment in Gases by Electron Impact. II. Negative Ion Formation. *J. Chem. Phys.*, 43(5):1480–1489, 1965. DOI: 10.1063/1.1696958.

[167] S. A. Lawton and A. V. Phelps. Excitation of the $b^1\Sigma_g^+$ State of O_2 by Low Energy Electrons. *J. Chem. Phys.*, 69(3):1055, 1978. DOI: 10.1063/1.436700.

[168] C. S. Weller and M. A. Biondi. Measurements of Dissociative Recombination of CO_2^+ Ions with Electrons. *Phys. Rev. Lett.*, 19(2):59–61, 1967. DOI: 10.1103/PhysRevLett.19.59.

[169] J. Thoenes and S. C. Kurzius. Plasma Chemistry Processes in the Closed Cycle EDL. Technical report drcpm-hel-cr-79-11-vol-1, Lockheed Missiles and Space Co Inc., Huntsville AL, 1979.

[170] T. G. Beuthe and J.-S. Chang. Chemical Kinetic Modelling of Non-Equilibrium Ar-CO_2 Thermal Plasmas. *Jpn. J. Appl. Phys.*, 36(Part 1, No. 7B):4997–5002, 1997. DOI: 10.1143/JJAP.36.4997.

[171] J. B. A. Mitchell and H. Hus. The Dissociative Recombination and Excitation of CO^+. *J. Phys. B: At. Mol. Phys.*, 18(3):547–555, 1985. DOI: 10.1088/0022-3700/18/3/029.

[172] D. McElroy, C. Walsh, A. J. Markwick, et al. The UMIST database for astrochemistry 2012. *Astron. Astrophys.*, 550:A36, 2013. DOI: 10.1051/0004-6361/201220465.

[173] D. Albritton. Ion-Neutral Reaction-Rate Constants Measured in Flow Reactors through 1977. *At. Data Nucl. Data Tables*, 22(1):1–101, 1978. DOI: 10.1016/0092-640X(78)90027-X.

[174] N. Adams, D. Smith, and D. Grief. Reactions of H_nCO^+ Ions with Molecules at 300 K. *Int. J. Mass Spectrom. Ion Phys.*, 26(4):405–415, 1978. DOI: 10.1016/0020-7381(78)80059-X.

[175] F. C. Fehsenfeld and E. E. Ferguson. Laboratory Studies of Negative Ion Reactions with Atmospheric Trace Constituents. *J. Chem. Phys.*, 61(8):3181–3193, 1974. DOI: 10.1063/1.1682474.

[176] M. Mcfarland, D. L. Albritton, F. C. Fehsenfeld, E. E. Ferguson, and A. L. Schmeltekopf. Flow-Drift Technique for Ion Mobility and Ion-Molecule Reaction Rate Constant Measurements. III. Negative Ion Reactions of O^- with CO, NO, H_2, and D_2. *J. Chem. Phys.*, 59(12):6629–6635, 1973. DOI: 10.1063/1.1680043.

[177] D. Price and J. Moruzzi. Negative Ion Molecule Reactions in CO_2 at High Pressures and Temperatures. *Vacuum*, 24(11-12):591–593, 1974. DOI: 10.1016/0042-207X(74)90038-4.

[178] F. C. Fehsenfeld, A. L. Schmeltekopf, H. I. Schiff, and E. E. Ferguson. Laboratory Measurements of Negative Ion Reactions of Atmospheric Interest. *Planet. Space Sci.*, 15(2):373–379, 1967. DOI: 10.1016/0032-0633(67)90201-2.

[179] S. G. Belostotsky, D. J. Economou, D. V. Lopaev, and T. V. Rakhimova. Negative Ion Destruction by $O(^3P)$ Atoms and $O_2(a^1\Delta_g)$ Molecules in an Oxygen Plasma. *Plasma Sources Sci. Technol.*, 14(3):532–542, 2005. DOI: 10.1088/0963-0252/14/3/016.

[180] J. L. Pack and A. V. Phelps. Electron Attachment and Detachment. II. Mixtures of O_2 and CO_2 and of O_2 and H_2O. *J. Chem. Phys.*, 45(11):4316–4329, 1966. DOI: 10.1063/1.1727491.

[181] M. H. Bortner, T. Bourer, and C. A. Blank. Defense Nuclear Agency Reaction Rate Handbook, Second Edition. Technical report ad 763699, 1972.

[182] J. B. Hasted and R. A. Smith. The Detachment of Electrons from Negative Ions. *Proc. R. Soc. London, Ser. A*, 235(1202):349–353, 1956. DOI: 10.1098/rspa.1956.0087.

[183] L. Frommhold. Über Verzögerte Elektronen in Elektronenlawinen, insbesondere in Sauerstoff und Luft, durch Bildung und Zerfall Negativer Ionen (O^-). *Fortschr. Phys.*, 12(11):597–642, 1964. DOI: 10.1002/prop.19640121102.

[184] J. T. Gudmundsson. A Critical Review of the Reaction set for a Low Pressure Oxygen Processing Discharge. Technical report rh-17-2004, University of Iceland, 2004.

[185] M. Burmeister and P. Roth. ARAS Measurements on the Thermal Decomposition of CO_2 Behind Shock Waves. *AIAA Journal*, 28(3):402–405, 1990. DOI: 10.2514/3.10406.

[186] T. C. Clark, S. H. Garnett, and G. B. Kistiakowsky. Reaction of Carbon Dioxide with Atomic Oxygen and the Dissociation of Carbon Dioxide in Shock Waves. *J. Chem. Phys.*, 51(7):2885–2891, 1969. DOI: 10.1063/1.1672428.

[187] D. Husain and A. N. Young. Kinetic Investigation of Ground State Carbon Atoms, $C(2^3P_J)$. *J. Chem. Soc., Faraday Trans. 2*, 71:525, 1975. DOI: 10.1039/f29757100525.

[188] R. R. Baldwin, D. Jackson, A. Melvin, and B. N. Rossiter. The Second Limit of Hydrogen + Carbon Monoxide + Oxygen Mixtures. *Int. J. Chem. Kinet.*, 4(3):277–292, 1972. DOI: 10.1002/kin.550040305.

[189] W. Tsang and R. F. Hampson. Chemical Kinetic Data Base for Combustion Chemistry. Part I. Methane and Related Compounds. *J. Phys. Chem. Ref. Data*, 15(3):1087–1279, 1986. DOI: 10.1063/1.555759.

[190] A. J. Dean, D. F. Davidson, and R. K. Hanson. A Shock Tube Study of Reactions of Carbon Atoms with Hydrogen and Oxygen using Excimer Photolysis of C_3O_2 and Carbon Atom Atomic Resonance Absorption Spectroscopy. *J. Phys. Chem.*, 95(1):183–191, 1991. DOI: 10.1021/j100154a037.

[191] D. L. Baulch, D. D. Drysdale, J. Duxbury, and S. Grant. *Evaluated Kinetic Data for High Temperature Reactions, Volume 3: Homogeneous Gas Phase Reactions of the O_2-O_3 System, the CO-O_2-H_2 System, and of the Sulphur-containing Species.* Butterworth, London, UK, 1976.

[192] C. J. S. M. Simpson, T. R. D. Chandler, and A. C. Strawson. Vibrational Relaxation in CO_2 and CO_2–Ar Mixtures Studied Using a Shock Tube and a Laser–Schlieren Technique. *J. Chem. Phys.*, 51(5):2214–2219, 1969. DOI: 10.1063/1.1672319.

[193] R. L. Taylor and S. Bitterman. Survey of Vibrational Relaxation Data for Processes Important in the CO_2-N_2 Laser System. *Rev. Mod. Phys.*, 41(1):26–47, 1969. DOI: 10.1103/RevModPhys.41.26.

[194] W. A. Rosser, A. D. Wood, and E. T. Gerry. Deactivation of Vibrationally Excited Carbon Dioxide (ν_3) by Collisions with Carbon Dioxide or with Nitrogen. *J. Chem. Phys.*, 50(11):4996–5008, 1969. DOI: 10.1063/1.1670996.

[195] K. F. Herzfeld. Deactivation of Vibrations by Collision in the Presence of Fermi Resonance. *J. Chem. Phys.*, 47(2):743–752, 1967. DOI: 10.1063/1.1711947.

[196] M. Capitelli, C. M. Ferreira, B. F. Gordiets, and A. I. Osipov. *Plasma Kinetics in Atmospheric Gases*. Springer Berlin Heidelberg, Berlin, Germany, 2000.

[197] R. D. Sharma. Near-Resonant Vibrational Energy Transfer Among Isotopes of CO_2. *Phys. Rev.*, 177(1):102–107, 1969. DOI: 10.1103/PhysRev.177.102.

[198] T. G. Kreutz, J. A. O'Neill, and G. W. Flynn. Diode Laser Absorption Probe of Vibration-Vibration Energy Transfer in CO_2. *J. Phys. Chem.*, 91(22):5540–5543, 1987. DOI: 10.1021/j100306a008.

[199] R. L. DeLeon and J. Rich. Vibrational Energy Exchange Rates in Carbon Monoxide. *Chem. Phys.*, 107(2-3):283–292, 1986. DOI: 10.1016/0301-0104(86)85008-X.

[200] C. Flament, T. George, K. Meister, et al. Nonequilibrium Vibrational Kinetics of Carbon Monoxide at high Translational Mode Temperatures. *Chem. Phys.*, 163(2):241–262, 1992. DOI: 10.1016/0301-0104(92)87106-J.

[201] Y. Itikawa. Cross Sections for Electron Collisions with Carbon Monoxide. *J. Phys. Chem. Ref. Data*, 44(1):013105, 2015. DOI: 10.1063/1.4913926.

[202] S. C. Baber and A. M. Dean. Reaction of atomic oxygen with carbon dioxide behind reflected shock waves. *J. Chem. Phys.*, 60(1):307–313, 1974. DOI: 10.1063/1.1680785.

[203] L. Drummond. Shock-initiated exothermic reactions. IV. The oxidation of carbon monoxide. *Aust. J. Chem.*, 21(11):2631, 1968. DOI: 10.1071/CH9682631.

[204] H. Hokazono and H. Fujimoto. Theoretical analysis of the CO_2 molecule decomposition and contaminants yield in transversely excited atmospheric CO_2 laser discharge. *J. Appl. Phys.*, 62(5):1585–1594, 1987. DOI: 10.1063/1.339606.

[205] J. Woodall, M. Agúndez, A. J. Markwick-Kemper, and T. J. Millar. The UMIST database for astrochemistry 2006. *Astron & Astr*, 466(3):1197–1204, 2007. DOI: 10.1051/0004-6361:20064981.

[206] J. T. Gudmundsson and E. G. Thorsteinsson. Oxygen discharges diluted with argon: dissociation processes. *Plasma Sources Sci. Technol.*, 16(2):399–412, 2007. DOI: 10.1088/0963-0252/16/2/025.